metals

Special Issue Reprint

Design, Processing and Characterization of Metals and Alloys

Edited by
Qinghuan Huo

mdpi.com/journal/metals

MDPI

Design, Processing and Characterization of Metals and Alloys

Design, Processing and Characterization of Metals and Alloys

Guest Editor

Qinghuan Huo

MDPI

Basel • Beijing • Wuhan • Barcelona • Belgrade • Novi Sad • Cluj • Manchester

Guest Editor
Qinghuan Huo
School of Materials Science
and Engineering
Central South University
Changsha
China

Editorial Office
MDPI AG
Grosspeteranlage 5
4052 Basel, Switzerland

This is a reprint of the Special Issue, published open access by the journal *Metals* (ISSN 2075-4701), freely accessible at: https://www.mdpi.com/journal/metals/special_issues/1B44F94487.

For citation purposes, cite each article independently as indicated on the article page online and as indicated below:

Lastname, A.A.; Lastname, B.B. Article Title. *Journal Name* **Year**, *Volume Number*, Page Range.

ISBN 978-3-7258-5633-6 (Hbk)
ISBN 978-3-7258-5634-3 (PDF)
https://doi.org/10.3390/books978-3-7258-5634-3

Contents

About the Editor

Qinghuan Huo

Qinghuan Huo is an Associate Professor in the School of Materials Science and Engineering, Central South University. He received a bachelor's degree in materials science and engineering at Central South University in 2011, obtained a master's degree in materials processing at Central South University in 2013, and obtained his doctorate degree in materials science at Tohoku University in 2017. He become one of the special researchers in the Department of Materials Science, Tohoku University, focusing on the special processing methods of Mg alloys. He joined Central South University in 2018 as an Associate Professor in the Department of Materials Processing in the School of Materials Science and Engineering. His research fields are microstructure characterization, plastic processing, and mechanical behaviors of light metals. Current research activities include the strength, ductility, creep, fatigue, plastic deformation, microstructure characterization, dislocation slip, dynamic precipitation and twinning of Mg alloys. He has taught two relevant undergraduate courses and one relevant graduate course, published over 60 academic papers in the journals ranking in JCR Q1 (as a First Author and Corresponding Author), and holds more than 20 patents for invention.

metals

MDPI

Editorial

Design, Processing and Characterization of Metals and Alloys

Qinghuan Huo

School of Materials Science and Engineering, Central South University, Changsha 410083, China; huoqinghuan@csu.edu.cn

The present Special Issue entitled "Design, Processing and Characterization of Metals and Alloys" aims to report the close relation among composition design, plastic processing, microstructure characterization of all metals and alloys such as iron, steel, Ti alloy and Mg alloy. In addition, this Special Issue also focuses on the improvement of mechanical properties and the optimization of service performance.

The work conducted by Suman et al. (contribution 1) provides valuable insights for optimizing high-chromium cast irons to enhance material performance and durability in demanding erosive environments by tailoring carbide distribution to specific operational conditions. In the studies on steel and multi-component alloys (contributions 2–4), the microstructure characterizations and macroscopic calculations are carried out to reveal the effect of metallurgical processes on mechanical properties. The microstructure evolutions of Ti alloy during hot processing and relevant methods for enhancing mechanical properties are also deeply studied by researchers (contributions 5,6). Their results point out that the particle-reinforced thought can be successfully applied to the dual-phase Ti alloy. Considering the low strength of present Mg alloys (contribution 7), lamellar structure is induced on the basis of the Mg-Gd series and excellent tensile results are achieved. Focusing on the high cost of rare-earth elements used for processing Mg alloys (contribution 8), die casting is also put forward for producing Mg-based materials.

Therefore, the close relations among design, processing and characterization of metals and alloys are provided in this Special Issue. We believe that the new information and innovations can be provided to researchers in Materials Science and Engineering. We welcome researchers to cite the publications in this Special Issue.

Funding: This research was funded by the Science and Technology Innovation Program of Hunan Province, grant number 2024RC3010.

Conflicts of Interest: The author declares no conflicts of interest.

List of Contributions:

1. Suman, A.; Fortini, A.; Zanini, N. Microstructural Insights into Solid Particle Erosion in a High-Chromium Cast Iron. *Metals* **2025**, *15*, 6.
2. Tedesco, M.M.; Licignano, P.; Mara, A.; Plano, S.; Gabellone, D.; Basso, M.; Baricco, M. Mechanical and Metallurgical Characterization of Advance High Strength Steel Q&P1180 Produced by Two Different Suppliers. *Metals* **2025**, *15*, 301.
3. Šimeková, B.; Dománková, M.; Kovaříková, I.; Kovačócy, P.; Martinkovič, M.; Šimek, M.; Ciuła, L. Microstructural and Mechanical Characterization of the Laser Beam Welded SAF 2507 Super-Duplex Stainless Steel. *Metals* **2024**, *14*, 1184.
4. Qiu, Y.; Shi, X.; Liu, X.; Chen, Z.; Wang, J.; Liu, X.; Bai, X.; He, F.; Wang, Z. Effect of Annealing and Double Aging on the Microstructure and Mechanical Properties of Hot-Rolled Al17Cr10Fe36Ni36Mo1 Alloy. *Metals* **2024**, *14*, 726.

5. Park, C.; Jo, H.; Kim, J.H.; Yeom, J.; Kang, N.; Lee, W. Hot-Deformed Microstructure and Texture of Ti-62222 Alloy. *Metals* **2025**, *15*, 244.
6. Qian, S.; Wang, N.; Chen, F.; Sun, Y.; Zhao, J.; Chang, H.; Feng, L.; Zhou, L. Microstructure Evolution and Mechanical Properties of B4C-Reinforced TC11 + xFe Composites Fabricated by HIP. *Metals* **2025**, *15*, 37.
7. Garcés, G.; Medina, J.; Pérez, P.; Barea, R.; Lim, H.; Kim, S.K.; Maawad, E.; Schell, N.; Adeva, P. Study of Tensile and Compressive Behavior of ECO-Mg97Gd2Zn1 Alloys Containing Long-Period Stacking Ordered Phase with Lamellar Structure. *Metals* **2024**, *14*, 530.
8. Han, J.T.; Ryu, C.M.; Moon, S.J. Investigation of Properties in Magnesium Alloy Thin Plates after Die Casting Processes. *Metals* **2024**, *14*, 970.

metals

MDPI

Article

Mechanical and Metallurgical Characterization of Advance High Strength Steel Q&P1180 Produced by Two Different Suppliers

Michele Maria Tedesco [1,2], Pietro Licignano [3], Antonio Mara [1], Stefano Plano [1], Davide Gabellone [1], Matteo Basso [4] and Marcello Baricco [2,*]

[1] Stellantis, Metals & Anticorrosion Department, Corso Settembrini 40, 10135 Turin, TO, Italy; michelemaria.tedesco@crf.it (M.M.T.); antonio.mara@stellantis.com (A.M.); stefano.plano@crf.it (S.P.); davide.gabellone@crf.it (D.G.)
[2] Department of Chemistry and NIS-INSTM, University of Turin, Via Pietro Giuria 7, 10125 Turin, TO, Italy
[3] Nuova Allemano, Via Giacomo Leopardi, 13, 10095 Grugliasco, TO, Italy; pietro.licignano@external.stellantis.com
[4] Stellantis, Material4Electrification, Via Norma 2, 80038 Pomigliano d'Arco Napoli, NA, Italy; matteo.basso@crf.it
* Correspondence: marcello.baricco@unito.it

Abstract: Through mechanical analysis, a comparison of the same type of cold rolled steel produced by two steel manufacturers, supplier 1 and supplier 2, has been carried out. The considered material is a steel that has undergone a quenching and partitioning heat treatment, i.e., a rapid cooling from the austenitizing temperature, followed by a holding treatment at a suitable temperature, so that the residual austenite is stabilized at room temperature. The following tests for mechanical properties were carried out: formability, through Nakajima test, tensile test, bending test, hole expansion test and fatigue strength analysis, through high cycle fatigue and low cycle fatigue test. In addition, to derive useful data for future simulations, tensile and Nakajima tests were analyzed by digital image correlation, which uses a monochrome camera to capture frames during the test, in order to analyze local deformations on investigated samples. Finite elements modeling has been carried out. A suitable calibration of a material card for the Abaqus Finite Element Analysis software has been performed. Through the combination of obtained results, a rational comparison of the two analyzed products has been obtained.

Keywords: quenching and partitioning steel; advance high strength steel; automotive applications

1. Introduction

Dual Phases (DP) steel was developed to produce thin, strong automotive steel sheets to improve fuel economy and to reduce gas emissions. DP, martensite/ferrite, steels are amongst the first advanced high strength steels (AHSS) developed for cold formed sheet applications in the automotive sector [1]. DP steels are high-strength steels with a high-volume fraction of martensite. This steel grade has high strength but low elongation and, consequently, poor formability, which limits its application for automotive sheet metal. As reported in ref. [2], which considers DPs by comparing them with third-generation AHSS steels, DPs have half the elongation (7.8% vs. 18.0%). The third-generation AHSS take advantage of the austenite-to-martensite transformation to improve hardening and retard material instability during deformation. It is also observed that, for the same tensile strength, third-generation steels exhibit higher ductility than DPs, indicating favorable

behavior in advanced stamping processes. To avoid the elongation problem, transformation-induced plasticity (TRIP) steels, which show high formability, can be considered. As shown in refs. [3,4], this grade of steel has a microstructure composed of ferrite (soft and ductile), bainite (which confers strength) and retained austenite, which, during deformation, transforms into martensite, further improving strength. This phenomenon is called the TRIP effect, which is the transformation of austenite into martensite under deformation, that generally increases the strength of the material, improving performance during cold forming. TRIP steels offer an exceptional combination of high mechanical strength and good ductility due to their microstructure.

However, the tensile strength of TRIP steels is lower than that of DP steels. To produce metallic materials with suitable mechanical properties for improving automotive safety and energy saving, a new type of steel called quenching and partitioning (Q&P) has been developed in recent years [5]. The idea behind this new family of steels is the so-called "quenching and partitioning" process, which consists of the diffusion of carbon from martensite to retained austenite (RA) for its stabilization. The aim is to produce steels in which significant fractions of appropriately localized RA are present in a martensitic matrix. In Q&P steels, the martensite has the scope to improve the tensile strength, while the RA increases the elongation. The presence of RA between martensite platelets improves the ability of grain boundaries to hinder the movement of dislocations, thus increasing strength and work hardening. Results are steels with tensile strengths above 1200 MPa combined with high ductility, i.e., an elongation higher than 14% [6].

The Q&P steel grade is subjected to a quenching and partitioning heat treatment, where there is initially complete austenization, by an increase in temperature, followed by quenching and isothermal maintenance with a cooling rate greater than 50 °C/s between the martensite start (Ms) and martensite finish (Mf) temperature [7,8]. The consequence of this heat treatment is the formation of a partially hardened martensitic or bainitic matrix (Figure 1) [6]. During isothermal maintenance (partition phase), carbon diffuses into the residual austenite leading to the enrichment of the latter [9]. This step allows the residual austenite to be stabilized at room temperature.

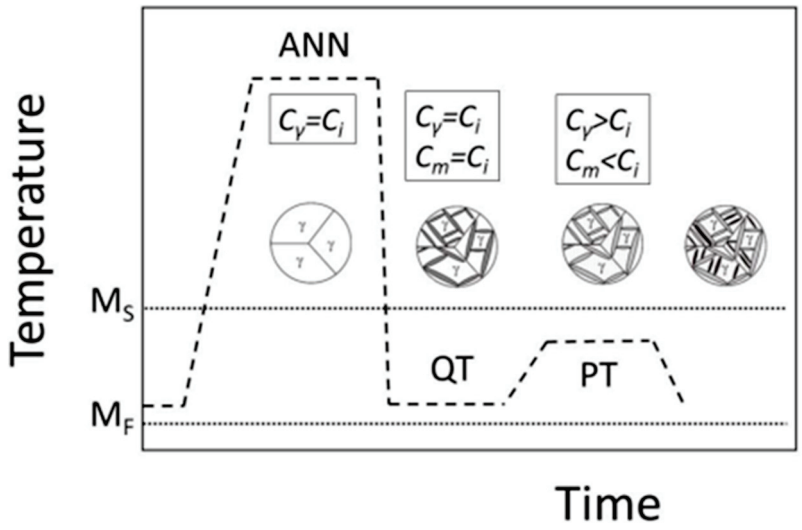

Figure 1. Q&P thermal process. ANN: Annealing Temperature; QT: Quenching Temperature; PT: Partitioning Temperature; M_S: Martensite start temperature; M_F: Martensite finish temperature; *Ci*, $C\gamma$, and C_m are the carbon contents in the initial alloy, austenite, and martensite, respectively. Reprinted from Ref. [10].

The Q&P steel is normally composed of carbon-depleted martensite and carbon-enriched retained austenite after full austenization. This microstructure allows for a high

strength and ductility that can outperform those of DP steels [11]. Q&P steels own an excellent combination of strength and overall deformability, but the high carbon content reduces weldability. This steel grade enjoys properties that allow it to be used as a substitute for DP in the manufacture of molded parts, due to its higher edge strength.

Challenging mechanical properties generally require alloy steels, which are very expensive, but may significantly decrease the vehicle weight. Q&P steels, which contain a small amount of alloying elements, could limit the cost of raw materials, though reducing fuel consumption and thus, carbon dioxide emissions [12]. This study analyzes the mechanical and microstructural properties of a Q&P steel produced by two different suppliers, with the aim of evaluating its potential application in the automotive sector.

2. Materials and Methods

The characterization of materials plays a crucial role in the design and development of automotive components. Through the use of mechanical tests, valuable information can be obtained to characterize and validate the application of materials in the automotive field, such as mechanical strength, sheet metal formability, and behavior under dynamic loads, which are essential elements to meet the increasingly stringent demands of the industry.

2.1. Selected Q&P Steels

Q&P1180 steel is named for the ultimate tensile strength, in this case 1180 MPa. The plates analyzed came from two international steel suppliers, both with global supply capabilities. For production reasons of the two suppliers, obtained samples have two different thicknesses. For supplier 1, the thickness is 1.67 mm, while, for supplier 2, it is 2.0 mm.

Table 1 shows the range of chemical compositions of Q&P1180 steels produced by the two different suppliers.

Table 1. Chemical composition range (wt%) of Q&P1180 steels provided by supplier 1 and supplier 2.

Supplier	C	Si	Mn	Al	Cu	Ti + Nb	Ni + Cr + Mo	P	S	B
1 min	0.18	1.6	2.6	0.01	0.00	0.01	0.05	0.00	0.000	0.001
1 max	0.20	1.8	3.0	0.06	0.05	0.05	0.20	0.01	0.010	0.005
2 min	0.10	1.2	2.2	0.02	0.00	0.02	0.06	0.00	0.001	0.000
2 max	0.16	1.9	3.3	0.04	0.01	0.03	0.09	0.01	0.003	0.001

The heat treatment is aligned with that already reported in the study covered in ref. [6], for which there is an annealing temperature of about 870 °C, quenching temperature of about 300 °C and partitioning temperature of about 400 °C. Following these annealing temperatures, the carbon content of RA increases [6].

The chemical composition of steel from suppliers 1 and 2 are similar to the Q&P grades studied by Xia et al. [13]. As it is possible to observe, the composition of steel obtained from supplier 2 has less C and Si, if compared with that provided by supplier 1. This difference facilitates the welding operation, because of the lower carbon equivalent value, but it leads to the requirement of faster cooling during production in the steel mill.

2.2. Microstructural and Chemical Analysis

Microstructural analysis was obtained by a Reichert–Jung MeF3 M 1 optical microscope, using UNI 3244:1966 [14] to evaluate nonmetallic inclusions in steels. Nittal 3% reagent was used to reveal the microstructure, as indicated in ASTM E407-07 (reapproved

2015) [15]. For quantitative chemical analysis, OES-Quantometer-ARL3460 was used as the instrument.

2.3. Mechanical Tests

2.3.1. Bending Test

The VDA 238-100 [16] bend test was used to characterize the deformability and fracture limits of metal sheets, subjected to bending under severe plane strain conditions. This test is particularly important for the selection of advanced high-strength steels for energy-absorbing structural components [17]. The bending angle is the principal result obtained from this test. It is calculated by dividing the vertical deformation (difference between initial and final height of the point of load application) by the length of the sample. The universal tensile machine Sun 20 from Galdabini was used to obtain the bending value.

2.3.2. Formability Test

The Formability Test (FLD), according to ISO 12004 [18] allowed the formability of metal sheets to be evaluated. The FLD test determines the material failure limit through the formability limit curve (FLC), which is determined by cupping tests on sheet metal test specimens. Six different geometries (Figure 2) have been used for each strain state, going from a thin useful stretch for uniaxial study to a round one for biaxial deformations. These tests can be performed using hemispherical or flat punches, such as those defined by the Nakajima or Marciniak methods. The maximum deformations of the various types of specimens define the limit formability curve of the material [19]. The Hydraulic Erichseen machine was used to obtain FLD results.

Figure 2. Samples used in the formability test.

2.3.3. Hole Expansion Test

The Hole Expansion Test (HET) was used to determine the ductility of perforated plates, by quantifying the elongation capacity of the edge. High values of the hole expansion ratio are associated with steel grades with improved local formability. The sample that contains the hole is blocked in place, and a conical punch expands the initial hole. The test stops when a crack is observed through the thickness or when there is a decrease in load above a critical threshold. Hole expansion ratio (HER), also called hole expansion capacity (HEC), is the percent expansion of the initial hole diameter, usually denoted by the Greek letter lambda, λ. The Hydraulic Erichsen machine was used to obtain FLD results.

2.3.4. Fatigue Test

To evaluate the High Cycle Fatigue (HCF) behavior, fatigue tests are conducted in the longitudinal orientation to the rolling direction on hourglass specimens according to ISO 1099 [20]. The sample had a stress concentrator factor kt = 1.06. Cut edges have been smoothed off using abrasive papers to minimize the effect of the sample machining on the fatigue response. Fully reversed axial fatigue tests (stress ratio $R = -1$) have been carried out under load control, by using a RUMUL resonant fatigue machine, at a nominal

frequency of 100 Hz. Antibuckling guides have been used to prevent buckling in the fully reversed fatigue tests.

Data analysis has been performed, combining finite life and endurance limit testing. The endurance limit corresponding to a fatigue life of 5×10^6 cycles is based on staircase testing method following ISO 12107/UNI 3964 [21] std., employing 15 samples and 5 MPa stress increments. Median (R50) and reliability of 90% (R90) values for endurance limit have been evaluated following ISO-12107/UNI3964 std. Reliability of 90% and confidence of 90% (R90C90) values for endurance limit were evaluated by using the Dixon–Mood method. The output data are the following: endurance limit R50 ($S_A{}^{SC}{}_{R50}$), endurance limit R90 ($S_A{}^{SC}{}_{R90}$), and endurance limit R90C90 ($S_A{}^{SC}{}_{R90C90}$).

The medium-to-high-cycle fatigue life in the range between nearly 6×10^4 and 1×10^6 cycles was explored at various load levels, using up to four samples for each of them. The generation of the finite life portion of the median SN curves was obtained by a linear regression (Least Squares Analysis) in logarithmic coordinates of the experimental data according to Equation (1):

$$S_a = S_A \left(\frac{N_A}{N_f} \right)^{\frac{1}{k}} \tag{1}$$

where S_a is the engineering stress amplitude, S_A is the fatigue strength at knee of SN curve, N_A is the fatigue life at knee given by the intersection of the median finite life curve and the median endurance limit, N_f is number of cycles, and k is the slope factor of SN curve. The curve, representing a reliability of 90% (R90) was calculated by using the probability coefficients corresponding to a normal distribution (inverse of standard normal distribution based on reliability level of interest). The design curve, representing a reliability of 90% and a confidence of 90% (R90C90), was calculated using the modified Owen's approach. It was assumed that the design SN curve (R90C90) has the same slope as the median SN curve (R50). The output data are the following: fatigue strength at knee of SN curve R50 ($S_A{}^{SN}{}_{R50}$), fatigue strength at knee of SN curve R90 ($S_A{}^{SN}{}_{R90}$), fatigue strength at knee of SN curve R90C90 ($S_A{}^{SN}{}_{R90C90}$), fatigue life at knee of SN curve (N_A) and slope factor of SN curve (k).

To evaluate the Low Cycle Fatigue (LCF) behavior, fatigue tests have been conducted in the longitudinal orientation to the rolling direction on constant cross section specimens, according to ISO 12106 [22]. Cut edges have been smoothed off using abrasive papers to minimize the effect of the sample machining on the fatigue response. Fully reversed axial fatigue tests (strain ratio $R = -1$) were carried out under strain control by using an MTS servo hydraulic fatigue machine at a constant strain rate. Antibuckling guides were used to prevent buckling in the fully reversed fatigue tests. To define the strain–life curve, Morrow's equation (Equation (2)) was used [11]:

$$\varepsilon_a = \frac{\sigma'_f}{E} \left(2N_f \right)^b + \varepsilon'_f \left(2N_f \right)^c \tag{2}$$

where σ'_f is the fatigue strength coefficient, b is the fatigue strength exponent, ε'_f is the fatigue ductility coefficient, c is the fatigue ductility exponent, E is the average cyclic modulus of elasticity and $2N_f$ is the number of reversals. The $\sigma_f{}'$ and b parameters represent the median stress–life curve (Basquin's equation) and $\varepsilon_f{}'$ and c represent the median plastic strain–life curve (Coffin-Manson equation). The design strain–life curves, representing a reliability of 90% and confidence of 90%, have been calculated using the modified Owen's approach. The output data are the following: fatigue strength coefficient R90C90 ($\sigma'_{f,R90C90}$) and fatigue ductility coefficient R90C90 ($\varepsilon'_{f,R90C90}$).

2.3.5. Tensile Test

The tensile test on the selected specimens was performed with a Sun 20 equipment from Galdabini (Cardano al Campo, VA, Italy), with a maximum load capacity of 200 kN tensile force, according to ISO 6892-1:2019 [23]. During the tensile tests, characterizations were performed to study the triaxiality of the material. To obtain this information, samples having different geometries, able to experience different stresses in the useful sections, were prepared. Investigated geometries are reported in Figure 3, and they can be defined as follows:

(a) dog-bone samples at L0 50: a classical tensile specimen subjected to σ load parallel to the movement of the traverse race;
(b) notched samples: a specimen with specular notches placed in the center of the useful section to simulate a point of greatest concentration of stresses during tension;
(c) shear samples: specimens having at the center of the useful section a portion of material perpendicular to the traverse race that is subjected to purely shear stress τ during the test.

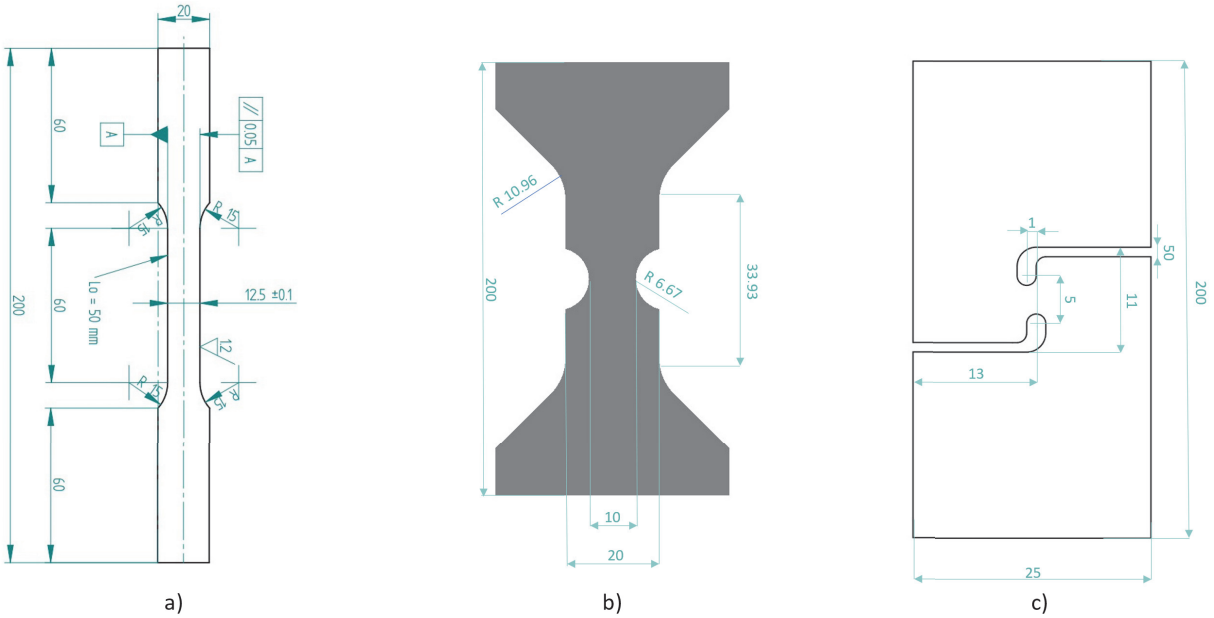

Figure 3. Sample geometries: (**a**) dog bone, (**b**) notch and (**c**) shear; all dimensions are in mm.

The output data are the following: yield strength ($Rp_{0.2}$), ultimate tensile strength (Rm), and elongation (A).

2.4. Virtual Simulation and Finite Elements Analysis

To collect data regarding the global and local deformation of the specimens during the test, the Digital Image Correlation (DIC) method was applied, using a monochrome camera. This was performed by collecting the various images (frames) taken by the camera while pulling the specimens at a rate of 2 mm/min.

Regarding virtual testing by means of a Finite Elements Analysis (FEA), it has to be considered that, during the design phases of vehicle structures, Computer-Aided Engineering (CAE) tools are normally used to carry out strength checks and damage prediction of components subjected to various load conditions, typical of vehicle operations (static, fatigue, thermo-mechanical, crash, etc.). To develop a FEA, it is necessary to employ analytical models that describe how the material deforms under the action of external loads. Typically, models are chosen to trace the stress and strain patterns that the material exhibits during a standard experimental test. For all metallic and nonmetallic materials, the chal-

lenge is to define analytical laws that correlate well with the plastic regime of the material and with the damage and ultimate failure phase. For metallic materials in particular, an appropriate yield function must be defined based on the hardening characteristics of the material. This approach is useful, for example, to calibrate the analytical model to the experimental data. The result of the calibration process is a material card that can be used for strength verification through FEA analysis of vehicle systems and components made from the analyzed material. The FEA analysis was carried out on the three types of specimens, as shown in Figure 4. Considering the small thickness, which leads to the assumption of a plane stress state, a two-dimensional model was realized for each specimen, with an appropriate refining of the computational grid to capture the variation of stresses in the plane, as reported in Figure 4. In terms of boundary conditions, a simulation mimicking the experimental test was performed, namely, controlling the displacement with one end of the sample clamped (Δ) and imposing a quasi-static displacement on the opposite end (D) (Figure 4).

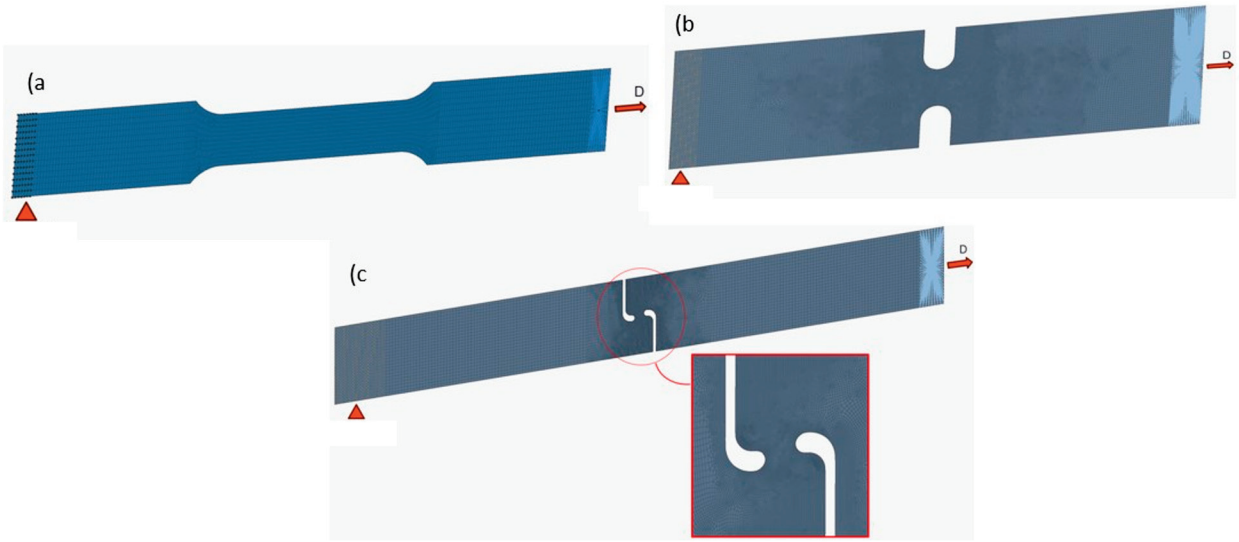

Figure 4. Samples recreated for simulation and their boundary conditions: (**a**) dog bone sample, (**b**) notch sample, and (**c**) shear sample. Δ is the clamped side, and D is the direction of the tensile force.

The experimental stress–strain curve obtained from the tensile tests was referred to each geometry for the simulation. From an analytical point of view, two approaches were used simultaneously:

1. In the first approach, the hardening behavior was analyzed using the Swift–Voce hardening equation for the tensile specimens, while a Johnson–Cook model was used for the notch and shear specimens.
2. In the second approach, considering the last section of the σ–ε curve, for an efficient calibration of the numerical techniques, it was necessary to define the parameters of a progressive damage mechanics model. Figure 5 shows a depiction of the progressive damage model. In this type of modeling, it is necessary to define a damage initiation criterion that defines the point at which the stiffness of the material begins to degrade [24]. The ductile criterion, which is useful for damage initiation due to the nucleation and growth or the coalescence of voids, assumes that the plastic deformation at damage initiation is a function of stress triaxiality and strain rate. The material behavior is described as undamaged up to point d (Figure 5). Therefore, only the Swift–Voice (or Johnson–Cook) model will work in this section. Subsequently, depending on the local triaxial stress, damage starts at point d and progresses to complete failure in section d–e.

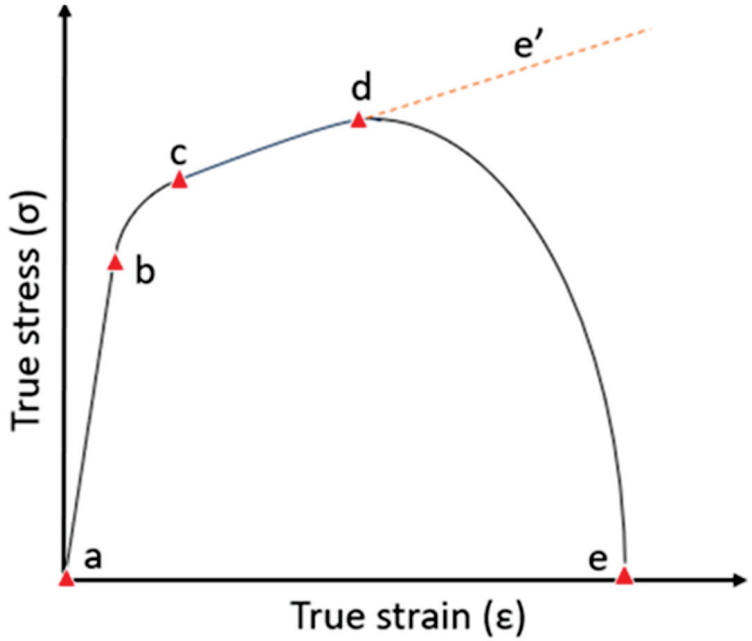

Figure 5. Graphic depiction of the progressive damage method. (a) starting point of tensile test, (b) end of elastic behavior, (c) starting point of plastic behavior, (d) damage starts, (e) complete failure of sample, (e′) end of test in ipotetical true curve without damage condition.

The calibration procedure has been carried out according to the following stages:

- convert engineering stress–strain curve to true curve;
- extract only the plastic part of the stress–strain curve true;
- calibration of an analytical model on the plastic part of the true stress–strain curve.
- define the parameters of the damage initiation and evolution starting from experimental data;
- preparation of the FEM model of the sample;
- apply load to specimen, determine stress–strain curve and compare to experimental curve;
- adjust the parameters of the analytical model and damage initiation and evolution, repeat the running of the simulation, and compare again with the experimental data until the desired correlation quality is obtained.

The program employed for virtual testing was Abaqus 2022 FEA software.

The Swift model (Equation (3)) aims to model the plastic behavior of the material in the early part of the strain hardening curve by considering the rapid work hardening that the material achieves, whereas the Voce model (Equation (4)) focuses more on the acquisition of stress saturation as deformation increases in materials that show a clear asymptotic behavior near the maximum stress. To calibrate the analytical model on the plastic section of the stress–strain curves, a combination of two approximation models, namely Swift and Voice (Equation (5)), was used, as implemented for the simulation in the software. The set of equations to be considered is therefore:

$$\text{Swift model}: \quad \sigma_{sw} = A\left(\varepsilon_p + \varepsilon_0\right)^n \tag{3}$$

$$\text{Voce model}: \quad \sigma_V = \sigma_0 + Q\left(1 - e^{-\beta\varepsilon_p}\right) \tag{4}$$

$$\text{Swift–Voce model}: \quad \sigma_{Sw-V} = (1-\alpha)\sigma_V + \alpha\sigma_{sw} \tag{5}$$

where

- σ_{sw} is the flow stress for the Swift model,

- σ_v is the flow stress for the voce model,
- A is strength coefficient,
- ε_p is the true plastic strain,
- ε_0 is the residual deformation due to the sheet metal forming process,
- n is the Swift hardening exponent, indicating how rapidly the material strengthens with plastic deformation,
- β is the Voce hardening parameter, which controls the saturation behavior of the stress-strain curve.
- Q in approximate way is the differences between yield stress and the stress at saturation
- α is the coefficient that combines the swift and voce model.

Another analytical model used is the Johnson–Cook hardening model. The Johnson–Cook model aims to provide an accurate description of the behavior of materials under dynamic loading conditions, considering variations in temperature and strain rate without considering the thermal effect of the hardening part of the Johnson–Cook model that specifically describes how the flow stress of a material evolves with plastic deformation. It is given by the following formula (Equation (6)):

$$\sigma = A + B\varepsilon^n \tag{6}$$

where

- σ is the flow stress.
- A is the initial yield stress.
- B is the strain hardening coefficient.
- ε is the plastic strain.
- n is the strain hardening exponent.

For simulations, an isotropic hardening model was used in which the hardening surface of the material changes size uniformly in all directions. In this way, stress increases or decreases in all directions.

3. Results and Discussion

3.1. Q&P 1180 Microstructure Analysis

Figure 6 shows the optical micrography of Q&P1180 obtained from supplier 1 (a) and supplier 2 (b). In both cases, a matrix of tempered martensite is observed, with traces of residual austenite RA (marked with arrows in the photos). The observed microstructures confirm a proper cooling process during production, although the chemical compositions show some differences, as mentioned earlier. The microstructure is comparable with those observed by Xia et al. [13], Nyyssönen et al. [25], and Kaar et al. [26].

3.2. Formability

Results on HET and bending test are reported in Table 2. For the HET test, 30 samples were examined for each supplier and an average strain value slightly higher for the Q&P 1180 obtained from supplier 1 has been obtained. A similar range for the bending angle α can be observed by both suppliers after the testing of five samples each. The HET results of both Q&P1180 steels are higher than DP1180 [27] proving the good flangiability of this new steel family compared to the currents.

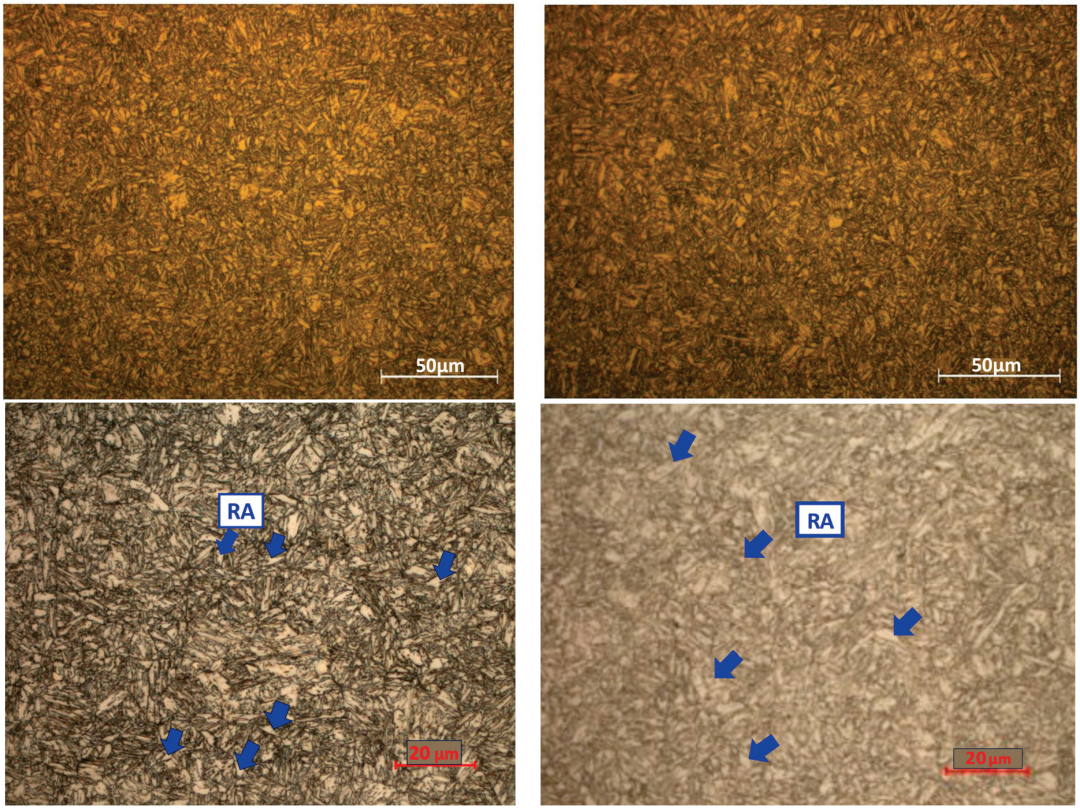

(**a**) (**b**)

Figure 6. Micrography of Q&P1180 obtained from (**a**) supplier 1 and (**b**) supplier 2. The top images are at 500× magnification, those below at 1000× magnification. RA represents the retained austenite.

Table 2. HET and bending test results for Q&P 1180 steels obtained from different suppliers.

	Supplier 1	**Supplier 2**
HET	Av. strain % = 34.0	Av strain % = 28.0
Bending	$\alpha = 152 \div 155$	$\alpha = 152 \div 154$
FLD0	0.134	0.144

Through the Nakajima test, which provides the ability of the plates to deform to the point of failure, FLC was obtained for both materials, using a set of six geometries—five samples for each one–and results are shown in Figure 7. The lowest point of the FLD curve (FLD0) is reported in Table 2. It can be observed that the two materials obtained from different suppliers show similar trends for different sample geometries, with a slightly higher strain value before the cracking of the steel obtained from supplier 2. This difference can be associated with the different thicknesses of the samples. In fact, by increasing the thickness, the necking phase is extended before the crack nucleation and propagation into the sample. It can be concluded that the formability of Q&P1180 steel obtained from supplier 1 is comparable with that of the steel provided by supplier 2. In Figure 7, the comparison with a conventional Dual Phase 980 steel grade (DP980), which has 980 MPa minimum of tensile strength, is also reported. It is possible to observe that QP1180 grades have a similar formability compared to DP980, even if the tensile and yield strengths are higher. This result proves the better forming behavior of the new steel family compared to the conventional ones.

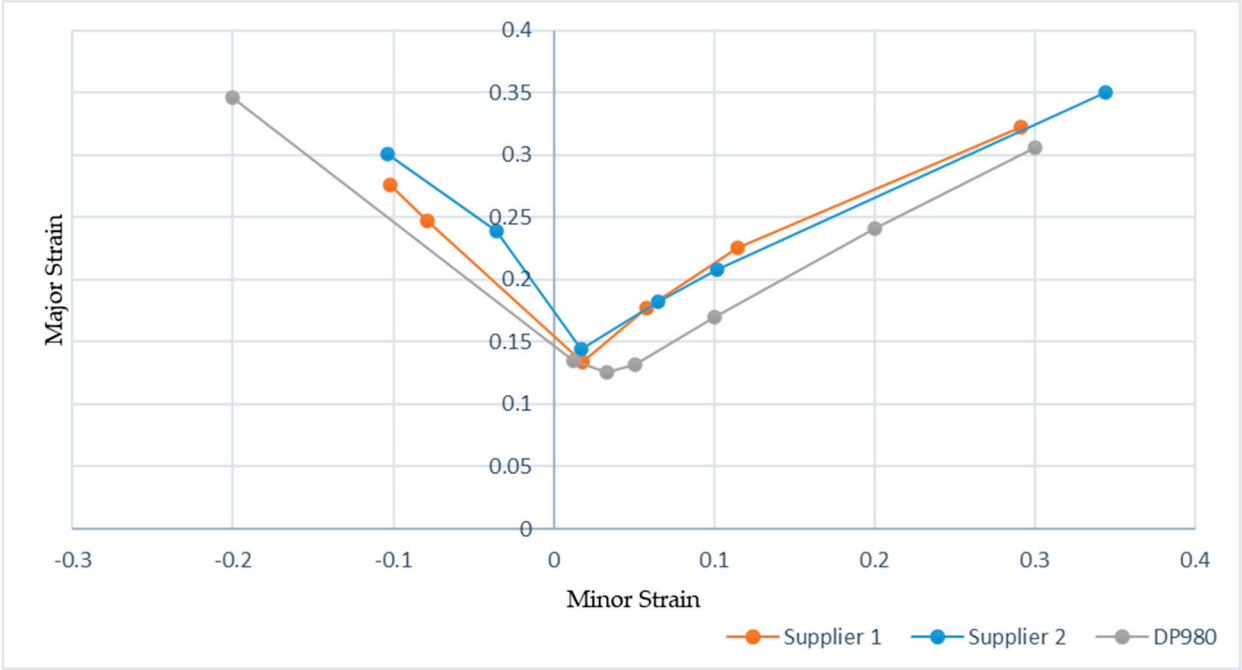

Figure 7. Formability limit curves for Q&P1180 steels obtained from supplier 1 and supplier 2. Results obtained for a conventional Dual Phase 980 steel grade are reported for comparison.

3.3. Fatigue

To study the fatigue behavior of investigated materials, the analysis was carried out for both HCF and LCF. This analysis required 2 HCF and 2 LCF characterizations involving 110 samples. Results of HCF are reported in Figures 8 and 9, that show the S-N curves obtained for samples provided by supplier 1 and supplier 2, respectively. Obtained values are summarized in Table 3.

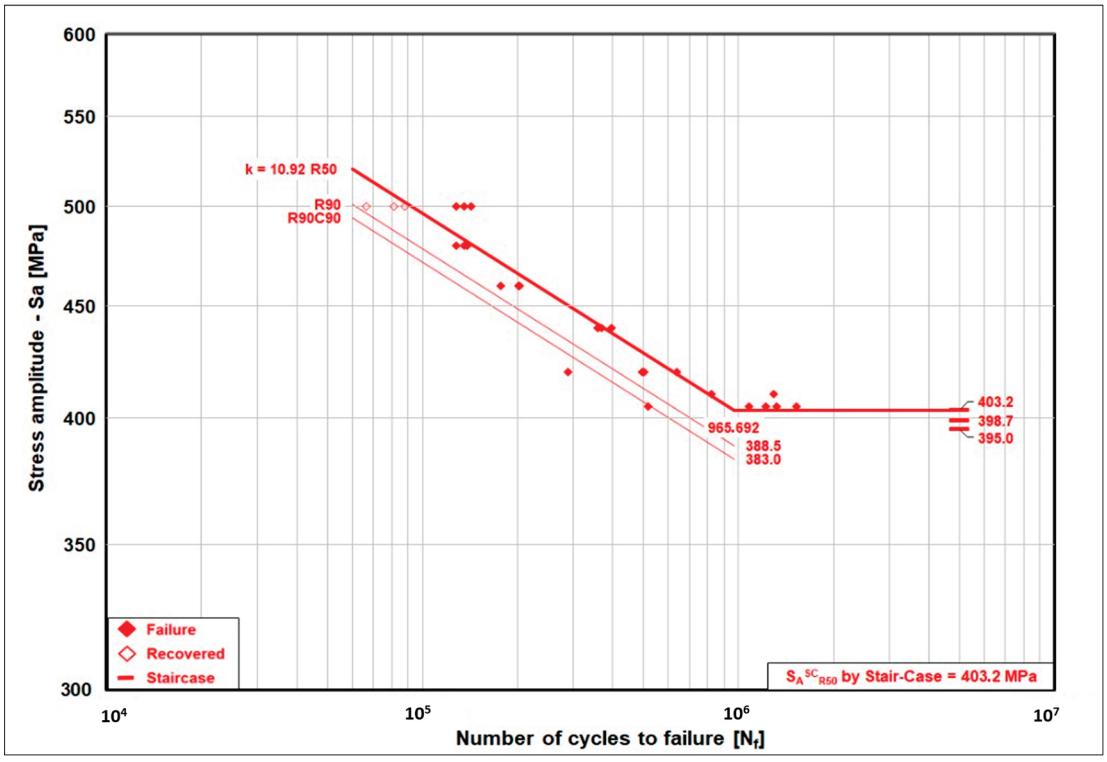

Figure 8. Woehler's curve in HCF for Q&P1180 steel obtained from supplier 1.

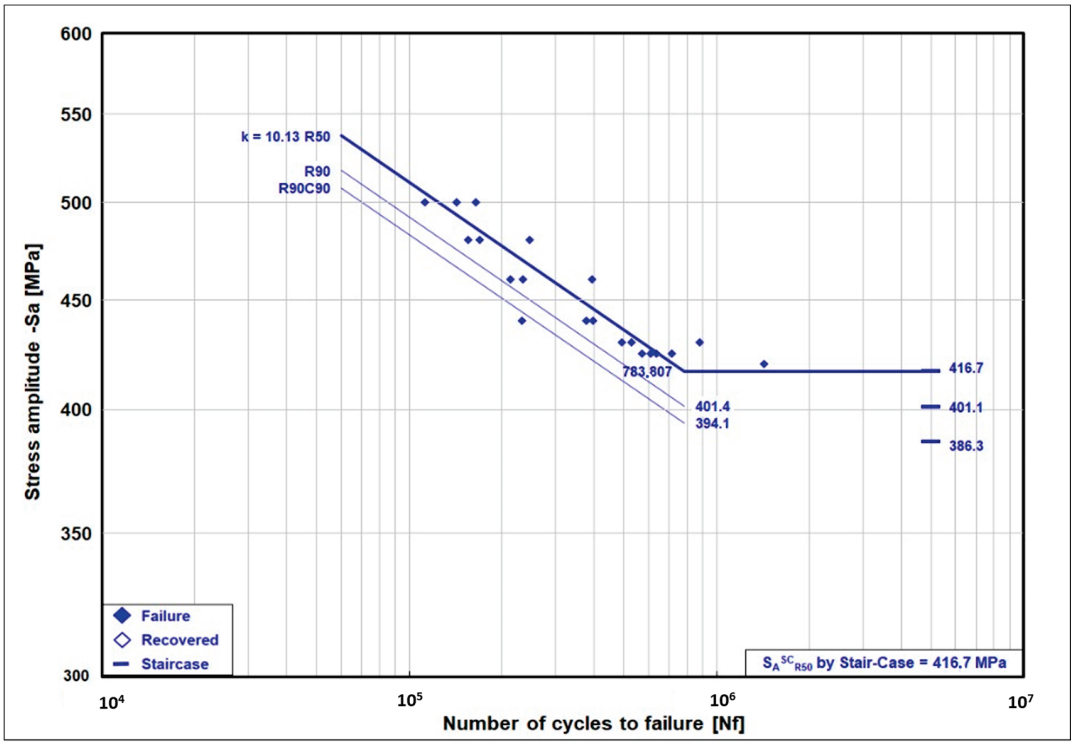

Figure 9. Woehler's curve in HCF for Q&P1180 steel obtained from supplier 2.

Table 3. Woehler's curves parameters of samples provided by supplier 1 and supplier 2.

Steel	Stair-Case				Constant of S-N Curve				
Name	$S_A{}^{SC}$ [MPa]			S.D. [MPa]	$S_A{}^{SN}$ [MPa]			N_A [Cycles]	k
	R50	R90	R90C90		R50	R90	R90C90		
Supplier 1	403.2	398.7	395.0	3.5	403.2	388.5	383.0	965,692	10.92
Supplier 2	416.7	401.1	386.3	9.1	416.7	401.4	394.1	783,807	10.13

The HCF behavior of the tested steels is quite similar (Table 3). Both S-N curves have the same slope factor (k) and close fatigue life at knee (N_A). The steel produced by supplier 2 has a little higher endurance limit R50 with respect to that provided by supplier 1, but it also has a higher scattering, which leads to a lower endurance limit, considering a reliability of 90% (R90) and reliability and confidence of 90% (R90C90).

Concerning LCF measurements, Figures 10 and 11 show results obtained for samples provided by supplier 1 and supplier 2, respectively. Obtained values are summarized in Table 4.

Looking to a comparison of LCF results for tested steels (Table 4), it is possible to highlight that, in the elastic field, for high levels of number of cycles, the Q&P1180 obtained from supplier 1 shows better behavior in terms of performance than that provided from supplier 2. However, as the strain amplitude increases until it reaches the value of 0.5%, the difference between the two materials falls to zero, while, for levels of strain amplitude higher than 0.5%, there is a reversed trend, so that the material obtained from supplier 2 shows better performance than that provided by supplier 1. This result may be attributed to the different static properties of the two materials. Specifically, an examination of the static tensile curves reveals that the steel from supplier 2 exhibits higher load values than that provided by supplier 1 near the yield point. This characteristic contributes to a reduced fatigue life under conditions of equivalent imposed deformation. Conversely,

with increasing deformation, the more pronounced softening observed in the material from supplier 2, compared to that obtained from supplier 1, accounts for its extended fatigue life. The gap between the R50 and R90C90 of fatigue strength coefficient and fatigue ductility coefficient indicates a similar level in terms of statistical dispersion of experimental results for both materials.

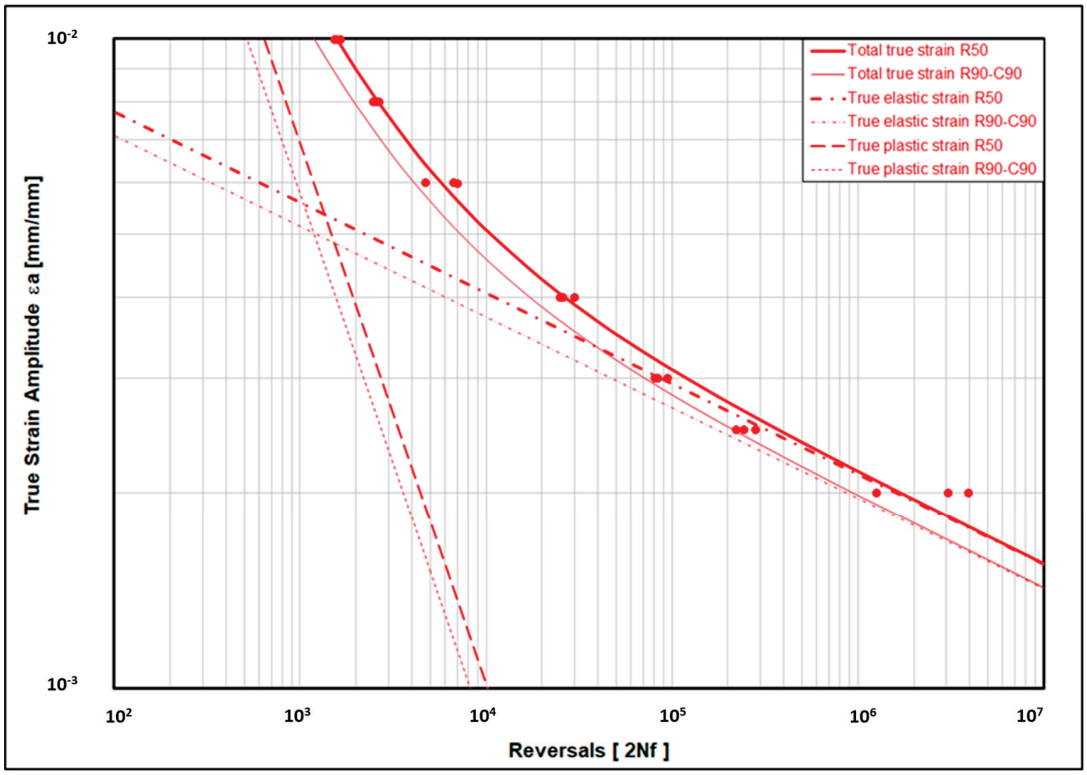

Figure 10. Morrow's curve in LCF for Q&P1180 steel obtained from supplier 1.

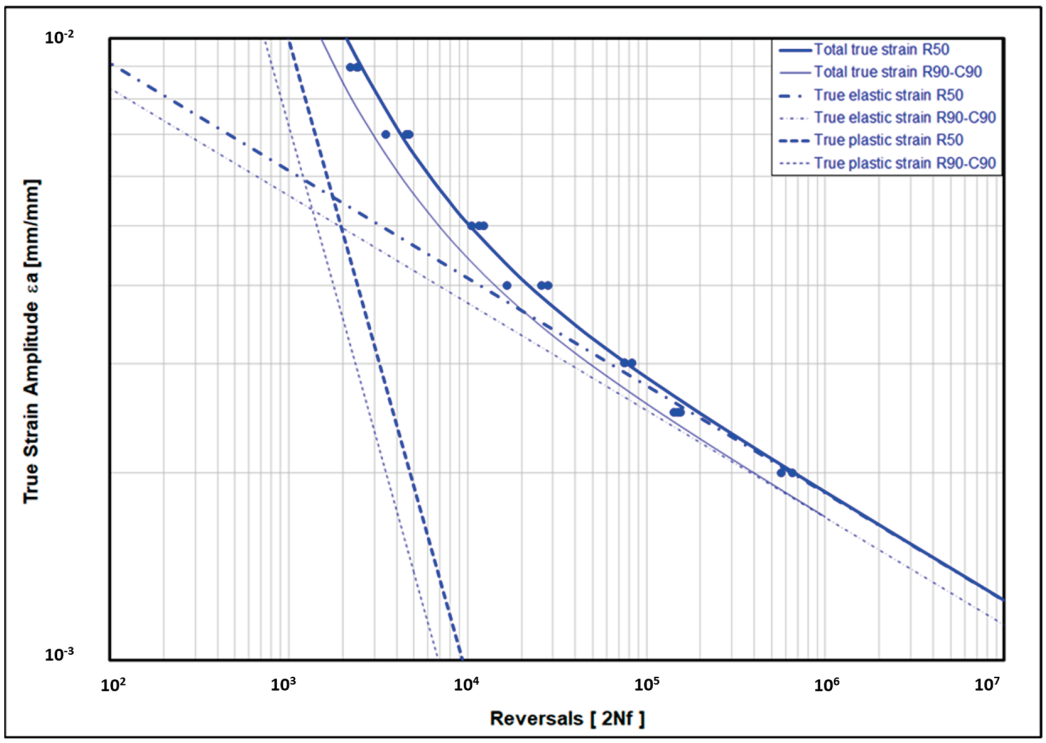

Figure 11. Morrow's curve in LCF for Q&P1180 steel obtained from supplier 2.

Table 4. Morrow's curves parameters of samples provided by supplier 1 and supplier 2.

Steel	Morrow's Curve Parameters						
Name	E [GPa]	Fatigue Strength Coefficient [MPa]		Fatigue Strength Exponent	Fatigue Ductility Coefficient		Fatigue Ductility
		σ'_t	$\sigma'_{f,R90C90}$	b	ε'_f	$\varepsilon'_{f,R90C90}$	c
Supplier 1	196.4	2881	2649	−0.140	2.145	1.791	−0.831
Supplier 2	196.7	3975	3625	−0.173	11.95	8.734	−1.027

It can be concluded that the experimental data do not highlight significant differences on fatigue properties between materials provided by the two suppliers.

3.4. Tensile Test

The mechanical properties were evaluated for dog-bone samples subjected to uniaxial loading. Specimens obtained in the three directions in relation to the rolling direction were tested to observe possible anisotropy. Five samples were tested for each orientation and then the curve that best approximated the test group was considered. Results are reported in Figures 12–14 for tests performed in longitudinal, diagonal, and transversal direction, respectively. Obtained data are summarized in Table 5.

From obtained results of tensile tests, it is observed that the values of mechanical properties are comparable with the typical values observed for Q&P steels, as reported in ref. [2], i.e., Rp about 900–1000 MPa, Rm about 1150–1230 MPa, and A about 5–19%. The tensile curves, in all examined directions, exhibit higher stress values at low deformation for the steel provided by supplier 2 compared to that obtained from supplier 1. This behavior may be attributed to variations in the deformation applied during the rolling process or differences in the time or temperature conditions during the annealing process. This type of behavior has a positive aspect, as previously observed, for the fatigue properties, although it limits the material's elongation.

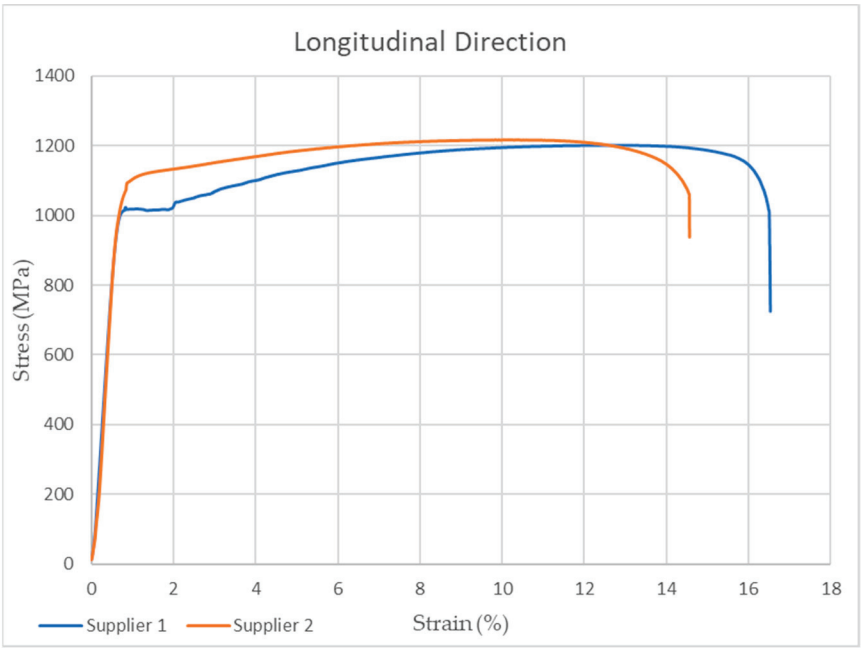

Figure 12. Tensile test of samples obtained from different suppliers measured along the longitudinal direction with respect to the rolling one.

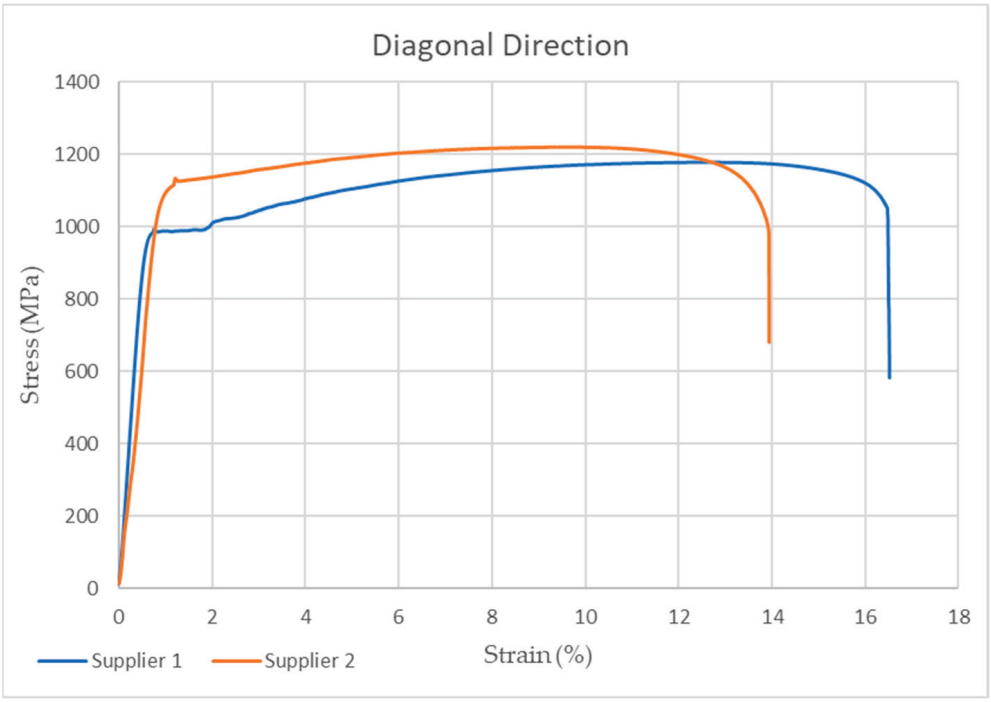

Figure 13. Tensile test of samples obtained from different suppliers measured along the diagonal direction with respect to the rolling one.

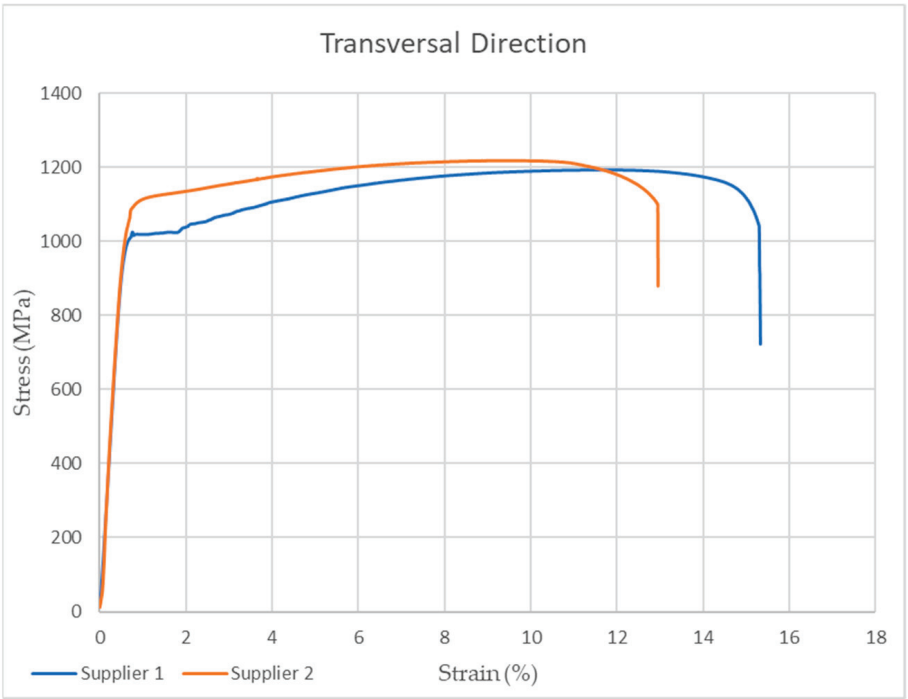

Figure 14. Tensile test of samples obtained from different suppliers measured along the transversal direction with respect to the rolling one.

Table 5. Mechanical properties of samples provided by supplier 1 and supplier 2.

Sample vs. Rolling Direct	Steelmaker	$Rp_{0.2}$ MPa	Rm MPa	A %
Longitudinal	Supplier 1	936	1204	14.1
	Supplier 2	931	1217	13.9
Diagonal (45°)	Supplier 1	952	1177	16.5
	Supplier 2	980	1219	14.0
Transversal (90°)	Supplier 1	901	1193	15.3
	Supplier 2	924	1218	13.0

3.5. Simulations

Since the two materials are comparable mechanically, one of the two was selected for virtual simulation in order to observe the most appropriate numerical model to convert the experimental stress and strain values into true values. Five samples were tested for each geometry. In the case of dog-bone and notch samples, for the comparison between the experimental data and the data derived from the FEA simulations of the tensile test, the plastic part of the true stress–strain curve has been modeled with the Swift–Voce equation, accompanied by a progressive damage mechanics model. Parameters used for the models used into FEA software are shown in Table 6. Figure 15 shows the calculated true stress-true strain curve superimposed on the experimental data for the tensile test of the dog-bone sample.

Table 6. Parameters for dog-bone tensile simulation.

Swift–Voce Model Parameters for the Tensile Simulation	
A = 1800	n = 0.15
s_0 = 1035 MPa	Q = 435 MPa
b = 11	a = 0.415
e_0 = 0.042	
Progress damage mechanics parameter for Abaqus standard	
Damage Initiation	
Criteria: Ductile	
Plastic Strain: 0.125	
Stress triaxiality: 450 MPa	
Strain rate: 0.003	
Damage Evolution	
Criteria: Displacement, softening exponential	
Total displacement: 0.14	
Exponent: 4	

From the simulation point of view, the L11 (true deformation in tensile direction) and the S11 (true stress in tensile direction) expressed during the test have been taken into account, as shown in the following Figure 16. These components are more consistent with the Swift–Voce model and demonstrate rigid behavior of the specimen during the test.

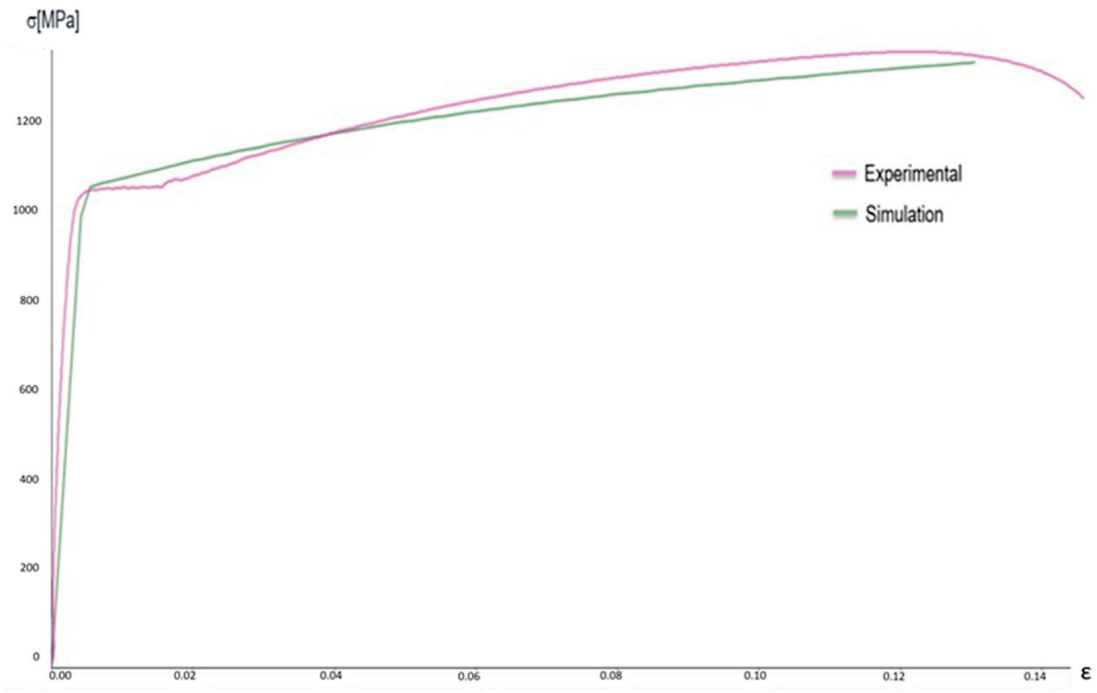

Figure 15. Comparison between simulated (green) and experimental (purple) tensile test curve of a dog-bone sample.

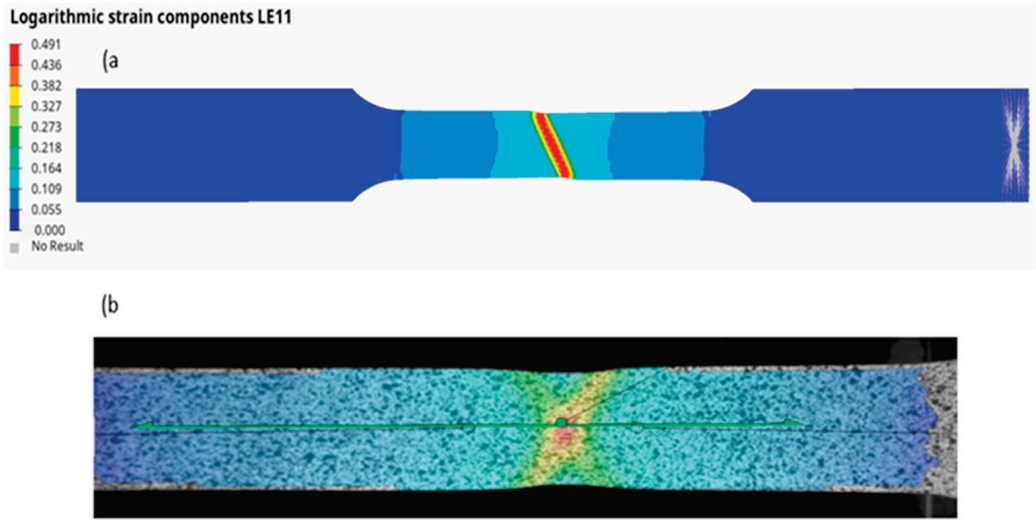

Figure 16. Logarithmic strain component (**a**) and real dog-bone sample maximum deformation (**b**).

The parameters for the notch sample used in the FEA software are shown in Table 7.

Figure 17 shows the calculated true stress–true strain curve superimposed on the experimental data for the tensile test of notch sample.

The L11 and the S11 for the notch sample are expressed in Figure 18.

In the case of the specimen subjected to shear stress, as mentioned, for calibrating the simulation to the experimental data, it was decided to model the plastic part of the stress–strain curve using the Johnson–Cook equation, and results are shown in Figure 19. In fact, in the case of the shear test, a larger deformation state than in the tensile and notch tests was obtained. In fact, as shown in Figure 20, the results of the calculation code must consider the true deformation component L12 and the stresses expressed by the von Mises

criterion. Table 8 shows the parameters obtained for the Johnson–Cook model and the progressive damage mechanic model.

Table 7. Parameters for notch tensile simulation.

Swift–Voce Model Parameters for the Notch Simulation	
A = 1644	n = 0.35
s_0 = 1030 MPa	Q = 650 MPa
b = 30	a = 0.635
e_0 = 0.35	
Progress damage mechanics parameter for Abaqus standard	
Damage Initiation	
Criteria: Ductile	
Plastic Strain: 0.07	
Stress triaxiality: 486 MPa	
Strain rate: 0.001	
Damage Evolution	
Criteria: Displacement, softening exponential	
Total displacement: 0.095	
Exponent: 4	

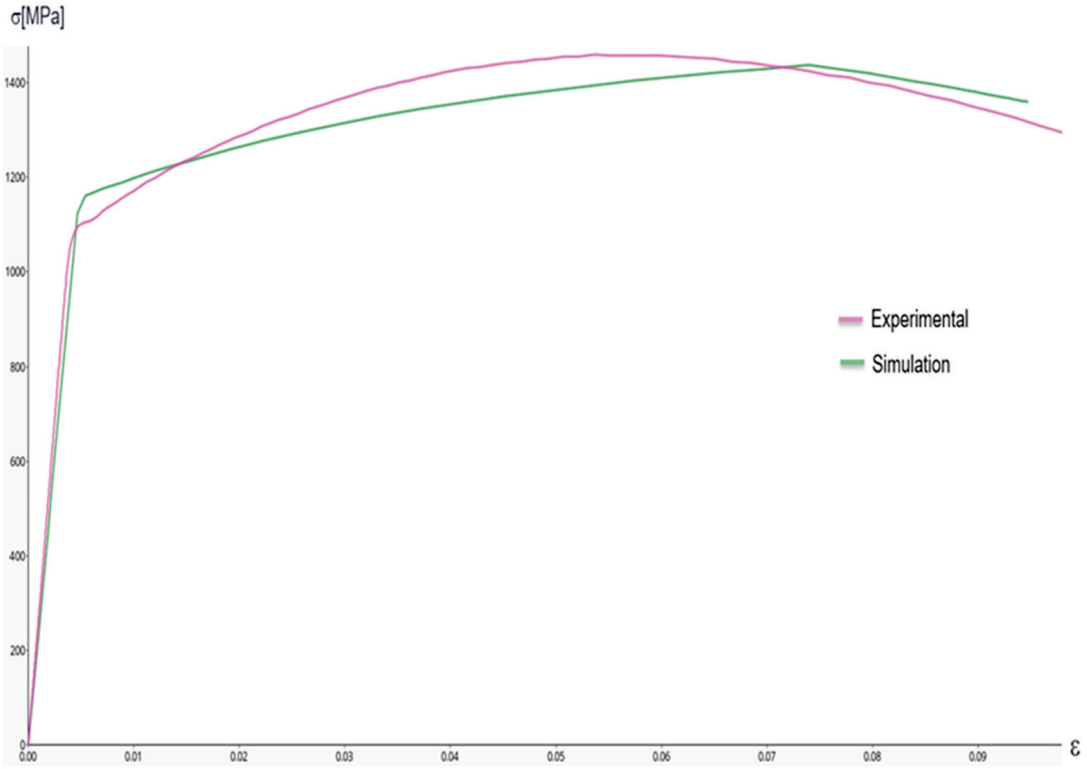

Figure 17. Comparison of simulated (green) and real (purple) curve of a notch sample.

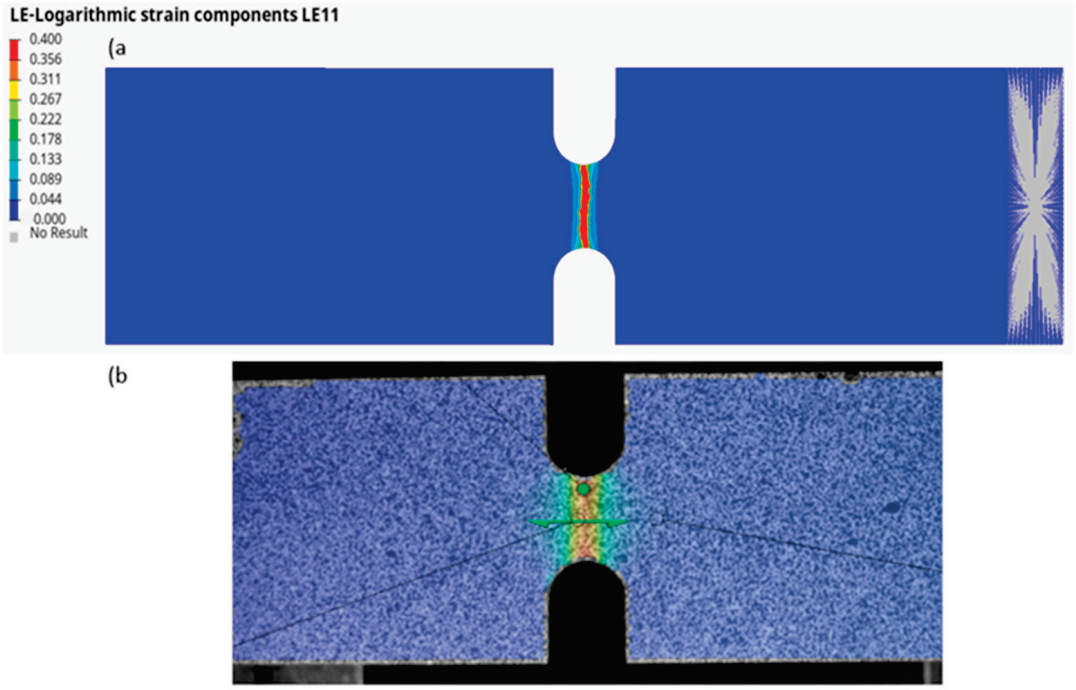

Figure 18. Logarithmic strain component (**a**) and real notch sample maximum deformation (**b**).

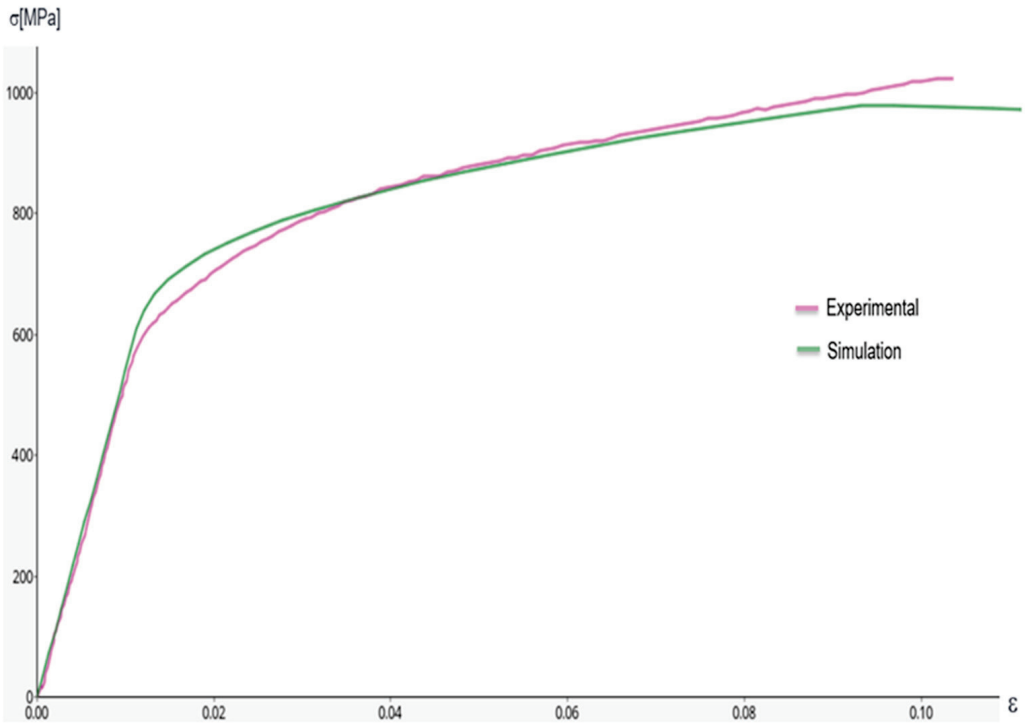

Figure 19. Comparison of simulated (green) and real (purple) curve of shear sample.

It is possible to observe that, even if there are slight differences between the experimental and simulated tensile curves, the FEM simulations properly predict the real behavior of different samples, as seen in Figure 20, where the simulated most stressed areas (Figure 20a) correspond to those observed during the experimental tests (Figure 20b).

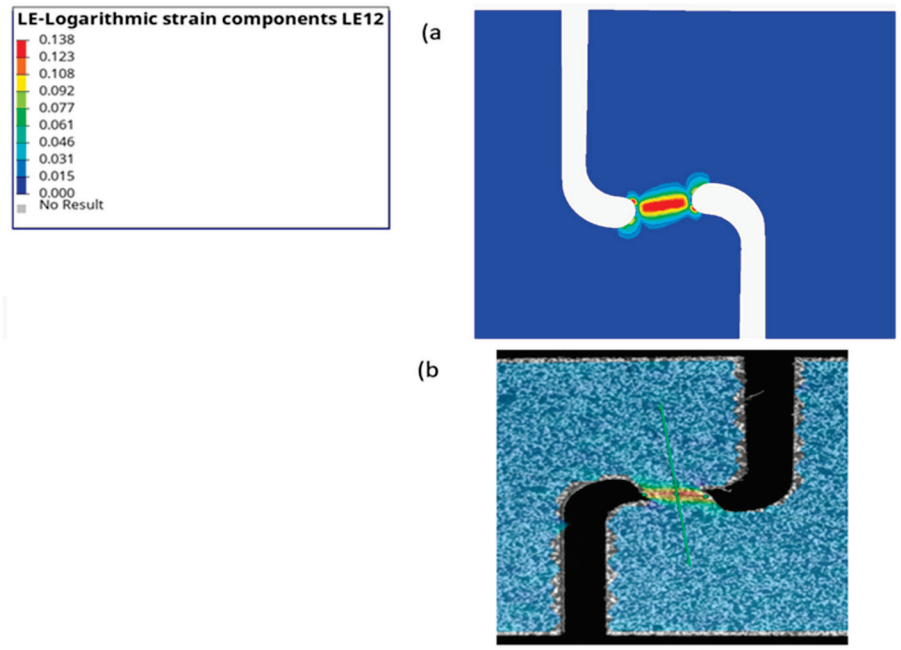

Figure 20. Logarithmic strain component (**a**) and real shear sample maximum deformation (**b**).

Table 8. Parameters for shear tensile simulation.

Johnson–Cook Model Parameters for the Shear Simulation	
A = 1644	n = 0.35
s0 = 1030 MPa	Q = 650 MPa
b = 30	a = 0.635
e_0 = 0.35	
Progress damage mechanics parameter for Abaqus standard	
Damage Initiation	
Criteria: Ductile	
Plastic Strain: 0.07	
Stress triaxiality: 486 MPa Strain rate: 0.001	
Damage Evolution	
Criteria: Displacement, softening exponential	
Total displacement: 0.095	
Exponent: 4	

In summary, microstructural analyses and mechanical tests have shown that the two investigated materials have more in common than the reverse. Optical microscopy confirmed that the two materials have the same constituent phases: tempered martensite matrix with dispersed retained austenite that influences the formability of the steel grade, promoting the TRIP effect during the plastic deformation. Through various mechanical tests, it was observed that both samples exhibit equal bending behavior, with an alpha range of 153°:155°. Both materials have similar yield strength and ultimate tensile strength, while the elongation-at-break values of steel obtained from supplier 1 are higher, albeit slightly, than those of the steel provided by supplier 2. The steel obtained from supplier 2 is slightly more formable, with higher FLC values, than that provided by supplier 1. As

already anticipated, this difference can be associated with the different thickness of the samples, which strongly influences the FLC curve.

As already mentioned, Q&P steel use in the automotive field is directed towards components previously manufactured in DP. Observed mechanical properties return an excellent behavior during the automotive crash events, being able to locally absorb the deformation without/delaying the component cracking. For this reason, the Q&P1180 steel could be suitable for windshield reinforcement, side-sill, or A pillar applications. In fact, during a pole lateral crash, there is a local deformation and, in general, the materials have to absorb the energy, limiting the intrusion as much as possible in order to guarantee the safety of the vehicle occupants. If the Q&P1180 is compared to the DP1180, with the same level of tensile strength, it is possible to observe 40% more elongation, which is a crucial point to stamp complex shapes as per the automotive market [28].

To be able to proceed with possible simulations of the Q&P1180 on the vehicle, a FEM method was identified to be able to convert the real data obtained through the mechanical tests into virtual data. An approximation of the true curve of the three analyzed geometries (dog-bone, notched and shear) was obtained. In particular, the dog-bone and carved samples were approximated by means of the Swift–Voce law, while the shear samples were approximated by using the Johnson–Cook law. In all cases, a progressive damage mechanism model was used, i.e., the consideration of the ascending section of the stress–strain curve of a tensile test in the simulation. All the simulations returned to a good correlation with experimental tests, which proves the proper approximation of tensile curves of different samples. So, such models could be used to predict the behavior of components made by Q&P1180.

4. Conclusions

The comparison of the Q&P1180 steels produced by supplier 1 and supplier 2 was carried out by means of micrographic analysis using an optical microscope and mechanical tests, to study mechanical strength, fatigue strength, ductility and formability. The following conclusions can be highlighted:

- Both steels have a microstructure characterized by a tempered martensite matrix, with residual austenite.
- Both exhibit comparable yield strength and ultimate tensile strength, with higher elongation in the case of Q&P1180 obtained from supplier 1.
- Both steels exhibit similar formability, as observed through the Nakajima test.
- The Abaqus program was used to simulate the material for each geometry treated and, through damage and anisotropy calculation methods, the graphs obtained are superimposable on experimental data of the samples tested in the laboratory, proving the good reliability of simulation compared to the physical tests.
- The Q&P1180 steel of both suppliers could be used as alternatives in automotive components, thanks to observed similar mechanical properties.
- The Q&P steel grades will be widely introduced in the automotive application, thanks to the opportunity to reduce the weight without compromising the safety and durability performances of the car.

Author Contributions: Conceptualization, M.M.T. and M.B. (Marcello Baricco); Methodology, M.B. (Matteo Basso), P.L., S.P., D.G. and A.M.; Writing—original draft preparation, M.M.T., M.B. (Matteo Basso), P.L., S.P., D.G. and A.M.; Writing—review and editing, M.M.T., M.B. (Matteo Basso), P.L., S.P., D.G., A.M. and M.B. (Marcello Baricco); Supervision, M.B. (Marcello Baricco). All authors have read and agreed to the published version of the manuscript.

Funding: Support from the Project CH4.0 under the MUR program "Dipartimenti di Eccellenza 2023–2027" (CUP: D13C22003520001) is acknowledged.

Data Availability Statement: The raw data supporting the conclusions of this article will be made available by the authors on request.

Conflicts of Interest: Authors Michele Maria Tedesco, Antonio Mara, Stefano Plano, Davide Gabellone and Matteo Basso are employed by Stellantis. Author Pietro Licignano is employed by Nuova Allemano. The remaining author declares that the research was conducted in the absence of any commercial or financial relationships that could be construed as a potential conflict of interest.

References

1. Maire, E.; Bouaziz, O.; Di Michiel, M.; Verdu, C. Initiation and growth of damage in a dual-phase steel observed by X-ray microtomography. *Acta Mater.* **2008**, *56*, 4954–4964. [CrossRef]
2. Noder, J.; Gutierrez, J.E.; Zhumagulov, A.; Dykeman, J.; Ezzat, H.; Butcher, C. A comparative evaluation of third-generation advanced high-strength steels for automotive forming and crash applications. *Materials* **2021**, *14*, 4970. [CrossRef] [PubMed]
3. Alcántara Alza, V.; Pelaez Chavez, V. TRIP steels: Factors influencing their formation, mechanical properties and microstructure—A review. *IOSR J. Mech. Civ. Eng.* **2022**, *19*, 37–60.
4. Liu, L.; He, B.; Huang, M.X. The role of transformation-induced plasticity in the development of advanced high-strength steels. *Adv. Eng. Mater.* **2017**, *20*, 1701083. [CrossRef]
5. Speer, J.; Matlock, D.K.; de Cooman, B.C.; Schroth, J.G. Carbon Partitioning into Austenite after Martensite Transformation. *Acta Mater.* **2003**, *51*, 2611–2622. [CrossRef]
6. Tedesco, M.M.; De Caro, D.; Rizzi, P.; Baricco, M. Effect of Composition and Thermal Treatments on Mechanical Properties and Applications of Quenching and Partitioning Steels. *Metals* **2023**, *13*, 1757. [CrossRef]
7. Edmonds, D.V.; He, K.; Rizzo, F.C.; de Cooman, B.C.; Matlock, D.K.; Speer, J.G. Quenching and Partitioning Martensite-A Novel Steel Heat Treatment. *Mater. Sci. Eng. A* **2006**, *438–440*, 25–34. [CrossRef]
8. De Moor, E.; Speer, J.G.; Matlock, D.K.; Kwak, J.H.; Lee, S.B. Effect of Carbon and Manganese on the Quenching and Partitioning Response of CMnSi Steels. *ISIJ Int.* **2011**, *51*, 137–144. [CrossRef]
9. Hausmann, K.; Krizan, D.; Pichler, A.; Werner, E. Trip-aided bainitic-ferritic sheet steel: A critical assessment of alloy design and heat treatment. In Proceedings of the Materials Science & Technology Conference and Exhibition 2013 (MS&T′13), Montreal, QC, Canada, 27–31 October 2013; pp. 209–218.
10. Carpio, M.; Calvo, J.; García, O.; Pedraza, J.P.; Cabrera, J.M. Heat Treatment Design for a Qp Steel: Effect of Partitioning Temperature. *Metals* **2021**, *11*, 1136. [CrossRef]
11. Jin, J.W.; Byun, S.H.; Lee, S.B.; Kim, S.I.; Oh, C.S.; Kang, N.; Cho, K.M. Mechanical properties comparison of DP, TRIP, Q&P steels as a function of heat treatment condition. In Proceedings of the International Conference on New Developments in Advanced High, Orlando, FL, USA, 15–18 June 2008.
12. Pastore, E.; De Negri, S.; Fabbreschi, M.; Ienco, M.G.; Pinasco, M.R.; Saccone, A.; Valentini, R. Experimental investigation on low-carbon quenched and partitioned steel. *La Metall. Ital.* **2011**, *103*, 25–35.
13. Xia, P.; Vercruysse, F.; Celada-Casero, C.; Verleysen, P.; Petrov, R.H.; Sabirov, I.; Molina-Aldareguia, J.M.; Smith, A.; Linke, B.; Thiessen, R.; et al. Effect of Alloying and Microstructure on Formability of Advanced High-Strength Steels Processed via Quenching 487 and Partitioning. *Mater. Sci. Eng. A* **2022**, *831*, 142217. [CrossRef]
14. *UNI 3244:1966*; Microscopic Examination of Ferrous Materials. Methods for Evaluating Non-Metallic Inclusions in Steels—JK (Jernkontoret) Scale, Worst Field Method. Italian National Unification Body (UNI): Milan, Italy, 1966.
15. *ASTM E407-07 (Reapproved 2015)*; Standard Practice for Microetching Metals and Alloys. ASTM International: West Conshohocken, PA, USA, 2015.
16. *VDA 238-100*; Plättchen-Biegeversuch für Metallische Werkstoffe/Plate Bending Test for Metallic Materials (Version 07/2020)—Gruppenlizenz (group license), AGB (GTC) Art. 10, 2. VDA: Berlin, Germany, 2020.
17. Noder, J.; Dykeman, J.; Butcher, C. New methodologies for fracture detection of automotive steels in tight radius bending: Application to V-bend test VDA 238-100. *Exp. Mech.* **2021**, *61*, 367–394. [CrossRef]
18. *ISO 12004:2008*; Metallic Materials—Sheet and Strip—Determination of Forming-Limit Curves. ISO (International Organization for Standardization): Geneva, Switzerland, 2008.
19. Kardes Sever, N. Material characterisation for strength and formability limits of DP 1180 sheet. *Canadian Metall. Q.* **2022**, *61*, 282–291.
20. *ISO 1099:2006*; International Organization for Standardization. Metals—Fatigue Testing—Vocabulary. ISO (International Organization for Standardization): Geneva, Switzerland, 2006.

21. *ISO 12107:2012*; Metals—Fatigue Testing—Statistical Planning and Analysis of Data. International Organization for Standardization: Geneva, Switzerland, 2012.
22. *ISO 12106:2022*; Metals—Fatigue Testing—Axial-Strain-Controlled Method. International Organization for Standardization: Geneva, Switzerland, 2022.
23. *ISO 6892-1:2019*; Metals—Tensile Testing—Part 1: Method of Test at Room Temperature. International Organization for Standardization: Geneva, Switzerland, 2019.
24. Dassault Systèmes Simulia Corp. *Abaqus, fe-safe, Isight, SIMULIA Execution Engine, Tosca Fluid, and Tosca Structure 2022 FD04*; Dassault Systèmes Simulia Corp.: Johnston, RI, USA, 2022.
25. Nyyssönen, T.; Oja, O.; Jussila, P.; Saastamoinen, A.; Somani, M.; Peura, P. Quenching and Partitioning of Multiphase Alumi-520 num-Added Steels. *Metals* **2019**, *9*, 373. [CrossRef]
26. Kaar, S.; Krizan, D.; Schneider, R.; Sommitsch, C. Impact of Si and Al on Microstructural Evolution and Mechanical Properties of Lean Medium Manganese Quenching and Partitioning Steels. *Steel Res. Int.* **2020**, *91*, 2000181. [CrossRef]
27. Liang, J.; Yang, D.; Chen, X.; Zhao, W.; Wang, G.; Yi, H. Hole expansion behavior of 1100 MPa grade dual-phase steel with superior stretch-flangeability. *Mater. Today Commun.* **2024**, *39*, 108929. [CrossRef]
28. Beden, S.M.; Abdullah, S.; Ariffin, A.K.; Al-Asady, N.A.; Rahman, M.M. Fatigue life assessment of different steel-based shell materials under variable amplitude loading. *Eur. J. Sci. Res.* **2009**, *29*, 157–169.

metals

MDPI

Article

Hot-Deformed Microstructure and Texture of Ti-62222 Alloy

Chanho Park [1], Haeju Jo [1], Jae H. Kim [2], Jongtaek Yeom [2], Namhyun Kang [1] and Wookjin Lee [1,*]

[1] School of Materials Science and Engineering, Pusan National University, Busan 46241, Republic of Korea; bamon12@pusan.ac.kr (C.P.); haejujo@pusan.ac.kr (H.J.); nhkang@pusan.ac.kr (N.K.)
[2] Titanium Department, Korean Institute of Materials Science, Changwon 51508, Republic of Korea; jaehkim@kims.re.kr (J.H.K.); yjt96@kims.re.kr (J.Y.)
* Correspondence: wookjin.lee@pusan.ac.kr

Abstract: The Ti-62222 (Ti-6Al-2Sn-2Zr-2Mo-2Cr) alloy has considerable potential for structural applications in the aerospace industry owing to its exceptional fracture resistance and specific strength. This study investigates the influence of local strain parameters and solution treatment and aging (STA) on the microstructure, texture evolution, and microhardness of a hot-forged Ti-62222 alloy. The strain distribution was simulated using the finite element method (FEM). The results showed that in the specimens before heat treatment, the morphology of the primary Ti α phase grains elongated perpendicular to the compression direction as the strain increased. In contrast, the post-heat-treated specimens (PHTSs) exhibited similar aspect ratios, regardless of the strain level, owing to grain spheroidization induced by the STA heat treatment process. Spheroidal primary Ti α phase and acicular Ti α′ phase were observed in the specimens before and after heat treatment. Texture analysis revealed that the specimens subjected to heat treatment had a weaker texture than the before-heat-treatment specimens. The near $(11\bar{2}0)//FD$ texture tended to develop along the direction perpendicular to the forging direction. The microhardness analysis results indicated that strain had no significant effect on the microhardness of either the as-forged specimen or the PHTS. After heat treatment, the specimens showed consistent microhardness values regardless of the strain level. The PHTS exhibited increased microhardness, attributed to the aging process during STA.

Keywords: Ti-6Al-2Sn-2Zr-2Mo-2Cr; hot compression; dynamic recrystallization; microstructure; EBSD; texture

1. Introduction

Titanium alloys are widely used in the aerospace, energy, military, and marine industries owing to higher stiffness, specific strength, and excellent corrosion resistance compared to other structural materials [1–13]. However, titanium alloys are prone to develop strong textures during plastic deformation [14–18]. This strong texture can result in significant anisotropy in the mechanical properties and plastic deformation behavior, necessitating further investigation [19–21]. Kobryn et al. [22] investigated the microstructure and texture evolution during the solidification of Ti-6Al-4V. Peters et al. [23] investigated the influence of texture on the fatigue properties of Ti-6Al-4V.

Among titanium alloys, the Ti-62222 alloy exhibits significant potential for structural applications in the aerospace industry owing to its superior fracture toughness and higher specific strength relative to Ti-6Al-4V [24], one of the most widely used commercial titanium alloys [25]. However, studies on texture evolution during the deformation of the Ti-62222 alloy remain limited.

Considering that the hot workability of titanium alloys decreases significantly with decreasing temperature [26], the production of components typically involves ingot casting which is followed by various hot deformation and heat treatment processes, broadly referred to as thermomechanical processing [21]. Consequently, extensive research has been conducted on the hot deformation behavior of titanium alloys to enhance their mechanical performance. Yang et al. [27] investigated the influence of temperature and strain rate during hot compression of Ti-6Al-4V on the microstructure and texture. The results indicate that at temperatures below 900 °C and strain rates exceeding 0.1 s^{-1}, the microstructure primarily comprises elongated Ti α grains. Compared to the as-received specimen, the texture was stronger in the specimen deformed at 930 °C and weaker in the specimen deformed below 930 °C. Warchomicka et al. [28] investigated the effect of strain rate on the microstructural evolution during hot deformation of the Ti-6Al-4V alloy. The results show that the dynamic recrystallization of the Ti α grain occurs at strains of 1 within the strain rate range of 0.1–5 s^{-1}. In the Ti α- β region, the Ti α grains maintain their shape during deformation up to a strain of 0.2. Zhang et al. [29] investigated the plastic flow behavior and microstructural evolution during the subtransus hot deformation of the Ti-6Al-4V alloy with three initial microstructures. The results indicate that the Ti α′ martensitic starting microstructure is more beneficial for achieving grain refinement in Ti-6Al-4V alloy. To date, most studies on the hot deformation behavior of titanium alloys have focused on conventional titanium alloys such as the Ti-6Al-4V, whereas research on the hot deformation behavior of the Ti-62222 alloy is limited. Additional research is essential to optimize industrial applications of the Ti-62222 alloy.

This study investigates the influence of local strain parameters and heat treatment on the microstructure, texture evolution, and microhardness of the hot-forged Ti-62222 alloy. The strain distribution within the specimens was evaluated using the finite element method (FEM). The microstructures of the specimens were analyzed using optical microscopy (OM), scanning electron microscopy (SEM), and electron backscatter diffraction (EBSD). The textures of the specimens were analyzed using an orientation distribution function (ODF).

2. Materials and Methods

The double cone Ti-62222 specimens—with a height of 77 mm and a minor and major diameter of 55 and 77 mm—were hot forged at 910 °C. A schematic of the hot-forging process is shown in Figure 1a, and the dimensions of the hot-forged specimen are shown in Figure 1b. After deformation, solution treatment and aging (STA) heat treatment were performed to investigate its effect on the microstructure, texture, and microhardness. The heat treatment consisted of solution treatment at 945 °C for 30 min, followed by air cooling and aging at 540 °C for 8 h, and then followed by further air cooling. On completion of processing, the specimens were cut parallel to the forging direction for cross-sectional analysis.

The FEM-based software DEFORM^{TM} V11 was used to simulate the deformation tests and analyze the deformation distribution within the sample. The plastic flow behavior of the Ti-6222 alloy for the FEM simulation at elevated temperatures was obtained from a compressive stress–strain curve of the alloy in the temperature range between 750 and 1050 °C. Based on the experimental compressive stress–strain curves, the flow stress of the alloy was assumed to be 325 MPa at 750 °C before decreasing linearly with increasing temperature to 40 MPa at 1050 °C. For the simulation, the Ti double cone was set as an elastic-plastic object while the forging dies were set as rigid objects. Their physical parameters, such as the elastic moduli, referred to the material database in Deform-3D. The Ti double cone was meshed with 272,548 meshes. The temperatures of the dies and the exterior were set to 910 °C. The film and friction coefficients between the double cone and

the dies were chosen as 5 and 0.3 N/s·mm·°C, respectively. Figure 2 shows the deformation distribution maps of the deformed specimens. Based on the strain levels, arbitrary locations within the specimen were labeled from A to R. The highest strain was observed at location A and the lowest at location R. The microstructural and textural evolution was investigated at each location.

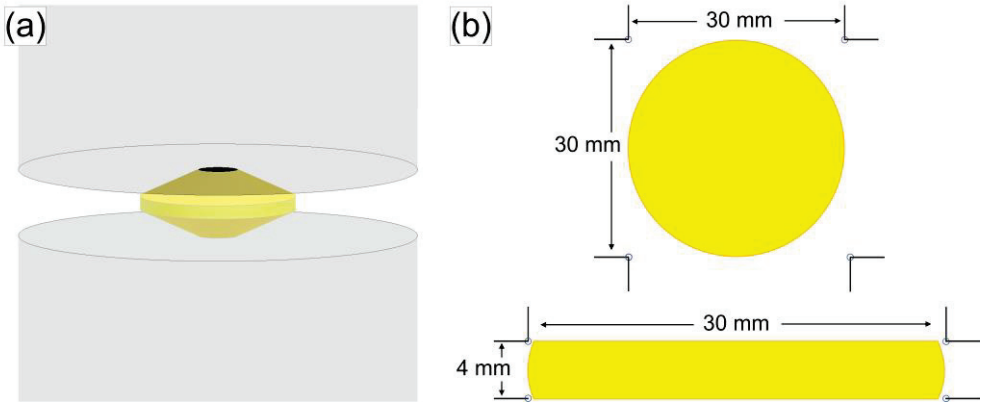

Figure 1. (**a**) Schematic of the hot forging process for the double cone specimen. (**b**) Specimen dimensions of the hot-forged specimen.

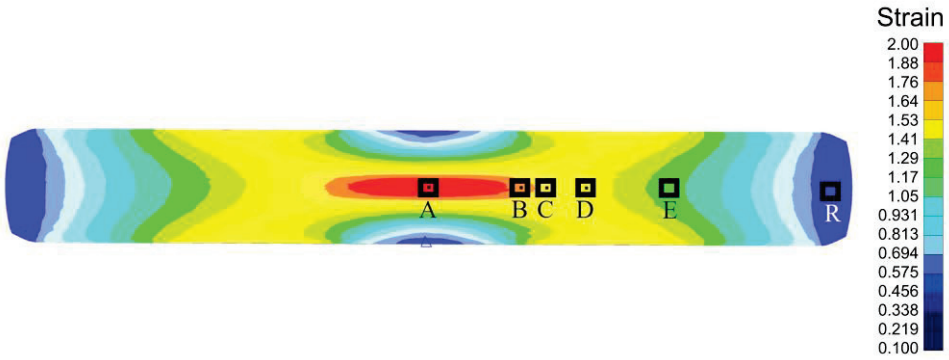

Figure 2. Deformation distribution map of deformed Ti-62222 specimens. Selected locations within the specimen are labeled from A to R based on strain levels.

The microstructures of the specimens were observed using an optical microscope (OM, Axiolab 5, Carl Zeiss, Jena, Germany) and SEM (Mira 3, TESCAN, Kohoutovice, Czech Republic). The specimens for the OM and SEM analyses were etched with Kalling etchant, a solution of copper chloride, hydrochloric acid, and ethanol. EBSD analysis (Aztec HKL, Oxford Inc., Oxford, UK) was conducted to further investigate the phase evolution. From OM images, the aspect ratio of the primary Ti α phase and the area ratio of each phase were analyzed using Image J (version 1.54g), an open-source image processing software.

For the texture evolution analysis, the ODF was calculated with multiple pole figure data using MTEX, a MATLAB-based data post-processing software. The MATLAB R2023a software was used for the data processing. The pole figures of the specimens were obtained using X-ray diffraction (XRD; SmartLab, Rigaku, Tokyo, Japan).

The microhardness of the specimens was measured using the HM200 Vickers microhardness test machine (Mitutoyo, Sakado, Japan). Test parameters during the hardness measurement were as follows: load = 3 N, load time = 7 s, and the interval between hardness indentations in the x and y directions = 0.3 mm. The microhardness distribution across the specimen was visualized as a microhardness map to analyze the effect of strain.

3. Results and Discussion

Phase evolution and phase analysis were conducted using an EBSD phase map and an inverse pole figure (IPF) map to investigate the microstructural changes during the high-temperature deformation process. The phase map analysis of the as-forged specimen presented in Figure 3a shows that the microstructure of the hot-forged Ti-62222 alloy consists of two distinct phases, both phases in a hexagonal close-packed structure but with different lattice parameters. The microstructure is composed of polygonal-shaped relatively coarse grains (Ti α) and a matrix comprising a mixture of two distinct phases (i.e., Ti α and Ti α′). The IPF map analysis establishes that grains with similar orientations are formed within a matrix (i.e., the surrounding matrix of primary Ti α grains) characterized by random orientations (Figure 3b). Based on the phase map and IPF map analysis in this study and on previous research on phase transformation during the hot deformation of Ti-62222 [30–33], the phase evolution process can be inferred as follows: during high-temperature compressive deformation, the high-temperature stable Ti β phase is formed as primary grains. As the temperature decreases, the Ti α+ β phases develop around the primary Ti β grains, followed by a diffusion-free transformation of the Ti β phase into the Ti α′ phase, resulting in regions containing a mixture of Ti α and Ti α′ phases.

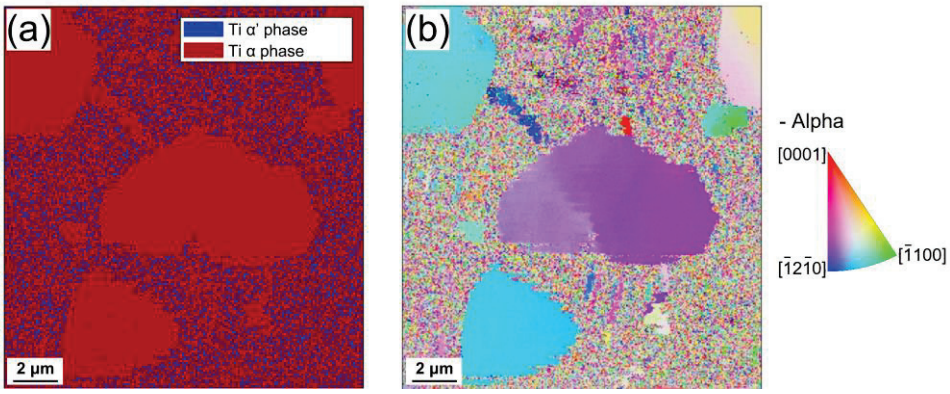

Figure 3. Cross-sectional EBSD analysis of the as-forged specimen: (**a**) phase map and (**b**) IPF map.

In a previous study [28], dynamic recrystallization of the Ti α grain was observed during the hot deformation process of Ti-6Al-4V at a strain of approximately 1 mm/mm. However, dynamic recrystallization of the primary Ti α grain was not observed during the hot deformation process in this study, even at higher strains of up to 2 mm/mm. From these results, it can be inferred that much higher plastic deformation or higher deformation temperature is required to achieve dynamic recrystallization in Ti-62222 in comparison to Ti-6Al-4V. This is probably because of the higher thermal stability of the primary α grain in Ti-6222 in comparison to that in Ti-6Al-4V.

Cross-sectional OM images by location for the specimens before and after heat treatment are shown in Figures 4 and 5, respectively. The primary Ti α phase grains elongated in a direction perpendicular to the compression axis as the strain increased in the as-forged specimens. The primary Ti α phase grains at location A, which experienced the highest strain, exhibited the most elongated morphology. The grain elongation could be observed at locations B, C, and D as well. However, at locations E and R, where relatively lower plastic strains are expected compared to locations A, B, C, and D, no significant grain elongation could be observed. This phenomenon can be attributed to the high-temperature deformation during the hot forging process, where grain elongation occurs in the direction perpendicular to the forging direction. Conversely, Ti α phase grains exhibit uniform morphology after the heat treatment, independent of the strain levels caused by grain spheroidization resulting from the STA heat treatment process. The aspect ratios of the

primary Ti α phase by location for specimens before and after heat treatment are shown in Figure 6a. The aspect ratio of the as-forged specimen exhibited a tendency to increase with increasing strain, owing to grain elongation occurring perpendicular to the forging direction during high-temperature deformation. In contrast, the post-heat-treated specimen exhibited consistent aspect ratios irrespective of the strain level, likely due to grain spheroidization facilitated by the STA heat treatment process. The area ratio indicating the fraction of the primary Ti α phase relative to the total area was analyzed by location for specimens both before and after heat treatment, as shown in Figure 6b. The area fraction was approximately 35% before heat treatment and 21% after heat treatment—considered to result from the partial dissolution of the primary Ti α phase and its transformation into the thermally stable Ti β phase during the STA heat treatment process.

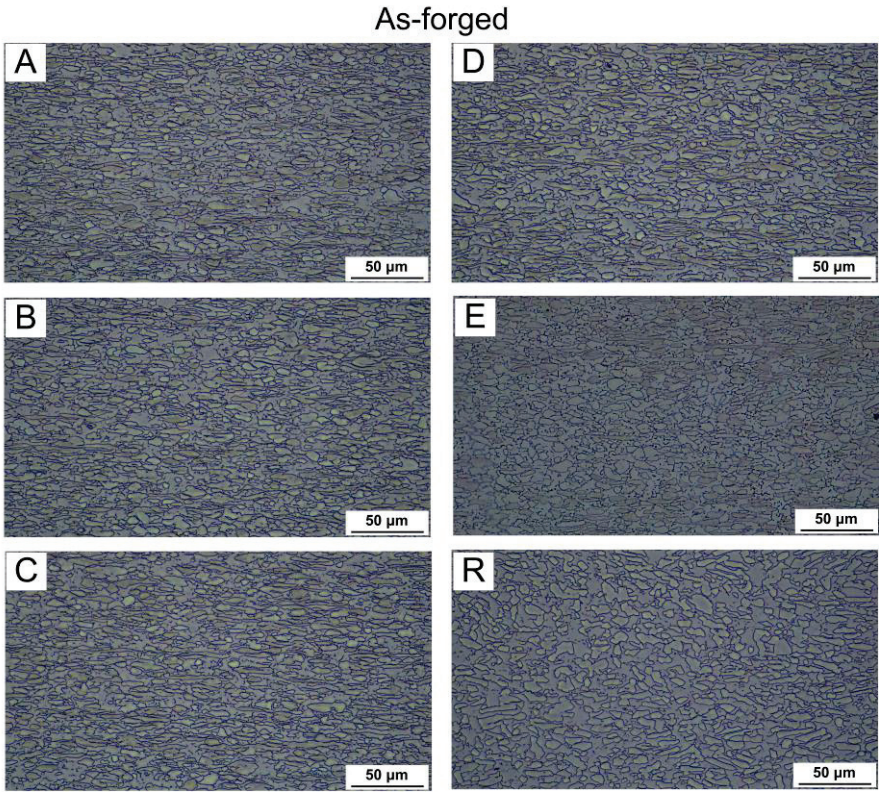

Figure 4. Cross-sectional OM images of as-forged specimens at locations A to R, representing different strain levels, observed to analyze microstructural evolution.

The effects of strain and heat treatment on the microstructures of the specimens were investigated using SEM, as shown in Figure 7. Both before and after heat treatment, the microstructure exhibited spheroidal primary Ti α and acicular Ti α′ phases. The acicular Ti α′ phase showed no significant changes in size or morphology regardless of the strain level, both before and after heat treatment. Additionally, it was observed that the heat treatment does not affect the morphology of the acicular Ti α′ phase. However, the spheroidal primary Ti α phase grains in the as-forged specimens were observed to be relatively more elongated at locations A, B, C, and D, which experienced higher strain levels in the forging process. At location E, the grains were less elongated in comparison to locations A–D; no grain elongation was observed at location R, which experienced minimal strain. These findings indicate that during the high-temperature deformation process, the morphology of the spheroidal primary Ti α phase grains becomes increasingly elongated with higher strain levels, whereas no elongation occurs below a certain strain level. In contrast, the post-heat-treated specimens showed no elongation of the spheroidal primary Ti α phase grains, regardless of the strain level, likely due to grain spheroidization induced by the

STA heat treatment process. Furthermore, the primary Ti α phase appears brighter in the heat-treated specimen in comparison to the as-forged specimen, indicating that the microstructural defects such as dislocations and low-angle grain boundaries in these phases were reduced due to the annealing effect during the heat treatment.

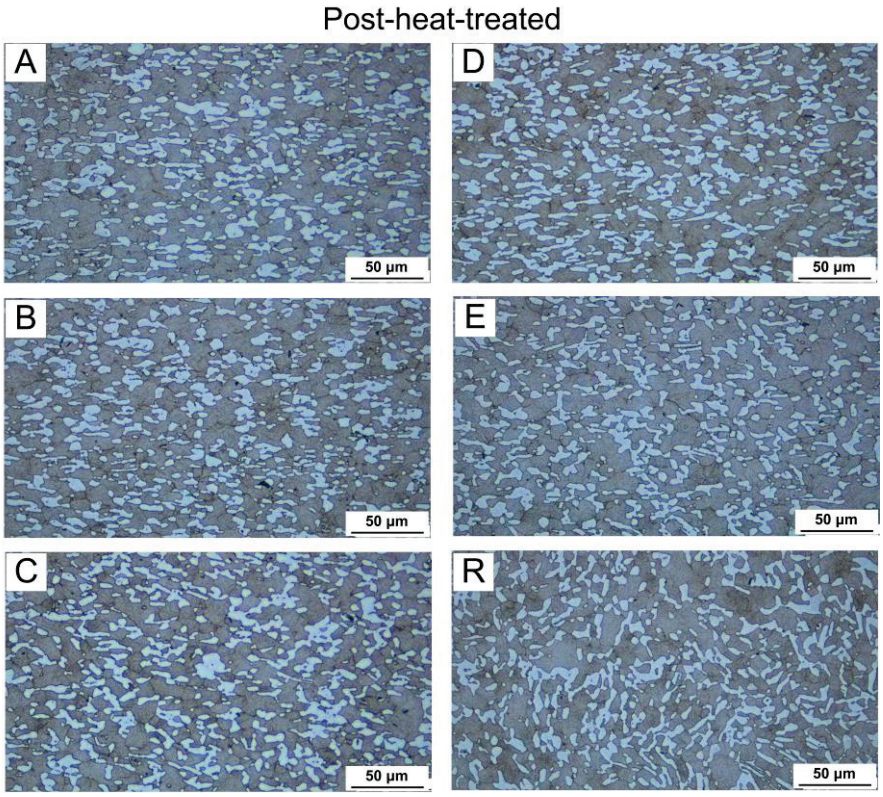

Figure 5. Cross-sectional OM images of post-heat-treated specimens at locations A to R, representing different strain levels, observed to analyze microstructural evolution.

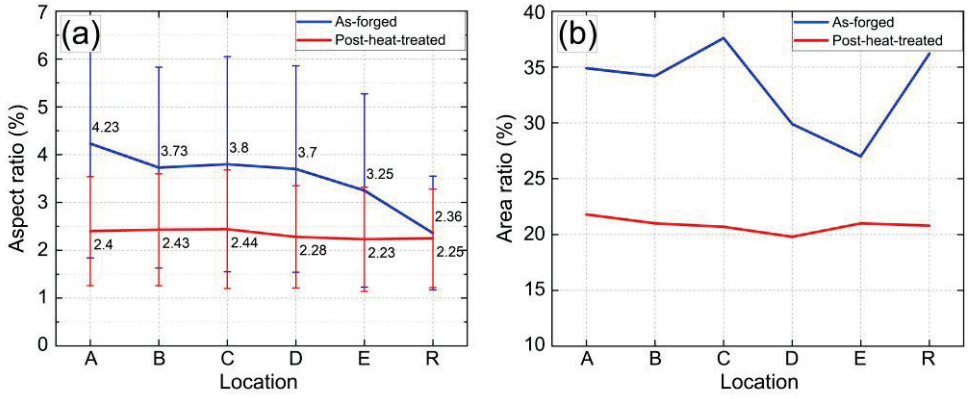

Figure 6. (**a**) Aspect ratio of primary Ti α phase by location for specimens before and after heat treatment. (**b**) Area ratio representing the proportion of the primary Ti α phase relative to the total area by location for specimens before and after heat treatment.

The ODF analysis results for the specimens were compared by location, both before and after the heat treatment, as shown in Figure 8. The textures of $(13\bar{4}0)//FD$, $(23\bar{5}1)//FD$, $(14\bar{5}2)//FD$, $(12\bar{3}0)//FD$, and $(12\bar{3}1)//FD$ were observed in the as-forged specimens. In contrast, in the post-heat-treated specimens, only the textures $(13\bar{4}0)//FD$, $(12\bar{3}0)//FD$, and $(12\bar{3}1)//FD$ were observed. These results reveal similarities in the $(13\bar{4}0)//FD$, $(12\bar{3}0)//FD$, and $(12\bar{3}1)//FD$ textures between the specimens before and after heat treatment, whereas the $(23\bar{5}1)//FD$ and $(14\bar{5}2)//FD$ textures observed in the as-forged specimens disappeared

after heat treatment. Moreover, the overall texture strength of the post-heat-treated specimens was weaker than that of the as-forged specimens. These results confirm that the strong texture formed in Ti-62222 after deformation can be weakened by heat treatment. The before and after heat treatment specimens exhibited the weakest texture at location R, where the strain level was the lowest, indicating that the deformation process significantly contributes to texture development in the Ti-62222 alloy. Texture analysis demonstrated a clear tendency for the near $(11\bar{2}0)//FD$ texture to develop along the direction perpendicular to the forging direction, confirming that the forging process significantly influenced the orientation of the texture. As the near $(11\bar{2}0)//FD$ texture is characteristic of typical Ti β forging textures, this analysis suggests that forging was conducted in a region comprising both Ti α and Ti β phases.

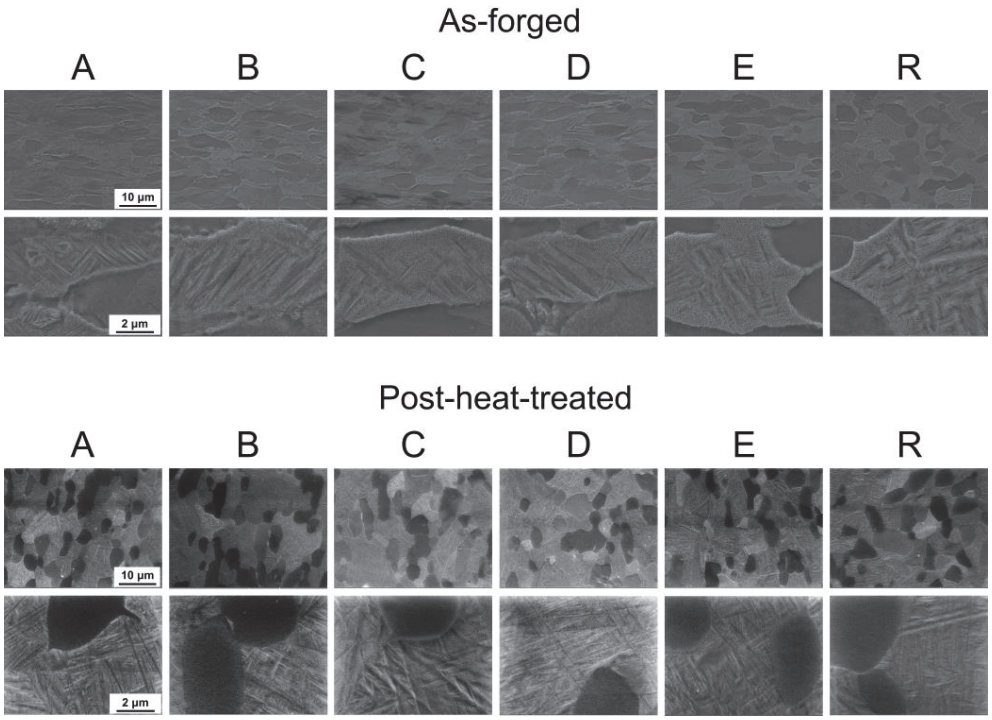

Figure 7. Cross-sectional SEM images of specimens at locations A to R, representing different strain levels, observed to analyze microstructural changes before and after heat treatment.

The microhardness was measured as the distance from the center of the as-forged and post-heat-treated specimens. The measured microhardness values are presented as microhardness maps and graphs in Figure 9. In the as-forged specimens and post-heat-treated specimens, consistent values were observed across the entire specimen, regardless of the strain level. These results indicated that the hot deformation of Ti-62222 had no significant effect on the hardness of the specimen. The average microhardness of the as-forged specimen was approximately 330 HV, whereas the post-heat-treated specimen exhibited a higher average microhardness of approximately 431 HV. In a previous study [34], Pinke et al. found that air cooling after solution heat treatment had no significant effect on the hardness of Ti alloys. However, subsequent aging treatment at 550 °C increased the microhardness due to precipitation of the fine Ti α phase from the Ti β phase. As shown in Figure 6b, the area ratio of the primary Ti α phase decreased after heat treatment. This phenomenon is attributed to the partial phase transformation of the primary Ti α phase into the thermally stable Ti β phase during the solution heat treatment in the STA process. Additionally, a portion of the transformed Ti β phase underwent further phase transformation into an acicular Ti α′ phase due to the rapid cooling rate during air cooling after solution treatment. Subsequently, the isothermal ω phase formed within

the remaining Ti β phase as the aging process progressed further, leading to an increase in hardness. Therefore, the hardness increase in the post-heat-treated specimens can be attributed primarily to the formation of the acicular Ti α′ phase and isothermal ω phase within the Ti β phase owing to the phase transformation induced by the STA heat treatment.

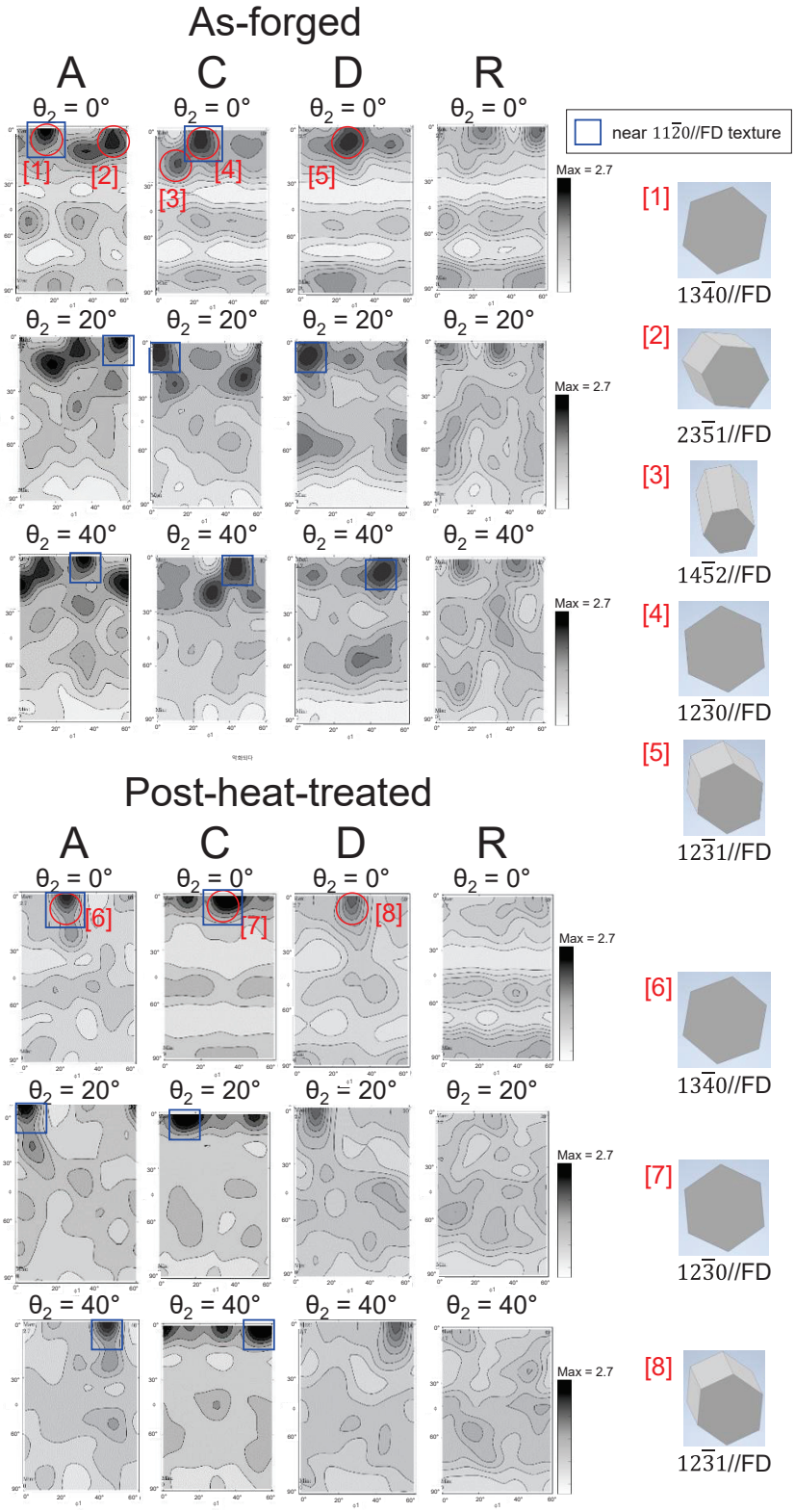

Figure 8. ODF analysis results of specimens at locations A, C, D, and R, corresponding to different strain levels, before and after heat treatment, to investigate texture evolution. The near (11$\bar{2}$0)//FD texture is highlighted with a blue box.

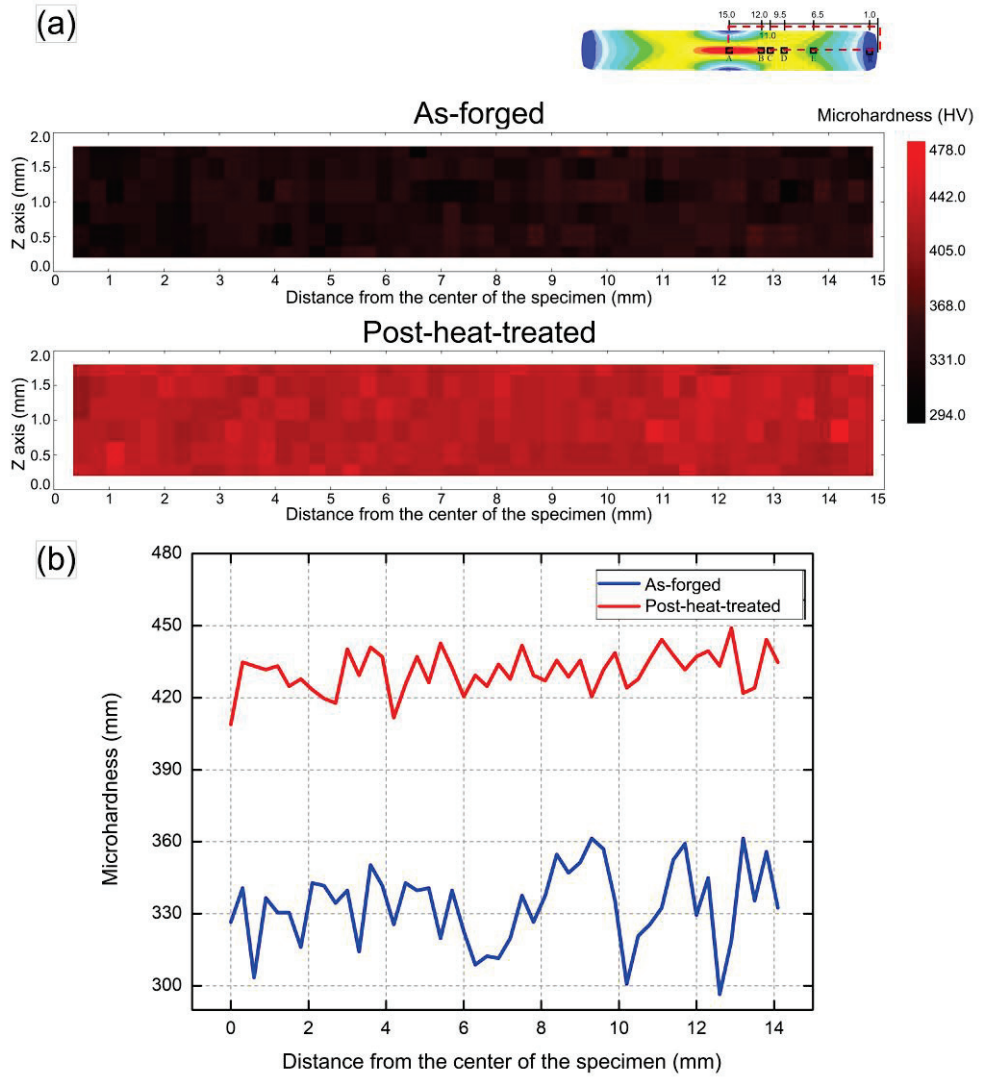

Figure 9. Microhardness measurement results by distance from the center of the specimen for the specimens before and after heat treatment: (**a**) microhardness map of the entire specimen and (**b**) microhardness values at a Z-axis depth of 1 mm plotted against the distance from the center of the specimen.

4. Conclusions

This study investigated the microstructure, texture evolution, and microhardness of hot-forged Ti-62222 alloys. The deformation distribution within the specimens was analyzed by simulating deformation tests using FEM to evaluate the effects of strain levels. STA was performed to examine the impact of the heat treatment. Additionally, phase map and IPF map analyses were conducted to investigate the phase evolution process during the hot deformation of Ti-62222.

1. During high-temperature compressive deformation, the thermally stable Ti β phase formed as primary grains. During cooling, Ti α+β phases developed around the primary β grains, followed by a diffusion-free transformation of the Ti β phase into the Ti α′ phase. This phenomenon resulted in regions containing a mixture of Ti α and Ti α′ phases in the hot-forged Ti-62222. The dynamic recrystallization of the Ti α phase is not observed during the hot forging process up to a strain of 2 mm/mm. It is inferred that much higher deformation is required for the dynamic recrystallization of Ti-62222 to occur during the hot deformation process, owing to the higher thermal stability of the α phase of this alloy in comparison to Ti-6Al-4V.

2. Both as-forged and post-heat-treated specimens exhibited spheroidal primary Ti α phase and acicular Ti α′ phase. The primary Ti α phase exhibited grain elongation, which became more pronounced with increasing strain levels. In contrast, the acicular Ti α′ phase showed no significant changes in size or morphology regardless of strain level. Spheroidization of the primary α phase occurred after the STA heat treatment.
3. Texture analysis established that the strong textures formed during deformation weakened after heat treatment. Particularly, the $(13\bar{4}0)//FD$, $(12\bar{3}0)//FD$, and $(12\bar{3}1)//FD$ textures were preserved, whereas the $(23\bar{5}1)//FD$ and $(14\bar{5}2)//FD$ textures disappeared after the heat treatment. The development of a near $(11\bar{2}0)//FD$ texture along the direction perpendicular to the forging direction confirms the considerable influence of hot deformation on texture orientation.
4. The microhardness measurement results indicated that strain had no significant effect on the microhardness of either the as-forged or the post-heat-treated specimens. In contrast, the post-heat-treated specimen exhibited higher average microhardness; this can be attributed to the aging process during STA.

Author Contributions: Conceptualization, W.L. and N.K.; funding acquisition, J.Y. and J.H.K.; investigation, C.P. and H.J.; methodology, J.H.K., J.Y., W.L. and N.K.; project administration, W.L.; validation, W.L. and N.K.; writing—original draft, C.P. and H.J.; Writing—review and editing, W.L. All authors have read and agreed to the published version of the manuscript.

Funding: This research was funded by a two-year research grant from Pusan National University.

Institutional Review Board Statement: Not applicable.

Informed Consent Statement: Not applicable.

Data Availability Statement: The original contributions presented in this study are included in the article. Further inquiries can be directed to the corresponding author.

Conflicts of Interest: The authors declare no conflicts of interest.

References

1. Collings, E.W. *Physical Metallurgy of Titanium Alloys*; Metallurgiya: Moscow, Russia, 1988.
2. Lin, J.; Ozan, S.; Li, Y.; Ping, D.; Tong, X.; Li, G.; Wen, C. Novel Ti-Ta-Hf-Zr Alloys with Promising Mechanical Properties for Prospective Stent Applications. *Sci. Rep.* **2016**, *6*, 37901. [CrossRef]
3. Gao, K.; Zhang, Y.; Yi, J.; Dong, F.; Chen, P. Overview of Surface Modification Techniques for Titanium Alloys in Modern Material Science: A Comprehensive Analysis. *Coatings* **2024**, *14*, 148. [CrossRef]
4. Yang, X.; Lin, B.; Zhang, H.; Tang, J.; Zhou, T.; Wang, Y.; Zheng, H.; Kuang, Y. Influence of Stress on the Corrosion Behavior of Ti Alloys: A Review. *J. Alloys Compd.* **2024**, *985*, 173346. [CrossRef]
5. Semenova, I.P.; Polyakov, A.V.; Dong, Y.; Sun, Z.; Alexandrov, I. V Microstructure and Mechanical Properties of Titanium Alloys Produced by Additive Technologies: New Approaches and Promising Areas of Research. *Metals* **2024**, *14*, 966. [CrossRef]
6. Guo, S.; Meng, Q.; Zhao, X.; Wei, Q.; Xu, H. Design and Fabrication of a Metastable β-Type Titanium Alloy with Ultralow Elastic Modulus and High Strength. *Sci. Rep.* **2015**, *5*, 14688. [CrossRef]
7. Shell, E.B.; Semiatin, S.L. Effect of Initial Microstructure on Plastic Flow and Dynamic Globularization during Hot Working of Ti-6Al-4V. *Metall. Mater. Trans. A* **1999**, *30*, 3219–3229. [CrossRef]
8. Devaraj, A.; Joshi, V.V.; Srivastava, A.; Manandhar, S.; Moxson, V.; Duz, V.A.; Lavender, C. A Low-Cost Hierarchical Nanostructured Beta-Titanium Alloy with High Strength. *Nat. Commun.* **2016**, *7*, 11176. [CrossRef]
9. Lin, N.; Zhang, H.; Zou, J.; Tang, B. Recent Developments in Improving Tribological Performance of TC4 Titanium Alloy via Double Glow Plasma Surface Alloying in China: A Literature Review. *Rev. Adv. Mater. Sci.* **2014**, *38*, 61–74.
10. Jin, H.X.; Wei, K.X.; Li, J.M.; Zhou, J.Y.; Peng, W.J. Research Development of Titanium Alloy in Aerospace Industry. *Chin. J. Nonferrous Met.* **2015**, *25*, 280–292.
11. Beese, A.M.; Carroll, B.E. Review of Mechanical Properties of Ti-6Al-4V Made by Laser-Based Additive Manufacturing Using Powder Feedstock. *JOM* **2016**, *68*, 724–734. [CrossRef]
12. Disegi, J.A.; Roach, M.D.; McMillan, R.D.; Shultzabarger, B.T. Alpha plus Beta Annealed and Aged Ti-15 Mo Alloy for High Strength Implant Applications. *J. Biomed. Mater. Res. Part B Appl. Biomater.* **2017**, *105*, 2010–2018. [CrossRef]

13. Cai, J.M.; Mi, G.B.; Gao, F.; Huang, H.; Cao, J.X.; Huang, X.; Cao, C.X. Research and Development of Some Advanced High Temperature Titanium Alloys for Aero-Engine. *J. Mater. Eng.* **2016**, *44*, 1–10.
14. Zhang, S.; Lin, Y.C.; He, D.-G.; Jiang, Y.-Q.; Zhang, H.-J.; Zeng, N.-F.; Wu, G.-C.; Naseri, M. Correlation between Plastic Deformation Mechanism and Texture Evolution of a near β-Ti Alloy Deformed in β Region. *Intermetallics* **2024**, *170*, 108333. [CrossRef]
15. Tong, Y.; Hua, K.; Sun, L.; Xie, H.; Zhao, M.; Zhou, L.; Wu, H.; Wang, H. Effect of Rolling-Texture Intensity on Fretting Damage and Subsurface Deformation Behavior in a High-Strength Titanium Alloy. *J. Mater. Sci. Technol.* **2024**, *196*, 200–214. [CrossRef]
16. Sun, T.; Deng, Y.; Liu, W.; Teng, H.; Wang, R.; Sun, C.; Deng, H.; Zhou, J. Substructure and Texture Evolution of a Novel Near-α Titanium Alloy with Bimodal Microstructure during Hot Compression in A+β Phase Region. *J. Alloys Compd.* **2024**, *996*, 174869. [CrossRef]
17. Fan, J.; Zhao, D.; Chen, Z.; Zhang, Z.; Wang, J.; Tang, B.; Chen, Z.; Wang, Q.; Kou, H.; Li, J. Tailoring Texture in a Near-α Titanium Alloy: Insights from Strain Paths and Cooling Rate Influences. *J. Mater. Res. Technol.* **2024**, *30*, 1388–1402. [CrossRef]
18. Wang, W.; Chen, C.; Zhao, R.; Gludovatz, B.; Lu, X.; Zhang, K.; Shuai, S.; Hu, T.; Xu, S.; Wang, J.; et al. A Laser Additive Manufactured Metastable Ti-10V-2Fe-3Al β-Titanium Alloy: Microstructure, Mechanical Properties, and Deformation Mechanisms. *Mater. Sci. Eng. A* **2024**, *890*, 145863. [CrossRef]
19. Skvortsova, S.V.; Ilyin, A.A. Mechanisms of Phase and Structural Transformations and Texture Formation in Titanium Alloy Sheet Semiproducts. *Russ. Metall.* **2007**, *2007*, 355–363. [CrossRef]
20. Obasi, G.C.; Birosca, S.; Leo Prakash, D.G.; Quinta da Fonseca, J.; Preuss, M. The Influence of Rolling Temperature on Texture Evolution and Variant Selection during A→β→α Phase Transformation in Ti–6Al–4V. *Acta Mater.* **2012**, *60*, 6013–6024. [CrossRef]
21. Semiatin, S.L. An Overview of the Thermomechanical Processing of α/β Titanium Alloys: Current Status and Future Research Opportunities. *Metall. Mater. Trans. A* **2020**, *51*, 2593–2625. [CrossRef]
22. Kobryn, P.A.; Semiatin, S.L. Microstructure and Texture Evolution during Solidification Processing of Ti–6Al–4V. *J. Mater. Process. Technol.* **2003**, *135*, 330–339. [CrossRef]
23. Peters, M.; Gysler, A.; Lütjering, G. Influence of Texture on Fatigue Properties of Ti-6Al-4V. *Metall. Mater. Trans. A* **1984**, *15*, 1597–1605. [CrossRef]
24. Evans, D.J.; Broderick, T.F.; Woodhouse, J.B.; Hoenigman, J.R. The Role of Intermetallic Precipitates in Ti-62222S. *Mater. Sci. Eng. A* **1996**, *213*, 37–44. [CrossRef]
25. Eylon, D.; Seagle, S.R. Titanium'99, Science and Technology. In Proceedings of the Ninth World Concerence on Titanium, Central Research Institute of Structural Materials (CRISM), Saint-Petersburg, Russia, 7–11 June 1999; pp. 866–875.
26. Semiatin, S.L.; Seetharaman, V.; Weiss, I. The Thermomechanical Processing of Alpha/Beta Titanium Alloys. *JOM* **1997**, *49*, 33–39. [CrossRef]
27. Yang, L.; Yang, Y. Deformed Microstructure and Texture of Ti6Al4V Alloy. *Trans. Nonferrous Met. Soc. China* **2014**, *24*, 3103–3110. [CrossRef]
28. Warchomicka, F.; Poletti, C.; Stockinger, M.; Henke, T. Microstructure Evolution during Hot Deformation of Ti-6Al-4V Double Cone Specimens. *Int. J. Mater. Form.* **2010**, *3*, 215–218. [CrossRef]
29. Zhang, Z.X.; Qu, S.J.; Feng, A.H.; Shen, J.; Chen, D.L. Hot Deformation Behavior of Ti-6Al-4V Alloy: Effect of Initial Microstructure. *J. Alloys Compd.* **2017**, *718*, 170–181. [CrossRef]
30. Lee, S.W.; Lee, H.J.; Kim, J.H.; Park, C.H.; Hong, J.-K.; Yeom, J.-T. Effect of Prior β Grain Size on the Martensitic Transformation of Titanium Alloys. *Mater. Charact.* **2021**, *182*, 111525. [CrossRef]
31. Zhang, X.D.; Bonniwell, P.; Fraser, H.L.; Baeslack III, W.A.; Evans, D.J.; Ginter, T.; Bayha, T.; Cornell, B. Effect of Heat Treatment and Silicon Addition on the Microstructure Development of Ti–6Al–2Cr–2Mo–2Sn–2Zr Alloy. *Mater. Sci. Eng. A* **2003**, *343*, 210–226. [CrossRef]
32. Wood, J.R.; Russo, P.A.; Welter, M.F.; Crist, E.M. Thermomechanical Processing and Heat Treatment of Ti–6Al–2Sn–2Zr–2Cr–2Mo–Si for Structural Applications. *Mater. Sci. Eng. A* **1998**, *243*, 109–118. [CrossRef]
33. Gupta, A.; Khatirkar, R.; Singh, J. A Review of Microstructure and Texture Evolution during Plastic Deformation and Heat Treatment of β-Ti Alloys. *J. Alloys Compd.* **2022**, *899*, 163242. [CrossRef]
34. Pinke, P.; Caplovic, L.; Kovacs, T. The Influence of Heat Treatment on the Microstructure of the Casted Ti6Al4V Titanium Alloy. *Slovak Univ. Technol. Bratislava. Web* **2011**, *11*. Available online: https://www.kfki.hu/anyagokvilaga/tartalom/2007/oktober/Pinke_2.pdf (accessed on 21 February 2025).

metals

Article

Microstructure Evolution and Mechanical Properties of B_4C-Reinforced TC11 + xFe Composites Fabricated by HIP

Shenwei Qian [1], Nan Wang [1], Feng Chen [1], Yangyang Sun [1,*], Jiong Zhao [2], Hui Chang [1], Liang Feng [1] and Lian Zhou [1]

[1] Tech Institute for Advanced Materials, College of Materials Science and Engineering, Nanjing Tech University, Nanjing 210009, China; 202261203182@njtech.edu.cn (S.Q.); 202452103017@njtech.edu.cn (N.W.); 202261203180@njtech.edu.cn (F.C.); ch2006@njtech.edu.cn (H.C.); feng2014@njtech.edu.cn (L.F.); zhoul@c-nin.com (L.Z.)
[2] Jiangsu Tiangong Technology Co., Ltd., Zhenjiang 212400, China; zhaojiong@jstgti.com
* Correspondence: sunyangyang0526@njtech.edu.cn

Abstract: The present study involved (TiB + TiC)/TC11 (Ti-6.5Al-3.5Mo-1.2Zr-0.3Si) + xFe titanium matrix composites (TMCs) reinforced by in situ TiB whiskers and TiC particles fabricated by hot isostatic pressing. Microstructure observation reveals a substantial distribution of in situ reinforcements, which form a network-reinforced structure at the prior particle boundaries of the TC11 matrix. The micro–nanoscale TiB whiskers and TiC particles within and surrounding this network serve as effective dislocation pinning. The enhancement of mechanical properties can be attributed to load-bearing strengthening, fine-grain strengthening, and dislocation strengthening. The hardness and compressive strengths were investigated through mechanical properties testing. The hardness increased by 19.4% (2 wt% B_4C-reinforced composites) compared with TC11 alloy. However, the addition of 2 wt% Fe at the same B_4C level (2 wt% B_4C + 2 wt% Fe-reinforced composites) resulted in a significant increase in hardness by 37.5% and 15.2% in compressive strengths of TMC and can be attributed to the solid solution strengthening effect and higher dislocation density provided by the addition of Fe. In addition, the optimal overall properties can be achieved by strictly regulating the addition ratio of 2 wt% Fe and 1 wt% B_4C, allowing for a compressive strength of 2301 MPa while still maintaining a compressive strain of 24.6%.

Keywords: titanium matrix composites; hot isostatic pressure; B_4C; mechanical properties; microstructure

1. Introduction

Titanium alloys are widely used in the petrochemical, biomedical, and aerospace fields due to their high strength, low density, and corrosion resistance [1–4]. Due to rapid advancements in various fields, the properties requirements for titanium alloys are becoming increasingly demanding. Titanium matrix composites (TMC) have emerged as a pivotal solution to tackle these challenges due to their exceptional properties, such as high specific strength and temperature stability [5–7]. In the latter quarter of the 20th century, TMC was extensively researched in the United States and Europe. The incorporation of ceramic reinforcements, such as TiC, SiC, and B_4C, is widely regarded as an effective method to achieve superior properties [8,9]. Reinforcement with different compositions can be generated through in situ reactions using the principles of powder metallurgy (PM), resulting in excellent metallurgical interfacial bonding and thermodynamic stability [10,11].

This process, such as hot isostatic pressing (HIP), significantly enhances the mechanical properties at both room temperature and high temperatures [12].

Solving the brittleness of TMCs has been the focus of extensive attention by researchers. The mechanical properties of the composite material primarily depend on the microstructure and properties of the matrix, as well as the type, mass fraction, distribution, and size of the reinforcement material. Additionally, they are influenced by the extent of interfacial bonding between the matrix and reinforcement. Researchers have improved both strength and plasticity by constructing a network reinforcement structure. Liu et al. [11] enhanced both the strength and ductility by preparing in situ reinforced (TiB + TiC)/Ti-6Al-4V composites with a network structure. Zhong et al. [13] constructed a two-scale network structure of TiB nanowires and micro-TiC particles combined with needle-like silicide, overcoming the strength–extensibility paradox. The in situ route of forming TMCs is a highly efficient and cost-effective method with a clean and strong reinforcement–matrix interface bonding, and the reinforcement is frequently precipitated from the matrix as either whisker or particle reinforcements [14,15]. Moreover, researchers have enhanced the ratio of TiB whiskers and formed nano-TiB whiskers to tackle the strength–ductility paradox [16,17]. Therefore, we introduced hybrid in situ TiB whisker and TiC particles through the process of PM-HIP, which has been proved effective in strengthening materials [18]. Furthermore, the addition of nano-B_4C powder leads to the formation of reinforcement with micro and nano sizes, and nano-sized reinforcements can provide significant strengthening in TMCs [19,20].

Moreover, the addition of Fe plays a crucial role in optimizing the strength and plasticity matching of titanium alloys. Researchers confirmed that Fe can affect the lattice distortion of titanium alloys, leading to significant solid solution strengthening [21–23]. Wang et al. [24] prepared in situ alloyed Ti–5Fe using selective laser melting (SLM), which achieved high tensile strength (865 MPa) with good elongation (12%). Niu et al. [25] studied Ti-Fe alloy and proved that the best overall properties were achieved by adding 2 wt% Fe.

Despite the significant enhancement of mechanical properties in titanium alloys through Fe addition, there is a lack of reports on further enhancing TMCs by the addition of Fe, and its influence on the mechanical properties and microstructure of TMCs remains unreported. Therefore, the addition of 1, 2 wt% Fe and addition of 0, 1, 2, 5 wt% B_4C are selected to enhance the Ti-6.5Al-3.5Mo-1.2Zr-0.3Si (TC11) alloy. In this study, the (TiB + TiC)/TC11 composite with a network-reinforced structure was prepared in situ by HIP by adding nano-B_4C powder to the TC11 matrix. In addition, Fe is added to obtain the best properties by regulating the content of B_4C and Fe. The microstructure and properties of all TMCs were studied and compared, providing a reference for the study of TMCs with good performance.

2. Materials and Methods

2.1. Material and Manufacture Process

The experimental material used in this work was titanium matrix composite prepared by two-step hot isostatic pressing (HIP). Pre-alloyed α + β titanium alloy Ti-6.5Al-3.5Mo-1.2Zr-0.3Si (referred to as TC11 hereafter) powder fabricated by a plasma rotating electrode process (PREP) (SHANGJI Co., Nanjing, China) with particle size ranges from 53 μm to 106 μm was used as a matrix material. The TC11 alloy was reinforced with in situ reinforcements through the incorporation of nano-B_4C powder with an average particle size of 50 nm. Additionally, nano-Fe powder with an average particle size of 50 nm was also added to investigate the microstructure and mechanical properties of the TMCs with the addition of Fe. The proportions of the three powders are shown in Table 1. The three powders were placed in a vacuum drying oven and heated at 100 °C for 4 h before

being put into a planetary ball-milling machine. The low-energy milling processes were conducted at 200 rpm for 6 h with an agate ball-to-powder weight ratio of 4:1. The ball-milled powders were loaded into stainless steel capsules with an inner diameter of 40 mm, a length of 150 mm, and a wall thickness of 2.5 mm, followed by 6 h of degassing at a vacuum of 1×10^{-3} pa and a temperature of 600 °C. The HIP process was conducted at 1050 °C/150 MPa for 4 h. After being cooled to room temperature, stainless steel capsules were removed by machining, followed by a two-step HIP sintering at 1150 °C/150 MPa for 4 h. The flow chart illustrating the fabrication process of (TiB + TiC)/TC11 composites through the HIP technique is presented in Figure 1.

Table 1. Mixture ratios of TC11, B_4C, and Fe powder (wt.%).

Number	TC11	B_4C	Fe
TC11	100	0	0
TMC1	98	2	0
TMC2	95	5	0
TMC3−F	97	1	2
TMC4−F	97	2	1
TMC5−F	96	2	2
TMC6−F	96	3	2

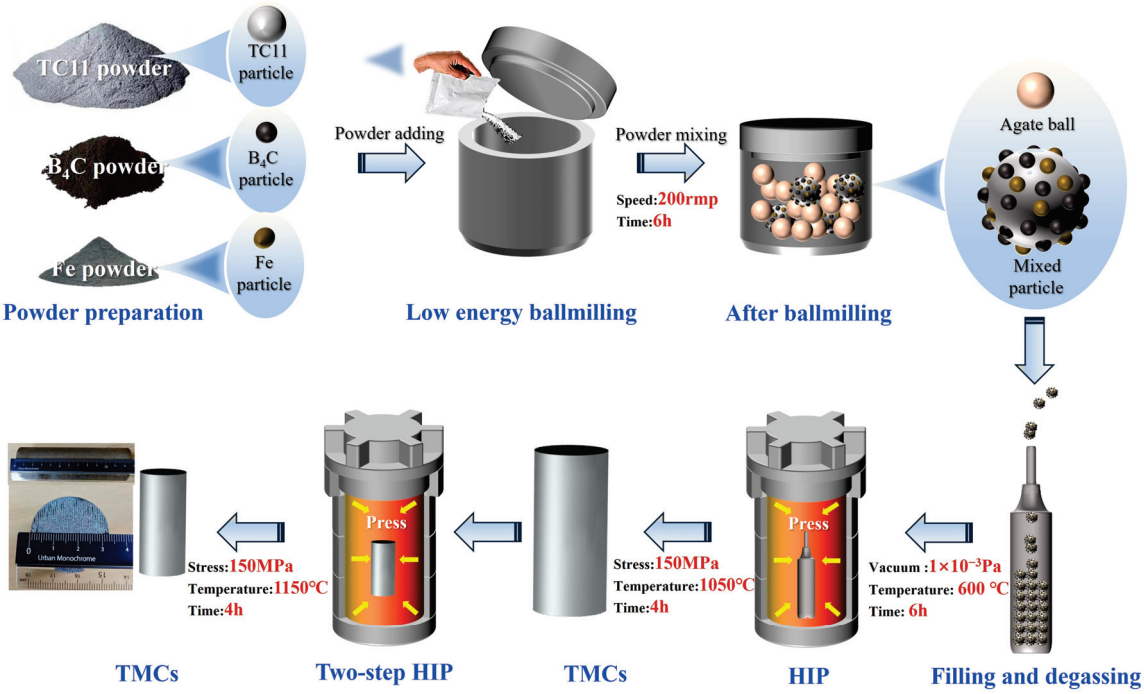

Figure 1. Flow chart of (TiB + TiC)/TC11 composites fabricated by hot isostatic pressing.

2.2. Microstructure and Morphology Characterization

The samples were separated from the prepared TMCs by wire cutting. The specific dimensions of each sample are depicted in Figure 2. The samples were subjected to X-ray diffraction (XRD, Rigaku SmartLab SE, AXT, Tokyo, Japan) for phase identification, operated with a Cu target at 35 kV and 40 mA using a continuous scan mode. A scan was conducted at 10°/min over a wide range of 30–80°. The samples for scanning electron microscope (SEM) observation were ground, polished, and etched by Kroll's reagent (10 vol% HF, 20 vol% HNO_3, and 70 vol% H_2O). Microstructure and morphology characterizations were conducted through a SEM (JSM6490LV, JEOL, Osaka, Jpapn). The microstructure

of initial powders was observed using a SIGMA field emission SEM (Zeiss, Oberkochen, Germany). The specimens were polished by argon ion-beam polishing (EM TIC 3X, Leica, Solms, Germany) at a voltage of 6 KV for 120 min and 4 KV for 30 min before electron backscatter diffraction (EBSD, C-SWIFT, Oxford, UK) observation. EBSD and AZtec software (Aztec Crystal 2.1.2, Oxford Instruments, Oxford, UK) were adopted to analyze the orientation of α-Ti, β-Ti, TiB, and TiC phases and phase content.

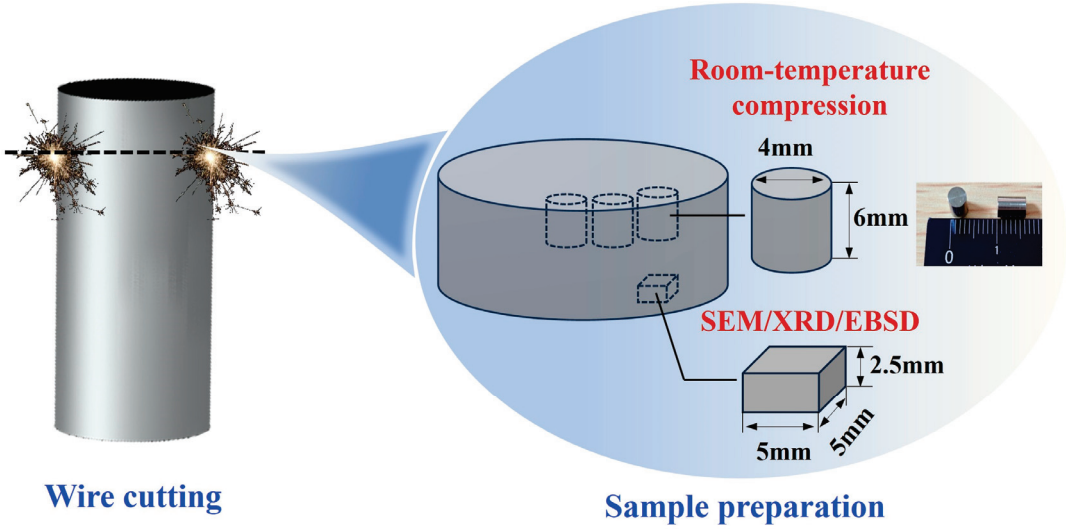

Figure 2. Sample preparation for SEM, XRD, EBSD, and room-temperature compression tests.

2.3. Mechanical Properties Testing

According to the Chinese Standard GB/T 7314-2017 [26], the room-temperature compression tests were executed on a universal testing machine (Instron 5569, Canton, MA, USA) with a loading rate of 0.1 mm/min, using a compression specimen size of Φ4 mm × 6 mm as shown in Figure 2.

Vickers hardness (HV) was measured using an HVS-1000 Vickers Hardness Tester, with a force of 20 N applied for 15 s. All the samples for hardness measurement underwent a sequential polishing process using sandpaper of varying grades, including 200, 400, 800, 1200, 1500, and 2000. A minimum of 15 tests were conducted to obtain the average result. The position for each test was set at a parallel interval of 20 μm, with the center of the sample as the starting point.

3. Results

3.1. Microstructure Characteristics of the Initial Powders

The microstructure characteristics of the B_4C powder, Fe powder, pre-alloyed TC11 powder, and mixed powder are summarized in Figure 3. Both the pre-alloyed TC11 powder (Figure 3a) and mixed powder (Figure 3d) exhibit excellent sphericity with no discernible defects, resulting in desirable powder flowability. This ensures the powder is well vibrated and fills the stainless steel capsules, which is conducive to the densification process [27]. The nano-B_4C powder (Figure 3b) and nano-Fe powder (Figure 3c) are uniformly adhered to the TC11 pre-alloy powder particles. The morphology of a single amplified particle of mixed powder, as depicted in Figure 3d, demonstrates a uniform combination of micro–nanoparticles achieved through low-energy ball milling.

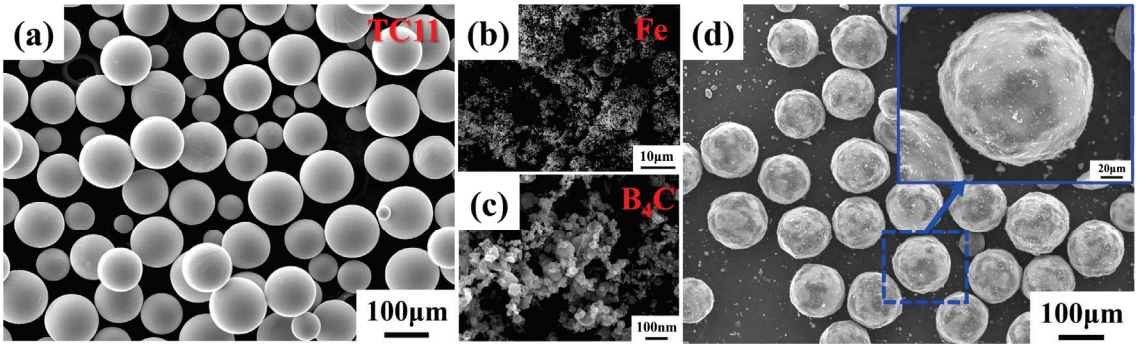

Figure 3. Microstructure characteristics of powders: (**a**) TC11 powder; (**b**) Fe powder; (**c**) B_4C powder; (**d**) mixed powder and amplified single particle.

3.2. Phase Composition

The XRD patterns of TMCs and TC11 alloy fabricated by HIP are shown in Figure 4. The results show that the α-Ti, β-Ti, TiB, and TiC peaks are clearly detected without the observation of the diffraction peak for B_4C. The XRD analysis reveals a low strength of β-Ti peaks, particularly in TC11, TMC1, and TMC2 without the addition of Fe, indicating limited precipitation of β-Ti grains. The addition of the β-stable element Fe results in the identification of more pronounced peaks in TMC3-F, TMC4-F, TMC5-F, and TMC6-F, as shown in the amplified spectrum B (Figure 4c). The raw material B_4C had been converted to the TiB whisker (TiB_w) and TiC particle (TiC_p) phases through the in situ reaction as $5Ti + B_4C \rightarrow 4TiB + TiC$ during the HIP process [28–30]. The intensity of TiC and TiB peaks increases with further addition of B_4C as shown by the amplified spectrum A in Figure 4b. The position of the matrix diffraction peak also shifted to the left due to an increase in the lattice constant of the TC11 matrix resulting from the formation of an interstitial solid solution with a solid solution of B and C atoms [31]. The HIP process did not introduce more reactions.

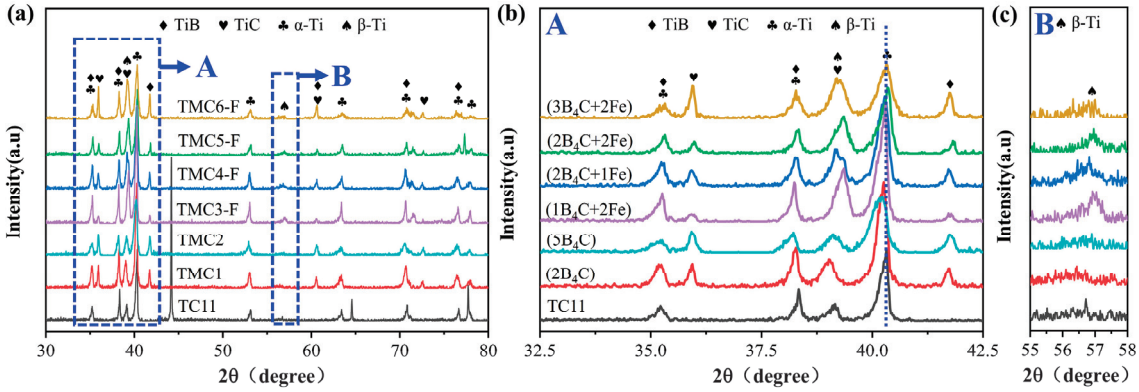

Figure 4. (**a**) XRD patterns of TC11 and TMCs; (**b**) amplified spectrum marked as A; (**c**) amplified spectrum marked as B.

3.3. Morphology of Microstructure

The SEM images of TC11 alloy and B_4C-reinforced TC11 composites demonstrate the evolution of microstructure, as shown in Figures 5 and 6. As shown in Figure 5a, the microstructures of TC11 matrix alloy consist of equiaxial α phase, platelet α phase, and residual β phase (β_r). The continuous grain boundary α phase (α_{GB}) and α/β colony structure with different orientations are also observed. In Figure 5b,c, it is observed that the in situ TiB and TiC reinforcements primarily accumulate at the prior particle boundaries (PPBs) and form a network structure. In addition, traces of nano-TiB whiskers (TiB_w)

and nano-TiC particles (TiC_p) can be found in the TC11 matrix slightly away from the PPBs, indicating that C atoms and B atoms in the (TiB + TiC)-rich region diffused a certain distance into the interior of the network structure. With the increase in B_4C addition, TiB_w and TiC_p grow and agglomerate on PPBs, resulting in the formation of a coarser and more continuous network structure. This alteration adversely affects the mechanical properties of TMCs [32]. It is noteworthy that the incorporation of 5 wt% B_4C and insufficient solid phase sintering resulted in the presence of pores at the PPBs in TMC6, with a nearly circular shape and an average size of 6.5 μm.

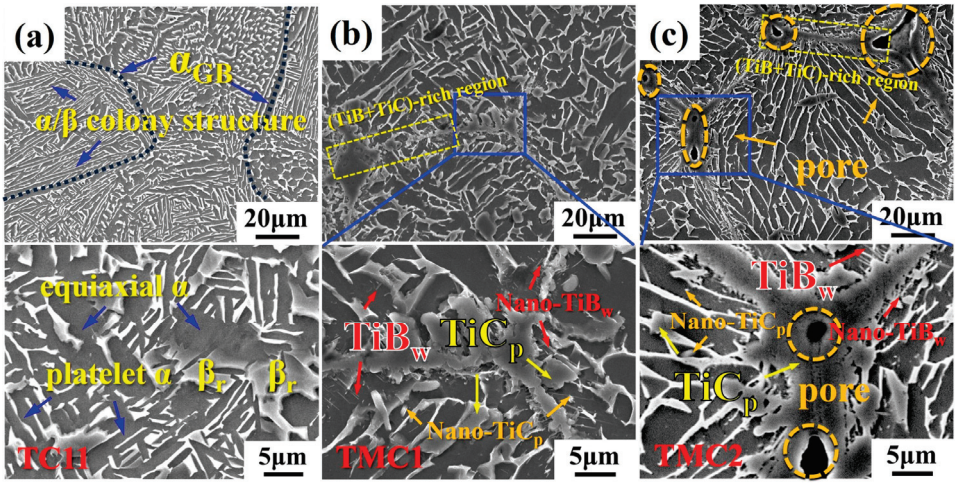

Figure 5. SEM micrographs of TC11 alloy and B_4C-reinforced TC11 composites: (**a**) TC11; (**b**) TMC1; (**c**) TMC2.

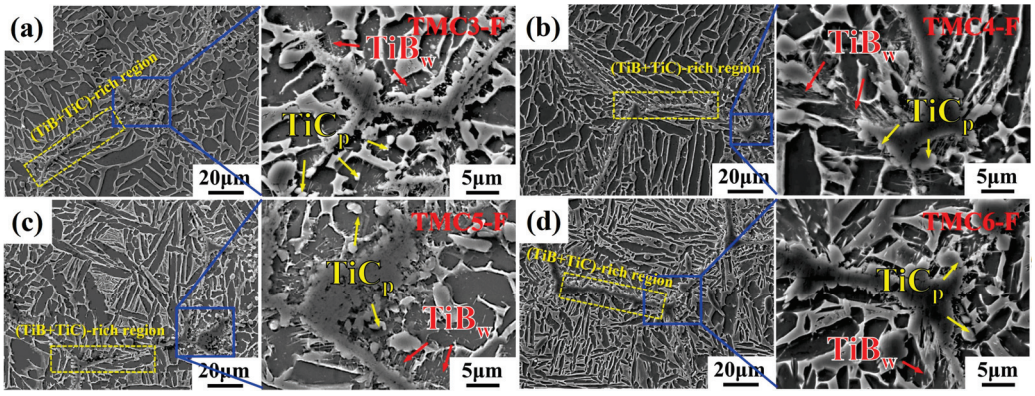

Figure 6. SEM micrographs of B_4C-reinforced TC11 composites with Fe addition: (**a**) TMC3-F; (**b**) TMC4-F; (**c**) TMC5-F; (**d**) TMC6-F.

Figure 6 presents the microstructures of the B_4C-reinforced TC11 composites with the addition of Fe. Compared with TC11 alloy, the microstructures of TMCs tend to be more equiaxial, which indicates that (TiB + TiC) dual phases can facilitate the formation of equiaxed grains. The comparison of TMC3-F, TMC5-F, and TMC6-F reveals that with the same amount of added Fe, an increase in added B_4C from 1 wt% to 3 wt% results in a higher reinforcement content and a more continuous network structure. When comparing TMC1, TMC4-F, and TMC5-F, it can be observed that an increase in added Fe from 0 wt% and 1 wt% to 2 wt% leads to more nano-TiB_w (TiB whiskers) clusters with diverse orientations and more nano-TiC_p (TiC particles) stacked densely between TiB_w near the network structure when the same amount of B_4C is added. In addition, more micron-scale TiB_w and TiC_p precipitate from the matrix. These changes prove that the addition of Fe promoted the in situ reaction and the distribution of elements. The addition of Fe can slightly alter the

phase content and size of the matrix, making it easier to form a narrower α phase, while the width and content of the β phase may increase accordingly.

The EDS mapping was introduced to determine the chemical composition of microstructure and reinforcing phases in (TiB + TiC)/TC11 composites fabricated by HIP. To determine the distribution of Fe elements in the composite, EDS scanning was conducted using TMC5-F as a representative sample, as shown in Figure 7a. The brighter regions indicate a higher concentration of these elements. EDS point scanning was also carried out to further verify the composition of the reinforcement-rich region, the results of which are consistent with the XRD results in Figure 4, indicating that the reinforcement consists of TiB and TiC. It is obvious that the matrix is primarily composed of Ti and Al, which are the most abundant elements in its composition. The B and C elements uniformly dissolve in the matrix and are enriched at the prior particle boundaries (PPbs), where they undergo in situ reactions with Ti elements to form the (TiB + TiC) network structure. The in situ nano-TiB_w exhibit a high aspect ratio, with a diameter of approximately 100 nm and lengths starting from several microns. They are arranged in parallel clusters and distributed around the network structure. TiC_p and TiB_w are interwoven and distributed near the network structure, with a small amount diffused into the matrix. The multiple reinforcements contribute to enhancing the properties of TMCs [33]. In addition, the Fe element is dissolved in the matrix, particularly in regions where the β phases are present, which has a distinctive performance in solid solution strengthening and improves the working properties [34,35].

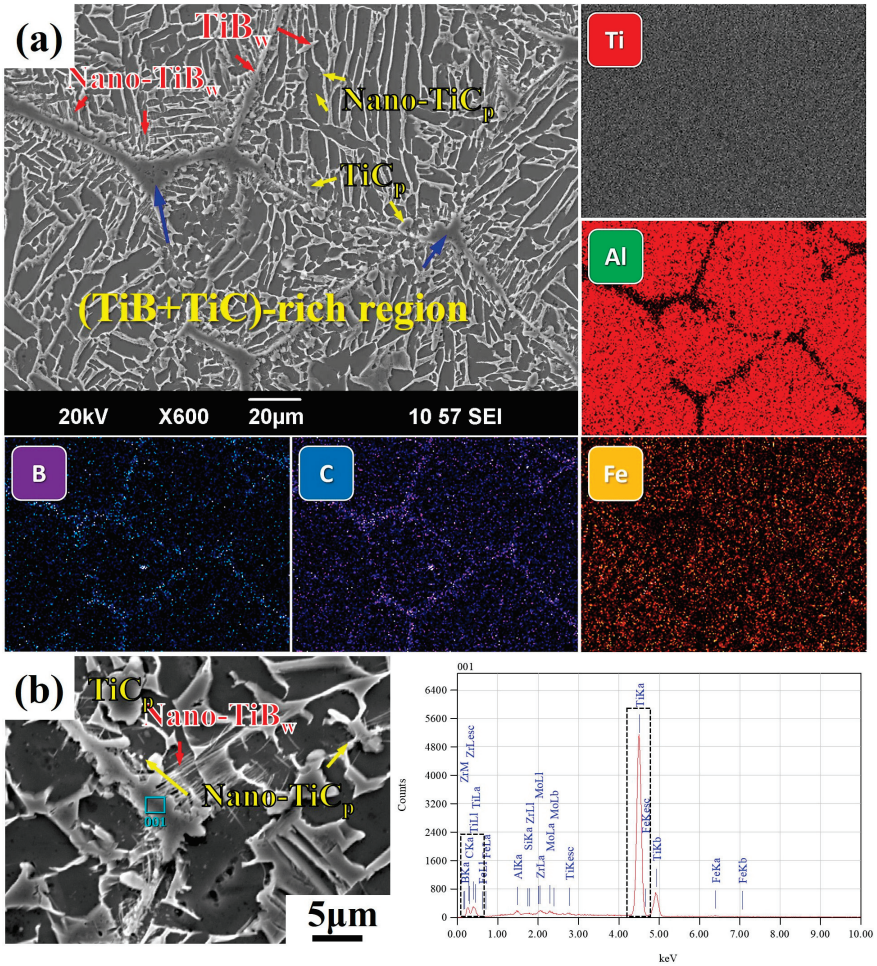

Figure 7. EDS results of TC11-2wt% B_4C with added 2wt% Fe (TMC5-F): (**a**) EDS mapping of TMC5-F; (**b**) EDS point scanning of (TiB + TiC)-rich region in TMC5-F.

3.4. EBSD Analysis

EBSD analysis was used to further investigate the crystal orientation and phase characteristics of 2 wt% B_4C-reinforced TC11 composites with added 2 wt% Fe or not. Figure 8 shows the band contrast (BC), inverse pole figure (IPF), and phases maps of the HIPed TMC1 and TMC5-F. The results show that the primary detection phase of TMC1 and TMC5-F was α-Ti with a relatively low content of β-Ti. According to the phase maps (Figure 8c,f), the distribution of the TiB and TiC reinforcement-rich region is marked in Figure 8a,d. Figure 8b indicates that the α-Ti grain orientations of the HIPed sample were randomized with $\{\bar{1}2\bar{1}0\}$ and $\{01\bar{1}0\}$. After adding Fe, a significant transformation from {0001} and $\{01\bar{1}0\}$ crystal orientations to $\{\bar{1}2\bar{1}0\}$ was observed, as shown in Figure 8e. This is because the addition of Fe exhibits distinct selectivity towards the grain orientation of the α phase and, as Fe addition increases, the α phase grain orientation becomes more concentrated, leading to a more pronounced isotropy [36]. The high-angle grain boundaries (>10°) predominated with a high proportion of 73.7% (TMC1) and 70.0% (TMC5-F), suggesting a rise in the number of small-angle grain boundaries when Fe is added. After HIP, the majority of β-Ti phase regions in TMC5-F were undetectable, consistent with the findings obtained from XRD analysis.

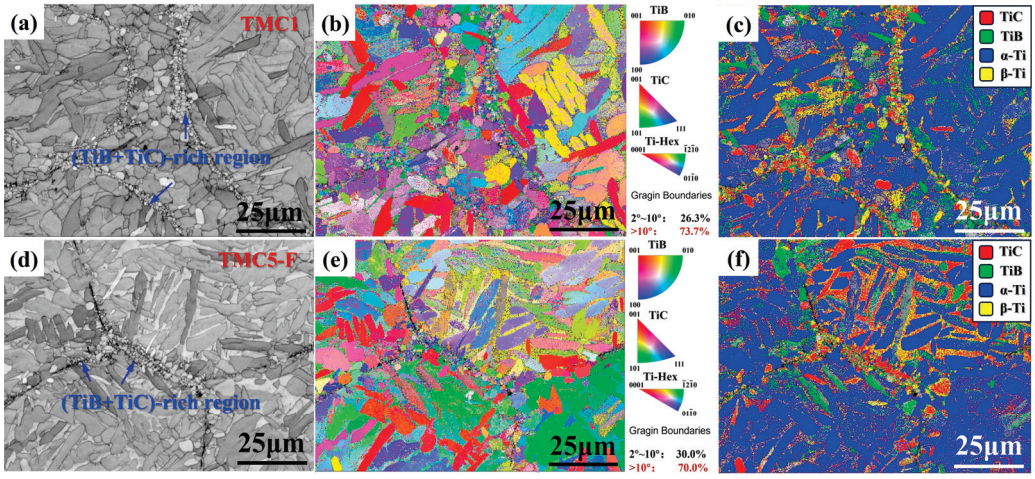

Figure 8. EBSD characterization of TMC1 (**a**–**c**) and TMC5-F (**d**–**f**): (**a**,**d**) BC maps; (**b**,**e**) IPB maps; (**c**,**f**) phase maps.

Furthermore, the effect of the addition of Fe on the texture strength of the α phase in TMC1 and TMC5-F was further analyzed, as shown by pole figure diagrams in Figure 9a,b. Both TMC1 and TMC5-F demonstrate greater texture strength along the (0001) orientation [37]. It is noteworthy that TMC5-F exhibits greater texture strength in the (11−20) and (10−10) directions compared to TMC1 due to the addition of 2 wt% Fe, resulting in a preferred orientation in the texture of the α phase compared to TMC1. In total, the HIPed TMC has no obvious texture, so its mechanical properties exhibit isotropy [27].

In order to qualitatively and quantitatively describe and compare the dislocation density of B_4C-reinforced TC11 composites with and without the addition of Fe, KAM maps were used to determine the change trend of dislocation density. An equation was introduced to determine the geometrically necessary dislocations (GNDs) for TMC1 and TMC5-F. The equation is as follows [38–40]:

$$\rho^{GND} = \frac{2KAM_{ave}}{ub} \quad (1)$$

Equation (1): ρ^{GND} is the GND density of the measurement point; KAM_{ave} is the average value of KAM derived from EBSD software; the EBSD scan step size is 180 nm, denoted as u; the Burgers vector of the titanium alloy, which is 2.951 nm for HCP titanium, is denoted as b. Figure 10 presents the KAM distribution maps and the computed GND density for TMC1 and TMC5-F. The value of the GND of the 2 wt% B_4C-reinforced TC11 composites (TMC1) is calculated as 1.89 × 10^{14} m^{-2} and increases to 2.09 × 10^{14} m^{-2} (increased by 10.6%) after the addition of 2 wt% Fe (TMC5-F). Compared with TMC1, TMC5-F has a higher dislocation density which can be attributed to the addition of Fe. Fe element can induce the precipitation of the β phase, resulting in more α/β interfaces. In addition, the addition of Fe promotes the precipitation of in situ reinforcement, and the interface number of reinforcements increases, resulting in a higher dislocation density. High dislocation density could significantly enhance tensile strength [41].

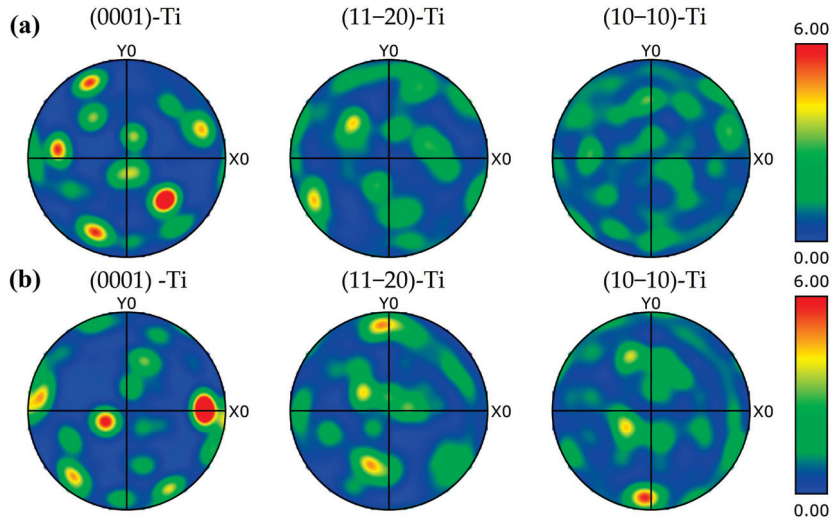

Figure 9. Pole figure of α phase: (**a**) TMC1; (**b**) TMC5−F.

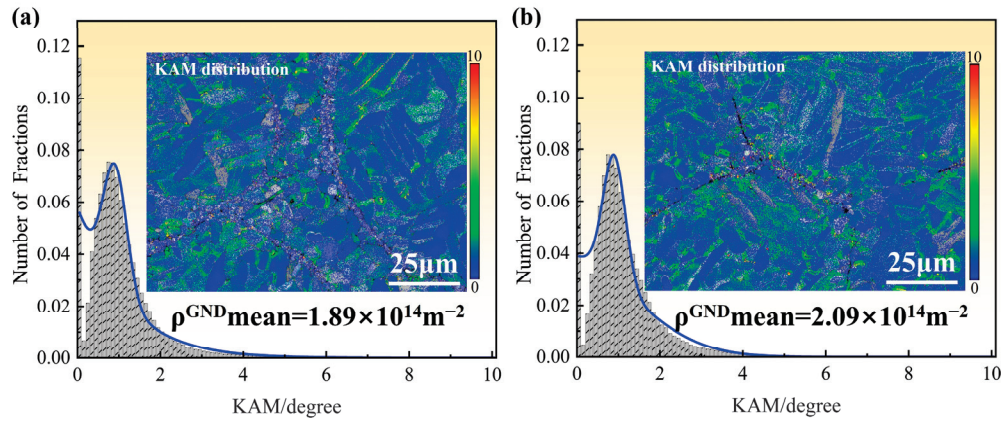

Figure 10. The KAM distribution, along with the mean GND density computed from the KAM maps: (**a**) TMC1; (**b**) TMC5−F.

3.5. Room Temperature Uniaxial Compression Experiment

Figure 11a demonstrates the compressive stress–strain curves of 2 wt% and 5 wt% B_4C-reinforced TC11 composites. With the increase in the addition of B_4C, the compressive yield strength reaches 1327 MPa (TMC1) and 1586 MPa (TMC2), respectively, which increased by 30.1% and 55.5% compared with TC11 alloy (1020 MPa). The stress–strain curves of 2 wt% B_4C-reinforced TC11 composites with the addition of 0, 1, 2 wt% Fe are shown in Figure 11b. The addition of Fe is observed to significantly enhance both the compressive yield strength

and compressive strength of the material, resulting in a 2.8% increase in compressive strength for TMC4-F and an 8.9% increase for TMC5-F compared to TC11. Moreover, when compared to TMC1 without added Fe, TMC4-F exhibits a 6.8% increase in compressive strength while TMC5-F demonstrates a remarkable 13.2% improvement. This indicates that the addition of 2 wt% Fe can improve the compressive strength of the material and maintain a certain plasticity. Therefore, the compression property of 1, 2, 3 wt% B_4C-reinforced TC11 composites with the addition of 2 wt% Fe is studied as shown in Figure 11c. It can be found that the compressive properties of the composites do not exhibit improvement with an increase in B_4C content when Fe is at 2 wt%. Moreover, the composites containing 1 wt% B_4C and 2 wt% (TMC3-F) Fe demonstrate superior compressive properties. TMC3-F has the highest compressive strength, reaching 2301 MPa, which represents a 15.2% improvement compared to TC11, while maintaining a certain compressive strain (24.6%).

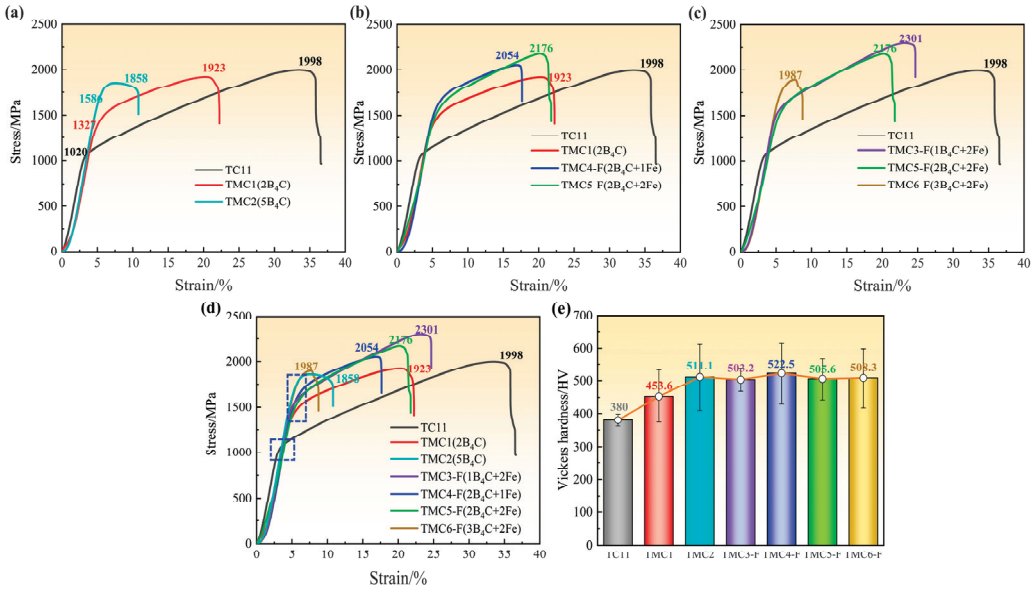

Figure 11. (**a**) The stress–strain curves of 2 wt% and 5 wt% reinforced TC11 composites; (**b**) The stress–strain curves of 2 wt% B_4C-reinforced TC11 composites with the addition of 0, 1, 2 wt% Fe; (**c**) The stress–strain curves of 1, 2, 3 wt% B_4C-reinforced TC11 composites with the addition of 2 wt% Fe; (**d**) The stress–strain curves of TMCs and TC11 alloy formed by HIP; (**e**) The Vickers hardness comparison of TMCs and TC11 alloy.

The compressive yield strength of all the TMCs markedly exceeds that of the TC11 alloy, as can be seen from the box selection area in Figure 11d. In general, the compressive strength of TMCs increased first and then decreased with the increased addition of B_4C. The comparison of TMC1, TMC4-F, and TMC5-F indicates that the addition of Fe can substantially increase the compressive strength without compromising the compressive strain. The addition of 2wt% Fe is observed to yield the most effective strengthening effect. In this case, the addition of 1wt% B_4C achieves optimal strength enhancement. Consequently, TMC3-F demonstrates the best balance between strength and plasticity. It is noteworthy that the strains of TMC2 and TMC6-F exhibit a significant reduction, despite their high yield strength. This indicates brittle fracture characteristics as both compressive strength and strain are considerably reduced.

Moreover, the hardness of all the TMCs is significantly increased and the increasing trend in hardness is consistent with the compressive yield strength, as shown in Figure 11e. The comparison of TC11, TMC1, and TMC2 reveals that (TiB + TiC) reinforcements can significantly harden the TC11 matrix, and the addition of more B_4C led to higher hardness. The addition of B_4C at 2 wt% and 5 wt% led to corresponding increases in the composite

hardness by 19.4% and 34.5%, respectively. Comparison of TMC1, TMC4-F, and TMC5-F reveals that the addition of Fe can significantly enhance the hardness. The hardness of TMC4-F is 15.2% higher than that of TMC1 and 37.5% higher than that of the TC11 alloy due to the addition of 1 wt% Fe. The addition of a reasonable amount of reinforcement and the appropriate adjustment of Fe have been shown to achieve better performance improvement in TMCs, as evidenced by their excellent compressive strength, hardness, and high strain, surpassing the simple addition of B_4C.

4. Discussion

Figure 12 shows the schematic microstructure diagram of microstructural evolution of the (TiB + TiC)-reinforced composites. TiB whiskers and TiC particles in the micro- and nanoscale were formed in the TC11 matrix of the HIPed TMCs, indicating a solid–solid reaction during the sintering of B_4C and Ti powders to form in situ TiC and TiB. After low-energy ball milling, the B_4C particles were uniformly distributed on the TC11 matrix particles, which provided the carbon source and boron source. The formation of TiB and TiC phases resulted from the reaction between B_4C and Ti as follows:

$$5Ti + B_4C = 4TiB + TiC \quad (2)$$

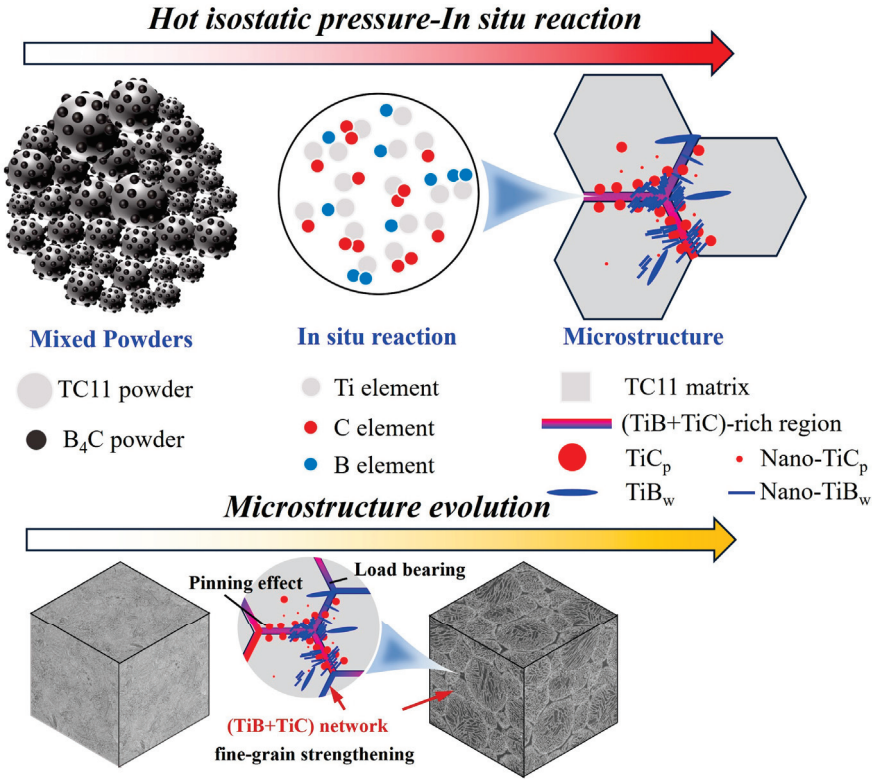

Figure 12. Schematic diagram of microstructural evolution of the HIPed (TiB + TiC)/TC11.

Under the high sintering temperature of 1050 °C and the isostatic pressure of 150 MPa, the rapid diffusion of titanium, carbon, and boron atoms was facilitated by the intense thermal atomic motion, resulting in nucleation and growth of TiB_w and TiC_p. The eutectic transformation between titanium and iron takes place at a temperature of 1085 °C; therefore, the sintering temperature is strictly controlled at 1050 °C to prevent reaction between the stainless steel capsules and the TC11 matrix [42]. Furthermore, by implementing a two-step HIP process after the removal of the stainless steel capsule, it ensured that the reinforcements were fully formed through in situ reactions. The B_4C particles tend to aggregate at prior particle boundaries (PPBs), which provide abundant sources

of boron and carbon. As a result, during the solid phase reaction, larger micron-sized TiC_p and TiB_w appear at PPBs. Furthermore, nanoscale TiB_w and TiC_p were observed within the matrix at a specific distance from the PPBs as a result of diffusion of boron and carbon atoms into the interior of the network structure [43]. Thus, the concentration of C and B elements mainly contributes to the grain size of TiB_w and TiC_p, while the growth morphologies in the reinforcements primarily contribute to their crystal structures. The growth of TiB_w is oriented along the [010] crystallographic axis in the longitudinal direction, resulting in TiB_w exhibiting a needle-like morphology [44,45]. The TiC grows in each crystal planes and tends to form granules.

The compression test and hardness test results indicate that the addition of the B_4C powder to the TC11 matrix improved the mechanical properties, and the addition of Fe provides an additional strengthening effect. The network structure, featuring the distribution of in situ TiB and TiC, effectively transfers the load while preserving a certain level of matrix plasticity. Microstructure formation shows that in situ networks refined the matrix grain, leading to a great improvement in mechanical properties. The nanoprecipitated phases TiC and TiB within the network simultaneously contribute to load transfer and precipitated phase strengthening. Since the interfacial strength of TiB-Ti and TiC-Ti is much higher than that of Ti-Ti, the formation of a large number of nano-TiB_w and nano-TiC_p provides more TiB-Ti and TiC-Ti interfaces, which leads to load-bearing strengthening effect while providing fine-grain strengthening, significantly increasing the strength of the material [46,47]. The solid solution strengthening caused by interstitial B and C elements is theoretically limited and can be disregarded. Since the thermal expansion coefficients of TiB and Ti are similar, the dislocation strengthening caused by TiB can be ignored [48]. The presence of TiC_p at the grain boundaries can account for the dislocation pinning effect and contribute to the enhanced strength observed in TMCs. The deformation compatibility between Ti and TiC differs, resulting in stress concentration at the interface between hard TiC particles and Ti. However, excessive addition of B_4C promotes crack propagation and defect formation, which accounts for the presence of pores in TMC2. Therefore, incorporating an appropriate amount of B_4C to induce nanoscale in situ reinforcements can mitigate this effect and provide dislocation strengthening. The reinforcements act as obstacles against dislocations, thereby enhancing the mechanical properties of materials.

The additional strengthening effect provided by Fe is due to the solid solution strengthening of Fe. Moreover, the addition of Fe can further facilitate the in situ formation of TiB_w and TiC_p, as shown in Figure 13. As shown in Figure 4b, the presence of the TiFe-base intermetallic phase was not detected in TMC, and Fe was incorporated into TMCs as a β stable element, resulting in an increased intensity of the β peak attributed to the addition of Fe. In addition, Fe exhibits a significant solid solution strengthening effect due to its strong ability to induce lattice distortion in titanium alloy. The strain caused by the lattice distortion can increase the Young's modulus and bulk modulus of the β phase, thus affecting the plasticity of the material [49]. Thus, the combination of in situ reinforcement and Fe solid solution strengthening can result in an additional strengthening effect. However, S. Pouzet et al. [50] reported that the content of B_4C is typically limited to no more than 3 wt% in order to ensure sufficient plasticity which is consistent with our experimental results. Therefore, the precise control of the reinforcement and Fe content in the particle is crucial for achieving optimal performance balance.

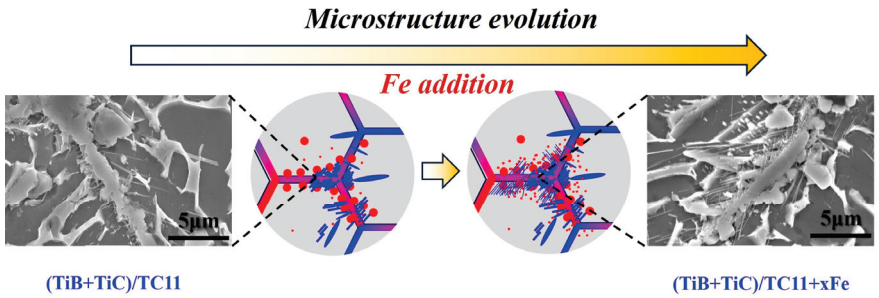

Figure 13. Schematic diagram of microstructural evolution of the HIPed (TiB + TiC)/TC11 + xFe.

5. Conclusions

In this work the microstructure evolution and mechanical properties of (TiB + TiC)/TC11 + xFe composites fabricated by HIP were systematically investigated. The findings can be summarized as follows:

(1) After low-energy ball milling, the nano-B_4C and nano-Fe powders were uniformly attached to the micron-sized TC11 particles. The HIP sintering process facilitated the formation of in situ TiB and TiC reinforcements at the PPBs, resulting in well-defined network-reinforced structures.

(2) Nano-TiB_w with high length-to-diameter ratio and granular TiC_p are distributed around the network structure, while a small amount of TiC_p and TiB_w is also dispersed within the network structure due to element diffusion, which provided load-bearing strengthening, fine-grain strengthening, and dislocation strengthening.

(3) The B_4C-reinforced TC11 composites presented an increment in hardness and compressive yield strength, which gradually increased with more in situ TiB and TiC formation. After the addition of Fe, the composite demonstrates enhanced compressive strength, compressive strain, and hardness.

(4) The addition of Fe can provide additional solid solution strengthening, thereby further enhancing the strength while maintaining compressive strain. Furthermore, by optimizing the ratio of B_4C and Fe additions, superior comprehensive performance can be achieved with a 15.2% increase in compressive strength while preserving excellent compressive strain of 24.6% (TMC3-F).

Author Contributions: Conceptualization, L.Z., H.C., L.F. and Y.S.; methodology, S.Q.; software, S.Q.; validation, S.Q., N.W., F.C., Y.S., J.Z. and H.C.; formal analysis, S.Q.; investigation, S.Q. and F.C.; resources, H.C., L.F. and J.Z.; data curation, S.Q.; writing—original draft preparation, S.Q.; writing—review and editing, S.Q. and Y.S.; supervision, S.Q., N.W., F.C., Y.S., J.Z., L.F. and L.Z.; project administration, Y.S., J.Z., H.C. and L.Z.; funding acquisition, H.C. and L.Z. All authors have read and agreed to the published version of the manuscript.

Funding: The authors gratefully acknowledge financial support from the Frontier R&D Program Project of Jiangsu Province (BF2024008) and National Natural Science Foundation of China (No.51931008), a project funded by the Priority Academic Program Development of Jiangsu Higher Education Institution (PAPD).

Institutional Review Board Statement: Not applicable.

Informed Consent Statement: Not applicable.

Data Availability Statement: The raw data supporting the conclusions of this article will be made available by the authors on request.

Conflicts of Interest: Author Jiong Zhao was employed by the company Jiangsu Tiangong Technology Co., Ltd. The remaining authors declare that the research was conducted in the absence of any commercial or financial relationships that could be construed as a potential conflict of interest.

References

1. Abd-Elaziem, W.; Darwish, M.A.; Hamada, A.; Daoush, W.M. Titanium-Based alloys and composites for orthopedic implants Applications: A comprehensive review. *Mater. Design* **2024**, *241*, 112850. [CrossRef]
2. Boyer, R.R. An overview on the use of titanium in the aerospace industry. *Mater. Sci. Eng. A* **1996**, *213*, 103–114. [CrossRef]
3. Chang, J.H.; Wen, J.F.; Cao, R.; Yan, Y.J.; Sui, R.; Tu, S.T. Effect of lapped sequence on corrosion behavior and mechanism of pure titanium/galvanized steel joint using cold metal transfer joining technology. *Int. J. Press. Vessel. Pip.* **2024**, *209*, 105203. [CrossRef]
4. Liu, Z.M.; Xin, S.W.; Zhao, Y.Q. Research Progress on the Creep Resistance of High-Temperature Titanium Alloys: A Review. *Metals* **2023**, *13*, 1975. [CrossRef]
5. Huang, J.K.; Liu, S.E.; Yu, S.R.; Yu, X.Q.; Chen, H.Z.; Fan, D. Arc deposition of wear resistant layer TiN on Ti6Al4V using simultaneous feeding of nitrogen and wire. *Surf. Coat. Technol.* **2020**, *381*, 125141. [CrossRef]
6. Chen, H.; Mi, G.B.; Sun, Y.Z.; Li, P.J. Unique grain refinement mechanism of graphene oxide reinforced high-temperature titanium alloy matrix composite. *Mater. Today Commun.* **2024**, *41*, 110803. [CrossRef]
7. Grützner, S.; Krüger, L.; Radajewski, M.; Schneider, I. Characterization of In-Situ TiB/TiC Particle-Reinforced Ti-5Al-5Mo-5V-3Cr Matrix Composites Synthesized by Solid-State Reaction with B_4C and Graphite through SPS. *Metals* **2018**, *8*, 377. [CrossRef]
8. Alman, D.E.; Hawk, J.A. The abrasive wear of sintered titanium matrix-ceramic particle reinforced composites. *Wear* **1999**, *225*, 629–639. [CrossRef]
9. Smith, P.R.; Froes, F.H. Developments in Titanium Metal Matrix Composites. *JOM* **1984**, *36*, 19–26. [CrossRef]
10. Cao, X.J.; Liu, X.; Zhou, H.B.; Guo, Y.Q.; Ren, Z.K.; Guo, J.; Li, X.; Yang, J. Enhanced properties of titanium matrix composites via in-situ synthesized TiC_x and Ti_5Si_3 with network structure. *Mater. Chem. Phys.* **2024**, *314*, 128849. [CrossRef]
11. Wang, S.; An, Q.; Liu, W.Q.; Zhang, R.; Ma, Z.S.; Huang, L.J.; Geng, L. Towards strength-ductility enhancement of titanium matrix composites through heterogeneous grain structured Ti matrix design. *J. Alloys Compd.* **2022**, *927*, 167022. [CrossRef]
12. Fu, Y.; Xu, Y.D.; Wang, Y.Y.; Bai, Y.; Hao, H.; Zhu, X.R. Microstructures and mechanical properties of (TiB_w+Ti_5Si_3)/TC11 composites fabricated by hot isostatic pressing and subjected to 2D forging. *J. Alloys Compd.* **2023**, *966*, 171523. [CrossRef]
13. Zhong, Z.X.; Zhang, B.; Ye, J.; Ren, Y.H.; Zhang, J.W.; Ye, F. Synergistically enhanced the strength and ductility of network-structured titanium matrix composites reinforced with B-containing precursor-derived TiB nanowires. *Mater. Sci. Eng. A* **2024**, *891*, 145996. [CrossRef]
14. Tjong, S.C.; Mai, Y.W. Processing-structure-property aspects of particulate- and whisker-reinforced titanium matrix composites. *Compos. Sci. Technol.* **2008**, *68*, 583–601. [CrossRef]
15. Zherebtsov, S.; Ozerov, M.; Klimova, M.; Moskovskikh, D.; Stepanov, N.; Salishchev, G. Mechanical Behavior and Microstructure Evolution of a Ti-15Mo/TiB Titanium-Matrix Composite during Hot Deformation. *Metals* **2019**, *9*, 1175. [CrossRef]
16. Wang, Q.; Zhang, Z.H.; Su, T.J.; Cheng, X.W.; Li, X.Y.; Zhang, S.Z.; He, J.Y. A TiB whisker-reinforced titanium matrix composite with controllable orientation: A novel method and superior strengthening effect. *Mater. Sci. Eng. A* **2022**, *830*, 142309. [CrossRef]
17. Zhang, Q.; Sun, W.B.; Xu, S.L.; Zhang, X.J.; Wang, J.B.; Si, C.R. Nano-TiB whiskers reinforced Ti-6Al-4 V matrix composite fabricated by direct laser deposition: Microstructure and mechanical properties. *J. Alloys Compd.* **2022**, *922*, 166171. [CrossRef]
18. Tabrizi, S.G.; Sajjadi, S.A.; Babakhani, A.; Lu, W.J. Influence of spark plasma sintering and subsequent hot rolling on microstructure and flexural behavior of in-situ TiB and TiC reinforced Ti6Al4V composite. *Mater. Sci. Eng. A* **2015**, *624*, 271–278. [CrossRef]
19. Saba, F.; Zhang, F.; Liu, S.; Liu, T.F. Reinforcement size dependence of mechanical properties and strengthening mechanisms in diamond reinforced titanium metal matrix composites. *Compos. Part B Eng.* **2019**, *167*, 7–19. [CrossRef]
20. Zhang, X.J.; Song, F.; Wei, Z.P.; Yang, W.C.; Dai, Z.K. Microstructural and mechanical characterization of in-situ TiC/Ti titanium matrix composites fabricated by graphene/Ti sintering reaction. *Mater. Sci. Eng. A* **2017**, *705*, 153–159. [CrossRef]
21. Lin, D.J.; Lin, J.H.C.; Ju, C.P. Structure and properties of Ti-7.5Mo-Fe alloys. *Biomaterials* **2002**, *23*, 1723–1730. [CrossRef]
22. Dai, G.Q.; Niu, J.Z.; Guo, Y.H.; Sun, Z.G.; Dan, Z.H.; Chang, H.; Zhou, L. Microstructure evolution and grain refinement behavior during hot deformation of Fe micro-alloyed Ti-6Al-4V. *J. Mater. Res. Technol.* **2021**, *15*, 1881–1895. [CrossRef]
23. Liao, Y.; Bai, J.H.; Chen, F.W.; Xu, G.L.; Cui, Y.W. Microstructural strengthening and toughening mechanisms in Fe-containing Ti-6Al-4V: A comparison between homogenization and aging treated states. *J. Mater. Sci. Technol.* **2022**, *99*, 114–126. [CrossRef]
24. Wang, H.; Luo, H.L.; Chen, J.Q.; Tang, J.C.; Yao, X.Y.; Zhou, Y.H.; Yan, M. Cost-affordable, biomedical Ti-5Fe alloy developed using elemental powders and laser in-situ alloying additive manufacturing. *Mater. Charact.* **2021**, *182*, 111526. [CrossRef]
25. Niu, J.Z.; Guo, Y.H.; Li, K.; Liu, W.J.; Dan, Z.H.; Sun, Z.G.; Chang, H.; Zhou, L. Improved mechanical, bio-corrosion properties and cell responses of Ti-Fe alloys as candidate dental implants. *Mater. Sci. Eng. C* **2021**, *122*, 111917. [CrossRef] [PubMed]
26. *GB/T 7314-2017*; Metallic Metallic Materials—Compression Test Method at Room Temperature. Standards Press of China: Beijing, China, 2017.
27. Jin, J.Y.; Wang, S.; Lu, W.H.; Huang, L.J.; Gong, D.L.; Meng, F.C.; Liu, W.Q.; Chen, X.; Geng, L. Superior uniform deformation ability of intragranular nano TiB reinforced Ti-6.5Al-2Zr-Mo-V fabricated by hot isostatic pressing. *Mater. Sci. Eng. A* **2024**, *912*, 146993. [CrossRef]

28. Tsang, H.T.; Chao, C.G.; Ma, C.Y. Effects of volume fraction of reinforcement on tensile and creep properties of in-situ TiB/Ti MMC. *Scripta Mater.* **1997**, *37*, 1359–1365. [CrossRef]
29. Zhang, C.J.; Kong, F.T.; Xiao, S.L.; Zhao, E.T.; Xu, L.J.; Chen, Y.Y. Evolution of microstructure and tensile properties of in situ titanium matrix composites with volume fraction of (TiB plus TiC) reinforcements. *Mater. Sci. Eng. A* **2012**, *548*, 152–160. [CrossRef]
30. Sun, S.Y.; Lu, W.J. Effect of Hybrid Reinforcements on the Microstructure and Mechanical Properties of Ti-5Al-5Mo-5V-Fe-Cr Titanium Alloy. *Metals* **2017**, *7*, 250. [CrossRef]
31. Meng, X.; Min, J.; Sun, Z.G.; Zhang, W.S.; Chang, H.; Han, Y.F. Columnar to equiaxed grain transition of laser deposited Ti6Al4V using nano-sized B_4C particles. *Compos. Part B Eng.* **2021**, *212*, 108667. [CrossRef]
32. Wei, Z.J.; Cao, L.; Wang, H.W.; Zou, C.M. Modification and control of TiC morphology by various ways in arc melted TiC/Ti-6Al-4V composites. *Mater. Sci. Technol.* **2011**, *27*, 556–561. [CrossRef]
33. Zhong, Z.X.; Zhang, B.; Ren, Y.H.; Ye, J.; Zhang, J.W.; Ye, F. Microstructure evolution and mechanical properties of bioinspired web-liked (TiB + TiC + Ti_3Si)/TC_4 composites. *Mater. Charact.* **2024**, *207*, 113499. [CrossRef]
34. Chen, F.W.; Gu, Y.L.; Xu, G.L.; Cui, Y.W.; Chang, H.; Zhou, L. Improved fracture toughness by microalloying of Fe in Ti-6Al-4V. *Mater. Design* **2020**, *185*, 108251. [CrossRef]
35. Meier, M.L.; Lesuer, D.R.; Mukherjee, A.K. The Effects of the Alpha/Beta Phase Proportion on the Superplasticity of Ti-6Al-4V and Iron-Modified Ti-6Al-4V. *Mater. Sci. Eng. A* **1992**, *154*, 165–173. [CrossRef]
36. Guo, C.B.; Dai, G.Q.; Niu, J.Z.; Guo, Y.H.; Sun, Z.G.; Chang, H.; Zhang, Q.T. Fe nanoparticles modified pure Ti alloy on microstructure evolution and fine crystallization mechanism fabricated by additive manufacturing. *J. Mater. Res. Technol.* **2023**, *26*, 5860–5872. [CrossRef]
37. Wu, L.D.; Gao, Z.J.; Fan, Z.H.; Liu, C.H.; Liu, Y.Z. Microstructure and mechanical properties of in-situ hybrid reinforced (TiB plus TiC)/Ti composites prepared by laser powder bed fusion. *J. Mater. Res. Technol.* **2024**, *30*, 9258–9273. [CrossRef]
38. Luo, Z.; Sun, Y.P.; Li, W.Z.; He, J.M.; Luo, G.J.; Liu, H.S. Evolution of Microstructures, Texture and Mechanical Properties of Al-Mg-Si-Cu Alloy under Different Welding Speeds during Friction Stir Welding. *Metals* **2023**, *13*, 1120. [CrossRef]
39. Ma, Y.D.; Liu, G.S.; Yang, S.Q.; Chen, R.; Xu, S.P.; Shen, Y. Effects of Strain Rate on the GND Characteristics of Deformed Polycrystalline Pure Copper. *Metals* **2024**, *14*, 582. [CrossRef]
40. Sun, Y.Y.; Chen, F.; Qian, S.W.; Chang, H.; Zhang, W.S.; Feng, L.; Zhou, L. Low cycle fatigue behavior and deformation mechanism of Ti-6Al-4V-0.55Fe alloy under the control of strain and stress amplitudes. *J. Mater. Res. Technol.* **2024**, *33*, 5951–5961. [CrossRef]
41. Shang, C.; Hou, X.D.; Lu, Y.Z.; Zhang, R.Y.; Lu, X.; Yuan, C. Simultaneous improvement of strength and ductility of laser additively produced Ti6Al4V by adding tantalum. *J. Alloys Compd* **2024**, *976*, 173171. [CrossRef]
42. Bai, H.Q.; Zhong, L.S.; Cui, P.J.; Kang, L.; Liu, J.B.; Lv, Z.L.; Xu, Y.H. Fabrication of high strength and plasticity of iron matrix composite with Ti@ (TiC plus α-Fe) core-shell structure by near-eutectic temperature hot pressing sintering. *Vacuum* **2021**, *194*, 110574. [CrossRef]
43. Ma, Z.S.; Wang, S.; Huang, L.J.; An, Q.; Zhang, R.; Liu, W.Q.; Sun, F.B.; Chen, R.; Geng, L. Synergistically enhanced strength and ductility of TiB/(TA15-Si) composites: A two-step HIP strategy. *Compos. Part B Eng.* **2023**, *254*, 110583. [CrossRef]
44. Genç, A.; Banerjee, R.; Hill, D.; Fraser, H.L. Structure of TiB precipitates in laser deposited in situ, Ti-6Al-4V-TiB composites. *Mater. Lett.* **2006**, *60*, 859–863. [CrossRef]
45. Koo, M.Y.; Park, J.S.; Park, M.K.; Kim, K.T.; Hong, S.H. Effect of aspect ratios of in situ formed TiB whiskers on the mechanical properties of TiB_w/Ti-6Al-4V composites. *Scripta Mater.* **2012**, *66*, 487–490. [CrossRef]
46. Li, S.P.; Wang, X.Y.; Le, J.W.; Han, Y.F.; Zong, N.; Wei, Z.C.; Huang, G.F.; Lu, W.J. Towards high strengthening efficiency by in-situ planting nano-TiB networks into titanium matrix composites. *Compos. Part B Eng.* **2022**, *245*, 110169. [CrossRef]
47. Zheng, Z.K.; Zhang, Z.H.; Li, X.; Zhang, X.Z.; Sun, G.D.; Li, L.B.; Fu, Y.Q.; Elmarakbi, A.; Dong, L.L. Significantly improved strength of the TiC/TA19 composites via interface and dislocation strengthening. *Carbon* **2024**, *230*, 119581. [CrossRef]
48. Singh, G.; Ramamurty, U. Boron modified titanium alloys. *Prog. Mater. Sci.* **2020**, *111*, 100653. [CrossRef]
49. Skripnyak, N.V.; Ponomareva, A.V.; Belov, M.P.; Abrikosov, I.A. Ab initio calculations of elastic properties of alloys with mechanical instability: Application to BCC Ti-V alloys. *Mater. Design* **2018**, *140*, 357–365. [CrossRef]
50. Pouzet, S.; Peyre, P.; Gorny, C.; Castelnau, O.; Baudin, T.; Brisset, F.; Colin, C.; Gadaud, P. Additive layer manufacturing of titanium matrix composites using the direct metal deposition laser process. *Mater. Sci. Eng. A* **2016**, *677*, 171–181. [CrossRef]

metals

MDPI

Article

Microstructural Insights into Solid Particle Erosion in a High-Chromium Cast Iron

Alessio Suman, Annalisa Fortini * and Nicola Zanini

Department of Engineering, University of Ferrara, 44122 Ferrara, Italy; alessio.suman@unife.it (A.S.); nicola.zanini@unife.it (N.Z.)
* Correspondence: annalisa.fortini@unife.it

Abstract: Solid particle erosion (SPE) significantly limits the service life of High-Chromium Cast Irons (HCCIs), widely used in power generation and mining industries. This study investigates how microstructural features influence the erosion resistance of a Fe-Cr-C cast iron, focusing on the interplay between particle kinetic energy and carbide features, i.e., carbide volume fraction (CVF). Erosion tests, conducted per ASTM G76 standards, revealed that substrates with similar CVFs exhibited varying damage levels, even at consistent particle kinetic energies. The findings underscored that impact conditions have a greater influence on erosion resistance than CVF alone, emphasizing the critical role of carbide morphology and distribution in mitigating damage. This work provides valuable insights for optimizing HCCIs to enhance material performance and durability in demanding erosive environments by tailoring carbide distribution to specific operational conditions.

Keywords: high-chromium cast irons; solid particle erosion; carbide volume fraction; impact velocity; image analysis; erosion rate

1. Introduction

Solid particle erosion (SPE) is a widely studied phenomenon in the engineering field, characterized by material removal resulting from impacting particles [1–5]. This process poses significant challenges in applications such as gas turbines, slurry pumps, and heat exchangers, where repeated solid particle impacts cause mass loss, compromising durability and reliability [6–10]. Addressing erosion-related issues is crucial for extending the service life of these components and maintaining overall efficiency and safety. SPE is a complex, multi-faceted phenomenon influenced by a combination of parameters that determine the severity and nature of surface degradation. The literature extensively discusses these parameters, which include the carrying fluid (such as kinetic energy and thermodynamic states), the material properties of the impacted surface (e.g., microstructure and hardness), and the properties of the impacting particles (e.g., morphology, size, impact angle, velocity, and hardness) [2,11–14]. The erosion rate (ER), a crucial parameter for evaluating surface degradation, is defined as the rate at which material is removed from the surface, i.e., the mass or volume of material lost per unit of time or unit area. The key determinant is the angle at which particles strike a surface [15]. Ductile metals experience maximum ERs at low angles (20–30°) due to micro-cutting, while brittle materials experience peak ERs at near-normal impacts (90°), leading to crack formation and spallation. Particle characteristics, such as size, shape, and hardness, also critically influence erosion outcomes [16,17]. Another crucial factor influencing SPE is the velocity and, thus, the kinetic energy of the impacting

particles [18]. It has been observed that ER increases with particle size and kinetic energy up to a threshold, beyond which this relationship may become nonlinear due to particle-particle interactions [19,20].

Among the various weld overlay coating materials employed to counteract SPE (e.g., iron-based, cobalt-based, nickel-based, and copper-based alloys) [21], iron-based hardfacing materials are often favored [22–25]. This is largely attributed to their cost-effectiveness and performance characteristics. Notably, high chromium cast irons (HCCIs) are renowned for their excellent wear and corrosion resistance, which stem from their peculiar microstructure. They consist of hard primary and eutectic carbides (M_7C_3 or $M_{23}C_6$ types) embedded in a tough matrix. Broadly speaking, the primary carbides act as a barrier against erosion, whereas the surrounding matrix provides ductile support to the carbides.

As reported, SPE is a challenging phenomenon, and many investigations have explored specific aspects of the erosion phenomenon, focusing on individual parameters that influence erosive behavior. For instance, Sapate and Rama Rao [26,27], explored the relationship between carbide volume fraction (CVF) and ER under mild and severe erosion conditions, analyzing the protective role of carbides against softer erodents and the opposite effect in the presence of harder erodents. Chatterjee and Pal [22] analyzed the SPE of hardfacing deposits on gray cast iron, highlighting that CVF and carbide type significantly influence erosion resistance, with softer erodents causing less damage and hard erodents leading to severe wear in alloys with brittle carbides. Similarly, Stevenson and Hutchings [28] demonstrated that CVF is critical for erosion resistance, with results varying based on the relative hardness of the erodents. In parallel, the kinetic energy of impacting particles has been observed to play a fundamental role in intensifying erosion. As discussed by Finnie [29], who modeled the relationship between particle velocity and ER, higher kinetic energy amplifies surface damage. However, the effect of kinetic energy is often studied separately from microstructural considerations. Shitole et al. [30] investigated the influence of particle kinetic energy, varying with particle size, on SPE of metals. The findings suggested a direct correlation between increased kinetic energy and higher ERs, showing that higher-energy particles cause more severe material degradation.

In summary, while numerous studies have provided valuable insights into SPE, none, to the best of the author's knowledge, have comprehensively examined the combined effects of microstructural characteristics and the kinetic energy of impacting particles, often overlooking their complex interplay. The primary purpose of this study is to address this research gap by investigating how the microstructure of an HCCI interacts with particle kinetic energy to influence erosion resistance. Specifically, the study aims to determine why substrates with similar CVFs exhibit differing levels of damage under identical erosion conditions (i.e., the same particle kinetic energy), thereby advancing the understanding of structure-property relationships. To achieve this objective, a detailed microstructural analysis through optical and scanning electron microscopes was performed. The erosion tests, conducted in a dedicated test rig designed according to the guidelines outlined in the ASTM G76 standard [31], comprised a standard powder (ISO 12103-1 standard [32]) with different granulometric distributions. Tests were conducted at a 15° impact angle and by keeping kinetic energies constant. The findings reveal that substrates with the same CVFs can suffer different damage levels even when subjected to identical particle kinetic energies. This underscores the need for a quantitative approach to deepen our understanding of structure-property relationships, enhance microstructure design, and optimize processing methods. By providing new insights into the complex relationship between microstructure and erosion mechanics, this study advances the understanding of the erosion process and contributes to improving the design and durability of HCCIs for demanding applications.

2. Materials and Methods

In this study, a commercial hardfacing alloy was utilized, featuring an HCCI overlay applied on a low-carbon steel substrate. The overlay was deposited using an open-arc welding process with a flux-cored wire through commercial process parameters. The HCCI hardfacing electrodes were deposited onto a low-carbon steel plate, with the base steel and the hardfacing layer having a nominal thickness of 5 mm. To determine the chemical composition of the HCCI, Glow Discharge Optical Emission Spectroscopy (GDOES, Spectruma Analytik, Hof, Germany) was performed, and the result is summarized in Table 1.

Table 1. Chemical composition (wt.%) of the HCCI overlay.

Composition (wt.%)—Fe Balance							
C	**Mn**	**Si**	**Cr**	**Mo**	**Nb**	**W**	**V**
4.15	0.56	1.08	21.04	2.78	4.09	0.86	0.69

The microstructural analyses of the material were conducted using a Leica DMi8 A optical microscope (OM) (Leica, Wetzlar, Germany) and a Zeiss EVO MA15 (Carl Zeiss, Jena, Germany) scanning electron microscope (SEM), equipped with an Oxford X-Max 50 (Oxford Instruments, Abingdon-on-Thames, UK) Energy Dispersive Spectroscopy (EDS) X-ray microprobe for semi-quantitative analysis. SEM investigations comprised secondary electron (SEI) and backscattered electron (BSE) detectors. After standard metallographic preparation (up to 3 μm diamond polishing), the surface was etched with Kalling's reagent (5 g $CuCl_2$, 100 mL HCl, 100 mL C_2H_5OH). A detailed quantitative description of the microstructural features of the HCCI was conducted to deepen the role of the microstructure on the solid particle erosion phenomenon. The 20 mm × 20 mm (which represents the area of the target used in the erosion tests described hereafter) surface of each sample was divided into 9 regions of interest (ROIs), covering a total area of about 18 mm^2 per sample. Through ImageJ image analysis software (Version 1.53e, 2020, National Institutes of Health, Bethesda, MD, USA) [33], the stereological features of the Cr-rich carbides were determined. Figure 1 displays the sequence of the adopted image processing procedure. Figure 1a presents the original grayscale OM micrograph. The latter was converted into an 8-bit binary image, and contrast enhancement techniques were applied to facilitate feature extraction. By setting the threshold value for identifying the features under examination (specifically, the primary Cr-rich carbides), each particle was outlined, ensuring precise delineation of the carbides for accurate quantification. Figure 1b illustrates the outcome of particle analysis, where carbides below a specified area threshold were excluded, displaying only the outlines of the measured carbides. This selective exclusion was achieved by defining a minimum size threshold to filter out undesired carbides based on their area. This sequence was adopted to determine the CVF parameter, computed as the A_C / A_{TOT} ratio, where A represents the area, the subscripts C and TOT refer to carbides, and the total analyzed microstructure area.

Solid particle erosion tests were conducted per the ASTM G76 standard in an on-purpose bench. The bench has two main sections: the particle injection system and the impact test chamber. The particle injection system comprises a volumetric feeder that ensures a stable flow rate of erodent powder, which is calibrated for precise mass flow control by adjusting the motor speed via an inverter. Once dosed, the powder reaches a mixing chamber connected to the main airflow. Here, high shear forces generated by a Venturi nozzle prevent particle agglomeration, thus ensuring a consistent particle stream. The high-speed airflow carries the particles through the nozzle, where they are accelerated to the desired impact velocity. Nozzle geometry is optimized to guide the particle-laden

jet toward the target material with minimal dispersion. The specimen is placed in a target holder, which can be tilted to test different impact angles, i.e., from tangential (15°) to normal (90°) impacts. Figure 2 shows the test chamber. An exhaust fan coupled with a filtration system prevents particle dispersion outside the chamber. Further details regarding the test bench can be found in [34].

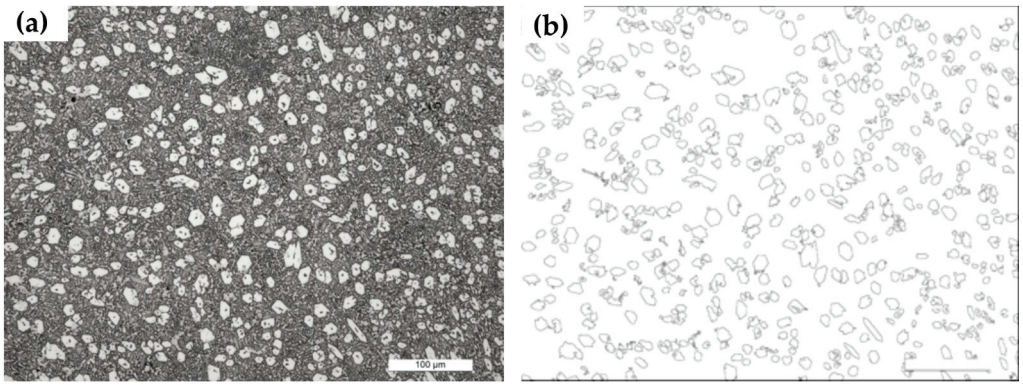

Figure 1. Sequence of the adopted image processing procedure with ImageJ image analysis software: (**a**) original grayscale OM micrograph and (**b**) outcome of particle analysis.

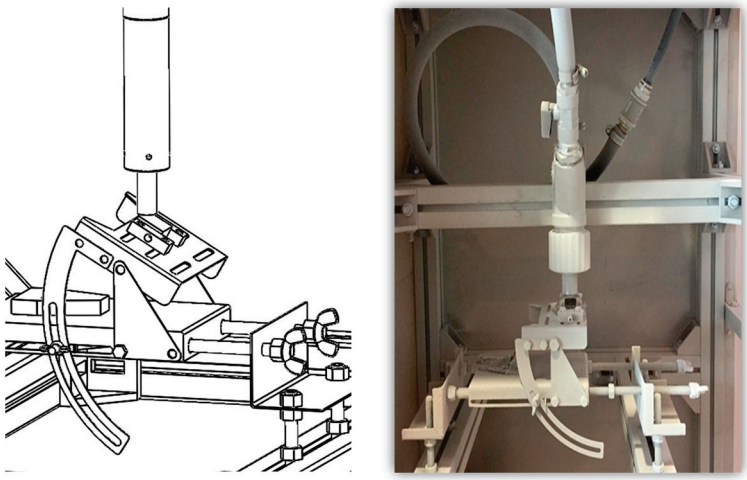

Figure 2. Scheme and image of the impact test chamber.

Tests were conducted on polished surfaces (3 µm diamond polishing) with an impact angle of 15°. The erodent powder selected was the controlled-grain-size standard Arizona dust quartz (ARD), in accordance with ISO 12103-1:2016. This commercial powder comprises 75% silica dioxide, 20% aluminum trioxide, and minor oxides (such as magnesium and iron) and is commonly used to test filtration systems and assess machine degradation. Two mean particle diameters of the ARD powder were chosen, specifically dmean = 4.8 µm (labeled as UF) and dmean = 25.5 µm (labeled as M). Test parameters, including flow rate, injected powder flow rate, and test duration, were established using computational fluid dynamics simulations to ensure a working condition with constant kinetic energy of the erodent particles. Hence, UF powder had an impact velocity of 205 m/s, whereas M powder had an impact velocity of 15.9 m/s. This difference in velocity compensates for the varying particle masses, ensuring that the tests were conducted under equivalent kinetic energy conditions. Erosion resistance was assessed by measuring the sample weight loss using a Kern ABT 100-5NM (Kern, Balingen, Germany) analytical balance with a resolution of 0.01 mg. The ER was computed as the ratio of sample weight loss to the mass of injected erodent, and ER values were averaged over five tests for each substrate-erodent combination.

On the worn surfaces, qualitative and quantitative analyses comprised observations using a HIROX-RH 2000 (Hirox Europe, Limonest, France) 3D digital microscope and using a Talysurf CCI-Lite (Taylor-Hobson, Leicester, UK) non-contact 3D profilometer, respectively.

3. Results and Discussion

Figure 3 shows the OM micrographs of the investigated HCCI, highlighting its main metallographic features. As seen, the microstructure is composed of primary carbides (i.e., the light phase in the micrographs) embedded in the surrounding matrix. Such a microstructure is in accordance with the chemical composition of the HCCI, and the as-welding morphology of M_7C_3 carbides of hypereutectic Fe-Cr-C alloy depends on the solidification rate [35]. Thus, some regions exhibit hexagon and hollow-hexagon morphologies of primary M_7C_3 carbides (see Figure 3a), whereas others display blade-like primary carbides (see Figure 3b). In addition to the morphologies, the distribution of the carbides differs since they appear relatively uniformly distributed in Figure 3a and form a star-like pattern emanating from nucleation centers in Figure 3b, as a result of directional solidification phenomena.

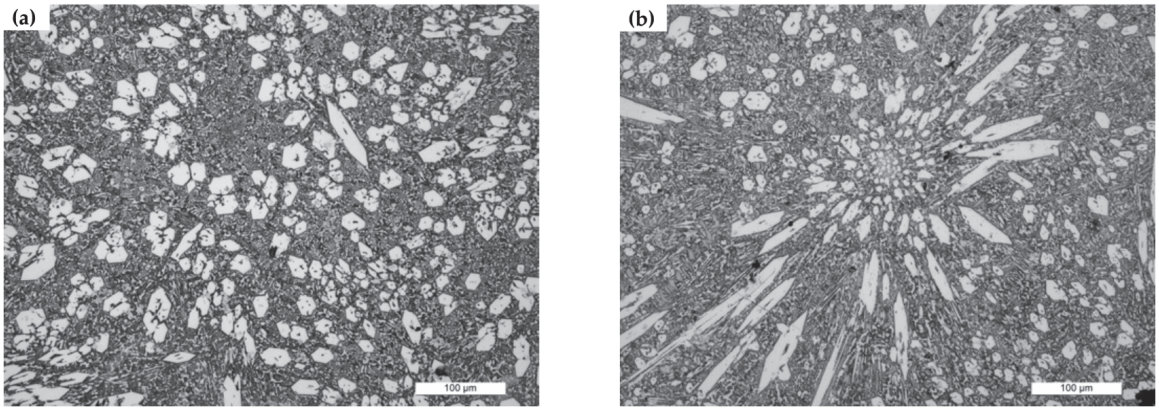

Figure 3. OM micrographs of the investigated HCCI: (**a**) hexagon and hollow-hexagon morphologies of primary M_7C_3 carbides; (**b**) blade-like morphology of primary M_7C_3 carbides.

The SEM analyses enabled us to attain more insight into the metallographic features of carbides and of the surrounding matrix. Figure 4a shows a low-magnification SEI-SEM micrograph representative of the HCCI microstructure. As seen, a large number of M_7C_3 carbides evenly distributed in the matrix are detectable, identifiable by their characteristic hexagonal shape. In addition, several eutectic carbides surrounding the primary ones are also visible (see the solid circles in Figure 4a). Such carbides are likely the M_6C-type ones, as previously observed in [36,37]. Given the Nb content in the alloy (see Table 1), the micrograph also revealed the presence of NbC with flower-like or polygonal shapes (see the dashed circles in Figure 4a). It has been established that the improvement of wear resistance by Nb addition depends on the very hard NbC (2400 HV) and on the dissolution of Nb in the matrix that promotes higher hardness [38–42]. From the high-magnification SEI- and BSE-SEM micrographs of Figure 4b,c additional microstructural features were detailed. The SEI-SEM micrographs of Figure 4b confirmed the presence of primary and eutectic carbides, Nb-rich carbides surrounded by an austenitic matrix with a small amount of martensite (see the arrows in Figure 4b). Readers seeking more in-depth insights on matrix microstructure and on the role of its structure in affecting SPE resistance are referred to a preceding study by the authors [43]. As previously observed [44], the local depletion of austenite from alloying addition promotes martensite formation at the matrix/carbide interface. In addition to the EDS point analyses of the M_7C_3 carbides (Figure 4d) and of the

NbC (Figure 4e), Figure 4f displays the spectrum of the detected Mo-rich carbides. Such carbides were also detected in a previous study by the authors [43] in which XRD analyses comprehensively detailed the phase compositions of the investigated HCCI. The formation of such hard carbides refines the primary M_7C_3 ones and improves the hardness and wear resistance of the material [40,45,46].

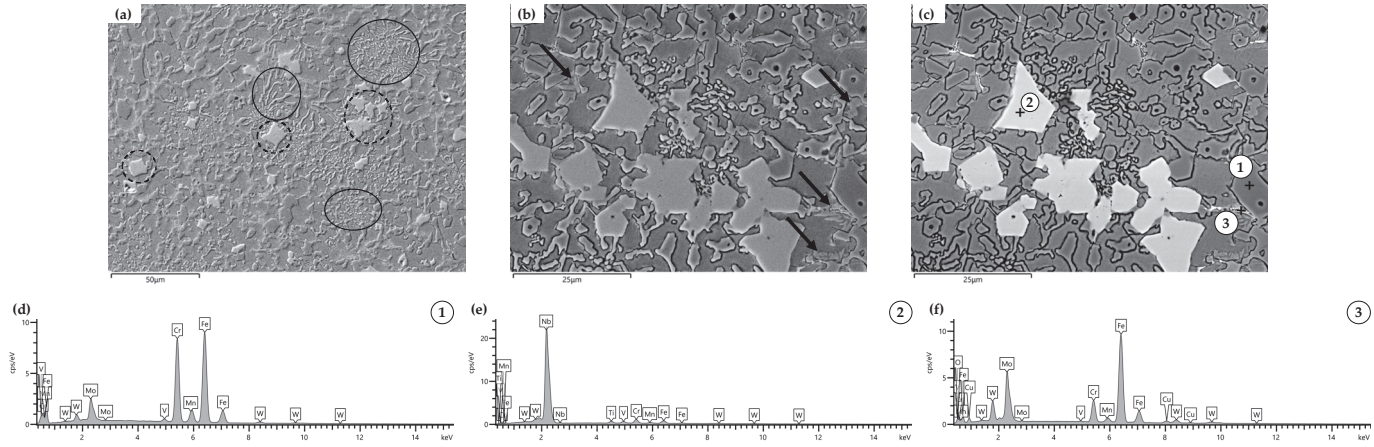

Figure 4. Micrographs of the investigated HCCI: (**a**) low-magnification SEI-SEM micrograph representative of the HCCI microstructure, eutectic carbides labeled with solid circles, and NbC labeled with dashed circles; (**b**) high-magnification SEI-SEM micrograph with martensite labeled with arrows (**c**) high-magnification BSE-SEM micrograph with labeled EDS point analyses; (**d**–**f**) EDS spectra of the point analyses labeled in (**c**).

The quantitative description of the microstructure was performed to further detail the carbide morphologies and their distribution within the microstructure. The qualitative and quantitative comparison among the different morphologies was considered, as reported in Figure 5, where the representative OM micrographs found within the microstructure of the investigated samples are shown. Table 2 reports the corresponding CVF parameters for each micrograph of Figure 5. As seen, according to the variations in carbide morphologies and dimensions, the CVF data vary from 0.14 up to 0.63 in the micrographs. It is worth noting that the adopted welding process is a commercial one, which inherently introduces variability in the microstructure due to local differences in solidification conditions. To provide context, the solidification of HCCI alloys is well understood in terms of equilibrium phase diagrams, as extensively discussed in the literature [47,48]. However, in commercial-grade materials, deviations from idealized solidification behavior are common due to the impact of real-world processing parameters, and understanding these deviations is essential for optimizing the performance of commercially manufactured components. Based on this experimental evidence, the CVF parameter was evaluated for both sample series tested with UF and M powders, respectively. The CVF was averaged on the surfaces of each sample series, i.e., covering a total area of about 54 mm^2. The results are collected in Table 3, which shows that the samples of the erosion tests had comparable CVF values. Such an outcome enables testing samples with comparable microstructure and, thus, only deals with the effect of particle dimension of the erodent powder.

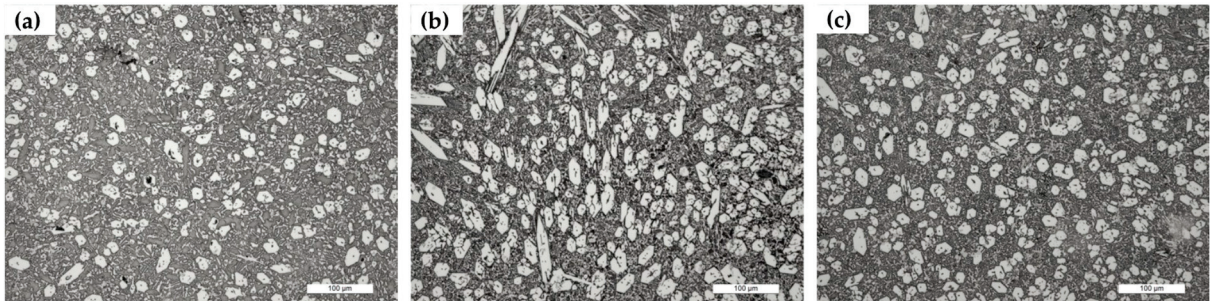

Figure 5. Representative OM micrographs of the varying morphology of primary carbides within the microstructure: (**a**–**c**) displays the variations in carbide morphologies and dimensions.

Table 2. CVF values of the representative OM micrographs in Figure 5.

Micrograph	CVF = A_C/A_{TOT}
a	0.14
b	0.63
c	0.42

Table 3. Erosion tests conditions and results: mean CVF values of the samples, kinetic energy, and ERs.

Sample Series	CVF = A_C/A_{TOT}	Kinetic Energy [J]	ER [μg/g]
UF	0.30 ± 0.14	6×10^{-8}	63.9
M	0.29 ± 0.12	2×10^{-7}	4.1

Table 3 also reports the condition (constant kinetic energy) and the obtained results (ERs) of the erosion tests. As seen, for the UF powder, the ER resulted in 63.9 μg/g, whereas for the M powder, the ER resulted in 4.1 μg/g. These outcomes highlighted that the CVF parameter is insufficient to account for the erosion resistance of the material. It is worth noting that by keeping the substrate characteristics (i.e., CVF), erodent powder type, and kinetic energy of the impacting particles constant, the result is 16 times greater ER for the UF powder. Based on these experimental findings, it emerges that for the investigated ARD-HCCI tribology coupling, the ER cannot be assessed according to the known literature models [2] where kinetic energy drives the magnitude of the damaging process.

To gain a deeper understanding of the wear damage that occurred, the worn surfaces were analyzed using a 3D digital microscope. Representative images, summarized in Figure 6, provide an overview of damage propagation across the matrix and carbides, effectively highlighting key differences in erosion behavior. From the comparison between the eroded surface of the HCCI exposed to ARD powder with a mean particle diameter of 4.8 μm (Figure 6a), i.e., UF powder, and with a mean particle diameter of 25.5 μm (Figure 6c), i.e., M powder, the difference in wear damage is evident. Consistent with the ERs data, the surface of Figure 6a exhibits remarkable wear damage with pronounced deformation features, including deep grooves. Such large-scale erosion marks suggest the particles' flow direction (from the top to the bottom in the image). By contrast, the surface morphology resulting from erosion by ARD powder with a mean particle diameter of 25.5 μm (Figure 6c) displays negligible deformation since the original microstructural features are still evident. Such outcomes are also confirmed by the high-magnification images reported in Figure 6b,d. The close-up of Figure 6b, which is a magnified view of the area depicted in Figure 6a, provides further evidence of the highly localized stresses upon impact, leading to material removal, confirming the severe abrasive wear mechanisms at play. The increased impact velocity of UF powder leads to more substantial material displacement compared to

the lower impact velocity associated with M powder, as seen by the comparison with the enlarged view of Figure 6d. This image highlights the smoother, eroded surface, suggesting a gradual material removal without significant plastic deformation due to the lower impact velocity.

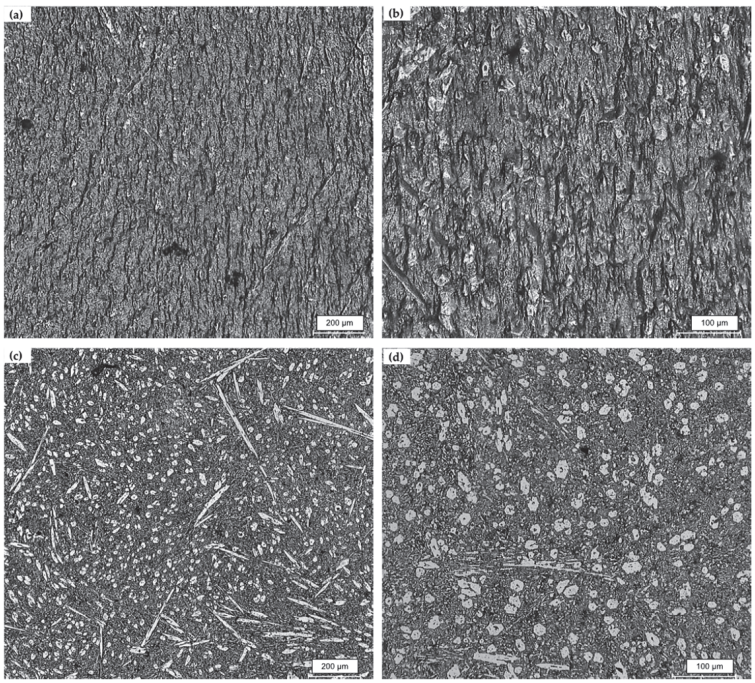

Figure 6. Digital microscope images of the worn surfaces: (**a**,**c**) low-magnification images of the surface eroded by ARD powder with a dmean = 4.8 µm and with a dmean = 25.5 µm, respectively; (**b**,**d**) high-magnification images of the surface eroded by ARD powder with a dmean = 4.8 µm and with a dmean = 25.5 µm, respectively.

Finally, the surface texture of the worn surfaces is compared in the 3D isometric views of Figure 7. As seen, these observations highlighted the contrasting erosion morphologies resulting from the different sizes and velocities of the erodent particles. The surface eroded by ARD powder with a dmean = 4.8 µm (Figure 7a) is more worn, as confirmed by the areal surface roughness parameter Sa, i.e., the arithmetical mean height. For Figure 7a, the Sa resulted in 2.24 ± 0.13 m, whereas for Figure 7b, it is 0.10 ± 0.02 µm. Hence, the smaller particles produce deeply grooved textures and pronounced ridges, indicating more aggressive material removal caused by the higher impact velocity that generated concentrated localized stresses upon impact. This leads to significant surface deformation, characterized by material displacement and detachment, and a rough topography marked by sharp peaks and valleys. Such morphology is consistent with the abrasive nature of high-velocity impacts, where the particles repeatedly erode the surface through mechanical wear. In contrast, larger impacting particles, moving at a lower velocity, produce smoother surfaces. The lower velocity reduces the severity of material removal. These contrasting morphologies highlight the critical role of erodent particle size and velocity in determining erosion mechanisms. Smaller particles at high velocities amplify surface roughness and material loss, while larger, slower particles predominantly cause negligible localized deformation, preserving much of the original surface integrity.

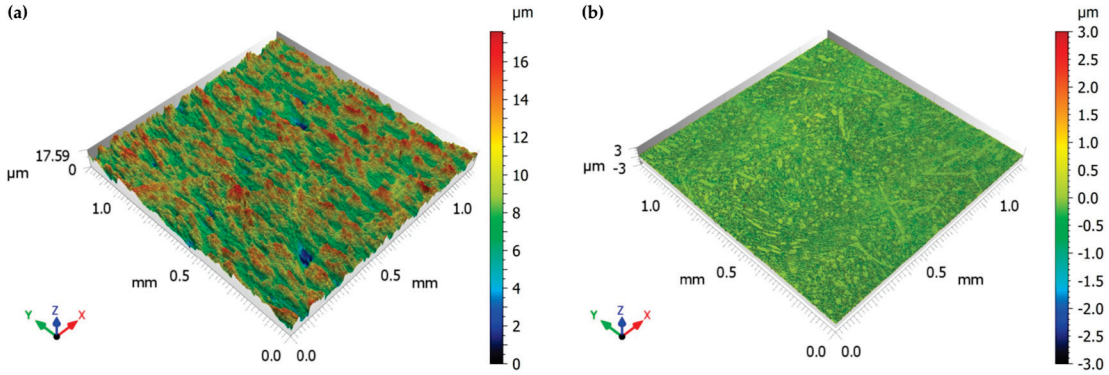

Figure 7. 3D isometric views of the worn surfaces eroded by ARD powder with: (**a**) dmean = 4.8 µm and (**b**) dmean = 25.5 µm.

4. Conclusions

This study analyzed the solid particle erosion resistance of a high chromium cast iron, focusing on the combined role of microstructural features and the kinetic energy of impacting particles. The following conclusions can be drawn based on the experimental outcomes resulting from both microstructural investigations and erosion tests.

- detailed quantitative microstructural analyses revealed that the CVF parameter was comparable across samples;
- erosion tests comprised two mean particle diameters of the ARD powder (dmean = 4.8 µm, labeled as UF, and dmean = 25.5 µm, labeled as M). Tests conducted at equal particle kinetic energy and CVF revealed varying damage levels in the substrates, highlighting that impact conditions, particularly velocity, outweigh the contribution of CVF alone. With UF powder, the HCCI substrate experienced markedly higher erosion rates (ER = 63.9 µg/g), characterized by severe surface damage and localized material removal. Conversely, M powder promoted lower erosion rates (ER = 4.1 µg/g) with minimal deformation;
- the erosion tests demonstrated a significant dependence of ER on the size and velocity of erodent particles, with smaller, faster particles causing more severe erosion (ER = 63.9 µg/g) due to their higher localized impact. Conversely, larger particles produced less pronounced wear (ER = 4.1 µg/g), inducing negligible deformation since the original microstructural features are still evident.

This study addresses critical gaps in the understanding of SPE behavior in HCCIs, providing valuable insights for optimizing the design and processing of HCCIs. The research sheds light on the interplay between carbide morphology, distribution, and SPE behavior, a partially underexplored area. By demonstrating how substrates with identical CVF exhibit varied erosion resistance due to differences in morphology and distribution, the study provides valuable insights for tailoring HCCI microstructures to enhance performance in demanding erosive environments.

Author Contributions: Conceptualization, A.S. and A.F.; methodology, A.S.; investigation, N.Z. and A.F.; data curation, A.F.; writing—original draft preparation, A.F.; writing—review and editing, A.S. and N.Z.; visualization, A.F. All authors have read and agreed to the published version of the manuscript.

Funding: This research received no external funding.

Data Availability Statement: The original contributions presented in this study are included in the article. Further inquiries can be directed to the corresponding author.

Acknowledgments: The authors wish to gratefully acknowledge Matteo Fucci for his support in the micrographic analyses. Our gratitude is also extended to Michele Gragnanini for his support with the non-contact 3D profilometer measurements.

Conflicts of Interest: The authors declare no conflicts of interest.

References

1. Budinski, K.G. Solid Particle Erosion. In *Friction, Wear, and Erosion Atlas*; CRC Press: Boca Raton, FL, USA, 2013; pp. 125–138.
2. Tarodiya, R.; Levy, A. Surface Erosion Due to Particle-Surface Interactions—A Review. *Powder Technol.* **2021**, *387*, 527–559. [CrossRef]
3. Ruff, A.W.; Wiederhorn, S.M. Erosion by Solid Particle Impact. In *Treatise on Materials Science and Technology*; Academic Press: Cambridge, MA, USA, 1979.
4. Kleis, I.; Kulu, P. *Solid Particle Erosion*; Springer: London, UK, 2008; ISBN 978-1-84800-028-5.
5. Fortini, A.; Suman, A.; Zanini, N. An Experimental and Numerical Study of the Solid Particle Erosion Damage in an Industrial Cement Large-Sized Fan. *Eng. Fail. Anal.* **2023**, *146*, 107058. [CrossRef]
6. Grant, G.; Tabakoff, W. Erosion Prediction in Turbomachinery Resulting from Environmental Solid Particles. *J. Aircr.* **1975**, *12*, 471–478. [CrossRef]
7. Alqallaf, J.; Ali, N.; Teixeira, J.A.; Addali, A. Solid Particle Erosion Behaviour and Protective Coatings for Gas Turbine Compressor Blades—A Review. *Processes* **2020**, *8*, 984. [CrossRef]
8. Parsi, M.; Najmi, K.; Najafifard, F.; Hassani, S.; McLaury, B.S.; Shirazi, S.A. A Comprehensive Review of Solid Particle Erosion Modeling for Oil and Gas Wells and Pipelines Applications. *J. Nat. Gas Sci. Eng.* **2014**, *21*, 850–873. [CrossRef]
9. Bousser, E.; Martinu, L.; Klemberg-Sapieha, J.E. Solid Particle Erosion Mechanisms of Protective Coatings for Aerospace Applications. *Surf. Coat. Technol.* **2014**, *257*, 165–181. [CrossRef]
10. Aldi, N.; Casari, N.; Pinelli, M.; Suman, A.; Vulpio, A.; Saccenti, P. Performance Modification of an Erosion-Damaged Large-Sized Centrifugal Fan. In *Volume 1: Aircraft Engine; Fans and Blowers; Marine; Wind Energy; Scholar Lecture*; American Society of Mechanical Engineers: Houston, TX, USA, 7 June 2021.
11. Liebhard, M.; Levy, A. The Effect of Erodent Particle Characteristics on the Erosion of Metals. *Wear* **1991**, *151*, 381–390. [CrossRef]
12. Ediriweera, M.; Chladek, J.; Ratnayake, C. Effect of Impact Angle, Exposure Time, and Particle Size on Impact Erosion. *Part. Sci. Technol.* **2021**, *39*, 10–18. [CrossRef]
13. Desale, G.R.; Paul, C.P.; Gandhi, B.K.; Jain, S.C. Erosion Wear Behavior of Laser Clad Surfaces of Low Carbon Austenitic Steel. *Wear* **2009**, *266*, 975–987. [CrossRef]
14. Nguyen, V.B.; Nguyen, Q.B.; Zhang, Y.W.; Lim, C.Y.H.; Khoo, B.C. Effect of Particle Size on Erosion Characteristics. *Wear* **2016**, *348–349*, 126–137. [CrossRef]
15. Oka, Y.I.; Okamura, K.; Yoshida, T. Practical Estimation of Erosion Damage Caused by Solid Particle Impact: Part 1: Effects of Impact Parameters on a Predictive Equation. *Wear* **2005**, *259*, 95–101. [CrossRef]
16. Abdian, K.; Eslami, A.; Ashrafizadeh, F.; Fadaeifard, F.; Yingxin, G.; Mendez, P.; Barnes, N. Solid Particles Erosion Performance of a Fe–Cr–C Chromium Carbide Overlay. *Metallogr. Microstruct. Anal.* **2023**, *12*, 1055–1061. [CrossRef]
17. Goodwin, J.E.; Sage, W.; Tilly, G.P. Study of Erosion by Solid Particles. *Proc. Inst. Mech. Eng.* **1969**, *184*, 279–292. [CrossRef]
18. Lindsley, B.A.; Marder, A.R. The Effect of Velocity on the Solid Particle Erosion Rate of Alloys. *Wear* **1999**, *225–229*, 510–516. [CrossRef]
19. Lin, F.Y.; Shao, H.S. Effect of Impact Velocity on Slurry Erosion and a New Design of a Slurry Erosion Tester. *Wear* **1991**, *143*, 231–240. [CrossRef]
20. Sapate, S.G.; RamaRao, A.V. Effect of Erodent Particle Hardness on Velocity Exponent in Erosion of Steels and Cast Irons. *Mater. Manuf. Process.* **2003**, *18*, 783–802. [CrossRef]
21. Badisch, E.; Roy, M. Hardfacing for Wear, Erosion and Abrasion. In *Surface Engineering for Enhanced Performance Against Wear*; Springer: Vienna, Austria, 2013; pp. 149–191.
22. Chatterjee, S.; Pal, T.K. Solid Particle Erosion Behaviour of Hardfacing Deposits on Cast Iron—Influence of Deposit Microstructure and Erodent Particles. *Wear* **2006**, *261*, 1069–1079. [CrossRef]
23. Jindal, C.; Singh Sidhu, B.; Kumar, P.; Singh Sidhu, H. Performance of Hardfaced/Heat Treated Materials under Solid Particle Erosion: A Systematic Literature Review. *Mater. Today Proc.* **2022**, *50*, 629–639. [CrossRef]
24. Singla, Y.K.; Maughan, M.R.; Arora, N.; Dwivedi, D.K. Enhancing the Wear Resistance of Iron-Based Alloys: A Comprehensive Review of Alloying Element Effects. *J. Manuf. Process.* **2024**, *120*, 135–160. [CrossRef]
25. Suman, A.; Fortini, A. Effects of Heat Treatment and Erosion Particle Size on Erosion Resistance of a Hypereutectic High-Chromium Cast Iron. *Coatings* **2024**, *14*, 66. [CrossRef]

26. Sapate, S.; Rama Rao, A. Effect of Carbide Volume Fraction on Erosive Wear Behaviour of Hardfacing Cast Irons. *Wear* **2004**, *256*, 774–786. [CrossRef]
27. Sapate, S.G.; RamaRao, A.V. Erosive Wear Behaviour of Weld Hardfacing High Chromium Cast Irons: Effect of Erodent Particles. *Tribol. Int.* **2006**, *39*, 206–212. [CrossRef]
28. Stevenson, A.N.J.; Hutchings, I.M. Wear of Hardfacing White Cast Irons by Solid Particle Erosion. *Wear* **1995**, *186*, 150–158. [CrossRef]
29. Finnie, I. Erosion of Surfaces by Solid Particles. *Wear* **1960**, *3*, 87–103. [CrossRef]
30. Shitole, P.P.; Gawande, S.H.; Desale, G.R.; Nandre, B.D. Effect of Impacting Particle Kinetic Energy on Slurry Erosion Wear. *J. Bio-Tribo-Corros.* **2015**, *1*, 29. [CrossRef]
31. *ASTM G76-18*; Standard Test Method for Conducting Erosion Tests by Solid Particle Impingement Using Gas Jets. ASTM International: West Conshohocken, PA, USA, 2018.
32. *ISO 12103-1:2016*; Road Vehicles—Test Contaminants for Filter Evaluation—Part 1: Arizona Test Dust. ISO: Geneva, Switzerland, 2016.
33. Schneider, C.A.; Rasband, W.S.; Eliceiri, K.W. NIH Image to ImageJ: 25 Years of Image Analysis. *Nat. Methods* **2012**, *9*, 671–675. [CrossRef]
34. Fortini, A.; Suman, A.; Vulpio, A.; Merlin, M.; Pinelli, M. Microstructural and Erosive Wear Characteristics of a High Chromium Cast Iron. *Coatings* **2021**, *11*, 490. [CrossRef]
35. Liu, S.; Zhou, Y.; Xing, X.; Wang, J.; Ren, X.; Yang, Q. Growth Characteristics of Primary M7C3 Carbide in Hypereutectic Fe-Cr-C Alloy. *Sci. Rep.* **2016**, *6*, 32941. [CrossRef] [PubMed]
36. Li, P.; Yang, Y.; Shen, D.; Gong, M.; Tian, C.; Tong, W. Mechanical Behavior and Microstructure of Hypereutectic High Chromium Cast Iron: The Combined Effects of Tungsten, Manganese and Molybdenum Additions. *J. Mater. Res. Technol.* **2020**, *9*, 5735–5748. [CrossRef]
37. Imurai, S.; Thanachayanont, C.; Pearce, J.T.H.; Tsuda, K.; Chairuangsri, T. Effects of W on Microstructure of As-Cast 28 Wt.%Cr–2.6 Wt.%C–(0–10)Wt.%W Irons. *Mater. Charact.* **2015**, *99*, 52–60. [CrossRef]
38. He-Xing, C.; Zhe-Chuan, C.; Jin-Cai, L.; Huai-Tao, L. Effect of Niobium on Wear Resistance of 15%Cr White Cast Iron. *Wear* **1993**, *166*, 197–201. [CrossRef]
39. Bedolla-Jacuinde, A. Microstructure of Vanadium-, Niobium- and Titanium-Alloyed High-Chromium White Cast Irons. *Int. J. Cast Met. Res.* **2001**, *13*, 343–361. [CrossRef]
40. Jain, A.-S.; Chang, H.; Tang, X.; Hinckley, B.; Zhang, M.-X. Refinement of Primary Carbides in Hypereutectic High-Chromium Cast Irons: A Review. *J. Mater. Sci.* **2021**, *56*, 999–1038. [CrossRef]
41. de Melo, I.N.R.; da Silva, A.E.; de Faria, F.G.; Pinheiro, I.P.; da Silva, L.R.; Paniago, R.M. Influence of Niobium Adding on the Microstructure and Abrasive Wear Resistance of a Heat-Treated High-Chromium Near-Eutectic Cast Iron Alloy. *Mater. Res.* **2022**, *25*, e20210562. [CrossRef]
42. Pourasiabi, H.; Gates, J.D. Effects of Niobium Macro-Additions to High Chromium White Cast Iron on Microstructure, Hardness and Abrasive Wear Behaviour. *Mater. Des.* **2021**, *212*, 110261. [CrossRef]
43. Fortini, A.; Suman, A.; Zanini, N.; Cruciani, G. Erosive Wear Behavior of High-Chromium Cast Iron: Combined Effect of Erodent Powders and Destabilization Heat Treatments. *Coatings* **2022**, *12*, 1218. [CrossRef]
44. Tabrett, C.; Sare, I. Effect of High Temperature and Sub-Ambient Treatments on the Matrix Structure and Abrasion Resistance of a High-Chromium White Iron. *Scr. Mater.* **1998**, *38*, 1747–1753. [CrossRef]
45. Scandian, C.; Boher, C.; de Mello, J.D.B.; Rézaï-Aria, F. Effect of Molybdenum and Chromium Contents in Sliding Wear of High-Chromium White Cast Iron: The Relationship between Microstructure and Wear. *Wear* **2009**, *267*, 401–408. [CrossRef]
46. Chung, R.J.; Tang, X.; Li, D.Y.; Hinckley, B.; Dolman, K. Microstructure Refinement of Hypereutectic High Cr Cast Irons Using Hard Carbide-Forming Elements for Improved Wear Resistance. *Wear* **2013**, *301*, 695–706. [CrossRef]
47. Lin, C.-M.; Chang, C.-M.; Chen, J.-H.; Hsieh, C.-C.; Wu, W. Microstructural Evolution of Hypoeutectic, Near-Eutectic, and Hypereutectic High-Carbon Cr-Based Hard-Facing Alloys. *Metall. Mater. Trans. A* **2009**, *40*, 1031–1038. [CrossRef]
48. Khvan, A.V.; Hallstedt, B.; Broeckmann, C. A Thermodynamic Evaluation of the Fe–Cr–C System. *Calphad* **2014**, *46*, 24–33. [CrossRef]

metals

MDPI

Article

Microstructural and Mechanical Characterization of the Laser Beam Welded SAF 2507 Super-Duplex Stainless Steel

Beáta Šimeková [1,*], Mária Dománková [2], Ingrid Kovaříková [3], Pavel Kovačócy [1], Maroš Martinkovič [1], Michal Šimek [4] and Luke Ciuła [5]

[1] Department of Welding and Joining of Materials, Institute of Production Technologies, Faculty of Materials Science and Technology in Trnava, Slovak University of Technology in Bratislava, J. Bottu 25, 917 24 Trnava, Slovakia; pavel.kovacocy@stuba.sk (P.K.); maros.martinkovic@stuba.sk (M.M.)
[2] Institute of Materials Science, Faculty of Materials Science and Technology in Trnava, Slovak University of Technology in Bratislava, J. Bottu 25, 917 24 Trnava, Slovakia; maria.domankova@stuba.sk
[3] Faculty of Special Technology, Alexander Dubček University of Trenčín, 911 06 Trenčín, Slovakia; ingrid.kovarikova@tnuni.sk
[4] First Welding Company, Inc., Kopčianska 804, 851 01 Petržalka, Slovakia; simek.michal@pzvar.sk
[5] LMC Construction, Inc., 608 E. Green Street, Bensenville, IL 60106, USA; luke@lmcteam.com
* Correspondence: beata.simekova@stuba.sk; Tel.: +421-908-119-601

Abstract: The influence of laser beam welding parameters (power, welding rate, focusing, head oscillation, shielding gas) on the microstructure, mechanical properties and corrosion resistance of the super-duplex stainless steel SAF 2507 was studied in this paper. The presented results clearly report the effects of welding parameter changes on the character of the steel's microstructure. The presence of secondary phase M_2N in weld metals has an important influence on their mechanical properties. Optimal mechanical properties, an acceptable ferrite/austenite ratio, and the minimum content of M_2N nitride required in the weld metal were acquired in the case the following application: 1100 W power, welding speed of 10 mm/s, focusing of 4 mm, and pure nitrogen shielding gas (20 L/min).

Keywords: super-duplex stainless steel; welding; microstructure; precipitation; mechanical properties; corrosion

1. Introduction

Duplex stainless steels (DSSs) and super-duplex stainless steels (SDSSs) are high-strength, corrosion-resistant materials extensively utilized in industries such as nuclear power, petrochemicals, marine applications, and fertilizers, especially in cryogenic environments. Their fine duplex microstructure, characterized by austenitic islands within a ferritic matrix, enhances both their mechanical properties and corrosion resistance [1–5]. Optimal properties in DSSs and SDSSs are achieved with an approximately 50% ratio of each phase. This balance between ferrite and austenite is primarily attained by adjusting the contents of chromium, nickel, and nitrogen, along with appropriate heat treatment. The significant presence of chromium, molybdenum, and nitrogen in these duplex alloys provides exceptional resistance to pitting corrosion in chloride-containing environments, while the relatively lower nickel content enhances their resistance to stress corrosion cracking compared to conventional austenitic stainless steels [6–13].

Duplex stainless steels offer a superior combination of mechanical properties and corrosion resistance compared to single-phased ferritic or austenitic stainless steels. These materials are primarily based on the Fe-Cr-Ni system and typically consist of two phases in roughly equal volume fractions: ferrite and austenite. Along with iron (Fe), chromium (Cr), and nickel (Ni), they also include various other elements that act as stabilizers for either the ferrite (such as molybdenum (Mo) and silicon (Si)) or the austenite (including nitrogen (N), carbon (C), manganese (Mn), and copper (Cu)). The effectiveness of these elements as

ferrite or austenite stabilizers can be quantified using chromium and nickel equivalents (Cr_{eq} and Ni_{eq}), as outlined in Equations (1) and (2) [14]:

$$Cr_{eq} = Cr + 1.37Mo + 1.5Si + 2Nb + 3Ti \quad (1)$$

$$Ni_{eq} = Ni + 0.3Mn + 22C + 14.2N + Cu \quad (2)$$

By using Cr_{eq} and Ni_{eq}, it is possible to predict the solidification sequence or mode:

(1) $\frac{Cr_{eq}}{Ni_{eq}} = 1.38 - 1.50 : L \rightarrow L + \gamma \rightarrow L + \gamma + \delta \rightarrow \gamma + \delta$ (austenitic-ferritic mode—AF)

(2) $\frac{Cr_{eq}}{Ni_{eq}} = 1.50 - 2.00 : L \rightarrow L + \delta \rightarrow L + \delta + \gamma \rightarrow \delta + \gamma$ (ferritic-austenitic mode—FA)

(3) $\frac{Cr_{eq}}{Ni_{eq}} > 2.00 : L \rightarrow L + \delta \rightarrow \delta$ (ferritic mode—F)

The ratio of ferrite to austenite content can be altered during the welding of duplex stainless steels (DSSs) and super duplex stainless steels (SDSSs). It is important to note that an austenite content of below 25% is typically deemed unacceptable for most industrial applications. The primary concern is that an excessively high ferrite content in both the heat-affected zone (HAZ) and the weld metal (WM) leads to a reduction in toughness and corrosion resistance [8,14–17].

Heat treatment of duplex stainless steels (DSSs) and super duplex stainless steels (SDSSs) at temperatures ranging from 320 to 950 °C can lead to property degradation due to the precipitation of brittle intermetallic phases, such as the sigma phase, chi phase, $M_{23}C_6$ carbide, or M_2N nitride (Figure 1) [18]. Research indicates that the sigma phase is particularly detrimental, as it adversely affects both weld toughness and corrosion resistance [12,13,19–25].

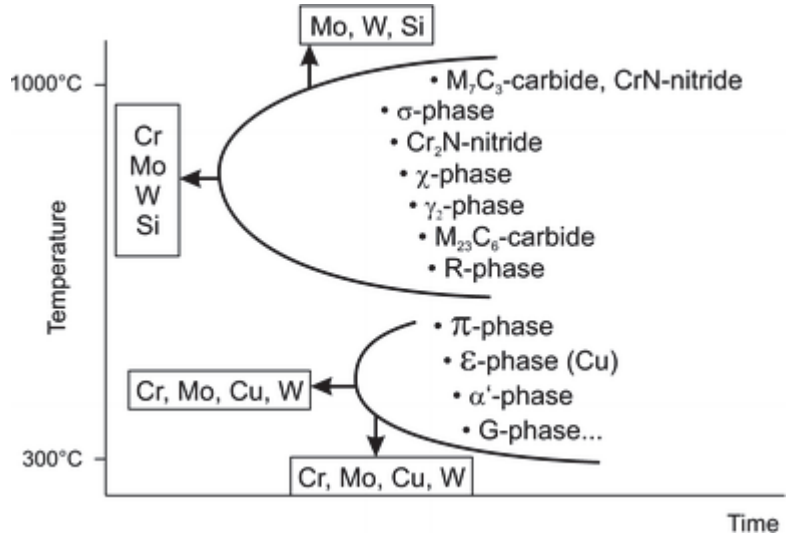

Figure 1. Precipitation diagram of the duplex stainless steels Reprinted from Ref. [18].

Numerous studies have investigated the welding of super duplex stainless steels (SDSSs) using various techniques, including Gas Tungsten Arc (GTA), Shielded Metal Arc Welding (SMAW), Plasma Arc Welding (PAW), Friction Welding (FW), Laser Beam Welding (LBW), and Electron Beam Welding (EBW) [26–29]. Research has shown [1,8,9,15,30,31] that fusion welding processes can adversely affect the desirable duplex microstructure of stainless steels, leading to the formation of harmful secondary phases. Furthermore, fusion welding typically results in increased ferrite content and the development of coarse grains within the weld joints, which can compromise both the corrosion resistance and mechanical properties of the welded assemblies.

Laser Beam Welding (LBW) is particularly effective for thicker sections due to its ability to enhance labor productivity, achieve a higher depth-to-width ratio in weld joints,

and minimize residual stress and distortion. Additionally, LBW often results in a reduction of secondary phases in the fusion zones.

Laser welding parameters can be precisely controlled and adjusted, allowing for the tailoring of heat input during the welding process [32,33]. This means that the cooling process can also be managed through these parameters to achieve the desired microstructure. Fiber lasers possess several key characteristics that make them ideal for welding applications. They offer excellent beam quality and operate at a short wavelength. The small diameter of the fiber results in a very fine beam focus, enhancing the laser's effectiveness. Due to the favorable properties of the laser beam, it is possible to weld at high speeds while still achieving adequate penetration. The short wavelength of the laser allows for effective absorption by nearly all metals and alloys. By leveraging these advantageous beam parameters along with high radiation absorption, it is feasible to transition from keyhole welding to laser welding simply by adjusting the welding parameters.

In laser welding, the heat input is primarily influenced by three factors: the absorption of laser beam irradiation, laser output power, and welding speed. Absorption is challenging to modify, as it is closely linked to the wavelength of the laser beam and the type of material being welded. Consequently, heat input can mainly be controlled by adjusting the laser output power or the welding speed. Specifically, as welding speed increases, heat input decreases, and vice versa. Increasing the laser output power results in greater heat input into the welded material. Since the welding speeds in laser welding are typically much higher than those used in conventional arc welding, the overall heat input to the material is significantly lower. This leads to a much higher cooling rate in laser welds compared to arc welds, resulting in distinct microstructural changes in the weld metal [31,32,34–39].

In this study, Laser Beam Welding experiments were conducted on super duplex steel DSS2057 sheets, employing a wide range of welding parameters. The impact of these parameters on various aspects, including the textural changes, penetration depth of the welded joints, fusion zone (FZ) width, and heat-affected zone (HAZ) width, was investigated. Changes in the microstructure of the base material (BS), FZ, and HAZ were characterized using light microscopy, scanning electron microscopy, and transmission electron microscopy. The resulting microstructures, along with the corrosion resistance, hardness, ultimate tensile strength, ductility, and corrosion behavior, were thoroughly evaluated. Additionally, the results from the tensile strength tests were correlated with the analysis of the fracture surface morphology of the test specimens.

2. Materials and Methods

The current investigations utilized 2 mm-thick sheets made from commercially available super-duplex stainless steel SAF 2507 (Sverdrup Steel AS, Stavanger, Norway). The chemical composition of the experimental steel is detailed in Table 1 (material sheets sourced from the supplier). The material supplier also provided the thermo-physical and minimum guaranteed mechanical properties in accordance with the relevant ASTM standards. The as-received sheets contained approximately equal contents of ferrite and austenite (Figure 2) (material sheets the supplier).

Table 1. Chemical composition of experimental steel SAF 2507 (wt. %).

	Chemical Composition (wt. %)									
	C	**Cr**	**Ni**	**Mo**	**N**	**Mn**	**Si**	**P**	**S**	**Fe**
Experimental SAF 2507 steel	max. 0.03	21.0–23.0	4.5–6.5	2.5–3.5	0.8–2.0	max. 2.0	max. 1.0	max. 0.03	max. 0.02	balance

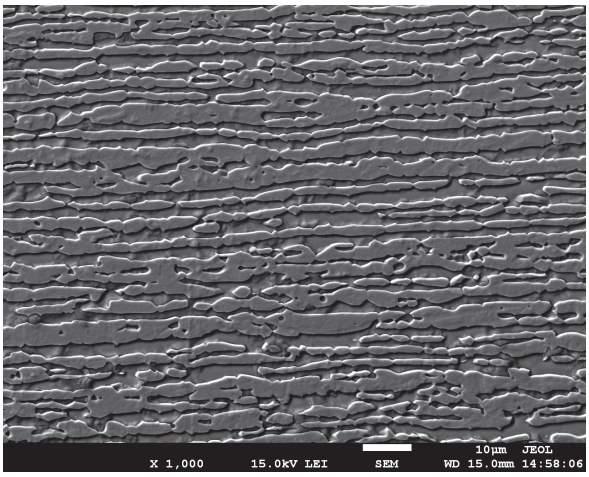

Figure 2. SEM analysis of the experimental steel.

The specimens were securely clamped to the fixture using sheets and clamps (see Figure 3a) to prevent any undesirable distortion that can occur during the welding process. Butt joints were created with no gap between the specimens, and the welding direction was set perpendicular to the sheet's rolling direction. A schematic illustrating the shielding of the welded joints is provided in Figure 3b. The welding experiments utilized a 5 kW IPG YLS-5000 fiber laser (IPG Laser GmbH, Burbach, Germany), equipped with a 100 μm optical fiber (IPG Laser GmbH, Germany) and a focal length of 250 mm. A dual shielding gas configuration was employed to maintain a stable keyhole throughout the welding process. In total, twelve welded joints were produced, each of them with different welding parameters. Based on the experiment where 12 samples were made, the following samples were selected after visual inspection. The four samples A, B, C, D (Table 2) with different content of austenite in the weld metals were chosen for the detailed material analysis.

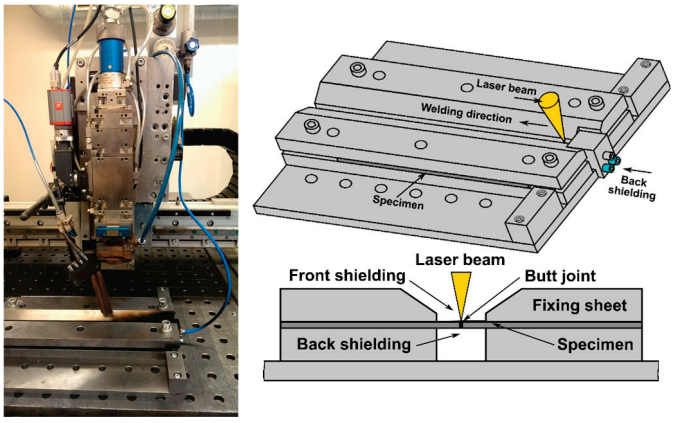

(**a**) (**b**)

Figure 3. Fixing system of specimens (**a**), a schematic showing the LBW process (**b**).

Table 2. Laser welding parameters.

Sample	Power (W)	Welding Speed (mm/s)	Focusing (mm)	Head Oscillation (mm)	Shielding Gas (L/min)
A	800	10	0	-	N (20)
B	1100	10	4	-	N (20)
C	500	7	0	2–1	N (20)
D	500	7	0	2.5–0.7	NH (20)

N—Pure Nitrogen, NH—Nitrogen + 10% Hydrogen.

For the keyhole welds, a laser output power in the range of 0.45–1.2 kW at welding speeds of 5, 7, 10 and 15 mm/s was used. Welds were made on plates of the size 2 100 × 100 mm (thickness × width × length). The heat input to the laser weld joint was calculated using the formula Q = μP/v, where Q denotes the heat input (J/mm), P represents the power of the laser beam (W), v is the welding speed (mm/s), and μ is the absorption coefficient of the laser irradiation in keyhole welding mode. A value of g = 0.9 was considered in the current study based on the literature data [40]. The heat input of the laser weld was calculated using an absorption rate of 90% for keyhole welding. In our experiment, three welding modes were used: 1—without rocking, 2, 3—with rocking (Table 3). The mode represents the trajectory (red line) along which the laser beam moved. Welding modes were used to increase the heat input to the weld pool and reduce the cooling rate.

Table 3. Welding modes used in experiment.

Welding Mode	1	2	3
Dimension X (mm)	1	1	0.7
Dimension Y (mm)	0	1	1.25
Heat input Q (J/mm)	Q	Q.1.414	Q.2.046
Weld joint No.	A, B	C	D

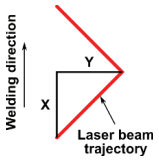

Q = 0.9.P/v (J/mm).

Cooling rates calculation:

$$R = -2\pi\kappa\rho C\left(\frac{vs}{P\eta}\right)^2 (T - T_0)^3 \quad (3)$$

in this context, R represents the cooling rate (K/s); T denotes the transformation temperatures of δ-γ (1473 K and 1073 K, equivalent to 1200–800 °C); T_0 is the room temperature (293 K); κ signifies thermal conductivity (14 W/mK); ρ is the material density (7800 kg/m^3); C refers to the specific heat (490 J/kgK); v indicates the welding speed (m/s); s is the thickness of the welded specimen (0.002 m); P represents the laser beam power (W); and η is the absorption coefficient (0.9) [31].

The calculated cooling rate R (Table 4) for Samples A–D in the range of 1200 to 800 °C is important for the phase composition of the weld metal/fusion zone.

Table 4. Cooling rates in experiment.

Weld Joint No.	A	B	C	D
R_{1200} (K/s)	426.2	225.4	267.4	127.7
R_{800} (K/s)	123.1	65.1	77.2	36.9

Microstructure analysis

The specimens intended for light microscopy (LOM) examination were first ground using a series of metallographic emery papers up to 1200 grit (Böhler, voestalpine High Performance Metals Slovakia, s.r.o., Martin, Slovakia), followed by polishing with a 1 μm diamond suspension. They were then chemically etched for 10 s using a solution composed of 80 mL distilled water, 40 mL hydrochloric acid (HCl), 4.8 g ammonium bifluoride (NH_4HF_2), and 1 g potassium disulfite ($K_2S_2O_5$). Microstructural observations were conducted using a NEOPHOT 32 light microscope (ZEISS, Jena, Germany) equipped with a CCD camera. For the identification of specific secondary phases, transmission electron microscopy (TEM) was employed on thin foil specimens. Small discs, 3 mm in diameter and approximately 0.1 mm thick, were jet-electropolished in an electrolyte solution of nitric acid and methanol (HNO_3:CH_3OH = 3:7) at 0 °C and 15 V to create transparent areas near the central hole. The jet-electropolishing process was carried out using TENUPOL 5 apparatus (Struers GmbH, Roztoky, Czech Republic). TEM observations were performed

with a JEOL 200 CX microscope (JEOL GmbH, Freising, Germany) operating at 200 kV and a Philips CM 300 at 300 kV (Oxford instruments, Abingdon, UK), both equipped with an energy-dispersive X-ray spectrometer (EDX) for microchemical analysis. Selected area electron diffraction was also used for phase identification. Additionally, high-resolution scanning electron microscopy (SEM) was performed on the fracture surfaces after tensile testing, using a JEM 7600F microscope (JEOL GmbH, Germany) operating at 30 kV and equipped with an X-ray spectrometer.

Ferric Chloride corrosion test

In this study, we employed the ASTM A923-06 standard—specifically, Method C, for detecting detrimental intermetallic phases in duplex austenitic/ferritic stainless steels, using a ferric chloride corrosion test to classify duplex stainless steel structures [41]. The test solution was created by dissolving 100 g of reagent-grade ferric chloride and $FeCl_3.6H_2O$ in 900 mL of distilled water, resulting in approximately 6% $FeCl_3$ by weight. Prior to testing, the pH of the solution was adjusted to around 1.3 using hydrochloric acid (HCl). Samples measuring approximately 50 × 25 mm were prepared by dry grinding to a 120-grit finish, in line with ASTM A923-06 requirements, followed by rinsing with acetone. Before the corrosion tests, the samples in their as-fabricated state were also ground to 120 grit. Each sample was weighed to the nearest 0.0001 g using an analytical balance KERN ALS 250-4A (Mettler-Toledo s.r.o., Bratislava, Slovakia), and dimensions were measured accurately. Testing was conducted in glass beakers containing at least 600 mL of the prepared solution. The test temperature was maintained at 40 °C (104 °F) with an accuracy of ±1 °C. Each sample was immersed for 24 h, after which they were cleaned, rinsed, and dried. The samples were then weighed again, and the corrosion rate was calculated in $mg/dm^2/day$ (mdd) based on the weight loss and total surface area [41]:

$$corrosion\ rate\ (mdd) = \frac{weight\ loss\ (mg)}{[specimen\ area\ (dm^2).time\ (days)]} \quad (4)$$

If the specimen shows a corrosion rate in excess of 10 mdd, one retest on two new specimens from the same product is permitted. No retest specimen shall exhibit a corrosion rate in excess of 10 mdd. The critical temperature was defined as the highest temperature at which the corrosion rate was below this limit.

Tensile test

The mechanical properties of the materials and weld joints were evaluated using a WPM ZDM 5/91/U2B tensile testing machine (VEB Thüringer Indust., Rauenstein/HBM, Germany), which has a maximum load capacity of 100 kN at room temperature. The measurement system is equipped with a dynamometer and a SPIDER 8 strain apparatus, allowing for the digitization of the measured data. Tensile test specimens were cut from the welded sheets using a water jet machine to avoid any unwanted thermal effects on the weld joints. A total of three specimens were tested for each combination of welding parameters, and the mean values along with the standard deviations of the collected data were calculated.

3. Results

3.1. Macrostructure and Microstructure Analysis

Cross section macrographs of the laser beam weld joints produced using optimized weld parameters are presented in Figure 4. Welds of the samples were relatively homogeneous, with full penetration and without observable discontinuities. Also, there were not any cavities or pores in penetration, although the base material of the SAF 2507 super duplex stainless steel was alloyed with nitrogen, and there is risk of porosity in laser beam welding. With increasing diameter oscillations of the laser beam, the thickness of the penetration increased. The observed surface welds were without imperfections. The HAZ of the experimental weld joints observed in the macrographs did not correspond to any significant modification (Figure 5). The microstructure of the HAZ was similar to that of the

base material. Remarkable changes were observed only in the high-temperature HAZ close to the fusion line. Increases in ferrite contents and growth of the grains were observed.

Weld No.	Laser Beam Power (W)	Welding Speed (mm/s)	Focal Position (mm)	Shielding Gas/Flow Rate (L/min.)	Mode/Heat Input (J/mm)	Weld No.	Laser Beam Power (W)	Welding Speed (mm/s)	Focal Position (mm)	Shielding Gas/Flow Rate (L/min.)	Mode/Heat Input (J/mm)
	Weld Face—Root Surface—Cross Section						Weld Face—Root Surface—Cross Section				
A	800	10	0	N/20	1/72	**C**	500	7	0	N/20	2/90.9
	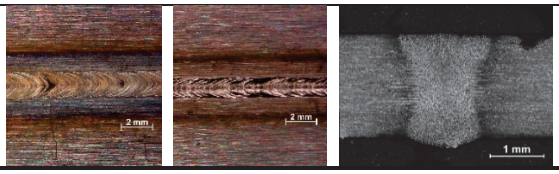						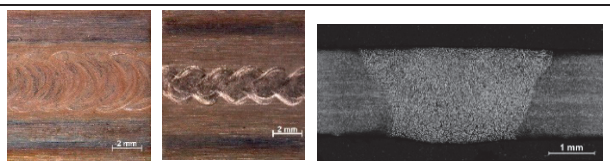				
B	1100	10	4	N/20	1/99	**D**	500	7	0	NH/20	3/131.5
	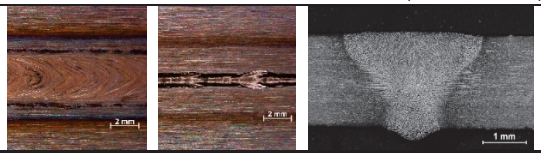						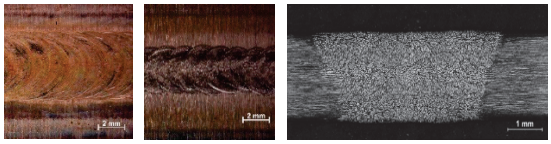				

N—Pure Nitrogen, NH—Nitrogen + 10% Hydrogen.

Figure 4. Weld face, root face, and cross section of joints produced with laser beam welding with different parameters (Samples (**A**–**D**)).

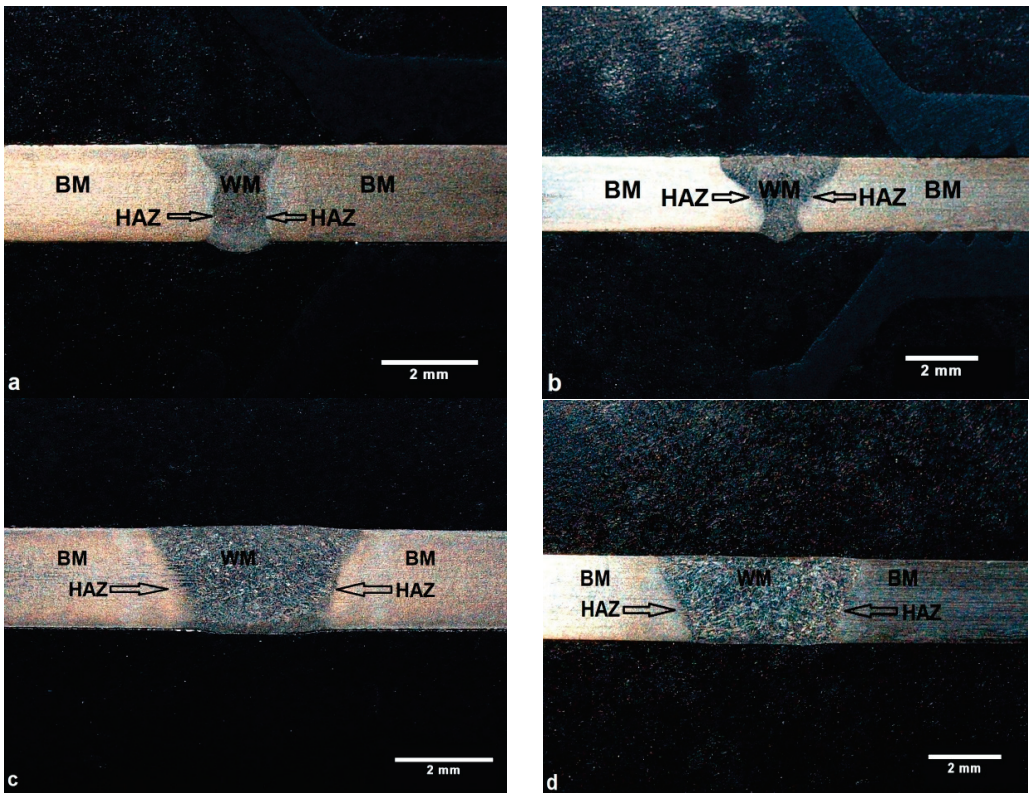

Figure 5. Cross-section of LB weld joints showing different welding regions: weld metal (WM), heat affected zone (HAZ), and base metal (BM) in the experimental samples: (**a**) Sample A, (**b**) Sample B, (**c**) Sample C, (**d**) Sample D.

The optical micrographs of the weld joints acquired at higher magnifications show the individual characteristic regions of the weld joints (BM, HAZ, and WM), as shown in Figure 6. The microstructure of the BM was duplex, with approximately equal volumes of

both ferrite and austenite phases. Grain boundaries were without the presence of secondary phases. The observed microstructure was typical for the solution annealed material state. The weld joints were characterized by narrow HAZs, and the width of the HAZs ranged between 10 and 50 μm (Figure 6). The material inside the HAZs manifested clear, evident growth of ferritic grains. This grain growth influenced the epitaxial growth of the columnar ferritic grains in the weld metal. The microstructure of the WM was formed by the ferritic matrix and the austenitic grains, which were at the columnar grain boundaries of the ferrite. Small austenitic grains of a regular geometric shape were observed inside the ferritic grains, too.

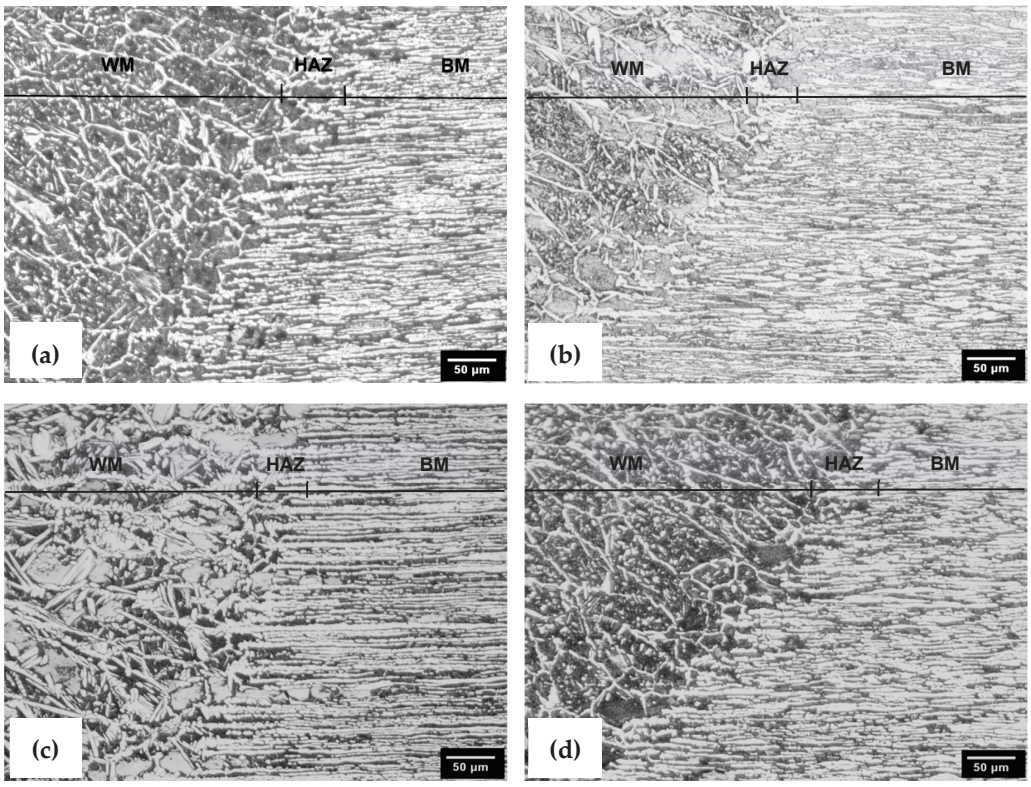

Figure 6. Microstructure of the LB experimental weld joints—WM, HAZ, and BM: (**a**) Sample A, (**b**) Sample B, (**c**) Sample C, (**d**) Sample D.

Figure 7 demonstrates the X-ray diffraction spectrum of the experimental steel (A—austenite and F—ferrite). Figure 8 shows TEM micrographs of the microstructures of the BM. The ferritic and austenitic grains are visible, and their grain boundaries and interiors are completely free from precipitates. The austenitic grains (Figure 8a) were almost completely free of lattice defects such as dislocations or twins. On the other hand, the ferritic grains in Figure 8b manifested a certain dislocation density. No precipitates were found in the material. One can thus summarize that the material state in Figure 8 corresponds well to near-equilibrium, which can be obtained by solution annealing, for instance. In other words, the TEM observations confirmed the results of the light microscopy examinations, as Figure 6 illustrates.

The WM microstructure consists of ferrite grains that are oriented parallel to the heat flux during welding. A network of austenite at the ferritic grain boundaries is well-visible on the micrographs. The characteristic EDS spectrum of austenite and ferrite is shown in Figure 9. Also, intragranular austenite or Widmanstätten austenite was formed in the form of needles (Figure 10).

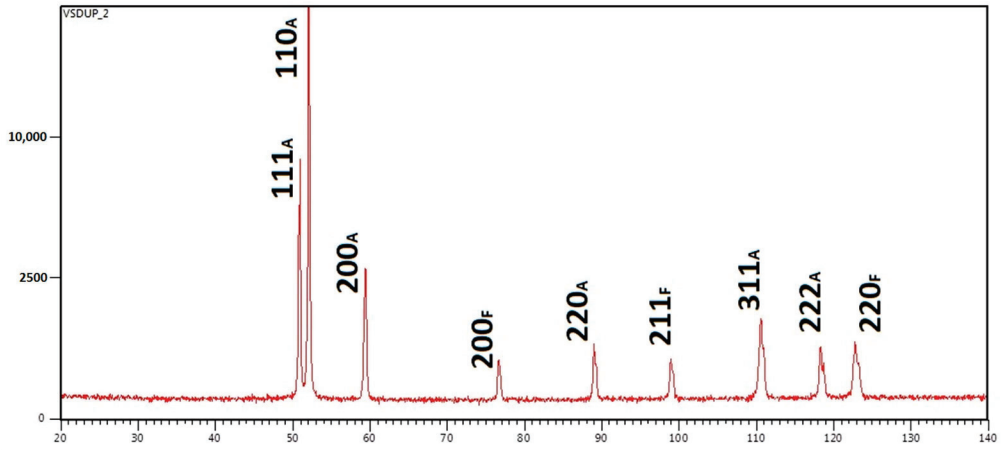

Figure 7. X-ray diffraction spectrum of the experimental steel (A—austenite and F—ferrite).

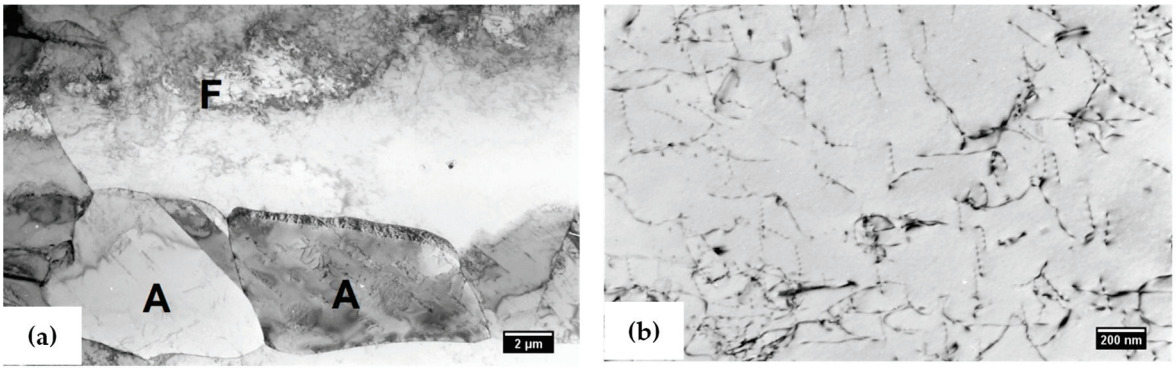

Figure 8. TEM image of BM: (**a**) details of polyhedral austenitic (A) and ferritic (F) grains, (**b**) details of dislocations inside the ferritic grain.

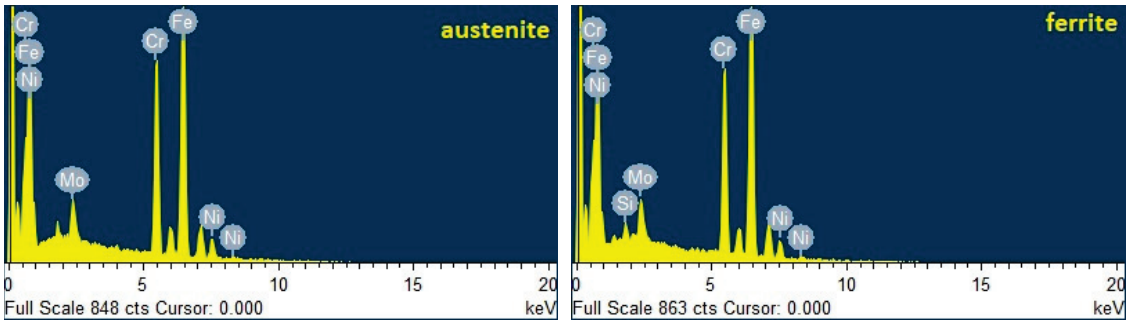

Figure 9. The EDS spectrum of austenite and ferrite measured in the weld metal region of Sample C.

The main object of the SEM analysis was to determine the volume fraction of austenite in the WM. Table 5 summarizes the austenite volume fraction in the weld metal of differently welded specimens. The samples made using the oscillating movement of the laser head were the ones with acceptable values of the volume fraction of austenite, in the range of 40–50%. Through the use of the oscillating motion of the laser head, we can achieve a suitable volume fraction of austenite. We reached this in Samples C and D. The increased heat input followed by slower cooling of the weld metal was due to the positive effect on the ferrite transformation to austenite.

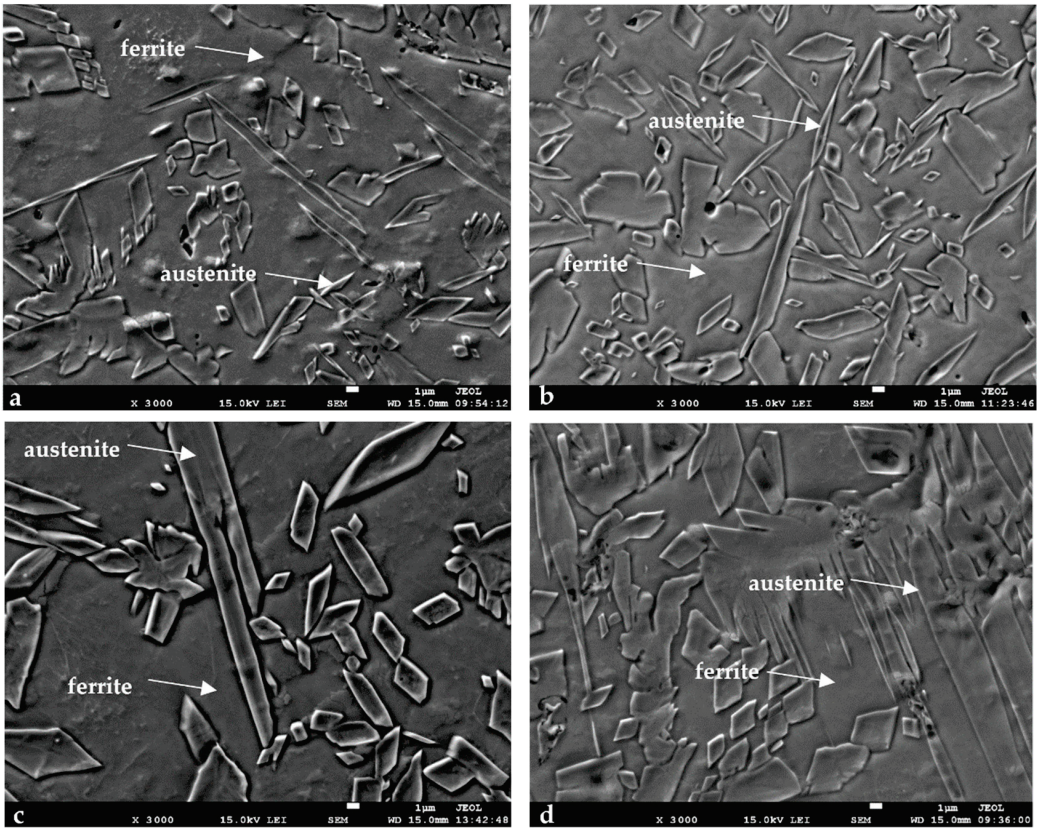

Figure 10. SEM micrographs showing the microstructure of the welded joints: (**a**) Sample A, (**b**) Sample B, (**c**) Sample C, (**d**) Sample D.

Table 5. Austenite volume fraction in the weld metal.

Sample	Fraction (vol. %)	Heat Input (J/mm)
A	28.6 ± 3.5	72
B	42.0 ± 2.8	99
C	53.5 ± 4.7	90.9
D	43.3 ± 3.6	131.5

The characteristic EDS spectrum of austenite and ferrite is shown in Figure 9. Table 6 summarizes the results of the statistical measurement of the chemical composition of the austenitic and ferritic regions in the EDS weld metal. At least 20 measurements were taken from each characteristic area of the weld metal.

Table 6. Results of the chemical composition ferritic and austenitic areas in the weld metal (Sample C).

Measured Area	Chemical Composition (wt. %)				
	Si	Cr	Fe	Ni	Mo
Ferrite	0.5 ± 0.1	26.2 ± 0.5	60.1 ± 1.1	6.9 ± 0.4	6.4 ± 0.8
Austenite	0.6 ± 0.1	26.6 ± 0.5	60.7 ± 0.8	7.7 ± 0.5	4.4 ± 0.4

The TEM micrographs in Figure 11 clearly delineate the microstructural differences between the weld metal of the differently welded samples. The microstructure of the weld metal of Sample A was composed of ferritic grains (denoted as "F"), intergranular austenite (denoted "A"), and Widmanstätten austenite, Figure 11a and the needles of Widmanstätten austenite had a thickness between 200 and 500 nm. It is also shown that the austenite contained a very low dislocation density. On the other hand, a much higher dislocation

density is a typical feature of ferritic grains' microstructure, Figure 11b. In addition, the microstructure inside the ferritic grains manifested clear indications of early-stage precipitation, since very small coherent clusters/precipitates identified nearby dislocations. The size of the clusters was in the range from 50 to 400 nm. At this point, it should be noted that Sample B had a very similar microstructure. The microstructure shown in Figure 11c,d depicts the weld metal of Sample C. Coarser particles were observed in the ferritic matrix. The size of the precipitates was in the range of 250 to 1800 nm. These relatively coarser particles, also observed in Sample D, were identified by electron diffraction as M_2N nitride. The characteristic EDS spectrum of M_2N nitride is shown in Figure 12.

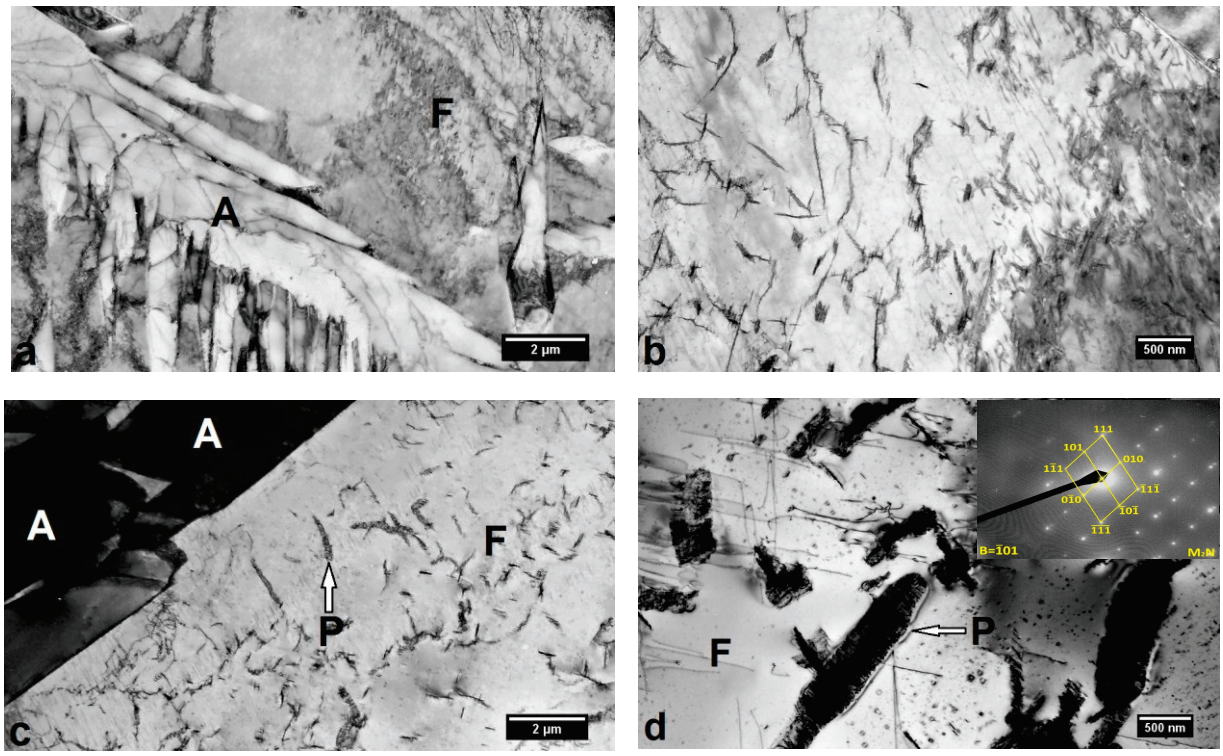

Figure 11. TEM micrographs showing details of the WM microstructure: (**a**) overview image of Sample A—austenite (A) at the ferritic grain boundary, (**b**) details of the ferritic (F) matrix—Sample A, (**c**) general view of the microstructure of Sample C—precipitates (P) inside the ferritic grain, (**d**) details of ferritic matrix with precipitates—Sample C.

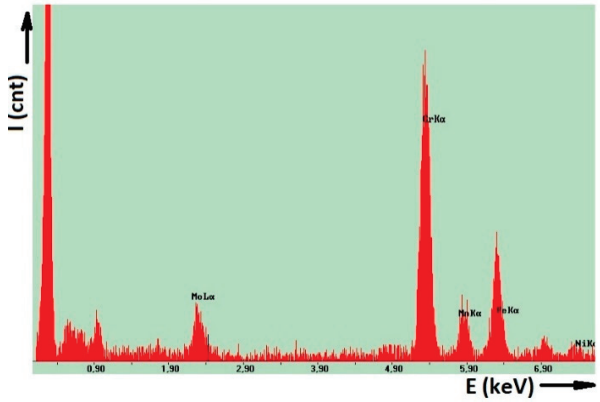

Figure 12. The characteristic EDS spectrum of M_2N nitride (analyzed using the TEM Philips 300CM and EDS Spectrometer, Oxford, UK).

3.2. Corrosion Test

The negative values can be seen from the results of the weight loss. These values present impurities on the samples after being tested from the environment or from the actual solution. The positive values present the corrosion loss, which was relatively small. None of the samples exceeded the critical value of the corrosion degree of 10 mdd. The test results indicate corrosion resistance in accordance with ASTM A 923-06 at the test temperature of 40 °C (104F).

The results of the ASTM A923-06 method C corrosion test are summarized in Table 7.

Table 7. Weight loss and degree weight loss of the samples after corrosion resistance test.

Sample	Weight of Sample (g)		Weight Loss (g)	Sample Area (dm^2)	Corrosion Degree (mdd)
	Prior to Test	After Test			
A	18.631	18.631	0	0.2894	0
B	19.585	19.585	0	0.2748	0
C	18.379	18.378	1	0.2774	3.6
D	17.115	17.116	−1	0.2644	−3.7

3.3. Hardness

Hardness measurements were carried out in the longitudinal direction on the cross-section of the weld joints. Figure 13 summarizes the results of the hardness measurements. According to the hardness trends, the values of hardness were about the same in all regions of the weld joints. The average hardness of the base metal was 259 ± 6 HV1. The average weld metal hardness (261 ± 10 HV1) was very similar to the base metal.

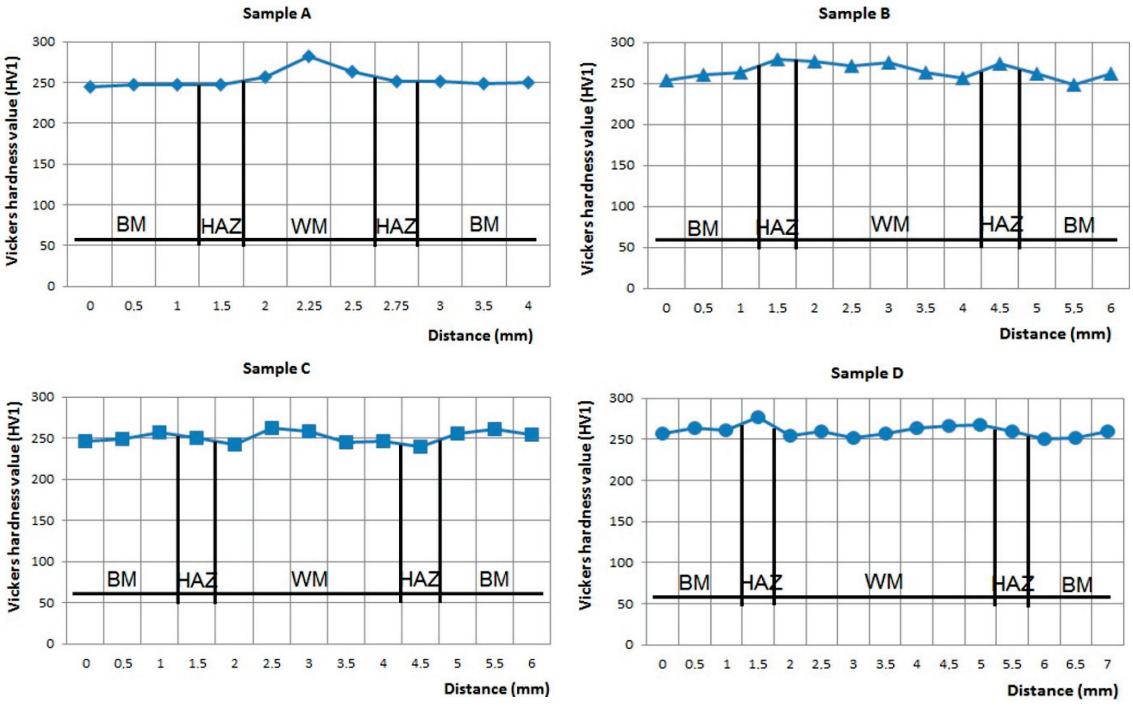

Figure 13. Hardness of weld joints in the longitudinal direction on the cross-section for (Samples (**A**–**D**)).

3.4. Tensile Test

The results of the tensile tests are summarized in Table 8. It is shown that Sample B manifests the best mechanical properties, i.e., the highest ultimate tensile strength at the highest ductility. Although the austenite content in this sample was not the highest, the values of ductility and the ultimate tensile strength were the highest of all the analyzed

samples. The lower value of the mechanical properties of Samples C and D as well as the area of quarry in the weld metal can be caused by the presence of needle precipitates inside the ferritic grains. The load-displacement diagram created during the tensile test is shown in Figure 14 for all samples.

Table 8. Values of tensile test of experimental steel weld joints.

Sample	Ductility (%)	Tensile Strength (MPa)	Area of Quarry
A	44.9	977.2	14 mm from the middle of the weld metal
B	48.5	978.9	18 mm from the middle of the weld metal
C	37.0	971.2	0.0 mm, quarry in the weld metal
D	31.5	954.4	0.0 mm, quarry in the weld metal

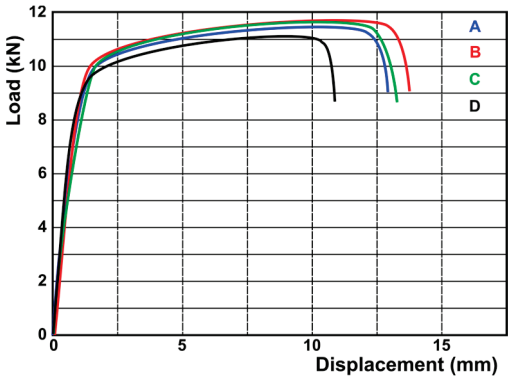

Figure 14. Shear strength test diagrams.

The SEM analysis of the fracture surface morphology showed the differences between the samples. In Figures 15 and 16 are shown SEM fractographs of the surfaces of the tensile test fracture obtained at room temperature. Equiaxed dimples of a rather uniform size were observed, which is expected in ductile rupture; this is typical for ruptures in the base metal (Figure 15a). The higher magnification view shows small dimples within dimples of a moderate size and very tiny voids in the membrane separating the dimples of moderate size (Figure 15b). There are almost no inclusions. A very similar fracture surface morphology was observed in the case of Sample B.

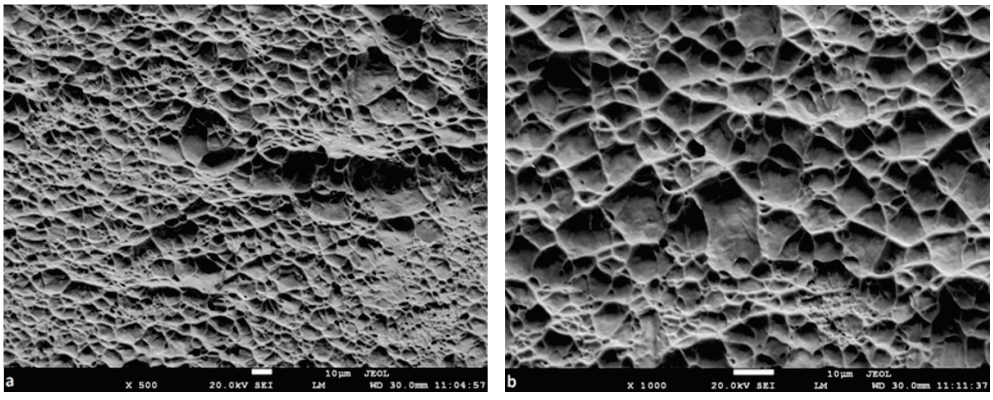

Figure 15. Fracture surface morphology of the base metal after tensile test, observed by SEM (Sample A), (**a**) ×500 magnification, (**b**) ×1000 magnification.

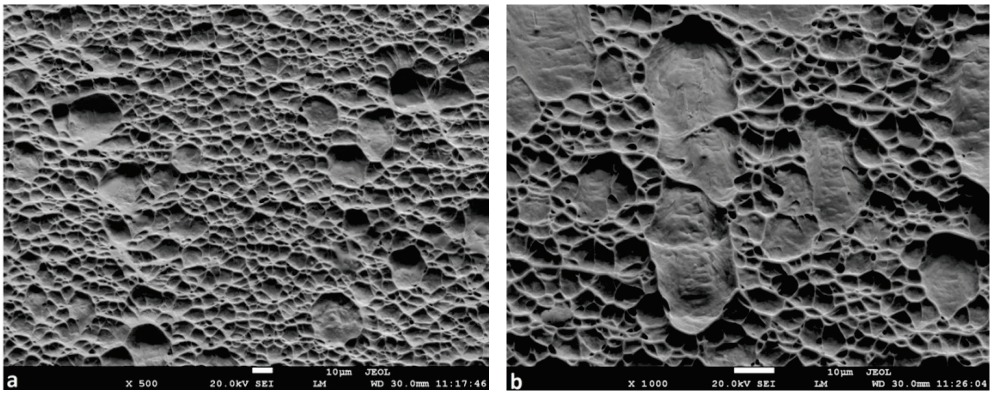

Figure 16. Fracture surface morphology of the weld metal after the tensile test, observed by SEM (Sample D), (**a**) ×500 magnification, (**b**) ×1000 magnification.

The SEM view image of the fracture surface of Sample D, Figure 16, shows a dimpled rupture in some regions. However, there is a certain number of cleavage facets present on the fractured surface, suggesting that the fracture propagated in a brittle manner in some sites. Figure 16b shows a higher-magnification SEM image of the area with the presence of a quasi-cleavage fracture. According to the size and shape of the area with quasi-cleavage morphology, we suppose that this kind of rupture took place in the ferritic grains. Also, one can suggest that the presence of a quasi-cleavage fracture could be attributed to needle-like precipitates inside the ferritic grains of the weld metal.

4. Discussion

After the process of laser beam welding, super-duplex stainless steel was subjected to material characterization. The influence of the changes in the welding process parameters (power, welding speed, focusing, head oscillation, shielding gas) on the consequent changes of the microstructure, phase composition, and mechanical and corrosion properties of the super-duplex stainless steel was investigated.

The weld metal observed exhibited different contents of austenite in the range of 28.6 to 53.5%. The highest content of austenite was found in Samples C and D. For these samples, the values of the heat input were 90.9 J/mm and 131.5 J/mm. One can expect a positive effect of head oscillation on achieving a higher heat input and austenite content in the weld metal. The cooling rates (solidification) of the weld metal are also important in the process itself, in order to achieve the desired structure. However, the detailed microstructure analysis by TEM showed the presence of big needle particles of M_2N nitride in the weld metal, which had a negative influence on the metal's mechanical properties—its ductility in particular.

Measurements of hardness did not reveal any significant differences in values for the base metal, heat affected zone, or weld metals. These differences were manifested during the tensile tests. The tensile strength and ductility of the analyzed samples differed: Samples C and D showed lower values of ductility than in the case of Samples A and B. This decrease in ductility can be caused by needle particles of nitride (M_2N), which were observed in the weld metal. SEM observations showed the influence of needle particles on their characteristics. The presence of quasicleavage fractures was observed in the ferritic matrix. An about 17% decrease in ductility was found in Sample D, where the biggest needle particles were observed. For Sample D, a shielding gas was used in combination with 90%N + 10%H. This can also result in a decrease in ductility in the weld metal. The results of the corrosion test did not indicate any significant differences in the analyzed samples. All samples were corrosion resistant. In our next work, we will be considering the use of ASTM A923-06 Method B for a more accurate assessment of corrosion resistance with regard to mechanical properties.

Evaluation of the material analysis results indicated that the laser beam welding process is a suitable technology for the fabrication of high-quality weld joints from super-duplex steel. The optimization of welding parameters is very important for the fabrication of weld joints with a suitable combination of mechanical and corrosion properties. We found that the best parameters for our experimental steel were as follows: 1100 W power, welding speed of 10 mm/s, focusing of 4 mm, and a pure nitrogen shielding gas (20 L/min). The weld joint prepared according to the above-mentioned parameters exhibited the best combination of mechanical and corrosion properties, a satisfactory microstructure, an acceptable austenite content, and only small coherent clusters in the ferritic matrix, without any degradation effect on its mechanical properties.

In following research works, the intention is to use a dual laser beam, where it will be possible to distribute the energy of the beam and thus influence the cooling rate of the weld metal. A positive effect in the formation of the ferrite and austenite phases is assumed.

5. Conclusions

In this study, experiments in Laser Beam Welding were conducted on super duplex steel DSS2507 sheets using a diverse range of welding parameters. The effects of these parameters on textural changes were investigated, focusing on the penetration depth of the welded joints, the width of the fusion zone (FZ), and the width of the heat-affected zone (HAZ). The microstructural changes in the base material (BS), FZ, and HAZ were characterized using light microscopy, scanning electron microscopy, and transmission electron microscopy. The resulting microstructures, along with properties such as the corrosion resistance, hardness, ultimate tensile strength, ductility, and corrosion behavior, were thoroughly evaluated. The findings from the tensile strength tests were correlated with the analysis of the fracture surface morphology of the tested specimens. The following conclusions can be drawn:

- The weld metal observed exhibited different content of austenite in the range of 28.6 to 53.5%. The highest content of austenite was found in Samples C—90.9 J/mm and D—131.5 J/mm. We can expect a positive effect of head oscillation on achieving a higher heat input and austenite content in the weld metal. The cooling rates of the weld metal are also important in the welding process.
- The detailed microstructure analysis by TEM showed the presence of the big needle particles of M_2N nitride in the weld metal. It had a negative influence on its mechanical properties, ductility in particular.
- The hardness measurements did not reveal any significant differences of values in the base metal, heat affected zone, or weld metals. All samples were corrosion resistant.
- Differences were manifested during the tensile tests. Samples C and D showed lower values of ductility. This decrease in ductility can be caused by needle particles of nitride (M_2N) in the weld metal. For Sample D, a shielding gas was used in combination with 90%N + 10%H. This can also result in a decrease in ductility in the weld metal of about 17%.
- From the experimental analysis, the results indicate that the laser beam welding process is a suitable technology for the fabrication of high-quality weld joints from superduplex steel. The optimization of welding parameters can be used to fabricate weld joints with a suitable combination of mechanical and corrosion properties.

Author Contributions: Conceptualization, B.Š. and M.D.; methodology, B.Š., M.D. and P.K.; software, M.Š., M.M. and M.D.; validation, P.K., I.K. and L.C.; formal analysis, B.Š., I.K., M.M. and L.C.; investigation, B.Š., M.D. and M.Š.; resources, B.Š., M.D., I.K., P.K., M.M. and M.Š.; data curation, P.K., M.Š. and L.C.; writing—original draft preparation, B.Š., M.D., I.K., P.K., M.M., M.Š. and L.C.; writing—review and editing, B.Š., M.D. and P.K.; visualization, I.K., M.Š. and L.C.; supervision, M.M. and P.K.; project administration, B.Š., P.K. and M.Š.; funding acquisition, B.Š. and P.K. All authors have read and agreed to the published version of the manuscript.

Funding: The research was carried out under the support of the Slovak Research and Development Agency under the contract APVV-21-0232, under the name "Investigation of the dual laser beam energy distribution on the microstructure and properties of duplex steels welded joints".

Data Availability Statement: Data are contained within the article.

Acknowledgments: I would like to take this opportunity to thank Peter Jurči, and Martin Sahul for their valuable advice.

Conflicts of Interest: Authors Michal Šimek and Luke Ciuła were employed by First Welding Company, Inc. and LMC Construction, Inc. The remaining authors declare that the research was conducted in the absence of any commercial or financial relationships that could be construed as a potential conflict of interest.

References

1. Zhang, Z.; Jing, H.; Xu, L.; Han, Y.; Zhao, L. Investigation on microstructure evolution and properties of duplex stainless steel joint multi-pass welded by using different methods. *Mater. Des.* **2016**, *109*, 670–685. [CrossRef]
2. Ramkumar, K.D.; Thiruvengatam, G.; Sudharsan, S.P.; Mishra, D.; Arivazhagan, N.; Sridhar, R. Characterization of weld strength and impact toughness in the multi-pass welding of super-duplex stainless steel UNS 32750. *Mater. Des.* **2014**, *60*, 125–135. [CrossRef]
3. Zhang, Z.; Jing, H.; Xu, L.; Han, Y.; Zhao, L.; Zhang, J. Influence of microstructure and elemental partitioning on pitting corrosion resistance of duplex stainless steel welding joints. *Appl. Surf. Sci.* **2016**, *394*, 297–314. [CrossRef]
4. Badji, R.; Bouabdallah, M.; Bacroix, B.; Kahloun, C.; Belkessa, B.; Maza, H. Phase transformation and mechanical behavior in annealed 2205 duplex stainless steels welds. *Mater. Charact.* **2008**, *59*, 447–453. [CrossRef]
5. Wang, S.; Ma, Q.; Li, Y. Characterization of microstructure, mechanical properties and corrosion resistance of dissimilar welded joint between 2205 duplex stainless steel and 16MnR. *Mater. Des.* **2011**, *32*, 831–837. [CrossRef]
6. García-Rentería, M.A.; López-Morelos, V.H.; García-Hernández, R.; Dzib-Pérez, L.; García-Ochoa, E.M.; González-Sánchez, J. Improvement of localised corrosion resistance of AISI 2205 Duplex Stainless Steel joints made by gas metal arc welding under electromagnetic interaction of low intensity. *Appl. Surf. Sci.* **2014**, *321*, 252–260. [CrossRef]
7. Kim, H.J.; Jeon, S.H.; Kim, S.T.; Lee, I.S.; Park, Y.S.; Kim, K.T.; Kim, Y.S. Investigation of the sensitization and intergranular corrosion of tube-to-tubesheet welds of hyper duplex stainless steel using an electrochemical reactivation method. *Corros. Sci.* **2014**, *87*, 60–70. [CrossRef]
8. Wang, S.H.; Chiu, P.K.; Yang, J.R.; Fang, J. Gamma phase transformation in pulsed GTAW weld metal of duplex stainless steel. *Mater. Sci. Eng.* **2006**, *A420*, 26–33. [CrossRef]
9. Garzón, C.M.; Ramirez, A.J. Growth kinetics of secondary austenite in the welding microstructure of a UNS S32304 duplex stainless steel. *Acta Mater.* **2006**, *54*, 3321–3331. [CrossRef]
10. Kang, D.H.; Lee, H.W. Study of the correlation between pitting corrosion and the component ratio of the dual phase in duplex stainless steel welds. *Corros. Sci.* **2013**, *74*, 396–407. [CrossRef]
11. Lai, R.; Cai, Y.; Wu, Y.; Li, F.; Hua, X. Influence of absorbed nitrogen on microstructure and corrosion resistance of 2205 duplex stainless steel joint processed by fiber laser welding. *J. Mater. Process. Technol.* **2016**, *231*, 397–405. [CrossRef]
12. Zhang, L.; Jiang, Y.; Deng, B.; Zhang, W.; Xu, J.; Li, J. Effect of aging on the corrosion resistance of 2101 lean duplex stainless steel. *Mater. Charact.* **2009**, *60*, 1522–1528. [CrossRef]
13. Zhang, Z.; Jing, H.; Xu, L.; Han, T.; Zhao, L. Effects of nitrogen in shielding gas on microstructure evolution and localized corrosion behaviour of duplex stainless steel welding joint. *Appl. Surf. Sci.* **2017**, *404*, 110–128. [CrossRef]
14. Herrera, C.; de Lima, N.B.; Kliauga, A.M.; Padilha, A.F. Microstructure and texture of duplex stainless steel after melt-spinning processing. *Mater. Charact.* **2008**, *59*, 79–83. [CrossRef]
15. Pekarinen, J.; Kujanpää, V. The effects of laser welding parameters on the microstructure of ferritic and duplex stainless steels welds. *Phys. Procedia* **2010**, *5*, 517–523. [CrossRef]
16. Sivakura, G.; Saravanan, S.; Raghukandan, K. Investigation of microstructure and mechanical properties of Nd:YAG laser welded lean duplex stainless steel joints. *Optik* **2017**, *131*, 1–10. [CrossRef]
17. Verma, J.; Taiwade, R.V. Effect of welding processes and conditions on the microstructure, mechanical properties and corrosion resistance of duplex stainless steel weldments—A review. *J. Manuf. Process.* **2017**, *25*, 134–152. [CrossRef]
18. Knyazeva, M.; Pohl, M. Duplex Steels. Part II: Carbides and Nitrides. *Metallogr. Microstruct. Anal.* **2013**, *2*, 343–351. [CrossRef]
19. Salgado, J.R.; Aquilar, M.A.D.; Domínguez, B.C.; Hernández, P.H.; Newman, R.C. Detection of secondary phases in duplex stainless steel by magnetic force microscopy and scanning Kelvin probe force microscopy. *Mater. Charact.* **2013**, *86*, 250–262. [CrossRef]
20. Miranda, M.A.R.; Sasaki, J.M.; Tavares, S.S.M.; de Abrew, H.F.G.; Neto, J.M. The use of X-ray diffraction, microscopy and magnetic measurement for analysis microstructural features of a duplex stainless steel. *Mater. Charact.* **2005**, *54*, 387–393. [CrossRef]
21. Du, J.K.; Wang, C.H.; Wang, K.C.; Chen, K.K. TEM analysis of 2205 duplex stainless steel to determine orientation relationship between M23C6 carbide and austenitic matrix at 950 °C. *Intermetalics* **2014**, *45*, 80–83. [CrossRef]

22. Fang, X.; Yin, W.; Qin, C.; Wang, W.; Lo, K.H.; Shek, C.H. The interface character distribution of cold-rolled and annealed duplex stainless steel. *Mater. Charact.* **2016**, *118*, 397–404. [CrossRef]
23. Silva, R.; Baroni, L.F.S.; Silva, M.B.R.; Afonso, C.R.M.; Kuri, S.E.; Rovere, C.A.D. Effect of thermal aging at 475 °C on properties of lean duplex stainless steel 2101. *Mater. Charact.* **2016**, *114*, 211–217. [CrossRef]
24. Llorca-Isern, N.; López-Lugue, H.; López-Jiménez, I.; Biezma, M.V. Identification of sigma and chi phases in duplex stainless steels. *Mater. Charact.* **2016**, *112*, 20–29. [CrossRef]
25. Badji, R.; Bouabdallah, M.; Bacroix, B.; Kahloun, C.; Bettahar, K.; Kherrouba, N. Effects of solution treatment temperature on the precipitation kinetics of σ-phase in 2205 duplex stainless steel welds. *Mater. Sci. Eng. A* **2008**, *496*, 447–454. [CrossRef]
26. Lakshminarayana, P.V.S.; Gautam, J.P.; Mastanaiah, P.; Reddy, G.M.; Bhanu Sankara Rao, K. Laser Beam Welding of Advanced High-Strength Steels (Dual Phase Steels). In *Recent Advances in Manufacturing, Automation, Design and Energy Technologies*; Lecture Notes in Mechanical Engineering; Natarajan, S.K., Prakash, R., Sankaranarayanasamy, K., Eds.; Springer: Singapore, 2022. [CrossRef]
27. Marques, E.S.V.; Pereira, A.B.; Silva, F.J.G. Quality Assessment of Laser Welding Dual Phase Steels. *Metals* **2022**, *12*, 1253. [CrossRef]
28. Mansur, V.M.; Mansur, R.A.d.F.; de Carvalho, S.M.; de Siqueira, R.H.M.; de Lima, M.S.F. Effect of laser welding on microstructure and mechanical behaviour of dual phase 600 steel sheets. *Heliyon* **2021**, *7*, 12. [CrossRef]
29. Zhang, H.; Xu, J.; Hao, D.; Esmail, O.M.A.O. Microstructure and Mechanical Properties of Laser-Welded Joints between DP590 Dual-Phase Steel and 304 Stainless Steel with Preset Nickel Coating. *Materials* **2023**, *16*, 2774. [CrossRef]
30. Udayakumar, T.; Raja, K.; Abhijit, A.T.; Sathiya, P. Experimental investigation on mechanical and metallurgical properties of super duplex stainless steel joints using friction welding process. *J. Manuf. Process.* **2013**, *15*, 558–571. [CrossRef]
31. El Nayal, G.; Beech, J. Relationship between composition, impurity content, cooling rate and solidification in austenitic stainless steel. *Mater. Sci. Technol.* **1986**, *2*, 603–610. [CrossRef]
32. Quintino, L.; Costa, A.; Miranda, R.; Yapp, D.; Kumar, V.; Kong, C.J. Welding with high power fiber lasers—A preliminary study. *Mater. Des.* **2007**, *28*, 1231–1237. [CrossRef]
33. Beyer, E. *Fiber Laser Welding*; Industrial Laser Solutions: Hallam, Australia, 2006; pp. 13–14.
34. Elmer, J.W.; Allen, S.M.; Eagar, T.W. Microstructural development during solidification of stainless steel alloys. *Metall. Trans. A* **1989**, *20A*, 2117–2131. [CrossRef]
35. Steen, W.M. *Laser Material Processing*; Springer: London, UK, 2003. [CrossRef]
36. Ion, J.C. *Laser Processing of Engineering Materials*; Elsevier: Oxford, UK, 2005.
37. Varbai, B.; Bolyhos, P.; Kemény, D.M.; Májlinger, K. Microstructure and corrosion properties of austenitic and duplex stainless steel dissimilar joints. *Period. Polytech. Mech. Eng.* **2022**, *66*, 344–349. [CrossRef]
38. He, H.; Forouzan, F.; Volpp, J.; Robertson, S.; Vuorinen, E. Microstructure and Mechanical Properties of Laser-Welded DP Steels Used in the Automotive Industry. *Materials* **2021**, *14*, 456. [CrossRef]
39. Sisodia, R.P.S.; Gáspár, M. Investigation of Metallurgical and Mechanical Properties of Laser Beam Welded and Post-weld Heat Treated DP1400 Steel. *J. Mater. Eng. Perform.* **2021**, *30*, 1703–1710. [CrossRef]
40. Svenungsson, J.; Choquet, I.; Kaplan, A.F.H. Laser Welding Process—A Review of Keyhole Welding Modelling. *Phys. Procedia* **2015**, *78*, 182–191. [CrossRef]
41. ASTM A 923–06 Standard Test Methods for Detecting Detrimental Intermetallic Phase in Duplex Austenitic/Ferritic Stainless Steels. Available online: https://www.astm.org/a0923-22.html (accessed on 2 June 2023).

metals

MDPI

Article

Investigation of Properties in Magnesium Alloy Thin Plates after Die Casting Processes

Jun-Tae Han †, Choong-Mo Ryu † and Seung-Jae Moon *

Department of Mechanical Convergence Engineering, Hanyang University, Seoul 04763, Republic of Korea; yggoggo@naver.com (J.-T.H.); chmo92@hanyang.ac.kr (C.-M.R.)
* Correspondence: smoon@hanyang.ac.kr
† These authors contributed equally to this work.

Abstract: This study systematically analyzed the effect of design conditions on filling behavior and product characteristics when forming thin plates of magnesium alloy (AZ91D) of 0.5 mm or less using the die casting method. As a research method, a casting analysis simulation program was used to predict filling and solidification behavior under various process conditions. The molten metal injection temperature (610~670 °C), mold temperature (160~220 °C), and cooling water temperature (10~55 °C) were selected as key variables, and an analysis was performed for a total of five conditions. A simulation was conducted to analyze the charging speed distribution, location of oxides and bubbles, and solidification pattern. As a result of the study, the flow of molten metal in the low and high-speed sections of the plunger, uniformity of product thickness, and supply conditions of the molten metal were confirmed to be major factors. It is important to manage the molten metal injection temperature at an appropriate level to minimize product defects. Based on these conditions, a prototype was manufactured, the microstructure was observed, and a fine and uniform grain structure was observed in most areas. In mechanical property evaluation, superior physical properties were secured compared to existing bulk materials.

Keywords: die casting; magnesium alloy; thin plate

1. Introduction

Recently, as environmental regulations have strengthened and demands for improved energy efficiency, lightweight materials in transportation equipment, and miniaturization have increased. Accordingly, the demand for aluminum and magnesium alloys, which are lightweight materials, is greatly expanding. Magnesium alloys have the lowest density among practical metals but exhibit excellent specific strength, as shown in Table 1, and are attracting attention as next-generation lightweight structural materials [1–5].

Table 1. Comparison of properties of die casting alloys (Mg, Al, Zn).

Element	Strength (MPa)	Density (kg/m^3)	Specific Strength (MPa m/kg)
Mg	250	1.81	138
Al	315	2.7	2.7
Zn	221	6.6	33

Die casting is a process suitable for mass production of products with complex shapes. As one of the main manufacturing processes for magnesium alloys, it is widely used in the manufacturing of precision products such as automobile parts and electronic parts. Recently, attempts have been made to achieve both weight reduction and thinning by forming magnesium alloys through the die casting process [6–8]. However, magnesium alloy is known to have many difficulties when casting thin plates due to its low fluidity and high reactivity. In particular, to obtain thin plate products of 0.5 mm or less, securing uniformity

of molten metal flow and controlling solidification defects are of utmost importance. To achieve this, in addition to optimizing alloy composition and process conditions, systematic analysis of various process factors such as mold and flow rate design, casting speed, molten metal, and mold temperature, and gas emissions is required.

Because about 85% of defects that occur in the die casting process are caused by the flow of molten metal, controlling the charging behavior of molten metal is of the utmost importance. The shape and arrangement of the gate and overflow, as well as the design of the cooling channel, are key factors that determine the charging behavior and solidification pattern of the molten metal in the product [9–13]. Recently, with the development of CAE (computer-aided engineering) technology, it has become possible to predict and optimize the effects of these design variables in advance using casting simulation [14–18].

Ma et al. characterized the microstructure of castings produced through high-pressure die casting using various parameters. The process was predicted through charging process simulation and compared with the actual produced sample [19]. Chang et al. conducted a casting simulation of magnesium alloy based on integrated computational materials engineering. The low-pressure casting optimization process of magnesium alloy thin-walled cylindrical parts was studied [20]. Li et al. optimized the die casting process parameters through numerical simulation of the magnesium die casting filling process. The optimized mold structure and process parameters were verified through die casting experiments. The productivity of magnesium alloy castings was improved [21].

This study aims to optimize mold design for manufacturing 0.5 mm thin plate die-casting products of magnesium alloy AZ91D. For this purpose, the following detailed goals were set. We designed the optimal gate system, overflow, air vent, and cooling system for sheet metal forming. Using a casting analysis program, we analyzed sheet metal filling and solidification behavior according to major design variables such as spout, overflow, and cooling channel. Based on the analysis results, an optimal design was derived and applied to produce a thin plate prototype of AZ91D alloy with a thickness of 0.5 mm. By evaluating the microstructure and mechanical properties of the manufactured prototype, changes in material properties according to design conditions were studied, and an optimal design plan for sheet metal forming was presented. Through this study, it is expected that the mold design technology for thin-walled magnesium die casting manufacturing and measures to reduce defects that may occur in the process can be put to practical use. Additionally, research processes linking experimentation and analysis can be applied to the optimization of other lightweight materials and precision casting processes.

2. Theoretical Background

2.1. Features of the Die Casting Process

Die casting is a process that mass-produces castings of complex shapes by injecting molten metal into a mold at high pressure. During molding, the time it takes to fill the cavity within the mold with molten metal is very short (0.01~0.1 s), and the solidification speed is fast (30~100 °C/s). A product with a dense structure and excellent mechanical strength can be obtained. In addition, thin products and complex shapes can be formed relatively easily, making it suitable for producing products that require high productivity and precision. It is applied to various fields such as automobiles, electronic products, and household goods, and die casting production of aluminum and magnesium alloys continues to increase due to increasing demand for lightweight materials.

The die casting process is largely divided into hot-chamber and cold-chamber methods. The hot-chamber method has high productivity because the injection cylinder is immersed in the molten metal and molten metal is supplied continuously. On the other hand, the cold-chamber method is a method of supplying molten metal into a mold with a ladle and is suitable for producing high-melting-point alloys or large products. The core mechanism of the die casting process is schematized in Figure 1.

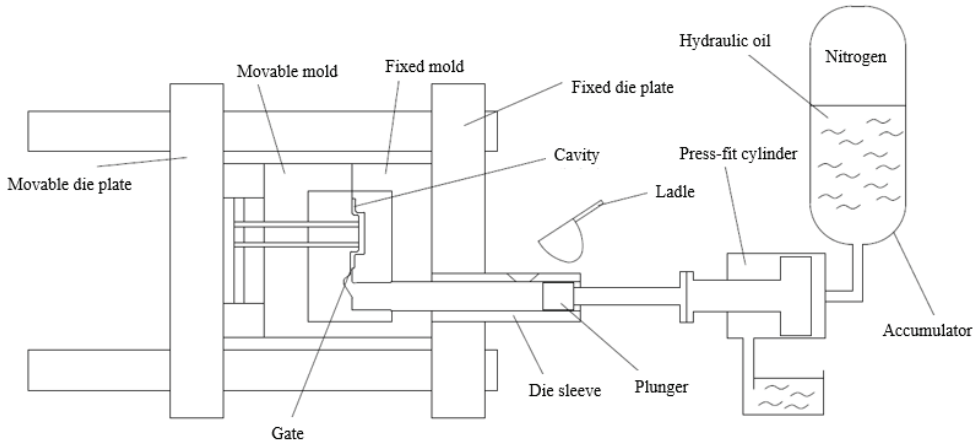

Figure 1. Cold chamber die casting machine.

A typical die casting process consists of low- and high-speed filling, pressure solidification, and ejection steps. In the low-speed stage, the air in the sleeve is discharged by the plunger advancement, and after the high-speed stage, the molten metal passes through the gate and fills the cavity. Within the cavity, the molten metal is cooled and solidified. During solidification, shrinkage is compensated through pressurization, and after final solidification, the mold is opened to extract the product. Plunger advancement is caused by the operation of the accumulator and is expressed in Equation (1), where E = power (kW), H = head (m), p = pressure (MPa), and Q = flow rate (m^2/s).

$$E = pqHQ = pQ \cdot 10^3 (\text{kW}) \tag{1}$$

In general, about 85% of quality problems in die casting parts are caused by the flow of molten metal, and the relationship between the pressure and flow rate of molten metal can be expressed by the following Equation (2). If the flow rate is expressed by the fluid continuity equation,

$$Q_a = Q_s = Q_p, \tag{2}$$

where, Q_a is the accumulator flow rate, Q_s is the hydraulic cylinder flow rate, and Q_p is the molten metal flow rate. Applying Bernoulli's theorem,

$$\frac{P_a}{\rho_a} + \frac{v_a^2}{2} = \frac{P_s}{\rho_s} + \frac{v_s^2}{2}, \tag{3}$$

where, P_a is the accumulator pressure, ρ_a is the fluid density of the accumulator, v_a is the accumulator flow rate, P_s is the hydraulic cylinder pressure, ρ_s is the hydraulic cylinder fluid density, and vs. is the hydraulic cylinder flow rate. If the flow coefficient C_a is applied under the conditions of Equations (2) and (3),

$$v_a = C_a \sqrt{\frac{2g(P_a - P_s)}{\rho_s}}, \tag{4}$$

where, C_a is the accumulator flow coefficient and g is the gravitational acceleration. By applying the continuity equation, the flow rate of the molten metal inside the plunger, v_p can be summarized as follows.

$$A_a v_a = A_p v_p, \tag{5}$$

$$v_p = \frac{A_a}{A_p} C_a \sqrt{\frac{2g(P_a - P_s)}{\rho_s}}, \tag{6}$$

where, A_a is the cross-sectional area of the accumulator and A_p is the cross-sectional area of the plunger. In this way, the flow of molten metal can be theoretically predicted using

Equation (6) above, but the flow of molten metal changes based on the shape of the cavity, the molten metal solidifies during filling, and heat exchange between the molten metal and the mold also occurs. In addition, it is difficult to calculate theoretically because the results vary due to pores caused by air mixing and segregation due to temperature gradients. However, recently, die casting process simulation using CAE technology has become common, which has significantly shortened the development period and cost by predicting the occurrence of defects in advance and optimizing process conditions.

2.2. Properties of Magnesium Alloys

Magnesium is the lightest material among the practically used metals and has excellent specific strength and castability. Because pure magnesium has low room-temperature strength and corrosion resistance, its practical application is limited. To overcome this, various alloys added with Al, Zn, Mn, etc. have been developed. The AZ91D alloy adopted in this study is a representative magnesium alloy for die casting containing 9% Al, 1% Zn, and 0.15% Mn, as shown in Table 2. Al increases strength and heat resistance by forming an intermetallic compound with Mg, and Zn contributes to strength improvement through solid solution strengthening. Mn forms a compound with Fe and plays a role in improving corrosion resistance. AZ91D alloy is easy to form into thin sections due to its excellent castability, and it has mechanical properties of 230 MPa in tensile strength and 3% elongation. In addition, the microstructure consists of an α-Mg matrix and a β-$Mg_{17}Al_{12}$ intermetallic compound, and the formation mechanism and distribution of these phases during the solidification process have a great influence on the final physical properties. The microstructure development process under equilibrium and non-equilibrium solidification conditions can be explained by referring to the phase diagram according to Al content.

Table 2. Types and chemical composition of alloys for die casting.

Element	AZ91D	ALDC12
Al	8.3~9.7	Bal.
Zn	0.35~1.0	1.0 or less
Mn	0.15 or higher	0.5 or less
Si	0.1 of less	9.6~12.0
Cu	0.03 or less	1.5~3.5
Ni	0.002 or less	0.5 or less
Fe	0.005 or less	0.9 or less
Mg	Bal.	0.3 or less
Sn	-	0.2 or less

2.3. Process Design Conditions for Sheet Metal Forming

To ensure the formability of thin plates in the die casting process, mold design and process optimization that can comprehensively control the flow, solidification behavior, and shrinkage defects of the molten metal are necessary. Through this, excellent quality can be maintained by uniform filling of the molten metal and control of solidification shrinkage. The most important design factors include the gate, overflow, air vent, and cooling channel.

2.3.1. Gate System Design

The gate is a passage through which molten metal flows into the mold, and it has a direct impact on product quality and productivity. Because securing the fluidity of the molten metal in a thin cavity is key in the case of thin plate products, a high gate speed (40 to 60 m/s) is required. The gate speed in the charging stage can be expressed as Equation (7), where A_p is plunger tip cross-sectional area, A_g is the gate area, v_i is the injection speed, and v_g is the gate speed.

$$v_g = v_i \frac{A_p}{A_g} \tag{7}$$

Here, the velocity times area is equal to the volumetric flow rate. When W_g is the cavity filling weight, t is the charging time, and ρ is the molten metal density, the charging time is Equation (8).

$$t = \frac{\rho}{Q_g} = \frac{W_g}{V \cdot v_g \cdot A_g} \quad (8)$$

If the gate speed is too high, mold erosion or oxide mixing may occur. The charging time must be set within an appropriate range.

2.3.2. Overflow and Air Vent Design

Overflow and air vent are very important elements in die casting mold design that play a role in minimizing casting defects through uniform filling of molten metal and discharge of air bubbles and oxides. In particular, optimal overflow and air vent design are essential when casting thin plates of materials with low fluidity and fast solidification speed, such as magnesium alloy. The overflow accommodates excess molten metal after cavity filling is completed and prevents defects due to solidification shrinkage. In the case of thin plate products, the overflow capacity relative to the product volume is around 20%. If the capacity is excessive, the coagulation time may be prolonged, and productivity may be reduced. The overflow capacity should be designed with the minimum capacity necessary to compensate for shrinkage. The thickness of the overflow should be 1.2 to 1.5 times the thickness of the product, but it is desirable to secure a minimum of 3 mm. The location of the overflow is determined at the final filling part to facilitate the flow of molten metal and promote the discharge of air bubbles. In the case of complex shapes, multiple overflows are distributed to prevent local stagnation of molten metal. At this time, it must be designed so that the molten metal arrives at the same time, considering the balance between each overflow. The direction of overflow should be perpendicular to the cavity, and, if necessary, tilted to facilitate discharge.

Air vents are used to suppress bubble defects by quickly discharging air and gases within the mold. During high-speed charging, high air pressure inside the cavity can interfere with the flow of molten metal. To effectively discharge air trapped in the cavity, the spacing, depth, and width of the air vent must be optimized. The spacing of air vents is usually less than 20 times the thickness of the product, but they are placed more densely in the final charging area. The depth should be at least 1/2 of the product thickness, and the width should be a uniform value of around 0.1 mm. The shape of the air vent is perpendicular to the filling direction and is tapered to prevent backflow of molten metal. In general, the taper angle is known to be in the range of 15 to 20°. A backflow prevention pin can be installed at the air vent entrance. Recently, there have been cases of improving exhaust efficiency by applying vacuum suction-type air vents. Because additional facility investment and process control are required in this study, cost-effectiveness must be carefully reviewed. For effective air vent design, preliminary flow analysis is essential. Through 3D charging simulation, the optimal solution can be efficiently derived by predicting the air pressure distribution according to the location and spacing of the air vent.

2.3.3. Cooling System Design

The cooling system is a key factor in controlling dimensional accuracy and mechanical properties by controlling shrinkage and residual stress during solidification. In the case of magnesium alloy thin plates, rapid cooling occurs due to their thin thickness. Therefore, uniform cooling control is of the utmost importance to prevent the occurrence of defects. To achieve this, optimal design of the cooling channel considering the shape and thickness distribution of the product must be preceded.

For thin plate products, it is recommended to place cooling pipes with a diameter of approximately 8 mm at 30 mm intervals. Considering heat transfer with the coolant, the distance from the product should be around 20 to 25 mm, but it should be placed somewhat further away from areas where shrinkage defects due to local overcooling are concerned. If

necessary, channels may be divided, or shutoff valves may be installed so that the cooling rate can be partially adjusted.

The temperature of the coolant is determined in the range of 20 to 30 °C, considering the difference from the preheating temperature of the mold. If the temperature is too low, caution is required, as deformation and stress may occur due to rapid cooling. Excessively high temperatures can reduce the cooling efficiency and increase the cycle time. The flow rate is generally 10 to 20 L/min depending on the channel diameter and product thickness. However, this is only a theoretical calculated value, and deviations are bound to occur in actual operating conditions. Feedback control through temperature monitoring is necessary.

Meanwhile, the design of the cooling channel can be theoretically calculated based on the heat capacity and shape of each product, mold material, etc. Cooling load (Q), heat transfer coefficient (h), cooling area (A), and mold–coolant temperature difference (ΔT) can be expressed as Equation (9).

$$Q = h \cdot A \cdot \Delta T. \quad (9)$$

The channel diameter and length that can satisfy this are calculated. However, not only is this a very cumbersome task, but errors also occur depending on assumptions. In recent years, design through filling and solidification analysis has become common, and through 3D heat flow analysis, the temperature distribution within the product can be predicted and the occurrence of local hot spots and cold spots can be identified in advance. Based on this, a plan must be devised to adjust the location and density of the cooling channel and apply auxiliary cooling means to the heat concentration area. In addition, to ensure cooling uniformity in multiple cavities with different shapes and thicknesses, there is a trend of considering balancing from the channel design stage.

The goal of cooling system design is to minimize residual stress and ensure dimensional stability through a uniform cooling rate. However, this is by no means an easy task, and it can only be achieved by complexly considering the effects of various factors such as material properties, product shape, and process conditions. The attitude of pursuing optimization through systematic analysis, data-based design, and continuous process monitoring and feedback is most important. This is an area that should be recognized and strengthened as a core technological competency, as it not only reduces defects, but also directly leads to cost reduction and quality competitiveness.

2.3.4. Casting Analysis Simulation

Because complex physical phenomena occur in a very short time in the die casting process, it is not easy to find optimal conditions through experimental approaches alone. Recently, the development of CAE technology has made it possible to simulate the die casting process, which can optimize process conditions and predict defects. Magma, Procast, and Anycasting are widely used as commercial casting analysis programs. These programs can link the charging and solidification processes of molten metal based on the finite element method (FEM) or finite difference method (FDM). It is possible to predict molten metal behavior according to key design variables such as gate, overflow, and air vent, and to visualize defect occurrence patterns.

Based on the theoretical background, we are implementing analysis simulation technology and can optimize cooling conditions to minimize temperature changes within the product by quantifying solidification time, temperature distribution, and shrinkage patterns. In addition, residual stress and distortion can be evaluated in advance, greatly reducing the time and cost required for mold modification. In addition, it is expected that casting defects can be fundamentally suppressed by identifying locations where temperature drop, or segregation occurs at the tip of the molten metal and reflecting this in the mold design.

Because the simulation results are only approximate solutions under assumed boundary conditions, comparison and verification with actual castings is essential. For highly accurate analysis, the construction of a basic database on the physical properties of molten

metal and mold materials, heat transfer conditions, and interface phenomena must be established in advance. In addition, the analysis model must be advanced through continuous feedback with experimental results that reflect the field conditions.

In this way, casting simulation technology can greatly contribute to overcoming existing empirical methods and accelerating process optimization. Its effectiveness is expected to be doubled in processes that require a high level of flow control, such as thin plate die casting. This can be a shortcut to stably produce high-quality products by establishing a design foundation through analysis and minimizing trial and error. However, interpretation itself should not be the goal, but should be thoroughly recognized and utilized as a tool forthe ultimate value of cost reduction and quality improvement.

3. Experiment Method

3.1. Optimizing Design Conditions through Simulation

In this study, we attempted to form 0.5 mm thin plate products using AZ91D material, one of the magnesium alloys for die casting. To minimize trial and error and derive the optimal mold design, analysis simulation was used, which enabled us to analyze filling and solidification behavior for various design variables and predict the possibility of casting defects. For the casting analysis simulation, Anycasting v6.9, a commercial program from Anycasting Software, was used to conduct the analysis.

3.1.1. Experimental Conditions and Variables

The magnesium alloy used in the simulation was AZ91D, and the phase diagram of the metal is shown in Figure 2. The liquidus and solidus temperatures were set at 595 °C and 470 °C, respectively.

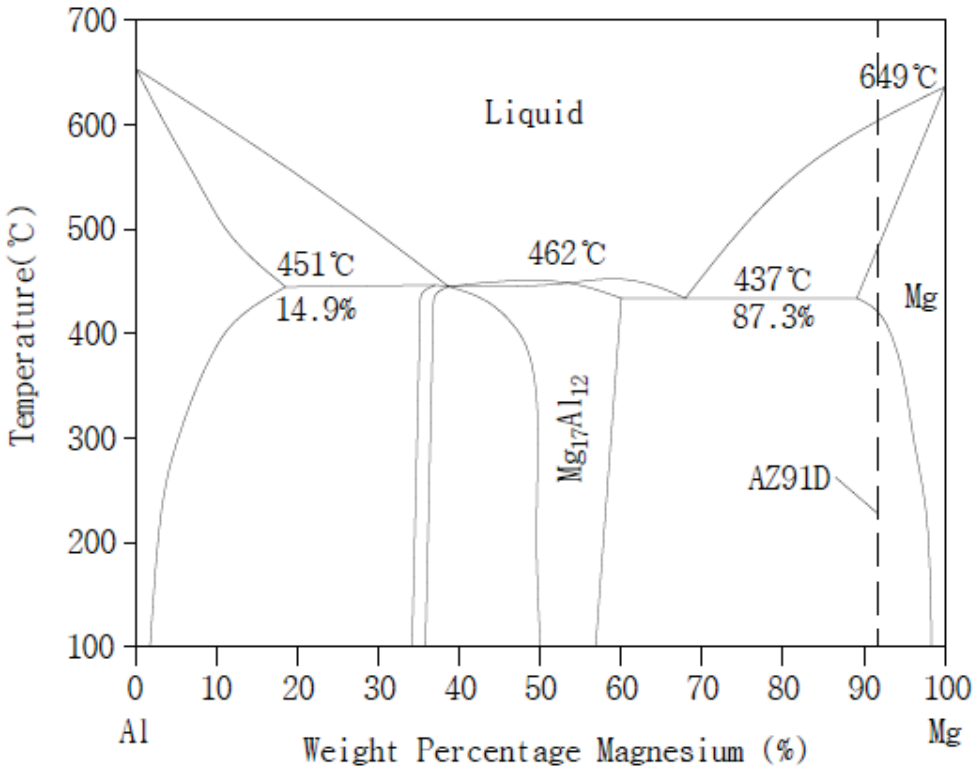

Figure 2. Mg-Al phase diagram.

The main experimental variables were molten metal injection temperature, mold temperature, and cooling water inlet and outlet temperatures, which are conditions that can be easily controlled on-site during actual product manufacturing. The experimental

conditions were shown in Table 3. In addition, the charging behavior of the molten metal was additionally observed by applying side and tunnel gates, respectively.

Table 3. Casting experimental conditions.

Sample	Molten Metal Injection Temperature (°C)	Mold Temperature (°C)	Coolant Temperature (°C)	
			Inlet	Outlet
CASE 1	640	190	25	40
CASE 2	670	220	25	40
CASE 3	610	160	25	40
CASE 4	670	190	10	40
CASE 5	610	190	40	55

The conditions of injection temperature has the following meaning. CASE 1 is a casting condition for die casting that generally uses magnesium alloy and was intended to be used as a standard by referring to the behavior shown in the simulation. CASE 2 and CASE 3 were set up to observe the difference in filling behavior at high and low temperatures, assuming changes in mold temperature according to changes in injection temperature. CASE 4 and CASE 5 changed the injection temperature but maintained the mold temperature by controlling the temperature of the coolant and were determined to compare the behavior according to the change in mold temperature due to the coolant.

In the gate method, a side gate was applied because it was impossible to change the structure by combining the cast product with its counterpart. Although there are limits to the area that can be selected depending on the shape of the casting, this experiment attempted to observe the charging behavior when the molten metal was charged at high speed by applying a tunnel gate to some sections.

3.1.2. Charging Behavior and Defect Prediction

Simulation was performed according to the above conditions, and the filling pattern of the molten metal and the location of occurrence of bubbles and shrinkage defects for each case were predicted. The physical properties of the AZ91D alloy used in the analysis were applied to the analysis using conditions considering changes in physical properties according to temperature, such as latent heat, density, and thermal conductivity, as shown in Table 4.

Table 4. Physical properties of AZ91D alloy.

Property	Unit	Temp. Condition (°C)	AZ91D Properties
Density	g/cm^3	20	1.81
Linear thermal experimental coefficient	μm/m·K	20–100	26
Specific heat of fusion	kJ/kg		370
Specific heat	kJ/kg·K	20	1.02
Thermal conductivity	W/K·m	20	51
Electrical conductivity	MS/m	20	6.6

The analysis model was constructed to include the product, runner, and overflow areas. The element network was divided into a total of 12.9 million elements by applying a hexahedral grid system. As a boundary condition, a temperature-dependent function was applied to the heat transfer coefficient between the mold and molten metal, and default settings were applied to radiation and convection heat transfer with the atmosphere.

We focused on predicting poor filling and pore defects, which can be vulnerable to thin plate shapes. For this purpose, the molten metal behavior was intensively analyzed in key areas such as areas around the gate and overflow, the corners of the product, and areas with fast cooling rates. Charging defects that may occur in the final charging stage and defects due to gas in the cavity were predicted. In addition, we attempted to optimize the

process conditions required for sheet metal forming by comparing solidification patterns, mold erosion, and oxide generation.

3.2. Prototype Production under Optimal Conditions

To facilitate the flow of molten metal, a gap was provided at the mold joint area such as the hole shape inside the product to minimize metal boundary defects. Burrs, overflows, gates, etc., were removed by trimming after casting production.

3.2.1. Materials and Equipment

An actual thin plate prototype was produced under optimal conditions selected based on the simulation results. The used material was AZ91D magnesium alloy ingot, and it was cast under the conditions of CASE 1. The die casting process used a cold-chamber-type 125-ton die casting machine, and a side gate was used as the gate. The gate into which the molten metal was injected is shown at location 1 in Figure 3.

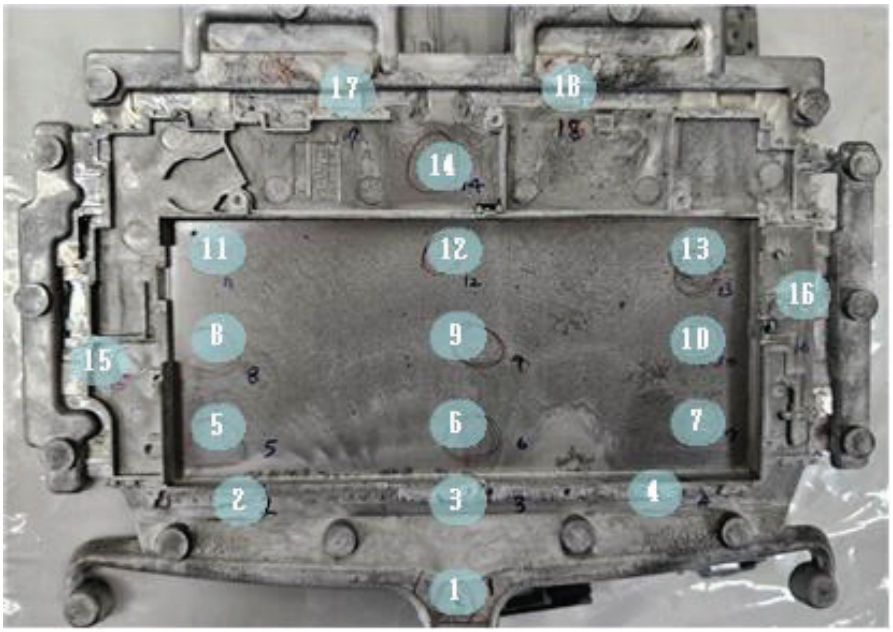

Figure 3. Microstructure observation positions (1–18) of the prototype.

3.2.2. Process Conditions

In the actual molding process, the temperature of the molten metal, mold temperature, cooling temperature, and flow rate were determined to be the same as the conditions of CASE 1 of the simulation. The melting furnace temperature was 680 °C to achieve an injection temperature of 640 °C. The casting speeds were 35 cm/s at low speed and 380 cm/s at high speed, and the low-speed section was set at 80 mm and the high-speed start section at 100 mm for a total sleeve length of 205 mm. The mold temperature controller value was fixed to 300 °C to maintain the mold temperature at 190 °C, and spraying was performed in stages of air 1 (0.3 s), release agent (0.2 s), air 2 (0.5 s), and air 3 (0.3 s). Under these conditions, multiple prototypes were manufactured, and various characteristics were evaluated. The tensile properties of 0.5 mm- thick specimens were evaluated using a universal material testing machine (SHIMADZU, Kyoto, Japan). A total of 6 specimens were manufactured, with 2 each at the left, right, and center positions centered on the thin part with a thickness of 0.5 mm. Measurements were taken twice at each location, and the average value was derived.

3.3. Evaluation of Prototype Properties

To evaluate the characteristics of the manufactured prototype, mechanical properties and microstructure were observed. By comparing the results analyzed through simulation, it was assessed whether there were actual defects within the expected range.

3.3.1. Microstructure Observation

The microstructure of the prototype was observed using an optical microscope Nikon TS100 (Nikon, Tokyo, Japan). For the observation location, the product was divided into certain sections as shown in Figure 4, and tissue photos were then taken for each area and the grain size and distribution of precipitates were compared and analyzed.

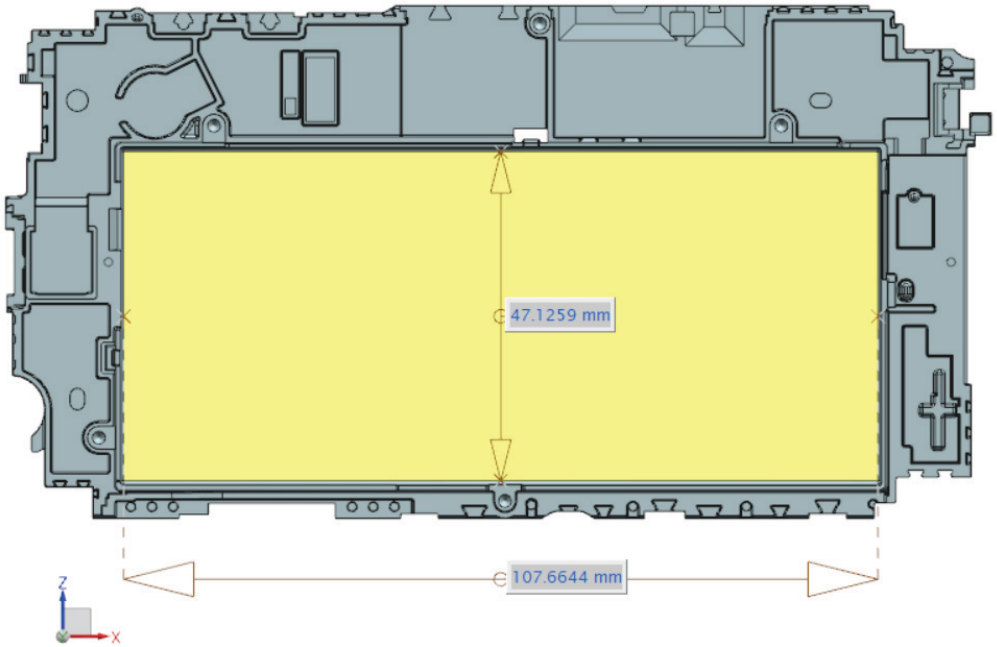

Figure 4. The location and dimensions of the 0.5 mm-thick, thin plate of the prototype.

3.3.2. Mechanical Property Measurement

Figure 4 shows the 0.5 mm-thick, thin plate part indicated in the drawing of the prototype. It was 107.66 mm in width and 47.13 mm in height. The prototype for which microstructure observation was completed, was used to measure the tensile strength and hardness. The tensile properties of 0.5 mm-thick specimens were evaluated using a universal testing machine and were performed under constant strain rate conditions at room temperature. The specimens were manufactured by sampling at the left (5, 8, 11), center (6, 9, 12), and right (7, 10, 13) locations centered on the thin-walled portion. Repeated measurements were taken at each location to derive the average value.

4. Results and Discussion

4.1. Simulation Analysis Results

To derive the optimal conditions for 0.5 mm thin plate products of AZ91D magnesium alloy, analytical simulation was used to analyze the filling and solidification behavior of molten metal according to casting conditions and to predict the occurrence of casting defects.

4.1.1. Changes in Charging Behavior Depending on Design Conditions

The charging behavior was analyzed by applying the casting temperature change previously determined in experimental conditions and variables to each condition. As shown in the simulation results of the CASE 1 (Figure 5a) condition, the color indicates

the charging time. The charging behavior spread rapidly from the center and bottom of the product, and a fast-filling rate was observed from the gate to the thin section. In addition, from the section after the thin-walled part, overall charging was uniform on the left and right sides. The rib portion in the front direction was shown to be charged late. This phenomenon appeared to be due to rapid charging of the molten metal and the molten metal on the bottom being charged first. After charging the thin part, the ribs, overflow, and chill vent were sequentially charged with molten metal. This shows the ideal charging state. The simulation results of CASE 2 (Figure 5b) shows similar charging to CASE 1 and because the conditions included a higher temperature than that in CASE 1, the charging time of the molten metal was reduced by about 1.8%. The simulation results of CASE 3 (Figure 5c) show that the charging behavior is like CASE 1, but the charging time increases by about 6.6% due to low-temperature molten metal charging compared to CASE 1. Additionally, the simulation results for CASE 4 (Figure 5d) show the same results as CASE 2. Likewise, it was confirmed that the simulation results of CASE 5 (Figure 5e) show the same results as CASE 3. As a result, based on an injection temperature of 640 °C and a mold temperature of 190 °C, under the conditions of 670 °C/220 °C in CASE 2, the overall charging speed increased due to increased molten metal fluidity and the charging time was shortened by about 1.8%. Under CASE 3 conditions of 610 °C/160 °C, the charging time tends to increase by about 6.6% along with a decrease in speed. This is believed due to changes in the viscosity of the alloy depending on the temperature. Meanwhile, in CASEs 4 and 5, where the coolant temperature was in the range of 10~40 °C and 40~55 °C, there was no significant change in charging speed. Through this, the initial temperature of the molten metal and mold had a dominant influence on the sheet filling behavior, and the contribution of the cooling rate was relatively small. Under low-temperature conditions below 610 °C, the risk of shrinkage defects would increase due to increased flow stagnation.

Figure 6 shows the results of a simulation by transforming the behavior of molten metal into particles to predict the turbulence phenomenon or flow of molten metal. When the side gate was applied, the molten metal showed normal charging behavior, while the tunnel gate showed that the molten metal was charged along the ribs in the front direction.

It was confirmed that the injection method and molten metal and mold temperature are important factors for molten metal filling in the die casting process.

4.1.2. Predicting Defect Occurrence Pattern

As a result of the simulation, the oxide distribution was as shown in Figure 7. It was generally concentrated in the overflow and chill vents, and it appears that oxides may have also been present in the ribs. As a result, it was confirmed that oxides were generated in the area where charging ended. More oxides were identified in CASE 3 (Figure 7c) and CASE 5 (Figure 7e). Due to the slowing of charging behavior due to the low injection temperature, the contact time between molten metal and air was prolonged, which is believed to have had a more dominant effect on oxide formation.

As a result of the simulation, the distribution of bubbles was generally expected in the overflow, runner, and gate, and the distribution and pressure of bubbles were found to be the lowest in CASE 1 (Figure 8a) casting conditions. In addition, the number of pores generated was high in the relatively low-temperature casting conditions of CASE 3 (Figure 8c) and CASE 5 (Figure 8e). This is believed to have been due to incomplete filling due to reduced fluidity and the resulting shrinkage defects. Porosity was evident near the edges of the product, and a local solidification delay was presumed to be the main cause.

Compared with CASE 1, the distribution of bubbles in CASE 2 (Figure 8b) casting conditions was similar in distribution and size, but the pressure of the bubbles was high. It appeared that the pressure increased as the mold temperature increased. In the casting conditions of CASE 4 (Figure 8d), the pressure of bubbles was lower than that of CASE 1, but the distribution of bubbles was found to be large. This phenomenon is believed to be caused by shrinkage defects as the mold temperature decreased.

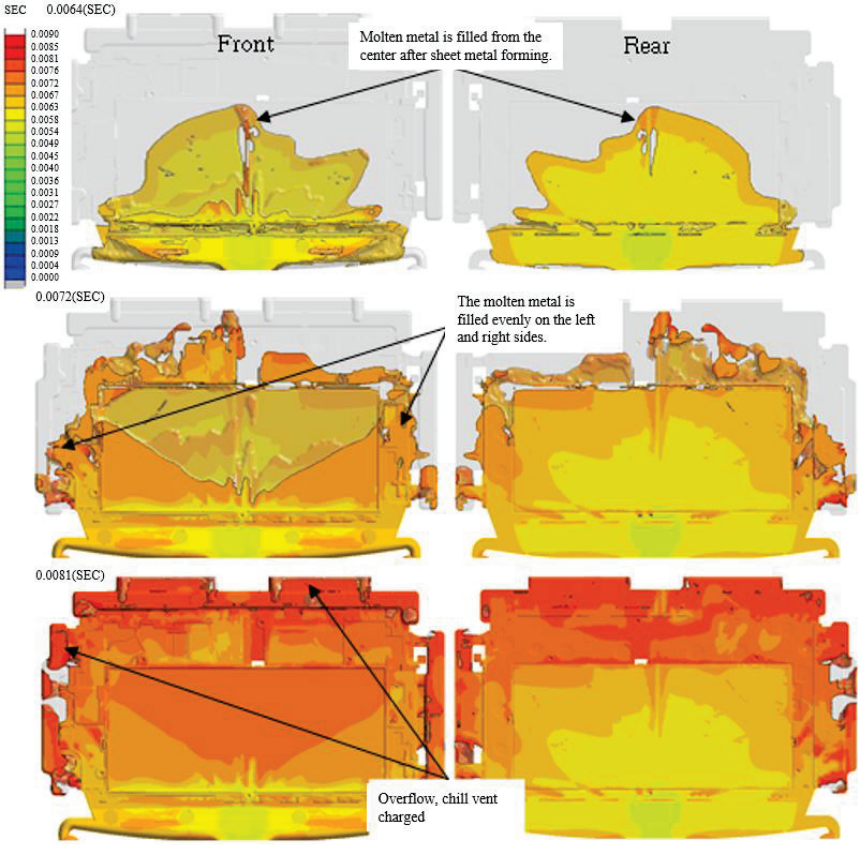

(**a**)

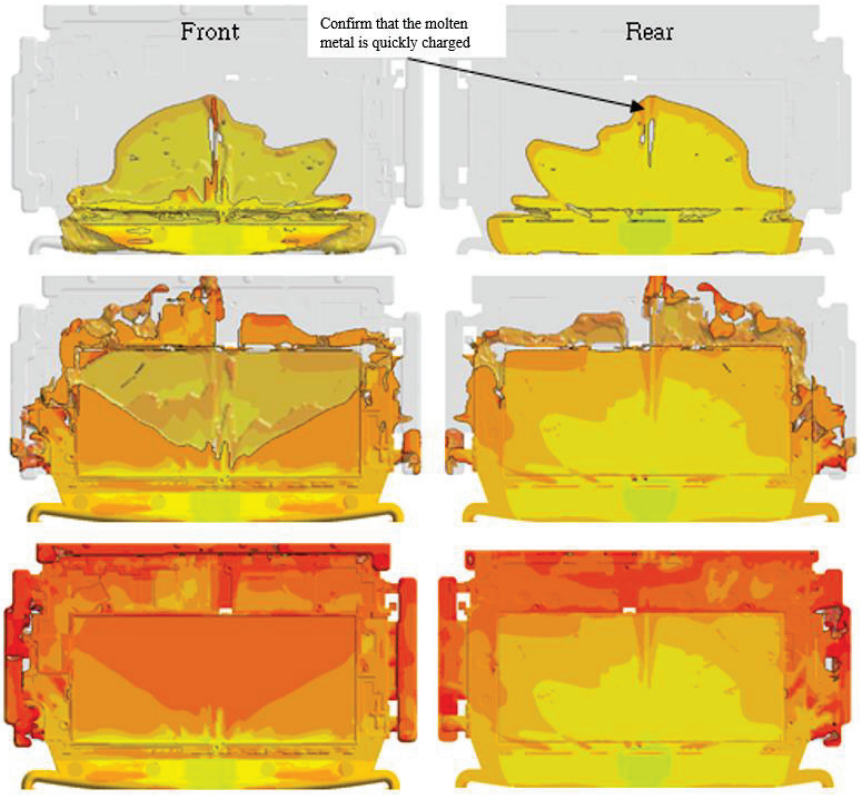

(**b**)

Figure 5. *Cont*.

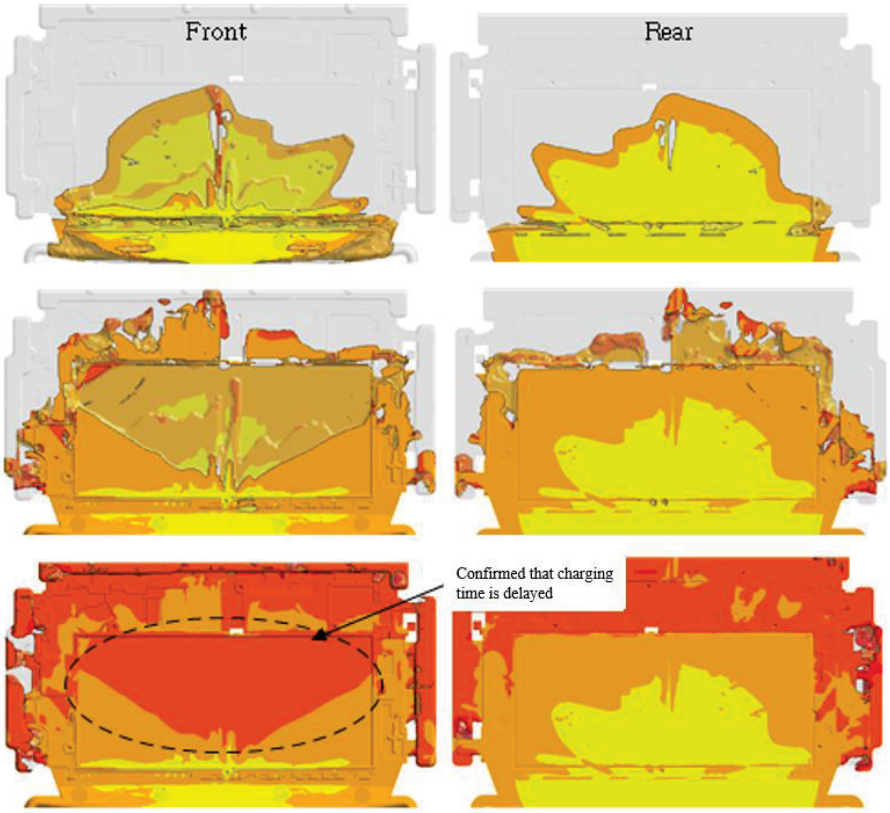

(**c**)

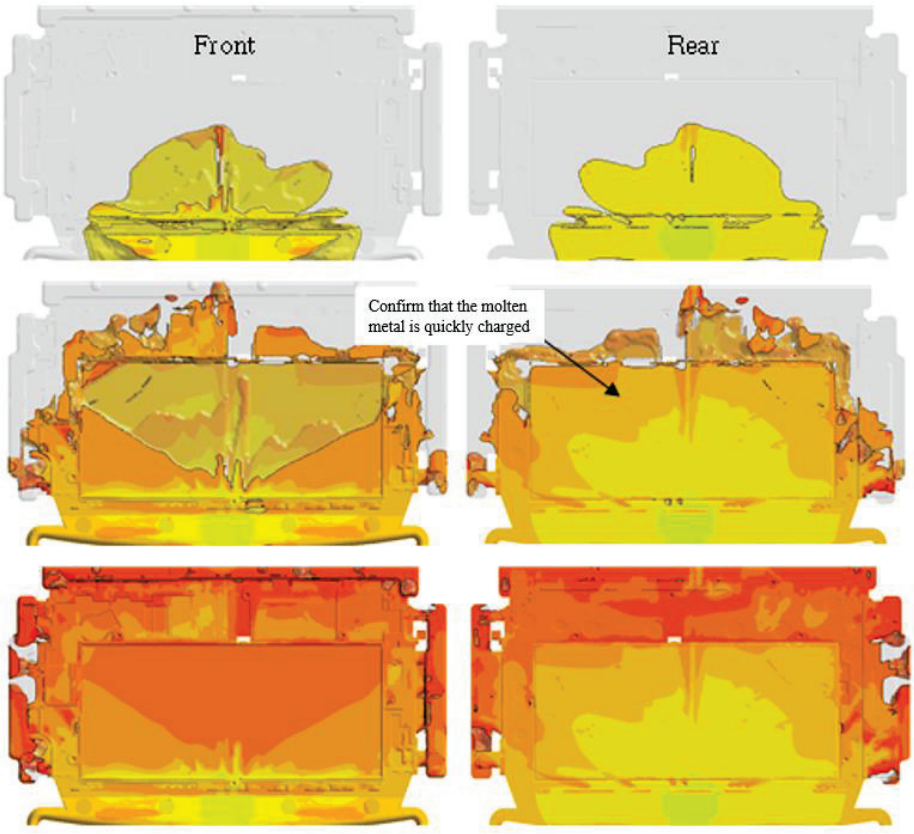

(**d**)

Figure 5. *Cont*.

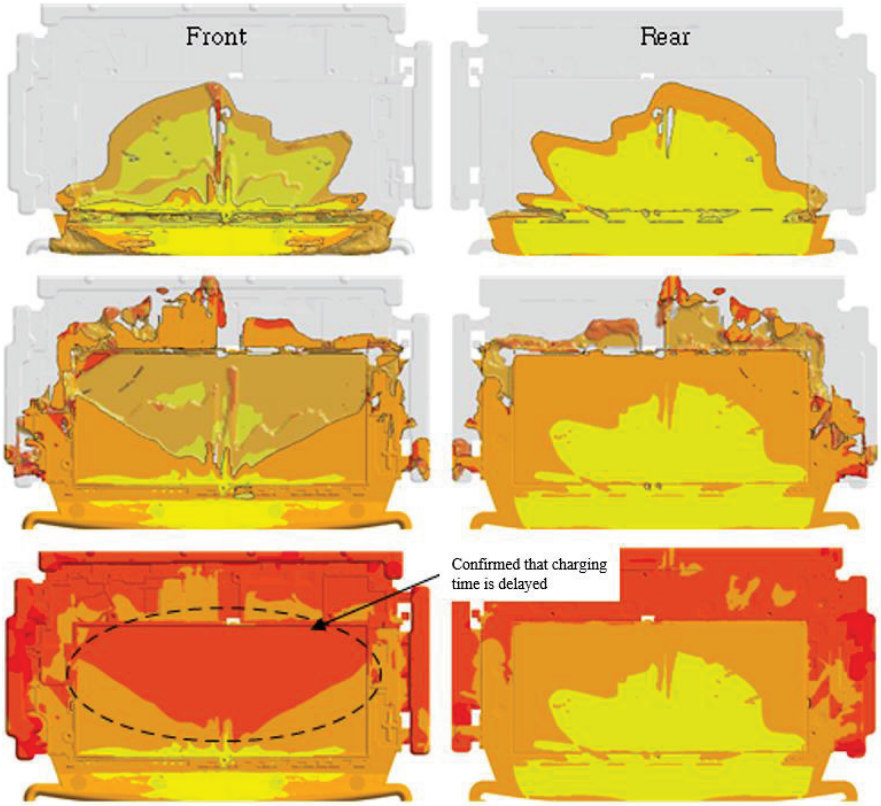

(**e**)

Figure 5. Charging speed distribution according to casting conditions. (**a**) CASE 1, (**b**) CASE 2, (**c**) CASE 3, (**d**) CASE 4, (**e**) CASE 5.

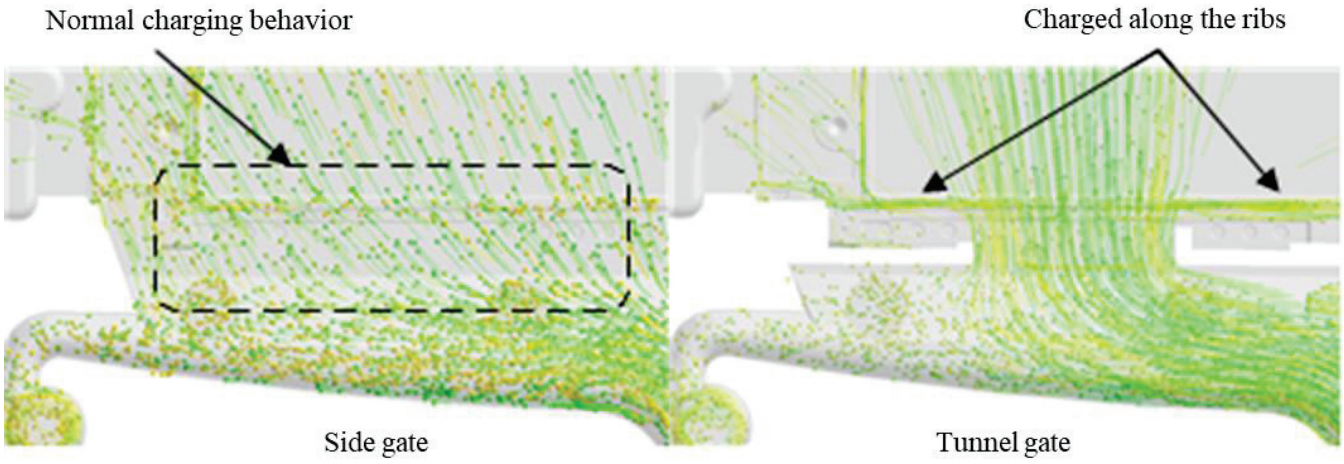

Figure 6. Charging behavior depending on gate type.

The simulation results of CASE 1 (Figure 9a) casting conditions showed a change in temperature due to solidification after the filling of the product was completed. Coagulation occurred first in the thin-walled area. Overflow, runner, etc., were the last to solidify. In the product department, solidification of the middle part of the rib progressed last. These results are believed to be caused by the fact that casting filling rate was slowest for the ribs and the temperature at the top of the ribs was relatively low, resulting in different solidification rates. Also, unlike other conditions, the casting conditions of CASE 3 (Figure 9c) and CASE 5 (Figure 9e) showed a faster solidification rate. These results are believed to be due to a decrease in mold temperature during the solidification process

caused by the relatively low injection temperature. As a result of the simulation, it was confirmed that the mold temperature of CASE 1 was 228 °C and that of CASE 5 was 222 °C.

4.2. Characteristics of the Prototype

4.2.1. Influence of Microstructure

The microstructure of a 0.5 mm thin plate prototype produced under the casting conditions of CASE 1 was photographed using an optical microscope. Table 5 shows the optical micrographs of the numbered portions in Figure 3. A generally uniform microstructure was observed. The primary α-Mg crystal grains became finer because of rapid cooling. The β-$Mg_{17}Al_{12}$ precipitate phase was distributed in a network at the grain boundaries, and some intermetallic compounds were also observed due to the addition of alloy elements.

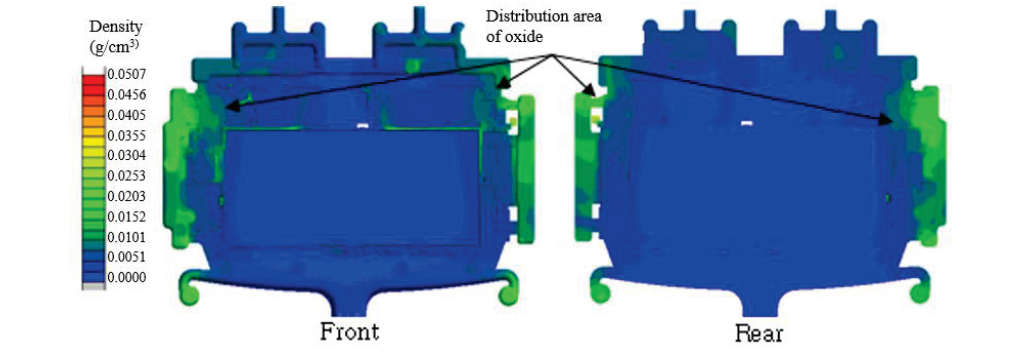

(**a**)

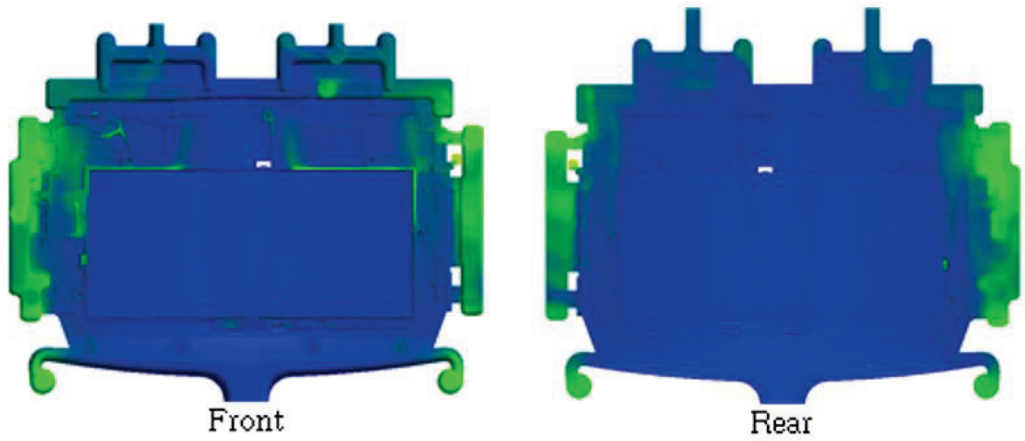

(**b**)

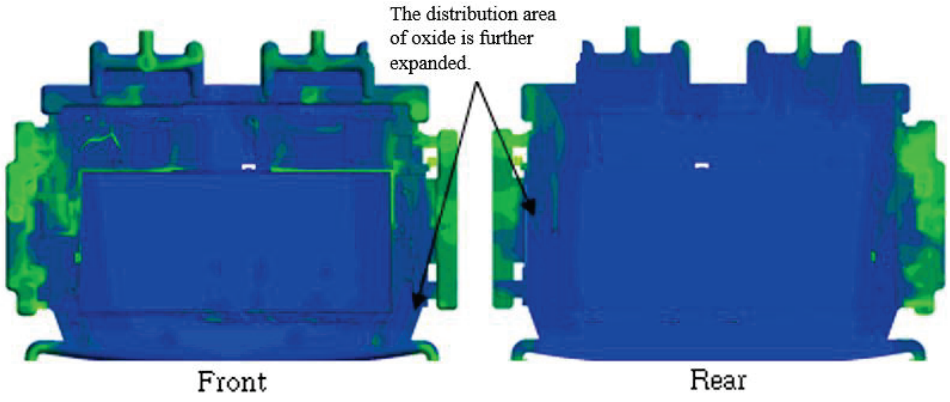

(**c**)

Figure 7. *Cont.*

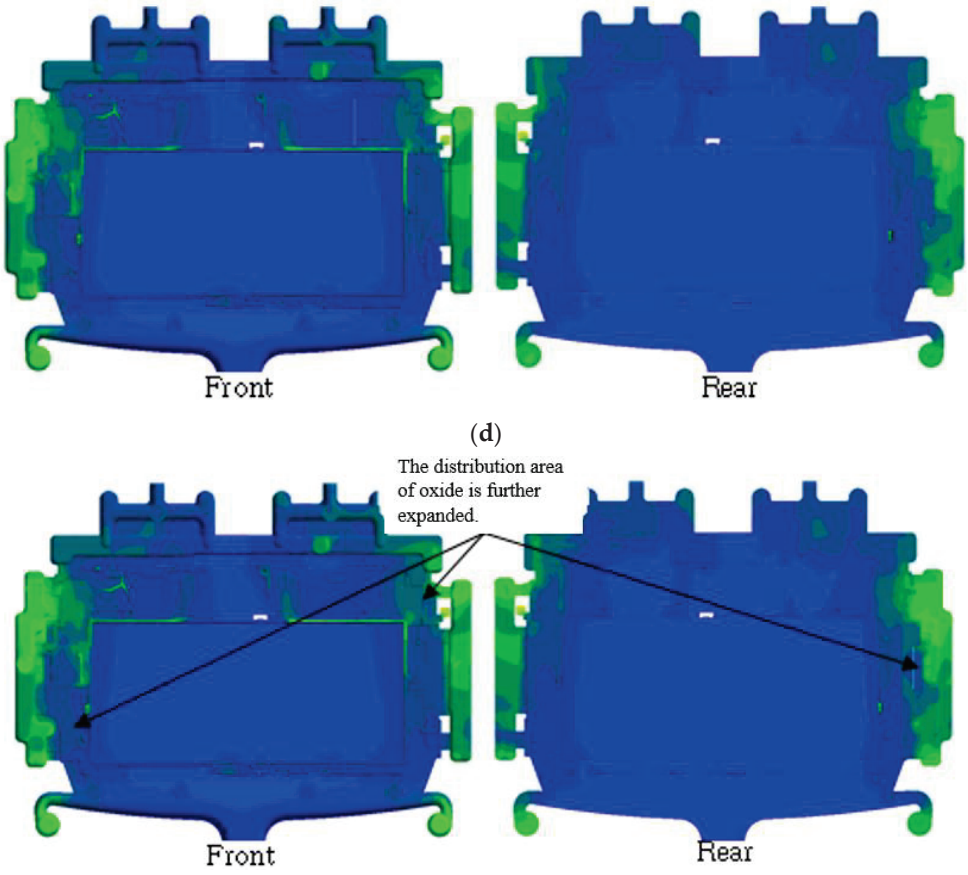

Figure 7. Oxide distribution during molten metal charging. (**a**) CASE 1, (**b**) CASE 2, (**c**) CASE 3, (**d**) CASE 4, (**e**) CASE 5.

The grains of runner No. 1 in Table 5 were clearly different from those of other parts. Considering that the crystal grains were large and dispersed, the thickness of this area was the thickest at 7 mm. It is expected that this phenomenon occurred as cooling slowed down. The microstructures of ingate Nos. 2, 3, and 4 had very fine crystal grain structures, and crystal growth was suppressed due to the rapid cooling rate, allowing a fine and uniform crystal structure to be observed. However, oxides or impurities that appeared dimly and brightly were also observed. At the beginning of the thin plate molding section, fine equiaxed crystal grain structures such as Nos. 5, 6, and 7 were observed, which is believed to have been due to rapid precipitation caused by the cooling rate. The microstructures of Nos. 8, 9, and 10, which were the midpoints of the sheet-metal-forming section, were the same as Nos. 5 to 7, but the unevenness increased in some areas. In No. 9, fine shrinkage or gas cavities were observed, which was believed to be a casting defect, but a uniform crystal structure was distinguished in most areas. Segregation and pores in dark areas were found in the microstructure of Nos. 11, 12, and 13 at the ends of the thin plate molding sections. This was expected to be a casting defect, but the crystal grains were fine, which is believed to have been due to the fast-cooling rate. A uniform equiaxed crystal structure was observed in the microstructure of the end part No. 14 of the product, and stable cooling conditions were observed. However, similarly to No. 12 and the microstructure, casting defects due to segregation pores were observed. In the left and right out-gate microstructures Nos. 15 and 16, the grain size increased due to slow cooling, and precipitates due to increased segregation began to form more clearly along the grain boundaries. Out gates Nos. 17 and 18 at the end showed diversity in the size and distribution of precipitates due to the rapid flow of molten metal and non-uniformity of cooling conditions.

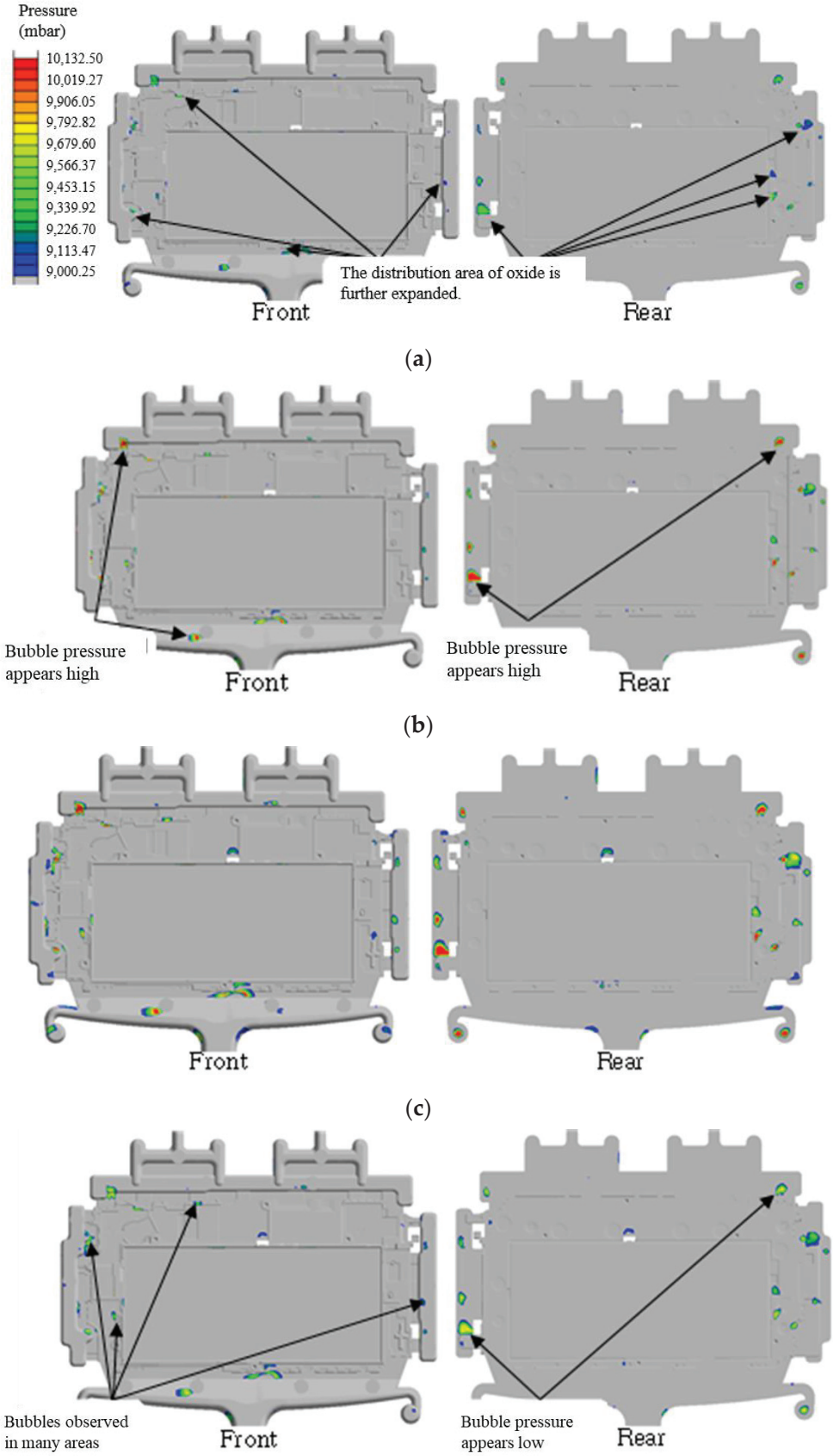

Figure 8. *Cont.*

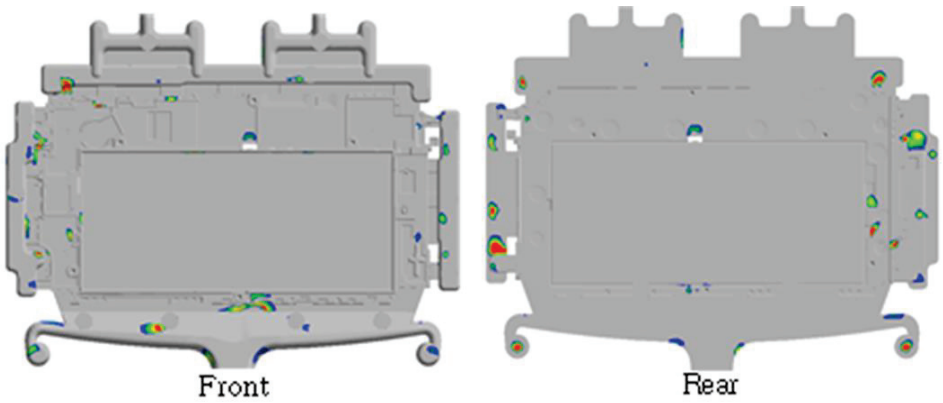

(**e**)

Figure 8. Prediction results of pore distribution according to casting conditions. (**a**) CASE 1, (**b**) CASE 2, (**c**) CASE 3, (**d**) CASE 4, (**e**) CASE 5.

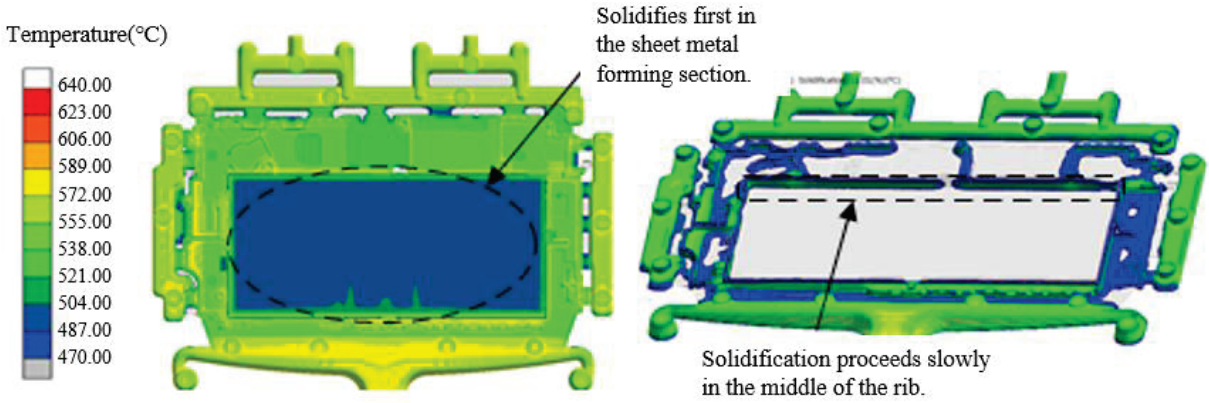

(**a**)

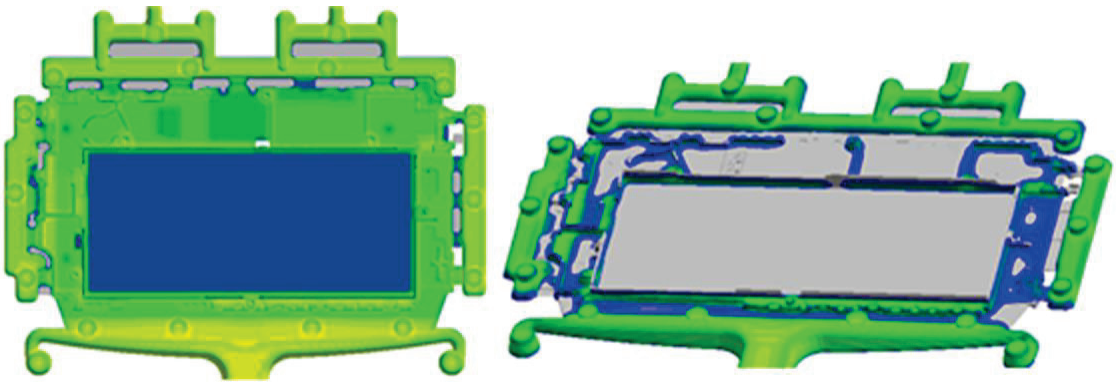

(**b**)

Figure 9. *Cont*.

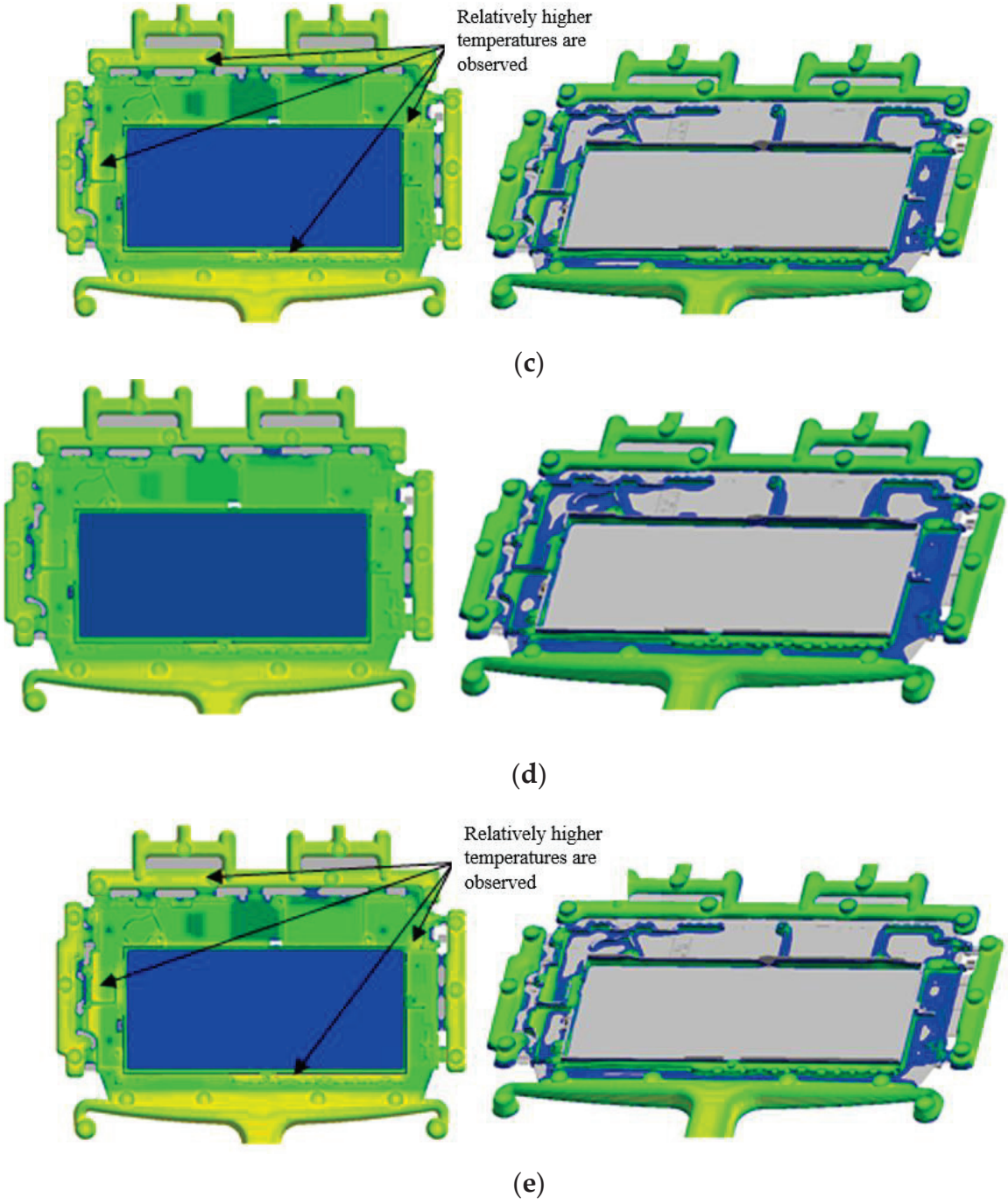

Figure 9. Solidification behavior results according to casting conditions. (**a**) CASE 1, (**b**) CASE 2, (**c**) CASE 3, (**d**) CASE 4, (**e**) CASE 5.

Almost no pores or shrinkage holes were found in the product, and a generally fine and uniform crystal structure was observed. This is believed to be the effect of uniform cooling and is interpreted as a result supported by the appropriate design of the spout, overflow, and air vent. The fraction of oxide inclusions was also at a very low level, and it was evaluated that the molten metal was effectively protected and purified. However, uneven distribution of precipitates was observed in some areas, which is expected to be due to variation in the cooling rate. The fine equiaxed crystal grain structure observed earlier was due to an increase in the nucleation rate and inhibition of crystal growth due to rapid cooling. By applying the model of the enthalpy method, it can be confirmed that the

grain size predicted from the cooling rate under this experimental condition matched well with the actual observation results.

Table 5. Microstructure of a thin plate prototype taken with an optical microscope.

Microstructure	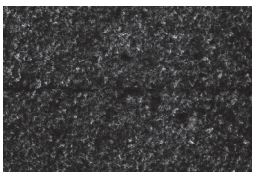	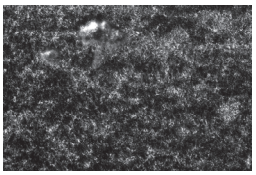	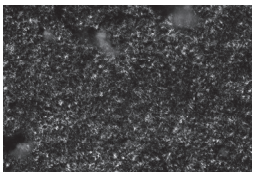
Measurement location	2 (Ingate left)	3 (Ingate center)	4 (Ingate right)
Microstructure	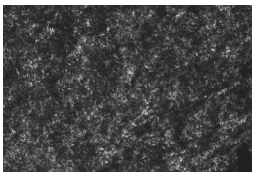	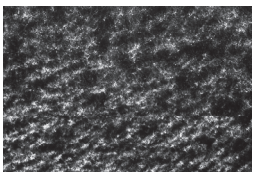	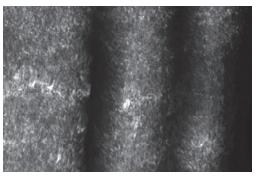
Measurement location	15 (Outgate left)	1 (Runner center)	16 (Outgate right)
Microstructure	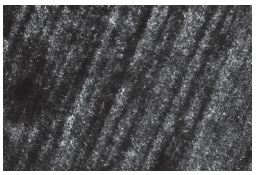	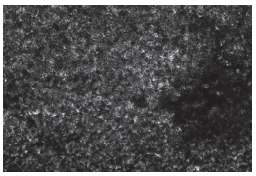	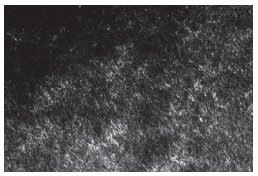
Measurement location	17 (Outgate left)	14 (Product center)	18 (Outgate right)
Microstructure	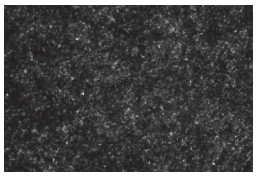	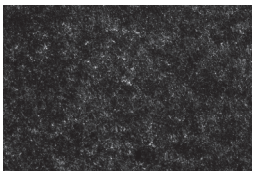	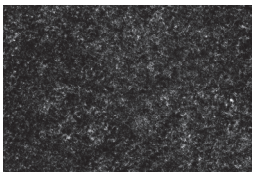
Measurement location	5 (0.5 mm left)	6 (0.5 mm center)	7 (0.5 mm right)
Microstructure	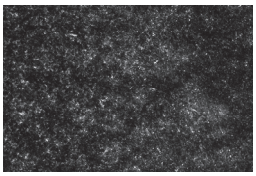	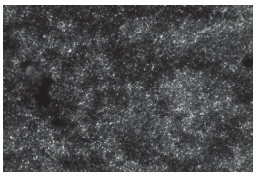	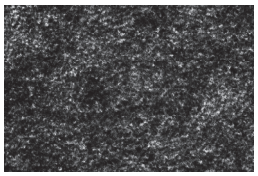
Measurement location	8 (0.5 mm left)	9 (0.5 mm center)	10 (0.5 mm right)
Microstructure	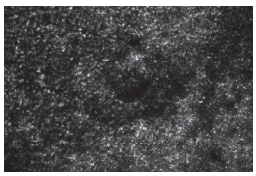	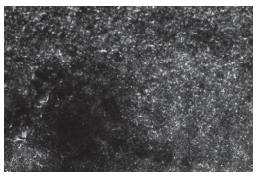	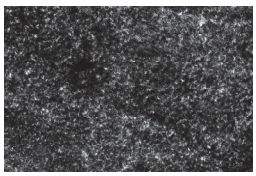
Measurement location	11 (0.5 mm left)	12 (0.5 mm center)	13 (0.5 mm right)

4.2.2. Influence of Mechanical Properties

The tensile properties of the 0.5 mm prototype manufactured under the casting conditions of CASE 1 showed an average tensile strength of 190~220 MPa from room-temperature testing, and excellent physical properties of at least 15% compared to existing bulk materials were observed. This is believed to be due to the grain refinement effect caused by rapid cooling. However, differences in physical properties were observed depending on

the prototype with casting defects. The strength of the center appeared to be somewhat lower than that of the surface, which is presumed to be the effect of local segregation or residual stress. Therefore, controlling the homogeneous microstructure is more important than anything else to ensure the reliability of thin plate products.

Meanwhile, hardness was measured using Mitutoyo's HM-100 model (Mitutoyo, Kanagawa, Japan), and relatively uniform values of an average of 54 to 58 Hv were obtained. However, the hardness itself was evaluated as not being very high. This was due to the unique characteristics of AZ91D, and it is believed that research on more precise heat treatment conditions is necessary to improve the strength and hardness.

5. Conclusions

In this study, a die casting process optimization method for manufacturing thin plate products of magnesium alloy AZ91D of 0.5 mm or less was presented. The effects of casting temperature and mold design variables on the quality of sheet metal were systematically analyzed through pre-filling and solidification analysis using a commercial analysis program. An actual prototype was manufactured by applying the derived optimal conditions, and an evaluation of the microstructure and mechanical properties was performed.

As a result of the simulation analysis results and mechanical properties, it was found that the occurrence of defects related to porosity and shrinkage was minimized along with uniform filling behavior under the conditions of molten metal injection temperatures of 640~670 °C and mold temperatures of 190~220 °C. In addition, the uniformity of the molten metal filling flow within the thin plate was improved through optimal design of the runner, gate, and overflow. It was confirmed that residual stress and deformation due to cooling rate deviation could be minimized by optimizing the cooling channel arrangement. Meanwhile, the 0.5 mm AZ91D alloy prototype manufactured under the above conditions showed a fine and homogeneous grain structure. This is believed to be due to the rapid cooling effect caused by high-speed charging. In addition, by securing the tensile strength of 190~220 MPa, it was possible to implement excellent properties that were 15% higher than the existing bulk material. The hardness also showed a uniform value of 54~58 Hv throughout the specimen, suggesting that quality stability can be improved through improved tissue homogeneity.

The above results are significant in that they succeeded in producing 0.5 mm ultra-thin plate products from magnesium alloys, which were previously considered difficult problems. The optimized process conditions were applied through computer simulation, and actual products were manufactured and verified based on this. The material's unique properties were implemented, and the occurrence of casting defects was suppressed.

However, for commercial product application, it is believed that long-term reliability evaluation and improvement of mechanical properties through alloy design are necessary. To expand demand in the transportation equipment field, which requires high strength and corrosion resistance, it is essential to utilize advanced elements and combine surface treatment technology. In addition, the development of bonding and coating technologies that take material compatibility into account should be developed in parallel.

Meanwhile, the thin plate casting process optimization system established in this study is expected to be applicable to other lightweight alloys and complex shape products other than magnesium. This is because mold design optimization and experimental verification processes based on filling and solidification simulation can greatly contribute to cost reduction and shortening the development period.

Author Contributions: Conceptualization, J.-T.H. and S.-J.M.; methodology, J.-T.H. and C.-M.R.; software, J.-T.H.; validation, J.-T.H. and C.-M.R.; formal analysis, J.-T.H. and C.-M.R.; investigation, J.-T.H. and C.-M.R.; resources, S.-J.M.; data curation, J.-T.H. and C.-M.R.; writing—original draft preparation, J.-T.H. and C.-M.R.; writing—review and editing, S.-J.M.; visualization, C.-M.R.; supervision, S.-J.M.; project administration, S.-J.M.; funding acquisition, S.-J.M. All authors have read and agreed to the published version of the manuscript.

Funding: This work was supported by the Korea Institute for Advancement of Technology (KIAT), titled "Development of a highly versatile quartz transmittance analysis system based on multi-wavelength laser to improve the semiconductor RTP process" (No. RS-2024-00434898).

Data Availability Statement: The original contributions presented in the study are included in the article, further inquiries can be directed to the corresponding author.

Conflicts of Interest: The authors declare no conflicts of interest.

References

1. Polmear, I.J. Magnesium alloys and applications. *Mater. Sci. Technol.* **1994**, *10*, 1–16. [CrossRef]
2. Yang, Y.; Xiong, X.; Chen, J.; Peng, X.; Chen, D.; Pan, F. Research Advances in Magnesium and Magnesium Alloys Worldwide in 2020. *J. Magnes. Alloys* **2021**, *9*, 705–747. [CrossRef]
3. Xu, T.; Yang, Y.; Peng, X.; Song, J.; Pan, F. Overview of Advancement and Development Trend on Magnesium Alloy. *J. Magnes. Alloys* **2019**, *7*, 536–544. [CrossRef]
4. Song, J.; She, J.; Chen, D.; Pan, F. Latest Research Advances on Magnesium and Magnesium Alloys Worldwide. *J. Magnes. Alloys* **2020**, *8*, 1–41. [CrossRef]
5. Ali, Y.; Qiu, D.; Jiang, B.; Pan, F.; Zhang, M.X. Current Research Progress in Grain Refinement of Cast Magnesium Alloys: A Review Article. *J. Alloys Compd.* **2015**, *619*, 639–651. [CrossRef]
6. Luo, A.A. Magnesium Casting Technology for Structural Applications. *J. Magnes. Alloys* **2013**, *1*, 2–22. [CrossRef]
7. You, B.S.; Yim, C.D.; Kim, S.H. Solidification of AZ31 Magnesium Alloy Plate in a Horizontal Continuous Casting Process. *Mater. Sci. Eng. A* **2005**, *413–414*, 139–143. [CrossRef]
8. Hu, L.; Chen, S.; Miao, Y.; Meng, Q. Die-Casting Effect on Surface Characteristics of Thin-Walled AZ91D Magnesium Components. *Appl. Surf. Sci.* **2012**, *261*, 851–856. [CrossRef]
9. Barone, M.R.; Caulk, D.A. Analysis of Liquid Metal flow in Die Casting. *Int. J. Eng. Sci.* **2000**, *38*, 1279–1302. [CrossRef]
10. Qin, X.-Y.; Su, Y.; Chen, J.; Liu, L.-J. Finite Element Analysis for Die Casting Parameters in High-Pressure Die Casting Process. *China Foundry* **2019**, *16*, 272–276. [CrossRef]
11. Syrcos, G.P. Die Casting Process Optimization Using Taguchi Methods. *J. Mater. Process. Technol.* **2003**, *135*, 68–74. [CrossRef]
12. Iwata, Y.; Dong, S.; Sugiyama, Y.; Iwahori, H. Change in Molten Metal Pressure and Its Effect on Defects of Aluminum Alloy Die Castings. *Mater. Trans.* **2014**, *55*, 311–317. [CrossRef]
13. Ibrahim, M.D.; Rahman, M.R.A.; Khan, A.A.; Mohamad, M.R.; Suffian, M.S.Z.M.; Yunos, Y.S.; Wong, L.K.; Mohtar, M.Z. Effect of Mold Designs on Molten Metal Behaviour in High-Pressure Die Casting. *J. Phys. Conf. Ser.* **2017**, *822*, 12029. [CrossRef]
14. Dumanić, I.; Jozić, S.; Bajić, D.; Krolo, J. Optimization of Semi-Solid High-Pressure Die Casting Process by Computer Simulation, Taguchi Method and Grey Relational Analysis. *Int. J. Met.* **2021**, *15*, 108–118. [CrossRef]
15. Fu, J.; Wang, K. Modelling and Simulation of Die Casting Process for A356 Semisolid Alloy. In *Proceedings of the Procedia Engineering*; Elsevier Ltd.: Amsterdam, The Netherlands, 2014; Volume 81, pp. 1565–1570.
16. Li, Y.; Wei, Z. Numerical Simulation of Filling Process in Die Casting. *Mater. Technol.* **2003**, *18*, 36–41.
17. Chen, Z.; Li, Y.; Zhao, F.; Li, S.; Zhang, J. Progress in Numerical Simulation of Casting Process. *Meas. Control* **2022**, *55*, 257–264. [CrossRef]
18. Dou, K.; Lordan, E.; Zhang, Y.J.; Jacot, A.; Fan, Z.Y. A Complete Computer Aided Engineering (CAE) Modelling and Optimization of High Pressure Die Casting (HPDC) Process. *J. Manuf. Process.* **2020**, *60*, 435–446. [CrossRef]
19. Ma, C.; Yu, W.; Zhang, T.; Zhang, Z.; Ma, Y.; Xiong, S. The Effect of Slow Shot Speed and Casting Pressure on the 3D Microstructure of High Pressure Die Casting AE44 Magnesium Alloy. *J. Magnes. Alloys* **2023**, *11*, 753–761. [CrossRef]
20. Chang, X.Y.; Shen, Q.; Fan, W.X.; Hao, H. Optimization of Magnesium Alloy Casting Process: An Integrated Computational Materials Engineering (ICME) Approach. *Mater. Sci. Forum* **2021**, *1035*, 808–812. [CrossRef]
21. Li, J.; Chen, L.; Jiang, S.; Gan, H.; Hao, W. Numerical Simulation and Process Optimization of Magnesium Alloy Vehicle Dashboard Cross Car Beam (CCB) Based on MAGMA. *Processes* **2023**, *11*, 16. [CrossRef]

metals

MDPI

Article

Effect of Annealing and Double Aging on the Microstructure and Mechanical Properties of Hot-Rolled $Al_{17}Cr_{10}Fe_{36}Ni_{36}Mo_1$ Alloy

Yunji Qiu [1], Xinbo Shi [1,2], Xiaoming Liu [1], Zhihua Chen [1], Jianbin Wang [1], Xin Liu [1], Xiaoyu Bai [1], Feng He [1] and Zhijun Wang [1,*]

[1] State Key Laboratory of Solidification Processing, Northwestern Polytechnical University, Xi'an 710072, China; qiuyunji@mail.nwpu.edu.cn (Y.Q.); shixb1023@mail.nwpu.edu.cn (X.S.); xmliu@mail.nwpu.edu.cn (X.L.); 239987149@mail.nwpu.edu.cn (Z.C.); jbwangdaniel@mail.nwpu.edu.cn (J.W.); liuxin2022@mail.nwpu.edu.cn (X.L.); baixiaoyu@mail.nwpu.edu.cn (X.B.); fenghe1991@nwpu.edu.cn (F.H.)
[2] Xi'an Superalloy Technology Co., Ltd., Xi'an 710299, China
* Correspondence: zhjwang@nwpu.edu.cn

Abstract: AlCrFeNi multi-component alloys with excellent mechanical properties have been designed and extensively investigated in recent years. The massive fabrication of sheets will be an effective way for industrial application, where hot rolling is the inevitable process. After hot rolling, the mechanical properties could be further tailored. In this study, the effects of heat treatments on a dual-phase $Al_{17}Cr_{10}Fe_{36}Ni_{36}Mo_1$ hot-rolled plate were systematically investigated, including: (i) annealing (700 °C, 850 °C, 1000 °C and 1150 °C for 1 h, respectively), (ii) solution and single aging (1150 °C for 1 h and 700 °C for 4 h), (iii) solution and double aging (1150 °C for 1 h, 700 °C for 4 h and 650 °C for 1 h). The B2 precipitates with varied morphologies were observed in the FCC matrix of the hot-rolled alloy after a heat treatment range from 700 °C to 1000 °C for 1 h, and the BCC particles in the B2 matrix were dissolved when the heat treatment temperature was higher than 1000 °C. The hot-rolled alloy heat treated at 700 °C for 1 h had the highest yield strength, and the hot-rolled alloy treated at 1150 °C for 1 h showed the lowest yield strength. After a solution at 1150 °C for 1 h, aging at 700 °C for 4 h and 650 °C for 1 h, the $L1_2$ phase and BCC particles were precipitated in the FCC and B2 matrices, and B2 nanoprecipitates were observed around the FCC grain boundaries. The solution and double aging alloy exhibit the tensile strength of 1365.7 ± 9.5 MPa, a fracture elongation of 14.2 ± 1.5% at 20 °C, a tensile strength of 641.4 ± 6.0 MPa, and a fracture elongation of 16.9 ± 1.0% at 700 °C, showing great potential for application.

Keywords: AlCrFeNi; multi-component alloys; heat treatment; microstructures; double aging

1. Introduction

The concept of multi-component alloys (MCAs) breaks the design bottleneck of traditional alloys with single or two main elements and has been explored extensively over the past two decades [1–4]. Initially, MCAs were studied based on single FCC, BCC or HCP structures, and the designed single-phase MCAs exhibited better mechanical and physicochemical properties than traditional alloys [5–10]. However, in recent years, research focus has gradually changed to dual-phase MCAs, and the heterophase structure was intentionally beneficial for improving the mechanical properties of alloys [11–13]. The Co-free system of AlCrFeNi dual-phase MCAs has attracted much attention in the field of physical metallurgy. Soft FCC and the hard B2 dual-phase MCAs have been developed, and showed excellent comprehensive properties [14]. Recently, a new $Al_{17}Cr_{10}Fe_{36}Ni_{36}Mo_1$ MCAs has been developed, and its excellent properties showed great potential for industrial applications [15]. The different element compositions will have distinct effects on the microstructure and mechanical properties of the alloy. By microalloying $Al_{17}Cr_{10}Fe_{37}Ni_{36}$ with Mo and W, a dual-phase MCA with an ultimate strength and fracture elongation of

1285 MPa and 16.0%, respectively, was obtained [16]. Liu et al. further investigated the impacts of non-metallic Si (0~4 at %) on the microstructure of the $Fe_{36}Ni_{36}Cr_{10}Mo_1Al_{17-x}Si_x$ alloy, and found that the increase in Si led to a change in the crystallization sequence during solidification [17].

In addition to adjusting the composition and proportion of elements, the microstructure and properties of MCAs can also be regulated and improved by a series of thermomechanical processes, such as annealing after cold rolling [12,18,19], warm rolling [20–22], hot rolling [23–25] and hot forging [26–29]. Wang et al. conducted phase selective recrystallization followed by aging at 700 °C of the as-cast alloy, which transformed the dendrite structure into an equiaxed structure and achieved a synergistic improvement in strength and plasticity [19]. Tripathy et al. modulated the continuous deformation-induced nanosheets structure by annealing at 800 °C after warm rolling at 400 °C [22]. Pradhan et al. explored the evolution of the grain boundary characteristics during dynamic recrystallization by controlling the hot rolling deformation reduction [23]. Sourav et al. conducted a detailed analysis of the microstructures of $Al_xCoCrFeNi$ (x = 0.3, 0.5, 0.7) alloys after hot forging and evaluated the contribution of different strengthening mechanisms [26]. In addition, Peng et al. explored the effects of simple heat treatments on the microstructures and mechanical properties of as-cast $AlCoCrFeNi_{2.1}$ eutectic high entropy alloy. They found that the FCC phase precipitated in the B2 matrix and the tensile strength of the alloy increased from 1007 MPa to 1173 MPa after being treated at 600 °C, 700 °C, and 800 °C, while the FCC phase dissolved into the B2 matrix and the elongation of the material was slightly increased after being held above 1000 °C [30].

In recent years, great progress has been made in microstructure regulation and the strengthening–toughening of MCAs. The effects of heat treatments on the hot-rolled $Al_{17}Cr_{10}Fe_{36}Ni_{36}Mo_1$ alloy remain to be further clarified. Therefore, it is essential to further explore the heat treatment process of an $Al_{17}Cr_{10}Fe_{36}Ni_{36}Mo_1$ hot-rolled plate to obtain the superior properties of the alloy. In this paper, the influences of various heat treatment temperatures on an $Al_{17}Cr_{10}Fe_{36}Ni_{36}Mo_1$ bulk hot-rolled plate were systematically investigated. The microstructures and mechanical properties of different heat treatment states were analyzed in detail, and the optimal heat treatment process was regulated. This work further complements the heat treatment behavior of the $Al_{17}Cr_{10}Fe_{36}Ni_{36}Mo_1$ hot-rolled plate and provides important guidance for the industrial application of AlCrFeNi dual-phase MCAs.

2. Experiments

2.1. Preparation and Pretreatment of Samples

The vacuum degassed chromium, aluminum bean, nickel plate, industrial pure iron and nickel molybdenum alloy were added into the vacuum induction melting furnace in proportion to fabricate an $Al_{17}Cr_{10}Fe_{36}Ni_{36}Mo_1$ ingot. Then, the vacuum induction ingot was further treated by electroslag remelting (ESR). After ESR, a diameter of ϕ 400 mm electroslag ingot was obtained by cooling for 1–3 h. Finally, the electroslag ingot was heated at 500 °C for 30 min, heated at 20 °C/min to 1170 °C for 20 min, and then hot-rolled repeatedly along the ingot axial direction up to 30 mm thickness. The width of the plate was 200 mm and the heat treatment experiments were conducted at 700 °C, 850 °C, 1000 °C, and 1150 °C for 1 h. The hot-rolled alloy was labeled as HR, and the heat-treated alloys under different heat treatment temperatures for 1 h were labeled as HR700, HR850, HR1000, and HR1150, respectively. The HR alloy was labeled as an HR-SA alloy after a solution at 1150 °C for 1 h and aging at 700 °C for 4 h and the HR-SA alloy was labeled as an HR-DA alloy after aging at 650 °C for 1 h. The hot-rolled samples were heated for heat treatments in a muffle furnace (Hefeikejing, Hefei, China, KSL-1200X) with an atmospheric environment (a temperature of 25.5 °C and a relative humidity of 60.5%). All heat treatment experiments were conducted by air cooling in order to avoid cracks.

2.2. Microstructural Characterization and Tensile Mechanical Property Tests

Cuboid samples with a size of 10 mm × 10 mm × 5 mm were taken at the quarter hot-rolled plate thickness position by the electro-spark wire-electrode cutting method; then, the samples in different heat treatment states were polished with 240-, 800-, 1500-, 2500-, and 4000-grit SiC papers to remove the oxide skin. The polished samples used in the microstructural characterization were electron-polished in a mixed solution of 90% anhydrous ethanol and 10% perchloric acid with a direct voltage of 30 V for 5 s at an ambient temperature. The TEM samples were mechanically abraded to an ~40 nm thickness, followed by electrolytic double spraying. An MTP-1A electrolytic double spray device was used to thin the sample in corrosive fluids of 90% anhydrous ethanol and 10% perchloric acid at −20 °C. The range of the voltage and current was 35–55 V and 45–75 mA, respectively. The microstructures of the hot-rolled alloy and different heat-treated alloys were characterized by an optical microscope (OM, OLYMPUS OLS4000, Tokyo, Japan) and a scanning electron microscopy (SEM, TESCAN MIRA3, Brno, Czech Republic) under a secondary electron mode. Electron back-scattered diffraction (EBSD, TESCAN MIRA3, Brno, Czech Republic) was used to further characterize the grain orientation and grain size. The nanoprecipitates were identified by transmission electron microscopy (TEM, Talos F200X, New York, NY, USA). The universal tensile tests at room temperature (20 °C) and elevated temperatures (600 °C, 700 °C, 800 °C and 900 °C) were conducted on a universal testing machine (UTM, TSMT EM6, Shenzhen, China) with a tensile strain rate of 10^{-3} s^{-1}. An extensometer (Sanjing Y12.5/5, Guangzhou, China) was used to monitor the strain for the room temperature testing and the thermostat and temperature controller were equipped to maintain a constant temperature for the high temperature testing. Tensile mechanical samples with a gauge dimension of 12.5 mm × 3.0 mm × 2.0 mm were used in this study. Samples of all the heat treatment state alloys were tested at least twice to verify the reproducibility of the tensile mechanical properties.

3. Results and Discussion

3.1. Short-Time Annealing at Different Temperatures

Figure 1 shows the alloys' microstructure at five different states. As Figure 1(a1–a3) shows, the microstructure under a hot-rolled state indicates a typical dual-phase structure, in which the white region is the FCC phase and the gray region is the B2 phase [19]. Moreover, the B2 phase was squished along the rolling direction. After short-time annealing at 700 °C, 850 °C, 1000 °C, and 1150 °C for 1 h (Figure 1(a2–e2)), there were some differences. The most obvious change was the randomly distributed particles in the FCC matrix and small FCC phases in the B2 matrix, whose density changed after annealing at different temperatures. Nevertheless, no regularity related to the temperature was found.

In order to further analyze the microstructural changes under different temperatures, the five states of the alloys were characterized by scanning electron microscopy (SEM). The matrix phase composition of the primary HR alloy (Figure 1(a3)) was further determined to be an FCC phase and B2 phase. And spherical BCC particles were observed in the B2 matrix phase, consistent with a previous report [19]. The HR700 alloy (Figure 1(b3)) has a similar microstructure to the HR alloy overall. However, some nanoprecipitates were observed in the FCC matrix of the HR700 alloy, which may have a vital impact on the mechanical properties of the alloy. For the HR850 alloy (Figure 1(c3)), some needle-like (NL) precipitates with widths of 200–400 nm precipitated in the FCC phase. The length of the needle-like structures seemed to be different due to the varied orientation of the NL structures. With heat-treatment temperature rises to 1000 °C (Figure 1(d3)), a large amount of the B2 phase with a size below 2 μm precipitated in the FCC phase. Moreover, the nano-scale spherical BCC precipitates that were originally distributed in the B2 matrix in the HR alloy disappeared, which might be dissolved by the higher temperature compared to the HR700 alloy and HR850 alloy. Similarly, the BCC particles in the HR1150 alloy (Figure 1(e3)) were also dissolved and the FCC matrix became clean and tidy. The clean and tidy FCC phase was formed since the small B2 phases in the original FCC matrix (HR alloy)

gradually aggregated into the larger particles. These results indicate that the heat treatment temperature can change the precipitation behavior as well as the phase composition of the alloy, which means that the mechanical properties can be regulated by choosing the right heat treatment process to adjust the precipitation behaviors.

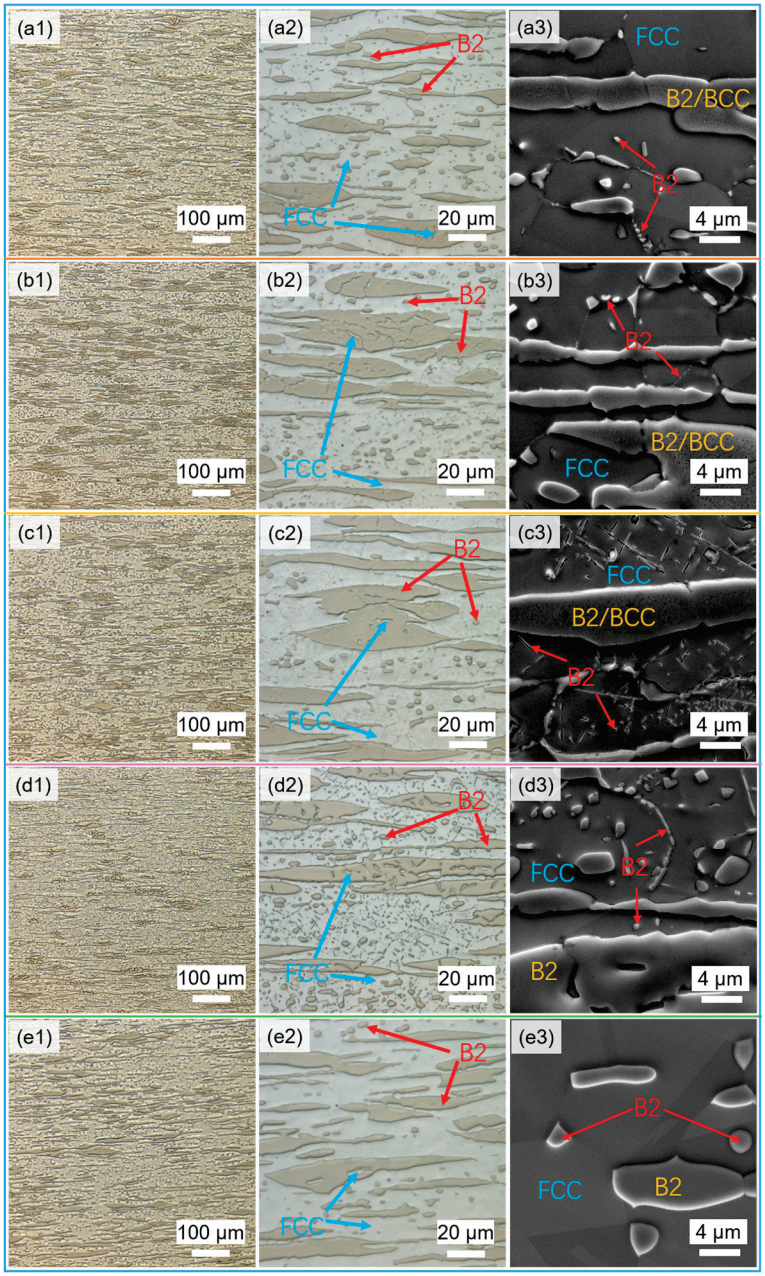

Figure 1. Microstructures of the five different states alloys: (**a1**–**a3**) images of HR alloy; (**b1**–**b3**) images of HR700 alloy; (**c1**–**c3**) images of HR850 alloy; (**d1**–**d3**) images of HR1000 alloy; (**e1**–**e3**) images of HR1150 alloy. The first two colored images were acquired by optical microscope while the black-and-white images were captured by scanning electron microscopy. On the right side of each image was the magnified image of the corresponding alloy.

Figure 2 shows the electron back scatter diffraction (EBSD) maps of the five different state alloys heat-treated at different temperatures. From the EBSD phase-index map (Figure 2(a1)) of the HR alloy, the structure of the B2 matrix (red color) was elongated along the rolling direction, and the B2 particles were dispersed in the FCC matrix (green color). According to the EBSD inverse pole figure (Figure 2(a2)), the HR alloy showed an obvious

equiaxial dual-phase structure, which indicates the occurrence of dynamic recrystallization in the rolling process. Compared with the HR alloy, more precipitates were observed in the FCC matrix of the HR700 alloy (Figure 2b), which was basically consistent with SEM results. As for the other three heat-treated alloys, numerous B2 precipitates were observed in the HR850 alloy and HR1000 alloy (Figure 2c,d), while the B2 particles in the HR1150 alloy (Figure 2(e1)) were coarsened into larger B2 islands. The average grain size of the FCC phase and B2 phase was calculated according to EBSD results (Figure 2(a3–e3)). The results show that the HR alloy, HR700 alloy, HR850 alloy, and HR1000 alloy had similar grain sizes, while the HR1150 alloy had the largest grain size.

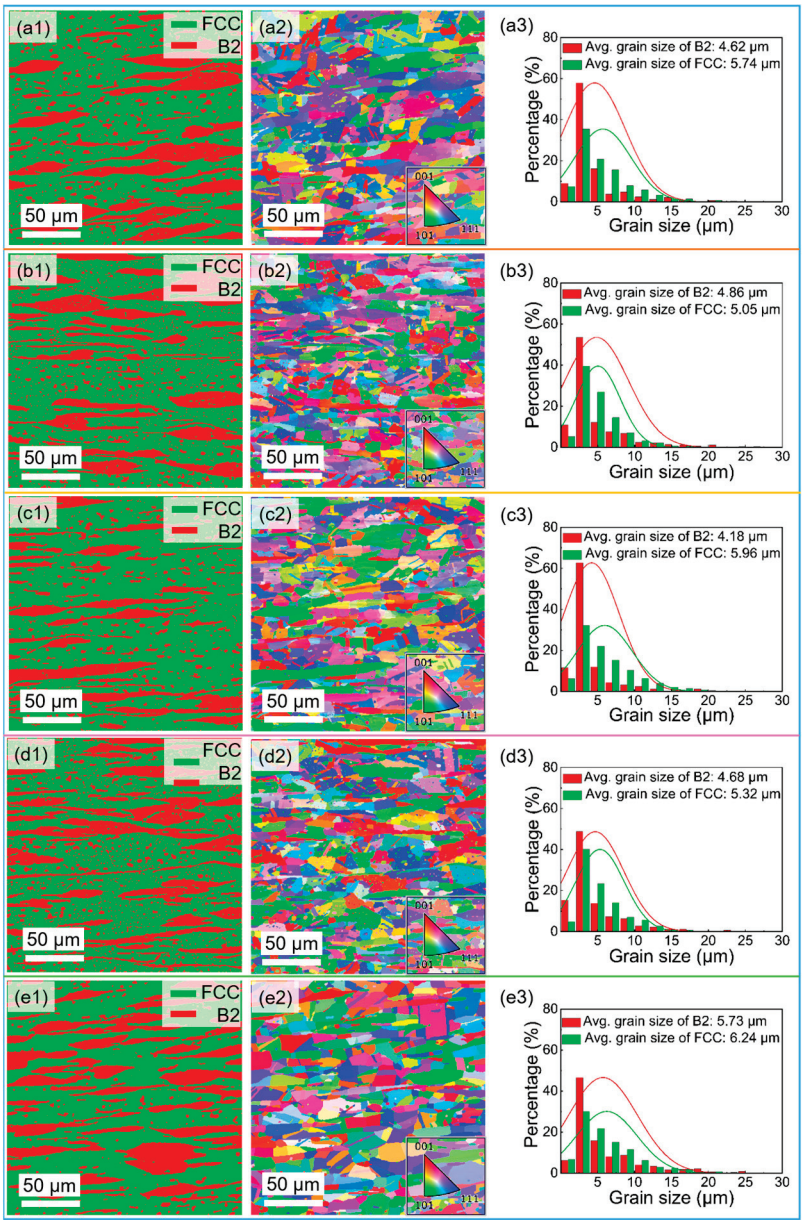

Figure 2. Electron back-scattered diffraction (EBSD) results of five different state alloys: (**a1**–**a3**) images of HR alloy; (**b1**–**b3**) images of HR700 alloy; (**c1**–**c3**) images of HR850 alloy; (**d1**–**d3**) images of HR1000 alloy; (**e1**–**e3**) images of HR1150 alloy. From left to right, the results for each alloy were phase map, EBSD inverse pole figure, and corresponding frequency distribution of grain size, respectively. Due to the dual-phase structure of this alloy, the grain sizes of the FCC phase and the B2 phase were calculated, respectively.

The changed microstructures indicate different mechanical properties. Tensile tests of the five alloys were carried out at room temperature; the engineering strain–stress curves and related data are shown in Figure 3 and Table 1, respectively. The results show that all alloys demonstrated a good combination of strength and elongation. The HR alloy with yield and ultimate strengths of 471.2 ± 6.5 MPa and 1019.2 ± 8.5 MPa has a fracture elongation of 20.1 ± 1.0%. After heat treatment at 700 °C, the yield strength, ultimate strength, and fracture elongation of the alloy were slightly increased to 568.4 ± 5.0 MPa, 1107.2 ± 9.0 MPa and 22.2 ± 1.5%, respectively. This is mainly due to the B2 precipitates in the FCC matrix. Compared with the HR alloy, the yield and the ultimate strength of the HR850 alloy, HR1000 alloy, and HR1150 alloy were reduced, while the ductility improved to some extent. Interestingly, the strength of the HR1000 alloy is greater than that of the HR850 alloy, mainly due to there being more B2 precipitates in the FCC matrix of the HR1000 alloy. The large grain size and aggregation of B2 particles result in the lowest yield strength (360.7 ± 5.0 MPa) and ultimate strength (955.9 ± 7.5 MPa) of the HR1150 alloy.

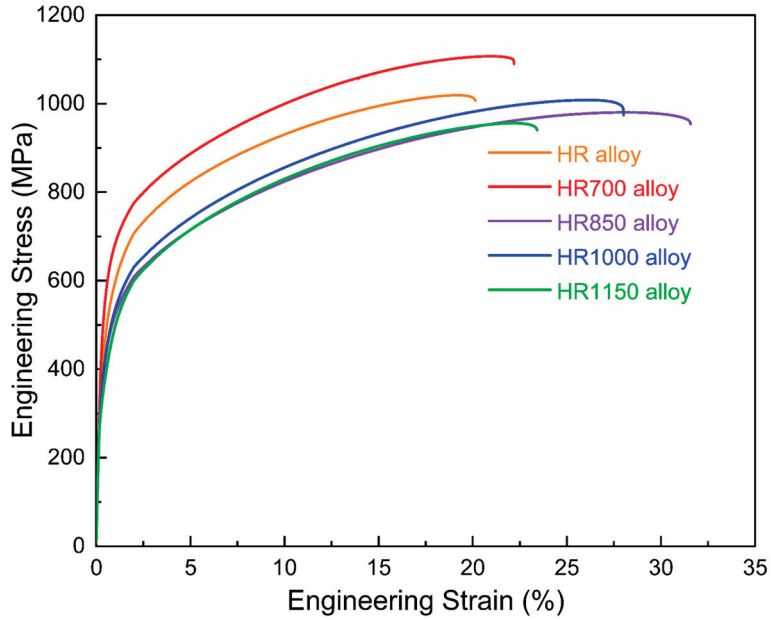

Figure 3. Stress–strain curves of HR alloy, HR700 alloy, HR850 alloy, HR1000 alloy and HR1150 alloy tested at room temperature.

Table 1. Tensile properties of HR alloy, HR700 alloy, HR850 alloy, HR1000 alloy and HR1150 alloy, where σ_s, σ_b and ε_p are the yield strength, ultimate strength, and fracture elongation, respectively.

Alloys	σ_s, MPa	σ_b, Mpa	ε_p, %
HR	471.2 ± 6.5	1019.2 ± 8.5	20.1 ± 1.0
HR700	568.4 ± 5.0	1107.2 ± 9.0	22.2 ± 1.5
HR850	400.8 ± 5.5	980.3 ± 7.0	31.6 ± 1.5
HR1000	414.1 ± 7.0	1008.1 ± 9.5	28.1 ± 1.0
HR1150	360.7 ± 5.0	955.9 ± 7.5	23.4 ± 1.0

3.2. Solution and Aging

According to the results in Section 3.1, the yield strength of the HR alloy will be increased at 700 °C due to the nanoprecipitates in the FCC matrix, and the yield strength of the HR1150 alloy will be reduced at 1150 °C for the dissolution of B2 precipitates in the FCC matrix. Therefore, 1150 °C was deemed a suitable temperature to remove the heterophases and 700 °C was considered a suitable temperature to trigger the precipitations. Meanwhile, the temperature of 650 °C, 50 °C below 700 °C, was also taken into account as the proportion

of nanoprecipitates might be increased without changing their size as much as possible. Inspired by the results and reasonable inference, the solution, solution and single aging (SSA), solution and double aging (SDA) processing technology was investigated. As shown in Figure 4, the dot line curves of Vickness hardness versus time was obtained by calculating the average hardness acquired under different processing technology. The red five-pointed star indicates the appropriate treatment time under different temperatures. It was clear that the solution time, not an obvious characteristic over time, was not a major factor. Therefore, the minimum time of 1 h solution was enough. Single aging at 700 °C reached its peak value after treatment for 4 h, different from the 650 °C with an upward trend in the test time. The above results suggest that the first-stage aging at 700 °C was beneficial for rapid precipitation within 4 h, better than 650 °C. The temperature of 650 °C was therefore followed after 700 °C to increase the volume fraction or amount of the nanoprecipitates. According to the red line at the top of the curves, the heat treatment process of that solution at 1150 °C for 1 h, aging at 700 °C for 4 h, and 650 °C for 1 h were thus determined and corresponding structural characterization and mechanical testing were also conducted.

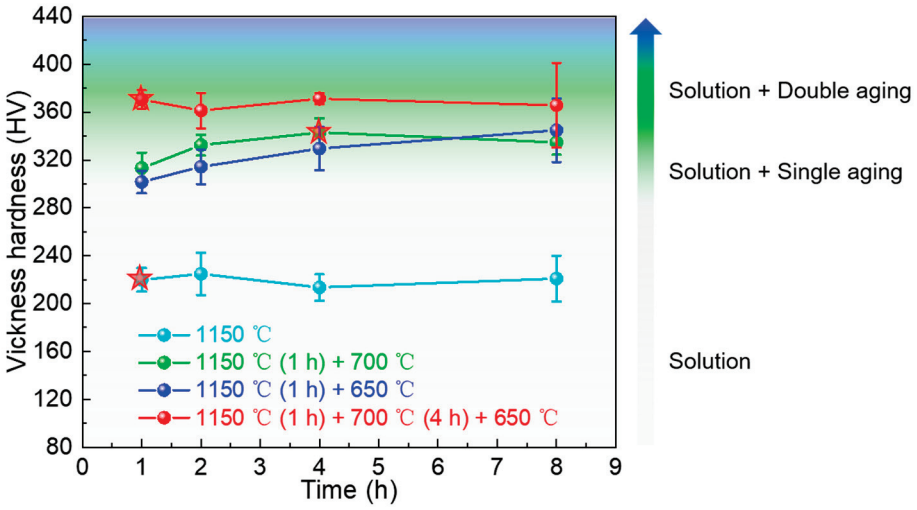

Figure 4. Vickness hardness curves of the HR alloy under different heat-treated processes. From down to up, it represents solution, solution and single aging, solution, and double aging process. The red five-pointed star in the curves indicate the suitable treating time.

Figure 5(a1,b1) show the microstructure of the HR-SA alloy and HR-DA alloy. Compared with the HR alloy, some precipitates were observed at the FCC grain boundaries in both alloys, which also had a similar precipitation behavior to the HR700 alloy. According to high-resolution SEM images (Figure 5(a2–a4,b2–b4)), nano-spherical and short rod-like precipitates were observed in the B2 matrix and FCC matrix of both the HR-SA alloy and HR-DA alloy. And what surprised us was that the number and size of the short rod-like precipitates in the HR-DA alloy were greater than those of the HR-SA alloy, and that the short rod-like precipitates would have a certain effect on the mechanical properties of the alloy.

According to the above results, the HR-SA alloy and HR-DA alloy had a similar precipitation behavior but a different amount and size of the short rod-like precipitates. The HR-DA alloy was further analyzed by transmission electron microscopy (TEM), as shown in Figure 6. Figure 6a shows the bright-field image of the B2 phase. Spherical nanoprecipitates with an average size of 30 nm were distributed homogeneously in the matrix phase. The corresponding selected-area electron diffraction (SAED) pattern is shown in Figure 6b, and the two-phase structures of BCC/B2 were further determined. The dark-field image (Figure 6c) was obtained by selecting $(100)_{B2}$ superlattice diffraction spots to verify the phase structure of the nanoprecipitates and matrix. The precipitates showed dark and the matrix showed bright, indicating that the matrix was the B2 phase. A

similar characterization was conducted on the FCC phase. Some rod-like structures with an average width of 20 nm were precipitated in the matrix (Figure 6d). A further SAED (Figure 6e) pattern and dark-field image (Figure 6f) indicated that rod-like $L1_2$ precipitates were dispersed in the FCC matrix. The above results confirm that after solution and double aging, nano-spherical BCC and rod-like $L1_2$ precipitates were observed in the B2 and FCC matrices of the HR-DA alloy, respectively.

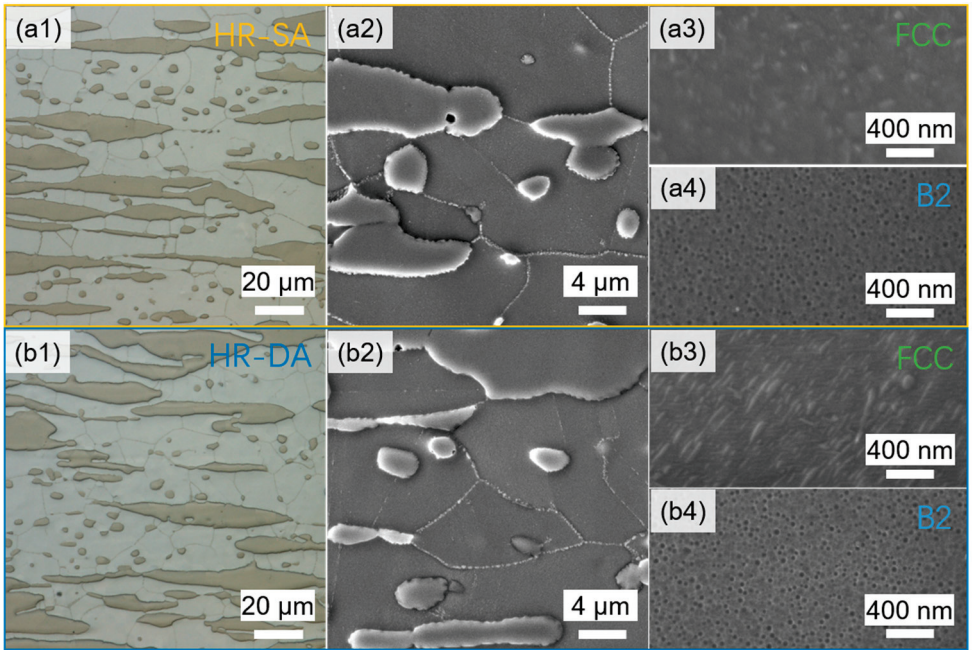

Figure 5. Microstructures of solution and aging alloys: (**a1**–**a4**) images of HR-SA alloy; (**b1**–**b4**) images of HR-DA alloy. The first colored image was acquired by optical microscope while the black-and-white images were captured by scanning electron microscopy. The two alloys were composed of FCC matrix and B2 matrix, and SEM images at magnified scale of the FCC matrix and B2 matrix for each alloy were placed on the right of this figure.

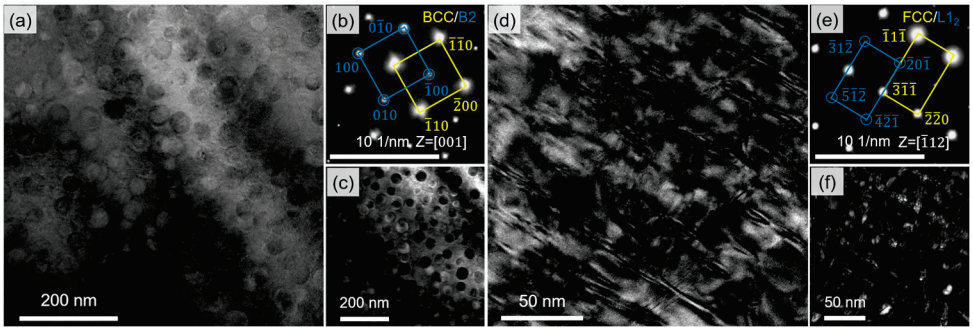

Figure 6. Transmission electron microscopy images of HR-DA alloy: (**a**) Bright-field image of BCC phase and B2 phase; (**b**) SAED pattern of BCC phase and B2 phase; (**c**) Dark-field image of BCC phase and B2 phase; (**d**) Bright-field image of FCC phase and $L1_2$ phase; (**e**) SAED pattern of FCC phase and $L1_2$ phase; (**f**) Dark-field image of FCC phase and $L1_2$ phase.

An uniaxial tensile test was performed to validate the differences in the mechanical properties for the HR-SA alloy and the HR-DA alloy, as shown in Figure 7a. The HR-SA alloy exhibits a yield strength of 713.0 ± 6.5 MPa and a tensile strength of 1263.9 ± 8.0 MPa, as well as a fracture elongation of 13.4 ± 1.6%. After further heat treatment at 650 °C, the yield strength, tensile strength, and fracture elongation of the HR-SA alloy increased to 813.2 ± 7.0 MPa, 1365.7 ± 9.5 MPa, and 14.2 ± 1.5% in the HR-DA alloy, respectively.

The enhancement of the HR-DA alloy's strength was mainly attributed to the greater precipitation of $L1_2$ in the FCC matrix, which occurred at 650 °C. Comparing the mechanical properties of the HR-DA alloy with those of other MCAs at 20 °C, shown in Figure 8a, our alloy reveals a great combination of strength and plasticity. The high temperature tensile behavior of the HR-DA alloy at 600–900 °C was tested, and the mechanical property results are shown in Figure 7b and Table 2. The yield and tensile strength displayed a declining trend while the elongation showed an increasing trend. The HR-DA alloy shows an excellent yield strength of 576.8 ± 5.5 MPa and a competitive fracture elongation of 16.9 ± 1.0% at 700 °C. When comparing it with other alloys at 700 °C, our alloy still exhibits better high-temperature mechanical properties (Figure 8b). During the elevated temperature deformation, the B2 nanoprecipitates at the FCC grain boundaries hindered the dislocation movement as well as the grain boundary sliding. The above results show that our well-prepared MCAs exhibit good mechanical properties in a wide temperature range.

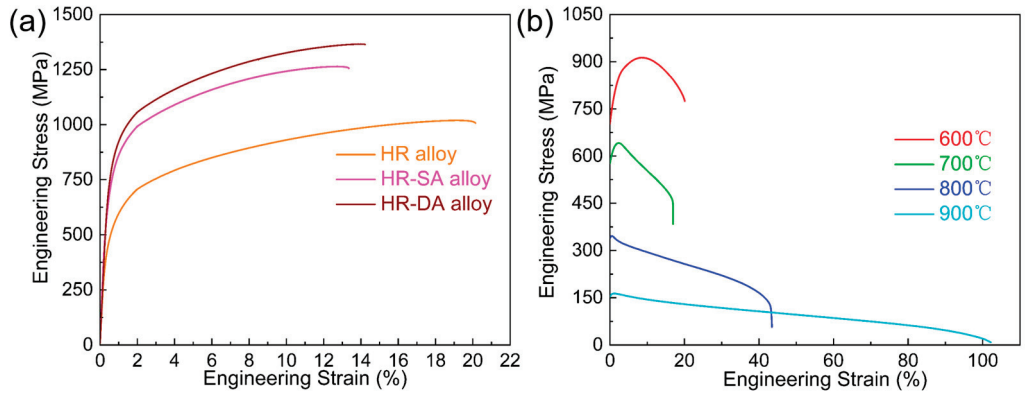

Figure 7. Tensile stress–strain curves of the alloys at different temperatures: (**a**) HR alloy, HR-SA alloy, and HR-DA alloy tested at room temperature; (**b**) HR-DA alloy tested at 600–900 °C.

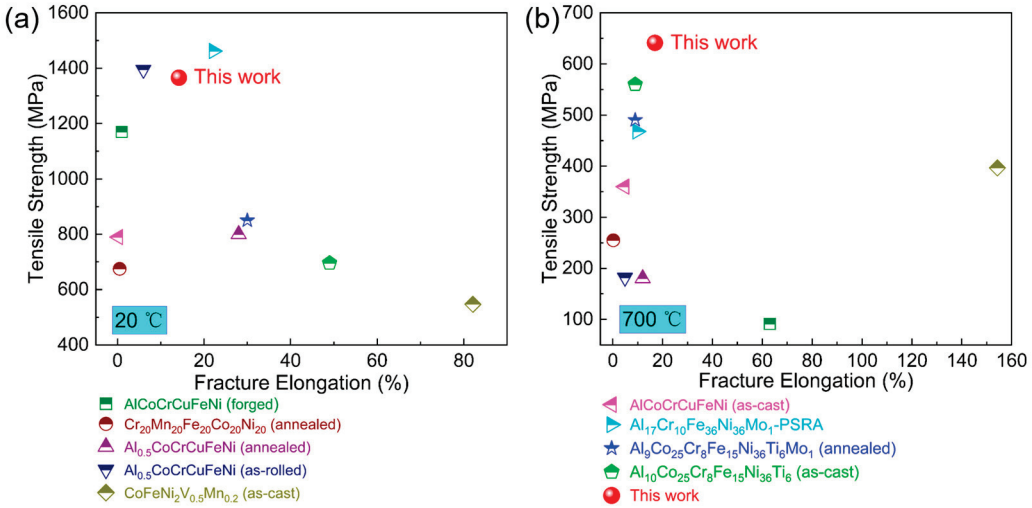

Figure 8. Comparison of tensile properties of HR-DA alloy with other MCAs at different temperatures (**a**) 20 °C and (**b**) 700 °C, respectively adapted from Refs. [31–37].

Table 2. Mechanical test results for HR-DA alloy at room temperature and elevated temperatures, where σ_s, σ_b and ε_p are the yield strength, ultimate strength, and fracture elongation, respectively.

Temperature °C	σ_s, MPa	σ_b, Mpa	ε_p, %
20	813.2 ± 6.5	1365.7 ± 11.5	14.2 ± 1.0
600	702.6 ± 7.0	913.1 ± 8.5	20.1 ± 1.5
700	576.8 ± 5.5	641.4 ± 6.0	16.9 ± 1.0
800	339.1 ± 7.5	346.3 ± 7.0	43.5 ± 1.5
900	152.9 ± 5.0	163.6 ± 5.5	102.2 ± 1.0

The tensile fracture morphologies of the HR alloy, HR-SA alloy, and HR-DA alloy at room temperature were characterized in order to further analyze the fracture behavior of the alloys. The three alloys' fracture surfaces had similar fracture morphologies, as shown in Figure 9. All alloys exhibited two classical structural characteristics of cleavage planes and dimples, which were indicated by blue arrows and red arrows, respectively. The soft FCC matrix has more slip systems and its fracture mode was mainly controlled by dimples. The brittle B2 matrix's fracture mode was mainly a cleavage fracture. During the rolling process, the B2 matrix was elongated along the rolling direction. Therefore, obvious disk-like cleavages with river patterns were observed in the fracture morphologies. The branches of the river patterns correspond to the various cleavage planes of the same crystal plane, and the flow direction of the river was consistent with the propagation direction of the crack. Large tearing edges were shown where the cleavage planes met the dimples, which is also consistent with a previous study [16]. The microstructures and fracture elongation of the HR alloy, HR-SA alloy, and HR-DA alloy were not very different, and the three alloys also had similar fracture modes.

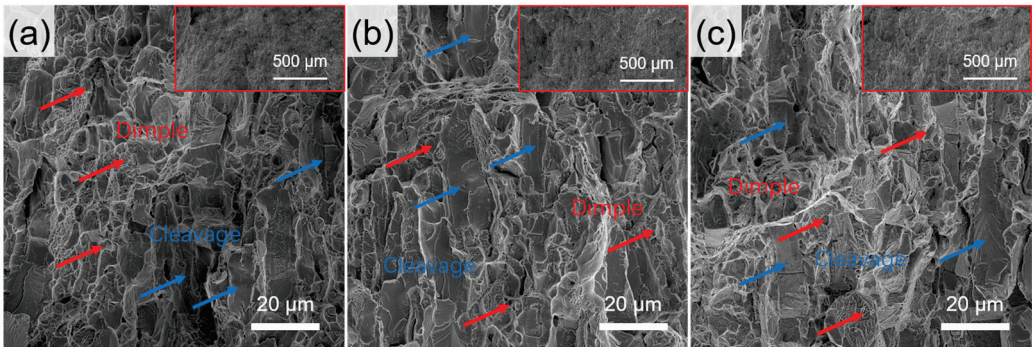

Figure 9. Secondary electron micrographs of the fracture morphology for (**a**) HR alloy, (**b**) HR-SA alloy, and (**c**) HR-DA alloy testing at room temperature. The insets show the macroscopic fracture of the corresponding alloys.

In order to further understand the fracture behaviors of the HR-DA alloy at different temperatures, the mechanical fracture morphologies of the HR-DA alloy at 600–900 °C are shown in Figure 10. This alloy had a similar fracture mechanism at 600 °C and 700 °C (Figure 10a,b), the fracture mode of the FCC matrix was mainly dimples (red arrows), and the fracture mode of the B2 matrix was mainly a cleavage fracture (blue arrows). When the testing temperature was elevated to 800 °C (Figure 10c), the fracture surface of our alloy showed an obvious necking phenomenon. The fracture morphology was mainly dominated by dimples with various sizes and some oxidation products; no significant cleavage planes and rive patterns were observed. When the temperature rose to 900 °C (Figure 10d), the fracture morphology showed larger and deeper dimples and more oxidation products were observed on the fracture surface. The above results show that the HR-DA alloy exhibited a mixed fracture mode when deformed at 600 °C and 700 °C. With the increase in temperature, the B2 matrix was softened. And the fracture mode of the B2 matrix changed

from a cleavage fracture to dimples, which was undesirable for the mechanical properties of our alloy.

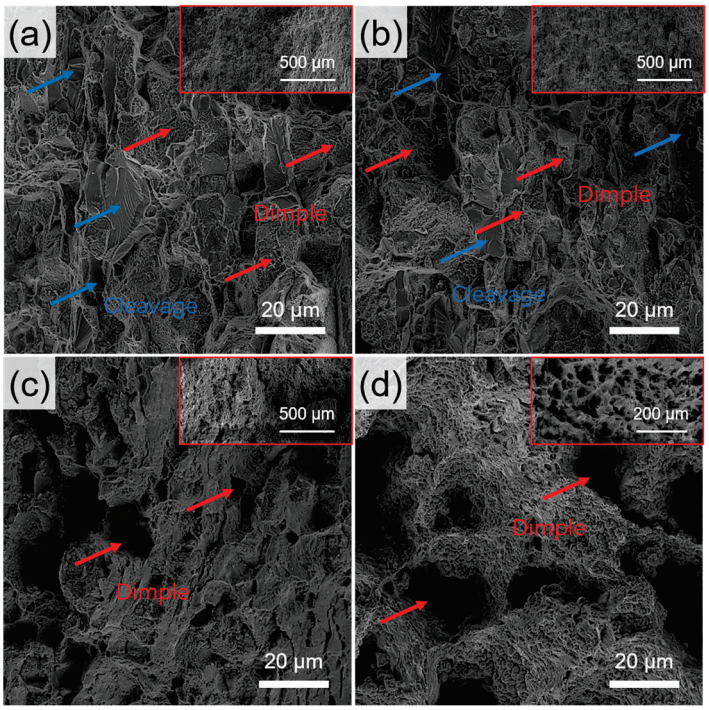

Figure 10. Secondary electron micrographs of the fracture morphology for HR-DA alloy testing at (**a**) 600 °C, (**b**) 700°C, (**c**) 800 °C, and (**d**) 900 °C. The insets show the macroscopic fracture of the corresponding temperatures and that they exhibited a significant necking phenomenon above 800 °C.

4. Conclusions

This work focused on the hot-rolled $Al_{17}Cr_{10}Fe_{36}Ni_{36}Mo_1$ large plate, investigating the effects of different heat treatments on the microstructure and mechanical properties. The main conclusions are as follows.

(1) The precipitation behaviors of the HR alloy can be affected by different annealing temperatures. In the FCC matrix, some B2 nanoprecipitates were observed in the HR700 alloy, the needle-like B2 structures were precipitated in the HR800 alloy, the island-like B2 precipitates were found in the HR1000 alloy, and the B2 precipitates rapidly coarsened into micron-scale structures in the HR1150 alloy. In addition, the BCC particles precipitated in the B2 matrix of the HR alloy were completely dissolved above 1000 °C.

(2) The HR-DA alloy showed better comprehensive mechanical properties than the HR-SA alloy. After the HR alloys were treated with SSA and SDA, short rod-like $L1_2$ precipitates were observed in the FCC matrix of both the HR-SA and HR-DA alloys, and the number and size of the $L1_2$ phases in the HR-DA alloy were greater than those of the HR-SA alloy. The $L1_2$ precipitates can greatly improve the strength of the alloy by hindering the movement of dislocation. Therefore, the HR-DA alloy shows the excellent tensile strength of 1365.7 ± 9.5 MPa and fracture elongation of 14.2 ± 1.5% at room temperature.

(3) The HR-DA alloy also showed acceptable mechanical properties at a high temperature. The $L1_2$ phases and B2 nanoprecipitates were observed in the FCC matrix and FCC grain boundaries, respectively. The high-density $L1_2$ phases significantly contributed to the yield strength and the B2 nanoprecipitates can effectively hinder the dislocation movement as well as the grain boundary sliding. These results led to the HR-DA alloy obtaining a high tensile strength of 641.4 ± 6.0 MPa and a fracture elongation of 16.9 ± 1.0% at 700 °C, showing great potential for elevated temperatures applications.

In the current study, we mainly focused on the influence of a heat treatment process on the microstructure and mechanical properties. The strengthening mechanisms of the HR-DA alloy will be further analyzed in a future investigation.

Author Contributions: Y.Q.: methodology, formal analysis, data curation, writing—original draft, writing—review and editing. X.S.: resources, writing—original draft, funding acquisition. X.L. (Xiaoming Liu): validation, formal analysis, writing—review and editing. Z.C.: data curation, writing—review and editing. J.W.: validation, formal analysis. X.L. (Xin Liu): validation, investigation. X.B.: investigation, data curation. F.H.: visualization, supervision. Z.W.: conceptualization, writing—review and editing, supervision, funding acquisition. All authors have read and agreed to the published version of the manuscript.

Funding: This research received no external funding.

Data Availability Statement: The raw data supporting the conclusions of this article will be made available by the authors on request.

Acknowledgments: The authors acknowledge Junjie Li and Jincheng Wang for their experimental and writing guidance.

Conflicts of Interest: Author Xinbo Shi was employed by the company Xi'an Superalloy Technology Co., Ltd. The remaining authors declare that the research was conducted in the absence of any commercial or financial relationships that could be construed as a potential conflict of interest.

References

1. Yeh, J.W.; Chen, S.K.; Lin, S.J.; Gan, J.Y.; Chin, T.S.; Shun, T.T.; Tsau, C.H.; Chang, S.Y. Nanostructured high-entropy alloys with multiple principal elements: Novel alloy design concepts and outcomes. *Adv. Eng. Mater.* **2004**, *6*, 299–303. [CrossRef]
2. Cantor, B.; Chang, I.; Knight, P.; Vincent, A. Microstructural development in equiatomic multicomponent alloys. *Mater. Sci. Eng. A* **2004**, *375*, 213–218. [CrossRef]
3. Varalakshmi, S.; Kamaraj, M.; Murty, B. Processing and properties of nanocrystalline CuNiCoZnAlTi high entropy alloys by mechanical alloying. *Mater. Sci. Eng. A* **2010**, *527*, 1027–1030. [CrossRef]
4. He, F.; Wang, Z.; Li, Y.; Wu, Q.; Li, J.; Wang, J.; Liu, C. Kinetic ways of tailoring phases in high entropy alloys. *Sci. Rep.* **2016**, *6*, 34628. [CrossRef]
5. Shun, T.-T.; Du, Y.-C. Microstructure and tensile behaviors of FCC $Al_{0.3}$CoCrFeNi high entropy alloy. *J. Alloys Compd.* **2009**, *479*, 157–160. [CrossRef]
6. Tang, K.; Chen, L.; Wang, S.; Wei, R.; Yang, Z.; Jiang, F.; Sun, J. Development of a large size FCC high-entropy alloy with excellent mechanical properties. *Mater. Sci. Eng. A* **2019**, *761*, 138039. [CrossRef]
7. Feuerbacher, M.; Lienig, T.; Thomas, C. A single-phase bcc high-entropy alloy in the refractory Zr-Nb-Ti-V-Hf system. *Scr. Mater.* **2018**, *152*, 40–43. [CrossRef]
8. Wang, Z.; Fang, Q.; Li, J.; Liu, B.; Liu, Y. Effect of lattice distortion on solid solution strengthening of BCC high-entropy alloys. *J. Mater. Sci. Technol.* **2018**, *34*, 349–354. [CrossRef]
9. Vaidya, M.; Sen, S.; Zhang, X.; Frommeyer, L.; Rogal, Ł.; Sankaran, S.; Grabowski, B.; Wilde, G.; Divinski, S.V. Phenomenon of ultra-fast tracer diffusion of Co in HCP high entropy alloys. *Acta Mater.* **2020**, *196*, 220–230. [CrossRef]
10. Yamabe-Mitarai, Y.; Yanao, K.; Toda, Y.; Ohnuma, I.; Matsunaga, T. Phase stability of Ti-containing high-entropy alloys with a bcc or hcp structure. *J. Alloys Compd.* **2022**, *911*, 164849. [CrossRef]
11. Dong, Y.; Gao, X.; Lu, Y.; Wang, T.; Li, T. A multi-component $AlCrFe_2Ni_2$ alloy with excellent mechanical properties. *Mater. Lett.* **2016**, *169*, 62–64. [CrossRef]
12. Wu, Q.; He, F.; Li, J.; Kim, H.S.; Wang, Z.; Wang, J. Phase-selective recrystallization makes eutectic high-entropy alloys ultra-ductile. *Nat. Commun.* **2022**, *13*, 4697. [CrossRef]
13. Li, H.; Zhou, Y.; Yu, L.; Chen, Q.; Liu, W.; Zeng, S.; Zhang, H.; Zhu, Y.; Zhang, H.; Zhang, H.; et al. Designing hierarchical eutectic high-entropy alloys via partial similar substitution in the Ni-Fe-Ti-Hf-Nb alloys. *Mater. Sci. Eng. A* **2023**, *880*, 145263. [CrossRef]
14. Jin, X.; Bi, J.; Zhang, L.; Zhou, Y.; Du, X.; Liang, Y.; Li, B. A new CrFeNi2Al eutectic high entropy alloy system with excellent mechanical properties. *J. Alloys Compd.* **2019**, *770*, 655–661. [CrossRef]
15. Wang, J.; Wu, Q.; Li, Y.; Wang, Z.; Li, J.; Wang, J. Phase selection of BCC/B2 phases for the improvement of tensile behaviors in FeNiCrAl medium entropy alloy. *J. Alloys Compd.* **2022**, *916*, 165382. [CrossRef]
16. Wang, J.; Wang, Z.; Shi, X.; Liu, X.; Jia, Y.; Li, J.; He, F.; Wang, J. Alloying behavior of W and Mo in the as-cast dual-phase FeNiCrAl multi-component alloys. *J. Alloys Compd.* **2023**, *951*, 169951. [CrossRef]
17. Liu, X.; Wang, J.; Shi, X.; Jia, Y.; Liu, L.; Li, J.; He, F.; Wang, Z.; Wang, J. Effects of metalloid Si on the microstructure and mechanical properties of $Fe_{36}Ni_{36}Cr_{10}Mo_1Al_{17-X}Si_X$ alloys. *J. Alloys Compd.* **2023**, *963*, 171164. [CrossRef]

18. Wani, I.S.; Bhattacharjee, T.; Sheikh, S.; Clark, I.T.; Park, M.H.; Kawa, T.O.; Guo, S.; Bhattacharjee, P.P.; Tsuji, N. Cold-rolling and recrystallization textures of a nano-lamellar $AlCoCrFeNi_{2.1}$ eutectic high entropy alloy. *Intermetallics* **2017**, *84*, 42–51. [CrossRef]
19. Wang, J.; Wang, Z.; Wu, Q.; Huang, Y.; Li, J.; He, F.; Wang, L.; Wang, J. Simultaneously enhance the tensile strength and ductility of dual-phase $Fe_{37}Ni_{36}Cr_{10}Al_{17}$ alloy via phase-selective recrystallization and aging. *Mater. Lett.* **2023**, *352*, 135182. [CrossRef]
20. Reddy, S.; Yoshida, S.; Sunkari, U.; Lozinko, A.; Joseph, J.; Saha, R.; Fabijanic, D.; Guo, S.; Bhattacharjee, P.; Tsuji, N. Engineering heterogeneous microstructure by severe warm-rolling for enhancing strength-ductility synergy in eutectic high entropy alloys. *Mater. Sci. Eng. A* **2019**, *764*, 138226. [CrossRef]
21. Reddy, S.; Sunkari, U.; Lozinko, A.; Saha, R.; Guo, S.; Bhattacharjee, P. Microstructural design by severe warm-rolling for tuning mechanical properties of $AlCoCrFeNi_{2.1}$ eutectic high entropy alloy. *Intermetallics* **2019**, *114*, 106601. [CrossRef]
22. Tripathy, B.; Ojha, P.; Bhattacharjee, P. Effect of warm-rolling on microstructure and superior mechanical properties of a cost-effective $AlCrFe_2Ni_2$ high entropy alloy. *J.Alloys Compd.* **2023**, *948*, 169783. [CrossRef]
23. Pradhan, S.; Tripathy, S.; Singh, R.; Murugaiyan, P.; Roy, D.; Humane, M.M.; Chowdhury, S.G. On the grain boundary character evolution in non equiatomic high entropy alloy during hot rolling induced dynamic recrystallization. *J. Alloys Compd.* **2022**, *922*, 166126. [CrossRef]
24. Liu, Z.; Xiong, Z.; Chen, K.; Cheng, X. Large-size high-strength and high-ductility $AlCoCrFeNi_{2.1}$ eutectic high-entropy alloy produced by hot-rolling and subsequent aging. *Mater. Lett.* **2022**, *315*, 131933. [CrossRef]
25. Kumar, P.; Samal, S.; Ghosh, A. Effect of hot rolling and annealing on microstructure and mechanical properties of the Fe-Co-Cr-Ni-V-Zr_x (x = 0–5) high entropy alloys. *J. Alloys Compd.* **2024**, *970*, 172447. [CrossRef]
26. Sourav, A.; Yebaji, S.; Thangaraju, S. Structure-property relationships in hot forged $Al_xCoCrFeNi$ high entropy alloys. *Mater. Sci. Eng. A* **2020**, *793*, 139877. [CrossRef]
27. Zhou, J.; Liao, H.; Chen, H.; Huang, A. Effects of hot-forging and subsequent annealing on microstructure and mechanical behaviors of $Fe_{35}Ni_{35}Cr_{20}Mn_{10}$ high-entropy alloy. *Mater. Charact.* **2021**, *178*, 111251. [CrossRef]
28. Sajadi, S.A.; Toroghinejad, M.R.; Rezaeian, A.; Wu, Z. Effect of annealing treatment on microstructural and mechanical properties of a hot-forged $FeCrCuMn_2Ni_2$ high-entropy alloy. *Materialia* **2022**, *26*, 101618. [CrossRef]
29. Karimzadeh, M.; Malekan, M.; Mirzadeh, H.; Saini, N.; Li, L. Hot deformation behavior analysis of as-cast CoCrFeNi high entropy alloy using Arrhenius-type and artificial neural network models. *Intermetallics* **2024**, *168*, 108240. [CrossRef]
30. Peng, P.; Feng, X.; Li, S.; Wei, B.; Zhang, M.; Xu, Y.; Zhang, X.; Ma, Z.; Wang, J. Effect of heat treatment on microstructure and mechanical properties of as-cast $AlCoCrFeNi_{2.1}$ eutectic high entropy alloy. *J. Alloys Compd.* **2023**, *939*, 168843. [CrossRef]
31. Kuznetsov, A.V.; Shaysultanov, D.G.; Stepanov, N.D.; Salishchev, G.A.; Senkov, O.N. Tensile properties of an AlCrCuNiFeCo high-entropy alloy in as-cast and wrought conditions. *Mater. Sci. Eng. A* **2012**, *533*, 107–118. [CrossRef]
32. Ming, K.; Li, L.; Li, Z.; Bi, X.; Wang, J. Grain boundary decohesion by nanoclustering Ni and Cr separately in CrMnFeCoNi high-entropy alloys. *Sci. Adv.* **2019**, *5*, eaay0639. [CrossRef]
33. Tsai, C.W.; Tsai, M.H.; Yeh, J.W.; Yang, C.C. Effect of temperature on mechanical properties of $Al_{0.5}CoCrCuFeNi$ wrought alloy. *J. Alloys Compd.* **2010**, *490*, 160–165. [CrossRef]
34. Tang, Z.; Senkov, O.N.; Parish, C.M.; Zhang, C.; Zhang, F.; Santodonato, L.J.; Wang, G.; Zhao, G.; Yang, F.; Liaw, P.K. Tensile ductility of an AlCoCrFeNi multi-phase high-entropy alloy through hot isostatic pressing (HIP) and homogenization. *Mater. Sci. Eng. A* **2015**, *647*, 229–240. [CrossRef]
35. Jiang, L.; Lu, Y.; Song, M.; Lu, C.; Sun, K.; Cao, Z.; Wang, T.; Gao, F.; Wang, L. A promising $CoFeNi_2V_{0.5}Mo_{0.2}$ high entropy alloy with exceptional ductility. *Scr. Mater.* **2019**, *165*, 128–133. [CrossRef]
36. Liu, X.; Wang, J.; Jia, Y.; He, X.; Wang, Z.; He, F.; Li, J.; Wang, J. Enhancing the High Temperature Tensile Strength of $Fe_{36}Ni_{36}Cr_{10}Mo_1Al_{17}$ Alloy by Substituting Al with Si. *Met. Mater. Int.* **2024**, *1*, 1–8. [CrossRef]
37. Haas, S.; Manzoni, A.M.; Krieg, F.; Glatzel, U. Microstructure and mechanical properties of precipitate strengthened high entropy alloy $Al_{10}Co_{25}Cr_8Fe_{15}Ni_{36}Ti_6$ with additions of hafnium and molybdenum. *Entropy* **2019**, *21*, 169. [CrossRef]

metals

MDPI

Article

Study of Tensile and Compressive Behavior of ECO-$Mg_{97}Gd_2Zn_1$ Alloys Containing Long-Period Stacking Ordered Phase with Lamellar Structure

Gerardo Garcés [1,*], Judit Medina [1], Pablo Pérez [1], Rafael Barea [2], Hyunkyu Lim [3], Shae K. Kim [3], Emad Maawad [4], Norbert Schell [4] and Paloma Adeva [1]

[1] Department of Physical Metallurgy, CENIM-CSIC, Avenida Gregorio del Amo 8, 8040 Madrid, Spain; judit.medina@cenim.csic.es (J.M.); zubiaur@cenim.csic.es (P.P.); adeva@cenim.csic.es (P.A.)
[2] Department of Industrial Engineering, Universidad Nebrija, Campus Madrid-Princesa, Santacruz de Marcenado, 27, 28015 Madrid, Spain; rbarea@nebrija.es
[3] Casting Research, Korea Institute of Industrial Technology (KITECH), 7-47 Songdo-dong, Yeonsu-gu, Incheon 406-840, Republic of Korea; hklim@kitech.re.kr (H.L.); shae@kitech.re.kr (S.K.K.)
[4] Institute of Materials Physics, Helmholtz-Zentrum Geesthacht, Max-Planck-Str. 1, 21502 Geesthacht, Germany; emad.maawad@hereon.de (E.M.); norbert.schell@hzg.de (N.S.)
* Correspondence: ggarces@cenim.csic.es; +34-915538900

Abstract: A suitable heat treatment in the $Mg_{97}Gd_2Zn_1$ (at.%) alloy in the as-cast condition results, after extrusion at high temperature, in a two-phase lamellar microstructure consisting of magnesium grains with thin lamellar shape precipitates and long fibers of the 14H-Long-Period Stacking Ordered (LPSO) phase elongated in the extrusion direction. The magnesium matrix is not fully recrystallized and highly oriented coarse non-dynamically recrystallized (non-DRXed) grains (17% volume fraction) elongated along the extrusion direction remain in the material. The deformation mechanisms of the extruded alloy have been studied measuring the evolution of the internal strains during in situ tension and compression tests using synchrotron diffraction radiation. The data demonstrate that the macroscopic yield stress is governed by the activation of the basal slip system in the randomly oriented equiaxed dynamic recrystallized (DRXed) grains. Non-DRXed grains, due to their strong texture, are favored oriented for the activation of tensile twinning. However, the presence of lamellar-shape precipitates strongly delays the propagation of lenticular thin twins through these highly oriented grains and they have no effect on the onset of the plastic deformation. Therefore, the tension–compression asymmetry is low since the plasticity mechanism is independent of the stress mode.

Keywords: magnesium alloys; mechanical properties; synchrotron radiation diffraction; long-period stacking ordered structures

1. Introduction

Mg-Rare earth (RE)-Zn alloys containing Long-Period Stacking Ordered (LPSO) phases exhibit high mechanical strength with substantial ductility [1–4]. Two types of these alloys can be distinguished depending on the presence or absence of the LPSO-phase in the as-cast condition. According to the RE elements added, these alloys can be referred to as Type I and Type II. Type I corresponds to Mg-(Y, Dy, Ho, Er, Tm)-Zn alloys in which the LPSO-phase is formed during the casting process [5–10]. In the case of Mg- (Gd, Tb,. . .)–Zn alloys, referred to as Type II, the LPSO-phase does not appear in the as-cast condition and a subsequent high-temperature thermal treatment is required to develop it [11–18]. After a solution treatment, a hardness peak can be reached by ageing the material at low temperatures. Yamasaki et al. [13] reported, in the $Mg_{97}Gd_2Zn_1$ (at.%) alloy, the formation during isothermal ageing of stacking faults and lamellar 14H phase at intermediate and high temperatures (300–500 °C), while intermetallic β' (orthor, Mg_7Gd [19]), β_1 (fcc, Mg_5Gd)

and β (fcc, Mg_5Gd) phases formed at low temperatures (~200 °C). On the other hand, Nie et al. [14] reported that the peak aged condition in $Mg_{98.6}Gd_1Zn_{0.4}$ (at.%) is caused by the formation of lamellar γ″ (ordered hexagonal structure, P6 $\bar{2}$m) and γ′ (disordered hexagonal structure, P$\bar{3}$m1). Since lamellar-shape precipitates are located parallel to the basal plane, these precipitates are considered to be ineffective obstacles to the motion of <a> dislocations along the basal plane. Nevertheless, a significantly low activity of the basal slip system in the Mg matrix in between LPSO lamellae, when interlamellar space is below 20 nm, has been also reported [20]. The high concentration of solute atoms near LPSO lamellae provides a strong solute strengthening effect. On the other hand, tensile twinning is also an important deformation system in magnesium alloys, especially in those alloys with intense texture. Lamellar-shape precipitates offer little resistance to the tensile twinning deformation mode [16], although they are effective in temporally delaying the coalescence twinning step [16,18,21]. Thus, microcracks can be initially nucleated along the (LPSO-phase/lamellar γ′ phase)/α-Mg matrix interfaces, and a significant stress dissipation is induced by mutual interactions between the tensile twinning and the kinking of the lamellar γ′ phase, leading to an increase in fracture toughness KIc [22]. At high temperatures, the presence of lamellar γ′ phase is an important obstacle to non-basal slip systems and it creates nucleation sites for extremely fine DRXed grains [23,24].

The hexagonal close-packed lattice of magnesium, with a limited number of active deformation systems, promotes the formation of a strong crystallographic texture when the alloy is thermomechanically processed, inducing the tension–compression yield asymmetry phenomenon. The mechanical asymmetry of magnesium alloys has been widely investigated, since it is an important factor limiting their industrial applications [25–29]. The tension–compression asymmetry in magnesium alloys containing LPSO-phases depends on the processing route and the microstructure [30]. Geng et al. [16] studied the influence of lamellar-shape precipitates on the tension–compression asymmetry in an extruded Mg-Gd-Zn alloy. Due to the weak texture generated during the full recrystallization process, the alloy showed negligible yield stress asymmetry. Yang et al. [18] also reported negligible yield stress asymmetry in a $Mg_{97.3}Gd_{2.1}Zn_{0.6}$ alloy characterized by highly oriented non-recrystallized grains with a high density of thin LPSO plates within the magnesium grains. It is expected that lamellar-shape precipitates could enhance dynamic recrystallization, minimizing the presence of non-DRXed grains. The study will be carried out through the measurement of the internal strains obtained using synchrotron radiation diffraction during in situ tensile and compressive tests.

2. Materials and Methods

Magnesium alloys with composition $Mg_{97}Gd_2Zn_1$ (at.%) were cast using an Environment Conscious (ECO) process, with the addition of 0.3 wt.% of CaO. The cast billet was thermally treated (TT condition) at 520 °C for 8 h while buried in MgO sand to minimize alloy oxidation. The cooling of the billets was carried out inside the furnace at 10 °Cmin^{-1}. The billet was machined at a 41 mm diameter and then it was extruded at an extrusion temperature of 350 °C, an extrusion rate of 0.5 mms^{-1} and an extrusion ratio of 18:1.

Microstructural characterization of the alloys was carried out by optical microscopy (OM) and scanning and transmission electron microscopy (SEM (JEOL-JSM 6500F, JEOL-JSM 6500F, JEOL, Tokyo, Japan and Hitachi S4800J, Hitachi High-Tech Corporation, Ibaraki, Japan) and TEM (JEOL JEM 2010, JEOL, Tokyo, Japan), respectively). Samples for SEM observation were prepared by mechanical polishing using colloidal silica. Samples were analyzed at an operating voltage of 15 kV in both SEMs. Volume fractions of each alloy constituent (LPSO phase, magnesium DRXed grains and magnesium non-DRXed grains) were evaluated as follows. Firstly, the volume fraction of the LPSO phase was evaluated in the polished sample using the Fiji Image J software 2.9.0 (LOCI, University of Wisconsin, Madison, WI, USA) [31]. The backscattered SEM image clearly differentiates the LPSO phase due to its higher gadolinium and zinc concentrations with respect to the magnesium phase. The volume fractions of the DRXed and non-DRXed grains were evaluated in

the extruded sample after etching using OM. In this condition, the LPSO-phase and non-DRXed grains had similar aspects. Therefore, the volume fraction of DRXed grains was also evaluated using again Fiji Image J software. The volume fraction of the non-DRXed grains was balanced with the other two constituents. The grain size was measured by quantitative image analysis.

TEM specimens of deformed samples were prepared by electrolytic polishing using a reactive mixture of 5.3 g lithium chloride, 11.2 g magnesium perchlorate, 500 mL methanol and 100 mL butoxy-ethanol at −50 °C and 50 V.

The crystallographic texture of the alloy was evaluated using the Electron Backscattered Diffraction (EBSD) technique and the Rietveld analysis of the synchrotron diffraction patterns. Specimens for EBSD measurements were finally etched using a solution of 7 mL acetic acid, 3 mL nitric acid, 30 mL of ethanol and 10 mL of water. EBSD acquisition was carried out in a direction perpendicular to the extrusion direction and the data were recorded and analyzed using Channel 5 software (Oxford Instruments, Abingdon, Oxfordshire, UK).

Synchrotron radiation diffraction was carried out during in situ tension and compression tests at the P07B-HEMS beamline of PETRA III, at the DeutschesElektronen-Synchrotron (DESY) (Hamburg, Germany). Cylindrical samples of diameter 5 mm and length 25 mm and cylinders of diameter 5 mm and length 10 mm were used in tension and compression, respectively. In both cases samples were machined along the extrusion direction and tested at a strain rate of 10^{-4} s^{-1} at room temperature. Samples were deformed in tension and compression in a tensile rig at an initial strain rate of 10^{-4} s^{-1}. The diffraction patterns were recorded using an exposure time of 0.5 s by a Perkin-Elmer XRD 1622 flat-panel detector (Perkin-Elmer, Waltham, MA, USA) with an array of 2048^2 pixels, and an effective pixel size of 200 × 200 μm^2. The beam energy was 87 keV, corresponding to a wavelength of 0.014 nm. LaB6 was used as a reference to calibrate the acquired diffraction spectra. The detector-to-sample distance was set to 1637 mm.

Conventional line profiles were obtained by azimuthal integration of the Debye–Scherrer rings. The synchrotron radiation beam was positioned at the center of the sample, with the gauge volume defined approximately by the beam section (0.8 × 0.8 mm^2) and the cylinder diameter. The elastic strain for each orientation can be calculated by the shift in the position of the diffraction peak:

$$\varepsilon_{hkl} = \frac{d_{hkl} - d_{0,hkl}}{d_{0,hkl}} \quad (1)$$

where d_{hkl} and $d_{0,hkl}$ are the planar spacing of the *hkl* plane in the stressed and stress-free crystal. The lattice spacing and the diffraction angle θ are related through Bragg's law.

The macroscopic texture was evaluated by Rietveld texture analysis using MAUD software (Luca Lutterotti, University of Trento, Italy) [32,33]. The 2D detector image is converted to a set of diffraction patterns using the Image J plugin in the software (LOCI, University of Wisconsin, WI, USA) [34,35], fitting the α-Mg (P63/mmc) and LPSO-14H (P63/mmc) [36]. The best fit to the experimental data was achieved using the E-WIMV algorithm with 5° resolution. This procedure was repeated within the compression test, obtaining the evolution of the texture as a function of the compressive strain. From the (0002) pole figure, the volume fraction of twins can be calculated following the procedure reported by Agnew et al. [37], given by

$$f_{tw} = \int_{\varphi=0}^{\varphi\approx 57^\circ} [I(\varphi) - I_0] \, sin\varphi \, d\varphi \quad (2)$$

where φ is the angle of tilt between the (0002) poles and the compression axis and $I(\varphi)$ is the intensity at that tilt angle φ.

3. Results

The microstructure of the alloy in the as-cast condition, shown in Figure 1a, is characterized by the coexistence of the magnesium matrix (grey phase) with the intermetallic Mg_3Gd phase (white phase) [13]. The magnesium phase around the intermetallic phase shows a contrast provoked by an increase of the gadolinium solid solution in the magnesium phase. After thermal treatment, the microstructure changes drastically (Figure 1b). On one hand, the Mg_3Gd phase transforms into the LPSO-phase with composition Mg-29%Gd-10%Zn-0.2%Ca (wt.%). On the other hand, the precipitation of fine lamellae inside the Mg grains takes place (Figure 1c). The volume fraction of the LPSO phase is 17%. After extrusion at 350 °C, coarse LPSO-phase is deformed and elongated along the extrusion direction (Figure 1d).

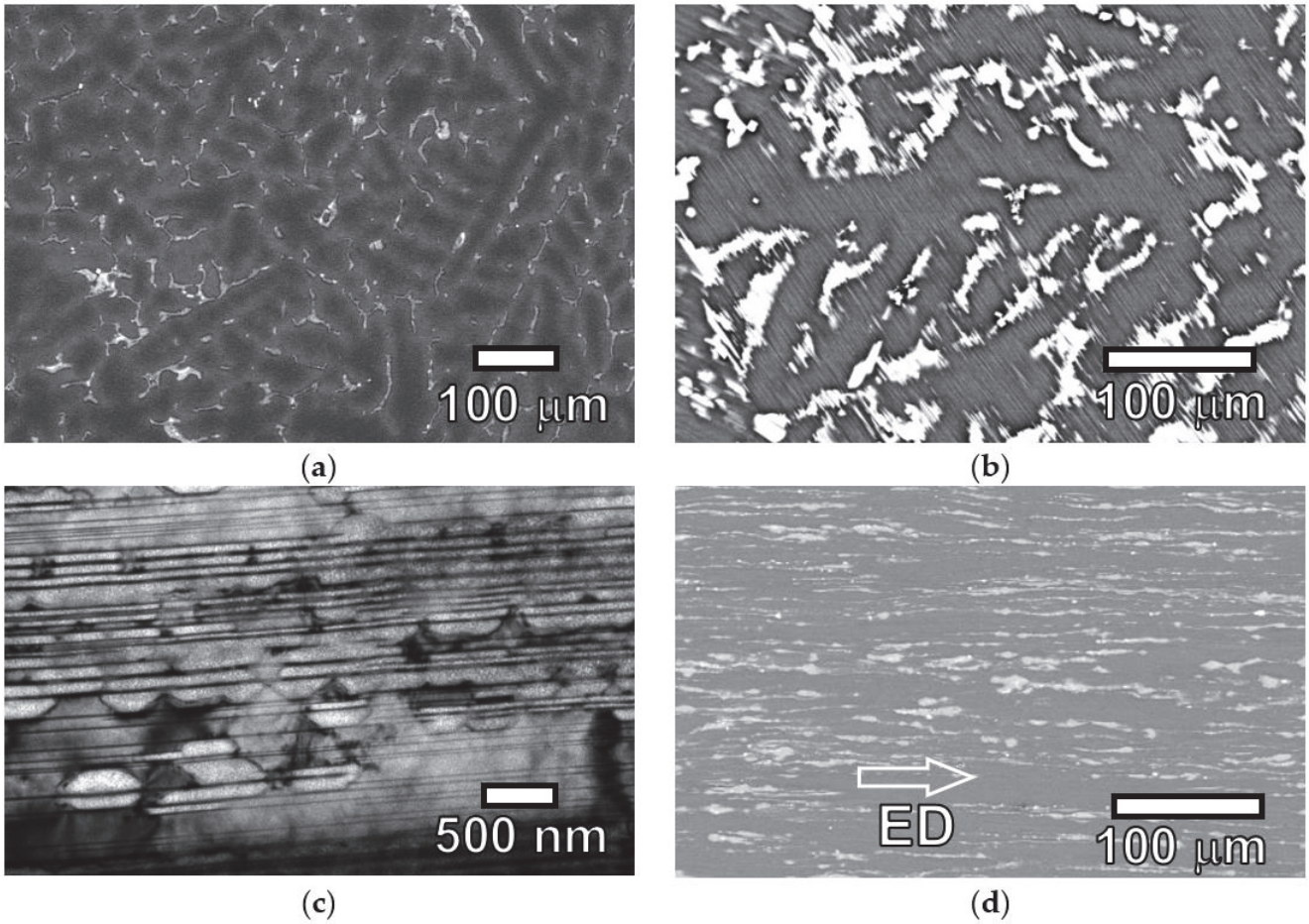

Figure 1. (**a**) Microstructure of the cast ECO-$Mg_{97}Gd_2Zn_1$ alloy. (**b**) Microstructure of the cast ECO-$Mg_{97}Gd_2Zn_1$ alloy after the thermal treatment, showing the lamellar structure in the magnesium phase. (**c**) Bright field image of the magnesium phase at the zone axis B = $[11\bar{2}0]$. (**d**) Microstructure of the extruded ECO-$Mg_{97}Gd_2Zn_1$ alloy along the extrusion direction (ED).

The grain structure after extrusion is shown in the orientation image maps (OIMs) of Figure 2a,b. The material is not completely recrystallized and the microstructure exhibits dynamic recrystallized (DRXed) grains with an average grain size of 1 μm (Figure 3) and non-dynamic recrystallized (non-DRXed) grains elongated along the extrusion direction, with a longer dimension of 300–400 μm. The volume fractions of fine DRXed and coarse elongated non-DRXed grains are 64 and 19%, respectively. DRXed grains are randomly oriented but the elongated, non-DRXed grains are highly oriented, with their basal plane parallel to the extrusion direction (grain A in Figure 2a), as observed in the (0002) pole figure of Figure 2c.

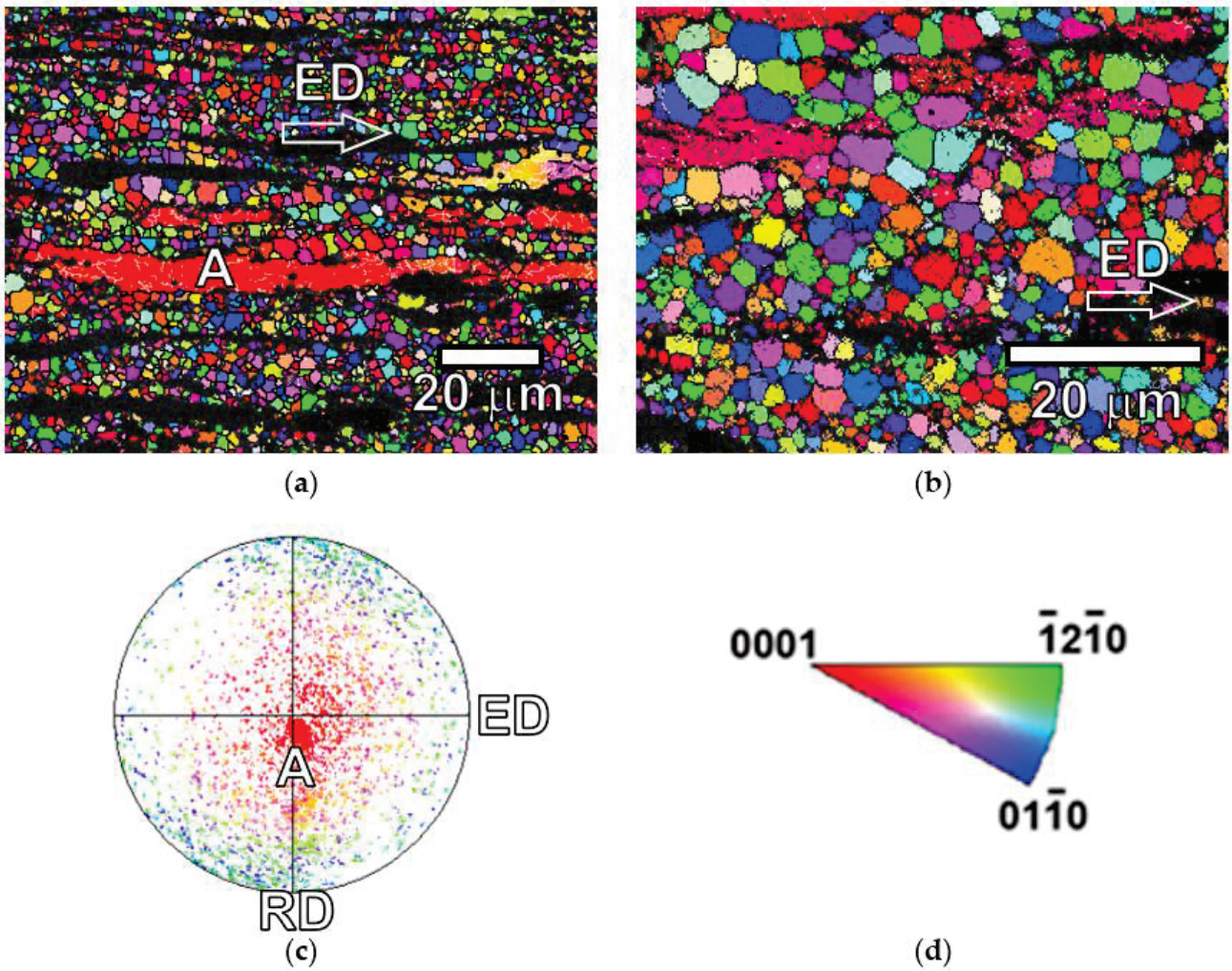

Figure 2. (**a**) Orientation image maps (OIMs) along the extrusion direction of the extruded ECO-$Mg_{97}Gd_2Zn_1$ alloy. (**b**) Detail of fine DRXed grains. (**c**) {0002} pole figure corresponding to EBSD map of (**a**). Red-orange intense accumulation in the radial direction comes from the non-DRXed grains (grain A). (**d**) IPF color key.

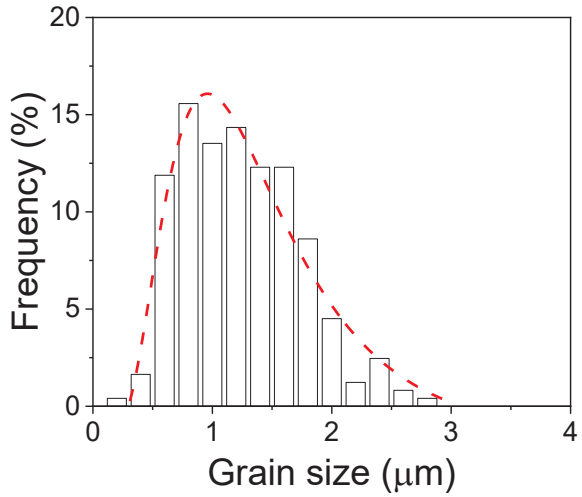

Figure 3. Grain histogram of DRXed grains.

The macroscopic texture was also evaluated using Rietveld texture analysis of the diffraction pattern obtained from the Debye–Scherrer diffracted rings. Figure 4 shows the Debye–Scherrer rings obtained before tension or compression tests for the extruded $Mg_{97}Gd_2Zn_1$ alloy (Figure 4a), as well as a detail of the innermost ring, corresponding to the (0002) diffracted ring of the 14H-LPSO phase. The intensity of each diffraction ring changes along the azimuthal angle due to the crystallographic texture of the magnesium and LPSO phases. Figure 4b shows the axial and radial diffraction pattern obtained from the integration of Figure 4a. In this plot, the different intensity of each diffraction peak corroborates the development of a crystallographic texture during the extrusion process. It is important to point out the presence of a strong diffraction peak in the radial direction at 0.45°, corresponding to the 0002-diffraction peak of the 14H-LPSO phase. In the axial direction, the most intense diffraction peak due to the magnesium phase corresponds to the $(10\bar{1}0)$ plane, which is perpendicular to the extrusion direction.

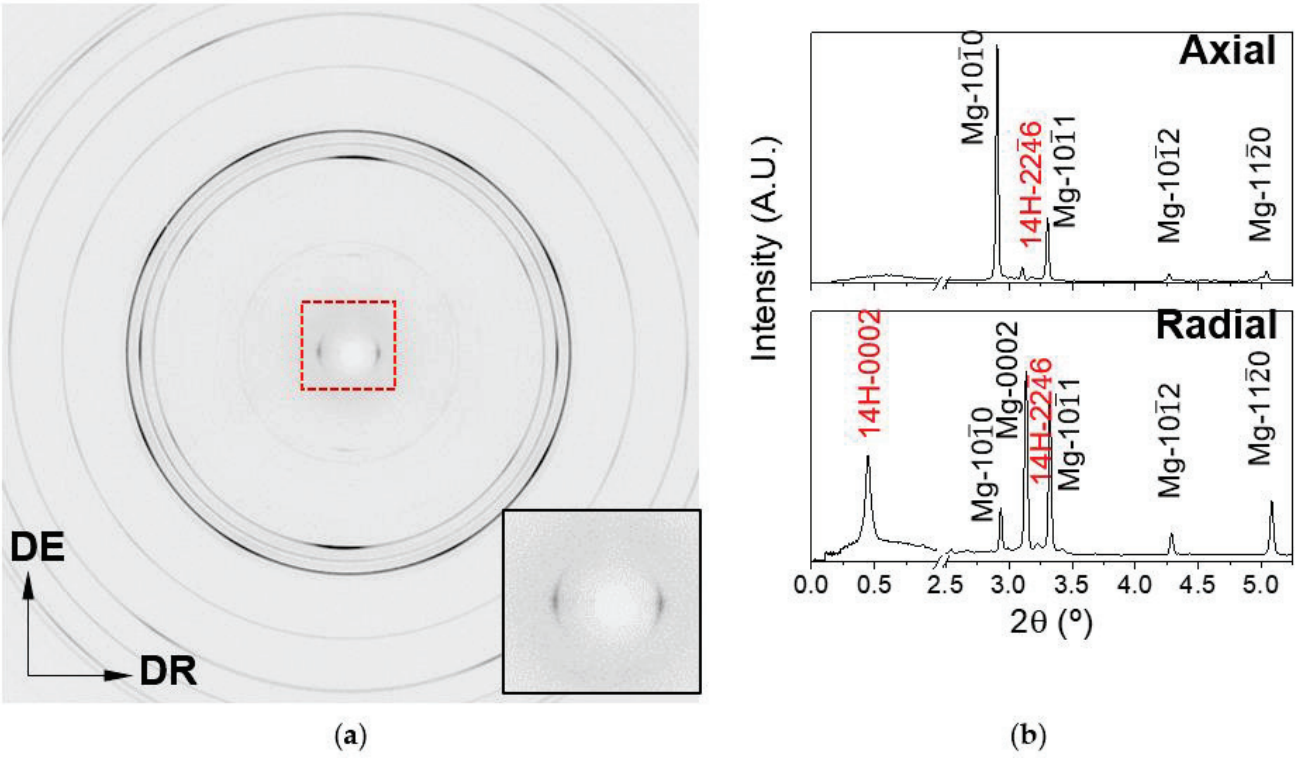

Figure 4. (**a**) Synchrotron radiation diffraction pattern recorded on the 2D flat-panel detector before the tension and compression tests. Detail of the innermost ring corresponding to the (0002) diffracted ring of the 14H-LPSO phase. (**b**) Axial and radial diffracted pattern integrated from (**a**).

Rietveld fitting of diffraction patterns in the axial, 45° between axial/radial direction and radial direction has been performed for the alloy in the as-extruded condition, assuming the presence of α-Mg and 14H-LPSO-phase (see Figure 5a–c). The pole figures obtained from the Rietveld texture analysis are presented in Figure 5d–f for the magnesium phase ($\{10\bar{1}0\}$ and (0002) pole figures) and LPSO-phase ((00014) pole figure).

Figure 6a–e show the microstructure using TEM of the non-DRXed grains, DRXed grains and short fibers of LPSO-phase, respectively. Non-DRXed grains (Figure 6a) are highly deformed due to the accumulation of a high dislocation density. Even more, sub-grains limited by low angle grain boundaries are observed within these grains (see white arrow in Figure 6a). Within these grains, a lamellar structure is still observed, as found for the TT condition. However, the thin γ lamellar precipitates, about 10–20 nm in thickness, become coarser than those seen in the TT alloy (Figure 6b). In any case, thin precipitates of several nm are still placed in the basal plane. These precipitates are coherent with the

magnesium matrix and generate diffuse streaks along the [0002] direction in the SAED pattern of Figure 6c.

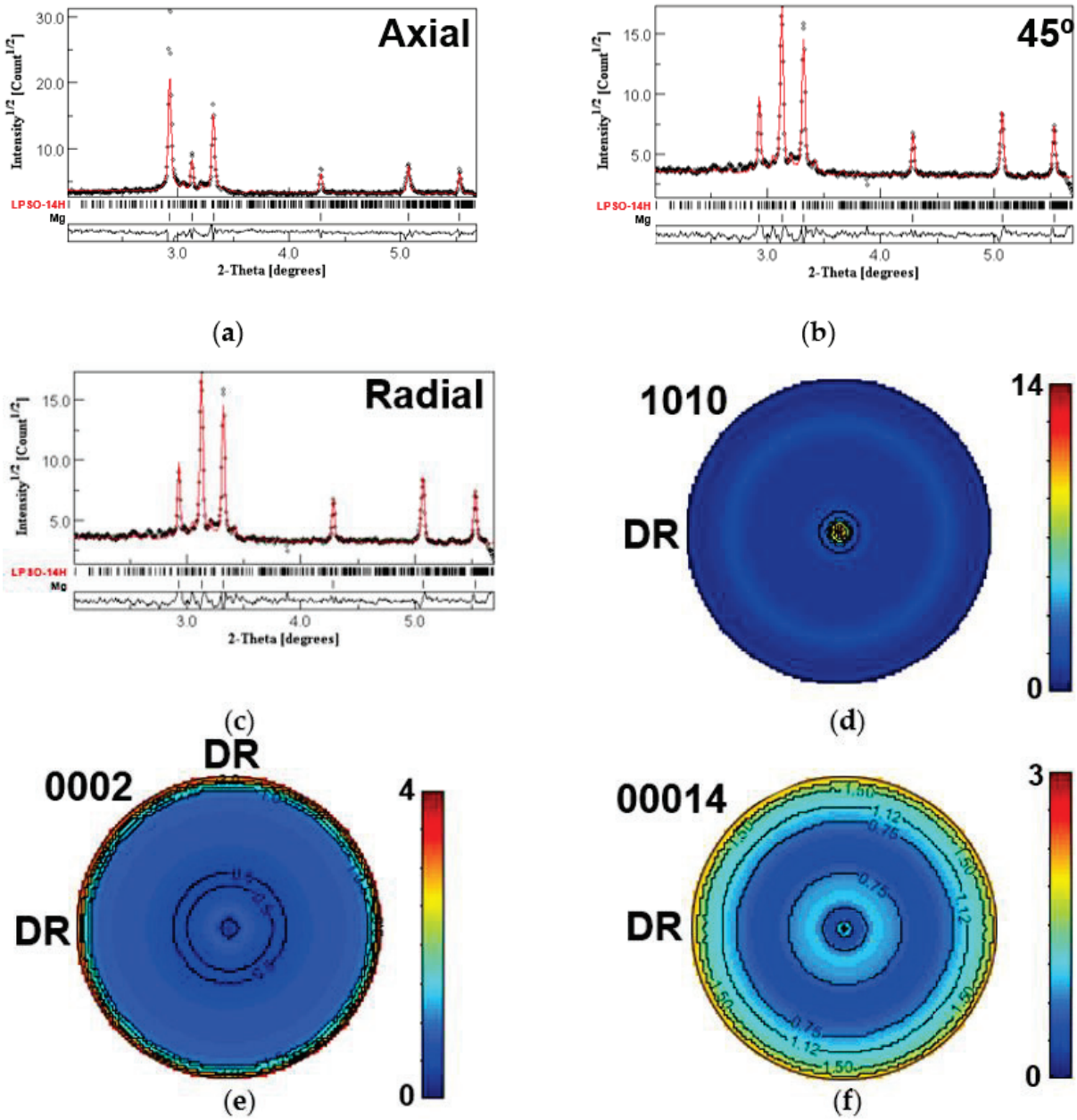

Figure 5. Rietveld analysis of diffraction patterns of extruded $Mg_{97}Gd_2Zn_1$ alloy: (**a**) axial, (**b**) 45° and (**c**) radial directions. (**d**) {0002} and (**e**) {10$\bar{1}$0} pole figures obtained from the magnesium phase and (**f**) {00014} pole figure from the 14H-LPSO phase.

Figure 6d shows a bright field image of DRXed grains. Thin basal precipitates are equally observed within these grains. When thin precipitates are tilted, a Moiré structure (white arrow in Figure 6d) reveals that they are planar defects, I_2 stacking faults, generated by the formation of Shockley partial dislocations. It is important to point out that this structure is not homogeneous over the entire grain.

Finally, Figure 6e–g show bright field images of the LPSO-phase and its corresponding SAED pattern at the zone axis B = [11$\bar{2}$0]. As found in the non-DRXed grains, the LPSO-phase is highly deformed. The thickness of the LPSO-phase fiber is around 1 μm. Inside

the LPSO-phase, a fringe structure with a spacing of about 1.8 nm along the c direction at the zone axis B = [11$\bar{2}$0] is measured, corroborating the formation of the 14H structure [38].

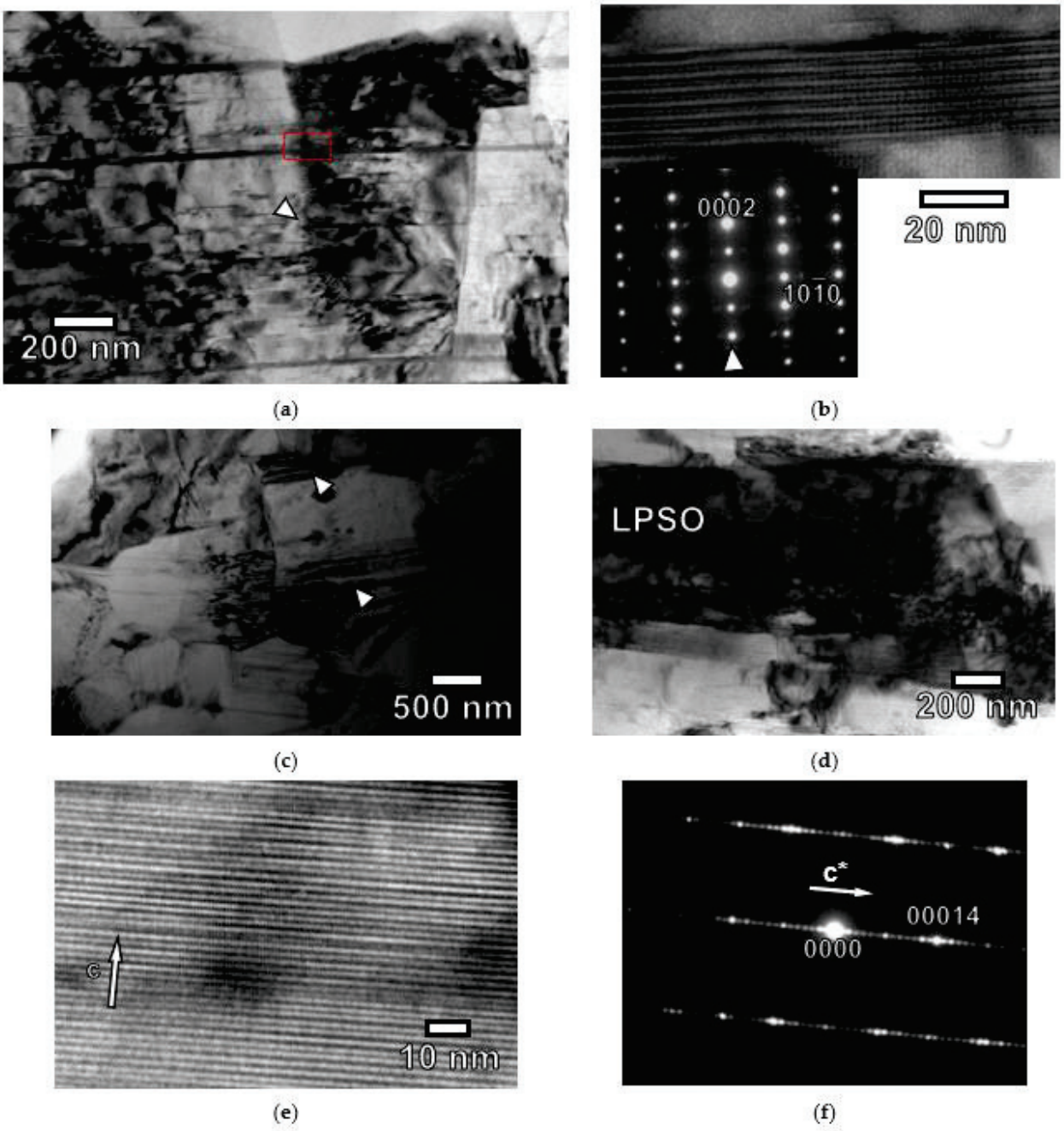

Figure 6. (**a**) Bright field image of a non-DRXed grain at the zone axis B = [11$\bar{2}$0]. (**b**) Detail of (**a**) corresponding to the 14H-LPSO lamellar structure and SAED pattern of the non-DRXed grain shown at the zone axis B = [11$\bar{2}$0]. (**c**) Bright field image of the DRXed grains. (**d**) Bright field image of the LPSO phase at the zone axis B = [11$\bar{2}$0]. (**e**) Detail of the LPSO phase shown in (**d**) with g = (0002). (**f**) SAED pattern of the LPSO phase at the zone axis B = [11$\bar{2}$0]. The image is rotated 90° with respect to (**e**).

Tensile and compressive curves obtained during the in situ experiments in the beamline for the extruded $Mg_{97}Gd_2Zn_1$ alloy are shown in Figure 7. The beginnings of the curves for both stress modes seem similar, at least until the point of 3% plastic strain. The yield stress is around 300 MPa in both cases. In compression, the sample was deformed to

the point of 10% plastic deformation. The curve exhibits a slightly sigmoidal or "S-type" concave shape, indicative of {10$\bar{1}$2}<10$\bar{1}$1> extension twinning activation. In any case, it was found that the material flows plastically at stresses slightly higher than those seen under tensile loading.

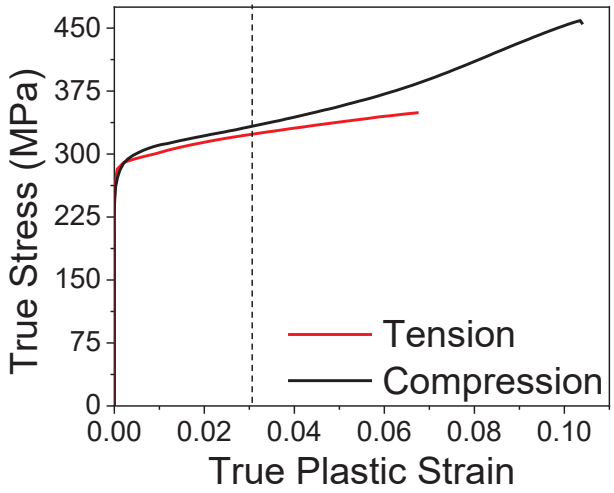

Figure 7. Tensile and compressive true stress–true strain curves for the extruded ECO-$Mg_{97}Gd_2Zn_1$ alloy obtained during the in situ experiments in the beamline.

The evolution of the elastic strains obtained from Equation (1) corresponding to the {10$\bar{1}$0}, {0002}, {10$\bar{1}$1}, {10$\bar{1}$2} and {11$\bar{2}$0} diffraction peaks for the magnesium phase and {4$\bar{2}\bar{2}$6} diffraction peak for the 14H-LPSO are plotted in Figure 8 for tension and compression tests, respectively. The tensile and compressive stress–strain curves obtained during the in situ diffraction experiment are also plotted in Figure 8a,b in order to correlate the evolution of the internal elastic strains and the macroscopic elasto-plastic behavior. The evolution of internal strains in the axial and radial directions are complementary. Therefore, the result described is focused on the internal strains in the axial direction due to their larger changes.

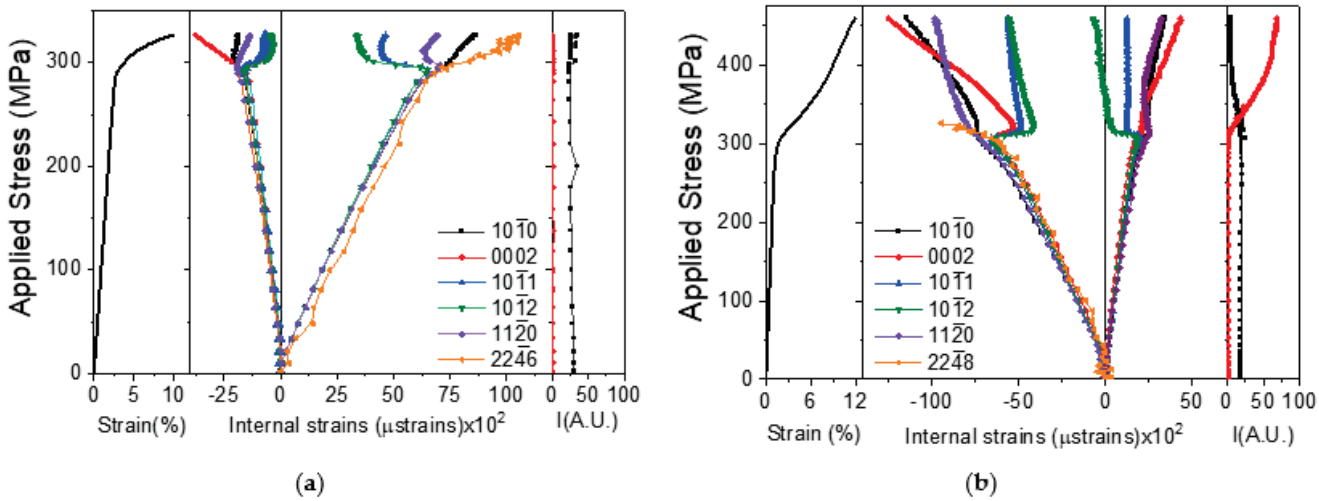

Figure 8. (**a**) Tensile and (**b**) compressive macroscopic stress–strain curves of the ECO-$Mg_{97}Gd_2Zn_1$ alloy obtained during the in situ experiments. Axial and radial internal strains as a function of the applied stress during in situ (**a**) tension and (**b**) compression tests at room temperature. Evolution of the integrated intensity of the {10$\bar{1}$0} and {0002} diffraction peaks during (**a**) tensile and (**b**) compressive tests.

In tension, the macroscopic yield stress, measured at 0.2% of the plastic deformation, was around 292 MPa. Below this stress level, the evolution of the elastic strains for all analyzed diffraction peaks of the magnesium phase as a function of the applied stress is completely linear. Magnesium alloys are elastically isotropic and no differences in the elastic strains for different orientations have been reported in the elastic regime [39]. The slope of the elastic strains corresponding to the diffraction peak of the LPSO-phase evolves in a similar way. The Young modulus of each family of grains was estimated through the slope of the elastic strains in the elastic regime, resulting in a value of 43 GPa. Above 300 MPa, elastic strains of $\{10\bar{1}1\}$ and $\{10\bar{1}2\}$ planes perpendicular to the tensile axis deviate from the straight line, decreasing the elastic internal strain from 6617 μ strains at 293 MPa to 4584 μ strains and 3560 μ strains at 312 MPa, for $\{10\bar{1}1\}$ and $\{10\bar{1}2\}$ diffraction peaks, respectively. After this stress was applied, the elastic strains were constant, which implies that these grains deform plastically.

The decrease in the elastic strains of grains oriented with the $\{10\bar{1}1\}$ and $\{10\bar{1}2\}$ grains perpendicular to the tensile axis is accompanied by an increase in the elastic strains for the grains oriented with their prismatic $\{10\bar{1}0\}$ planes perpendicular to the tensile axis and for the 14H LPSO-phase. It is interesting to point out that elastic strain of the LPSO phase increases faster (as a function of the applied stress) than the prismatic orientation.

The behavior of the elastic strains of grains oriented with their $\{11\bar{2}0\}$ planes perpendicular to the tensile axis is complex and presents three different stages. After yielding, and up to 298 MPa, the elastic strain increases, following a behavior similar to that of the elastic strains for the $\{10\bar{1}0\}$ diffraction peak. Then, the elastic strain decreases following a behavior similar to that of the elastic strains of $\{10\bar{1}1\}$ and $\{10\bar{1}2\}$ diffraction peaks, from 7170 μ strains at 298 MPa to 6359 μ strain at 312 MPa. Then, elastic strain remains almost constant, which implies that grains oriented with $\{11\bar{2}0\}$ planes perpendicular to the tensile axis deform plastically. Finally, the {0002} diffraction peak cannot be accurately fitted in the plastic regime because of its low intensity, as observed in Figure 8a.

In compression, the macroscopic yield stress was around 302 MPa. Below this level of stress, the evolution of the elastic strains as a function of the applied stress exhibits a linear elastic behavior, as found in tension tests. The slope is identical for all analyzed diffraction peaks for the magnesium phase, with a Young modulus of 47 GPa.

After yielding at 300 MPa, a value equal to that for the tensile test, the elastic strain of the $\{10\bar{1}1\}$ and $\{10\bar{1}2\}$ planes perpendicular to the compression axis deviate from the straight line, decreasing (in absolute values) the elastic internal strain from 6620 μ strains at 302 MPa to 4913 μ strains and 4119 μ strains at 320 MPa, for $\{10\bar{1}1\}$ and $\{10\bar{1}2\}$ diffraction peaks, respectively. After this applied stress, the elastic strains are again constant, which implies that these grains deform plastically.

During the compression test, the elastic strain of the grains oriented with $\{10\bar{1}0\}$ planes perpendicular to the compression axis follows the same linear slope observed in the elastic regime. On the other hand, the decrease (in absolute value) in the elastic strains of grains oriented with the $\{10\bar{1}1\}$ and $\{10\bar{1}2\}$ grains perpendicular to the compression axis is accompanied by the increase (in absolute value) in the elastic strains of the 14H LPSO-phase, as measured during the tensile test. However, above 320 MPa, it is not possible to fit this diffraction peak because the substantial increase in the intensity of the {0002} peak overlaps the 14H LPSO-phase peak.

The behavior of the elastic strains of grains oriented with their $\{11\bar{2}0\}$ planes perpendicular to the compression axis is similar to that seen in grains oriented with $\{10\bar{1}0\}$ planes perpendicular to the compression axis. After yielding, the evolution of the elastic strain remains almost linear or asymptotic. The later will imply that these grains are deforming plastically, as in the tension test.

Finally, the {0002} diffraction peak can be fitted, especially after yield, where its intensity increases continuously (see Figure 8b). The increase in the {0002} diffraction peak is caused by the activation of tensile twinning in non-DRXed grains. After yielding, the elastic strain of twins decreases (in absolute value) from 6620 μ strains at 302 MPa to 5352 μ

strains at 320 MPa. Above this applied stress, elastic strain of twins increases (in absolute terms) much faster than seen in the elastic behavior up to 12,470 μ strains at 459 MPa.

Figure 9 shows the bright field images of the extruded samples tested in compression (Figure 9a,b) and tension (Figure 9c) up to the level of 2% of plastic deformation in the zone axis of B = [11$\bar{2}$0]. Under compression, it is possible to observe the presence of tensile twin in highly oriented non-DRXed grains, which induces a rotation of almost 90° with respect to the parent grain, as was reported in the in situ tests under compression. Twins are very thin, and can pass among the lamellae presented in these grains. At the same time, twins are not observed crossing across the complete grain diameter, since they are temporarily pinned in thick γ precipitates. Twins are not observed in DRXed grains, where a high dislocation density is generated. Under tension, no twins were observed in either non-DRX or DRXed grains. A high dislocation density was observed in between the lamellar precipitates.

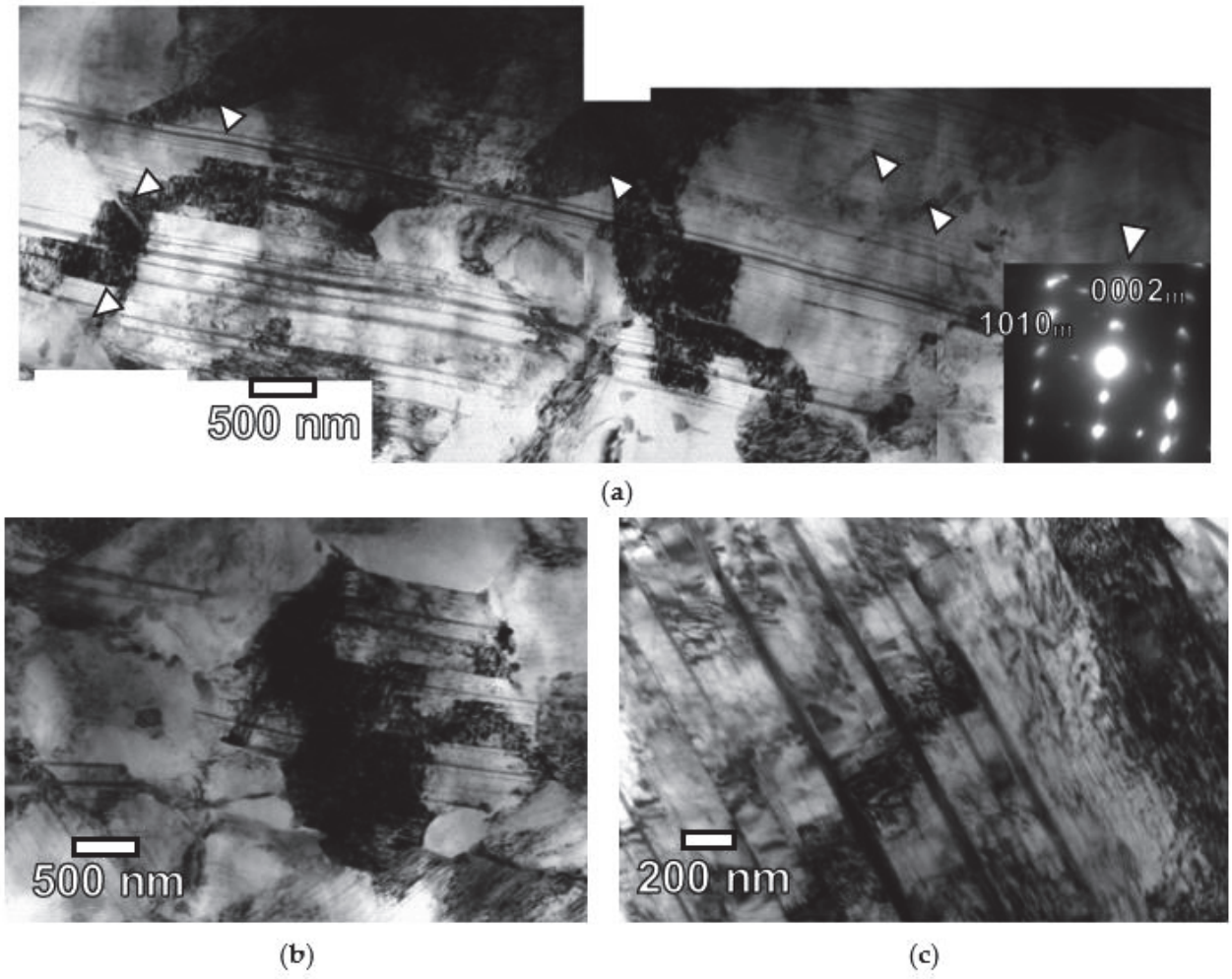

Figure 9. (**a**) Bright field image of a non-DRXed grain at the zone axis B = [11$\bar{2}$0], deformed 2% from plastic strain under compression. (**b**) Bright field image of a DRXed grain at the zone axis B = [11$\bar{2}$0] deformed 2% from plastic strain under compression. (**c**) Bright field image of a non-DRXed grain at the zone axis B = [11$\bar{2}$0] deformed 2% from plastic strain under tension.

4. Discussion

The microstructure of the extruded alloy exhibits a bimodal grain structure consisting of randomly oriented fine DRXed grains and non-DRXed grains, highly oriented, with their basal planes parallel to the extrusion direction. The volume fraction of non-DRXed grains measured in the alloy is lower (around 30% of volume fraction [30], using the same processing parameters) than that reported in $Mg_{97}Y_2Zn_1$ with similar volume fraction,

without the presence of the lamellar structure within the magnesium grains. It seems that lamellar precipitates facilitate the nucleation of DRXed grains at their interfaces.

The relative crystal orientation of both types of grains controls the activation of the different deformation systems of magnesium. The non-DRXed grains have their basal planes parallel to the tensile or compressive axis. Therefore, the activation of the basal slip system is inhibited in these grains. On the other hand, the activation of tensile twinning is activated only under compression. The crystal lattice is reoriented within twins, where the basal plane rotates 86° with the initial orientation. Therefore, the intensity of the (0002) diffraction peak increases when tensile twinning begins. Under tension, these grains cannot deform plastically and they behave in a purely elastic manner until the fracture. It would be expected that the presence of highly oriented non-DRXed grains would induce a strong tension–compression asymmetry in magnesium. However, the yield stress values are equal in both cases, and the tensile and compressive curves are similar up to the point of 3% plastic strain. Yang et al. [20] also reported, in an alloy with a similar composition but with a grain structure characterized mainly by highly oriented non-DRXed grains, the same tensile and compressive behavior at the beginning of the curve. They proposed that LPSO plates generated at the basal plane effectively impede both the dislocation motion and the twinning activity. It is interesting to note that in this study, the compression curve (from yield stress to 3% of plastic deformation) is slightly higher, compared to the tensile curve. The main microstructural difference, compared to the study of Yang et al., is the presence of dense LPSO phase observed in this study. We have previously observed that LPSO fiber induces a higher mechanical strength in the alloy, which increases with the increase in the volume fraction of the LPSO phase.

The randomly oriented DRXed grains are favorably oriented for the activation of the slip of <a> dislocation along the basal slip. Therefore, grains oriented with the $\{10\bar{1}1\}$ and $\{10\bar{1}2\}$ planes perpendicular to the tensile or compressive axes lose their linearity only at the point of macroscopic yield stress. Therefore, independently of the stress mode, the beginning of plastic deformation is controlled by the DRXed grains. Since the beginning of the macroscopic plastic deformation is controlled by the activation of the basal slip in the DRXed sample, no differences would be expected between yield stress under tension and compression at the beginning of the test. However, when twinning is activated in non-DRXed grains, the applied stress and work-hardening in the compression tests increase (around 3% of plastic strain). TEM observation demonstrated that twinning was active at 2% plastic deformation. At the same time, twins are extremely thin, due to the presence of lamellar-shape precipitates that delay their coalescence and growth. Yang et al. [18] have shown that LPSO plates plastically deform when they are engulfed by the twins, explaining the delay of the process of the coalescence and growth of twins.

During the initial state of plastic deformation, DRXed grains oriented with the $\{10\bar{1}1\}$ and $\{10\bar{1}2\}$ planes perpendicular to the loading direction undergo a strong relaxation once the alloy yields. Since this strain difference, measured using Equation (1), is purely elastic, the relaxation stress could be grossly estimated using the Young Modulus for the planes obtained from the slope of the internal strain as a function of the applied stress in the elastic zone ($\Delta\sigma = E(hkil) \times \Delta\varepsilon_{elas}$). The relaxation stresses in grains with $\{10\bar{1}1\}$ and $\{10\bar{1}2\}$ planes perpendicular to the loading axis after yield stress are listed in Table 1. These stresses should be borne by stiff phases, i.e., the LPSO phase, or other magnesium grains whose crystallographic orientation inhibits the activation of dislocation slip or twinning system ("hard grains" [39]). The LPSO phase exhibits a higher Young Modulus (around 55 MPa) compared to that of the magnesium phase [40,41]. The relaxed stresses are higher in the tension test than in the compression, indicating that non-DRXed grains behave as a reinforcing phase only in tension tests.

Finally, it is interesting to note that from the point of view of the design of these alloys, both kinds of LPSO phases (LPSO lamellar-shape precipitates within magnesium grains and LPSO fiber at grain boundaries) are contributing to the reinforcement of the magnesium phase, although in two different ways. While the LPSO lamellar-shape precipitate show

a high level of interaction with dislocations and twins within the magnesium grains, the LPSO fibers assumed an additional stress transferred by the magnesium phase.

Table 1. Internal strains and relaxed stresses at the beginning of macroscopic yield stress in the tensile and compression tests.

Plane	Internal Strains (μ Strains)	Stress (MPa)	Internal Strains (μ Strains)	Stress (MPa)
	Tension		Compression	
$\{10\bar{1}1\}$	2033	87	1707	73
$\{10\bar{1}2\}$	3057	131	2501	108

5. Conclusions

The evolution of the internal strains during in situ tension and compression tests has been measured in the extruded $Mg_{97}Gd_2Zn_1$ alloy containing Long-Period Stacking Ordered (LPSO) phase and a lamellar structure within the magnesium phase, using synchrotron diffraction radiation. The following conclusions can be drawn:

(1) The presence of the lamellar-shape precipitates within the Mg phase before the high temperature extrusion process promotes the recrystallization process due to the nucleation of fine equiaxed grains at the interface between the magnesium matrix and the lamellar-shape precipitates.
(2) The macroscopic yielding is controlled by the activation of the basal slip systems in the DRXed grains, leading to a low tension–compression asymmetry. During the onset of the plastic regime, these grains can release a significant part of the assumed stress, since they can transfer part of it towards hard phases.
(3) The elasto-plastic behavior of non-DRXed grains depends on the stress mode, tension and compression. Thus, these grains act as a reinforcing phase during tensile testing. Under compression, the activation of tensile twinning is activated. The presence of lamellar-shape precipitates delays the propagation of lenticular thin twins through the non-DRXed grains.

Author Contributions: Conceptualization, G.G. and P.P.; Methodology, G.G., J.M., P.P., R.B., H.L., S.K.K., E.M., N.S. and P.A.; Formal analysis, G.G. and J.M.; Investigation, G.G., J.M., P.P., R.B., H.L., S.K.K., E.M., N.S. and P.A.; Resources, H.L. and S.K.K.; Writing—original draft, G.G. and P.P.; Writing—review and editing, G.G., J.M., P.P., R.B., H.L., S.K.K., E.M., N.S. and P.A.; Funding acquisition, G.G. and P.A. All authors have read and agreed to the published version of the manuscript.

Funding: This research was funded by the Spanish Ministry of Science, Innovation and Universities, grant number TED2021-129580B-I00.

Data Availability Statement: The data presented in this study are available in this article.

Acknowledgments: Authors would like to acknowledge the Electron Microscopy Laboratory of CENIM-CSIC. The DeutchesElektronen-Synchrotron DESY is also acknowledged for the provision of beamtime at the P07B beamline of the Petra III synchrotron facility.

Conflicts of Interest: The authors declare no conflicts of interest. The funders had no role in the design of the study; in the collection, analyses, or interpretation of data; in the writing of the manuscript; or in the decision to publish the results.

References

1. Inoue, A.; Kawamura, Y.; Matsushita, M.; Hayashi, K.; Koike, J. Novel hexagonal structure and ultrahigh strength of magnesium solid solution in the Mg-Zn-Y system. *J. Mater. Res.* **2001**, *16*, 1894–1900. [CrossRef]
2. Yamasaki, M.; Hashimoto, K.; Hagihara, K.; Kawamura, Y. Effect of multimodal microstructure evolution on mechanical properties of Mg-Zn-Y extruded alloy. *Acta Mater.* **2011**, *59*, 3646–3658. [CrossRef]
3. Xua, D.; Hana, E.H.; Xua, Y. Effect of long-period stacking ordered phase on microstructure, mechanical property and corrosion resistance of Mg alloys: A review. *Prog. Nat. Sci. Mater. Inter.* **2016**, *26*, 117–128. [CrossRef]

4. Hagihara, K.; Kinoshita, A.; Sugino, Y.; Yamasaki, M.; Kawamura, Y.; Yasuda, H.Y. Effect of long-period stacking ordered phase on mechanical properties of Mg97Zn1Y2 extruded alloy. *Acta Mater.* **2010**, *58*, 6282–6292. [CrossRef]
5. Yiwen, C.; Jingya, W.; Weisen, Z.; Quan, L.; Mingdi, Y.; Tao, Y.; Xiaoqin, Z. CALPHAD-guided design of Mg-Y-Al alloy with improved strength and ductility via regulating the LPSO phase. *Acta Mater.* **2024**, *263*, 119521.
6. Itoi, T.; Seimiya, T.; Kawamura, Y.; Hirohashi, M. Long period stacking structures observed in Mg97Zn1Y2 alloy. *Scr. Mater.* **2004**, *51*, 107–111. [CrossRef]
7. Kawamura, Y.; Yamasaki, M. Formation and Mechanical Properties of Mg97Zn1RE2 Alloys with Long-Period Stacking Ordered Structure. *Mater. Trans.* **2007**, *48*, 2986–2992. [CrossRef]
8. Ding, S.J.; Xu, L.D.; Cai, X.C.; Gu, S.X.Y.; Wen, K.K.; Yu, H.; Chen, Z.; Sun, B.R.; Xin, S.W.; Shen, T.D. Exceptional thermal stability of ultrafine-grained long-period stacking ordered Mg alloy. *Rare Met.* **2022**, *41*, 1537–1542. [CrossRef]
9. Harjo, S.; Gong, W.; Aizawa, K.; Kawasaki, T.; Yamasaki, M. Strengthening of αMg and long-period stacking ordered phases in a Mg-Zn-Y alloy by hot-extrusion with low extrusion ratio. *Acta Mater.* **2023**, *255*, 119029. [CrossRef]
10. Tokuzumi, T.; Mitsuhara, M.; Yamasaki, S.; Inamura, T.; Fujii, T.; Nakashima, H. Role of disclinations around kink bands on deformation behavior in Mg-Zn-Y alloys with a long-period stacking ordered phase. *Acta Mater.* **2023**, *248*, 118785. [CrossRef]
11. Yamasaki, M.; Anan, T.; Yoshimoto, S.; Kawamura, Y. Mechanical properties of warm-extruded Mg-Zn-Gd alloy with coherent 14H long periodic stacking ordered structure precipitate. *Scr. Mater.* **2005**, *53*, 799–803. [CrossRef]
12. Chen, B.; Lin, D.L.; Zeng, X.Q.; Lu, C. Microstructure and mechanical properties of ultrafine grained Mg97Y2Zn1 alloy processed by equal channel angular pressing. *J. Alloys Compd.* **2007**, *440*, 94–100. [CrossRef]
13. Yamasaki, M.; Sasaki, M.; Nishijima, M.; Hiraga, K.; Kawamura, Y. Formation of 14H long period stacking ordered structure and profuse stacking faults in Mg–Zn–Gd alloys during isothermal aging at high temperature. *Acta Mater.* **2007**, *55*, 6798–6805. [CrossRef]
14. Nie, J.F.; Oh-ishi, K.; Gao, X.; Hono, K. Solute segregation and precipitation in a creep-resistant Mg-Gd-Zn alloy. *Acta Mater.* **2008**, *56*, 6061–6076. [CrossRef]
15. Chun, Y.B.; Geng, J.; Stanford, N.; Davies, C.H.J.; Nie, J.F.; Barnett, M.R. Processing and properties of Mg-6Gd-1Zn-0.6Zr: Part 1—Recrystallisation and texture development. *Mat. Sci. Eng. A* **2011**, *528*, 3653–3658. [CrossRef]
16. Geng, J.; Chun, Y.B.; Stanford, N.; Davies, C.H.J.; Nie, J.F.; Barnett, M.R. Processing and properties of Mg-6Gd-1Zn-0.6Zr: Part 2. Mechanical properties and particle twin interactions. *Mat. Sci. Eng. A* **2011**, *528*, 3659–3665. [CrossRef]
17. Sato, K.; Tashiro, S.; Matsunaga, S.; Yamaguchi, Y.; Kiguchi, T.; Konno, T.J. Evolution of long-period stacking order (LPSO) in Mg97Zn1Gd2 cast alloys viewed by HAADF-STEM multi-scale electron tomography. *Phil. Mag.* **2018**, *98*, 1945–1960. [CrossRef]
18. Yang, Q.; Lv, S.; Yan, Z.; Yan, Z.; Hua, X.; Qui, X.; Meng, J. Nano-steps in long-period stacking ordered structures for ductility asymmetry of a strong-textured Mg-Gd-Zn alloy. *Mater. Des.* **2021**, *201*, 109482. [CrossRef]
19. Nishijima, M.; Hiraga, K.; Yamasaki, M.; Kawamura, Y. Characterization of β′ Phase Precipitates in an Mg-5 at%Gd Alloy Aged in a Peak Hardness Condition, Studied by High-Angle Annular Detector Dark-Field Scanning Transmission Electron Microscopy. *Mater. Trans.* **2006**, *47*, 2109–2112. [CrossRef]
20. Li, Q.; Song, J.; Chen, Y.; Zhang, Q.; Zhu, Q.; Liu, Y.; Wang, J.; Zeng, X. In-situ TEM characterization of basal dislocations between nano-spaced long-period stacking ordered phases in MgYZn alloy. *Scr. Mater.* **2023**, *235*, 115601. [CrossRef]
21. Garces, G.; Máthis, K.; Barea, R.; Medina, J.; Pérez, P.; Stark, A.; Schell, N.; Adeva, P. Effect of precipitation in the compressive behavior of high strength Mg-Gd-Y-Zn extruded alloy. *Mat. Sci. Eng. A* **2019**, *768*, 138452. [CrossRef]
22. Ji, Z.K.; Qiao, X.G.; Yuan, L.; Cong, F.G.; Wang, G.J.; Zheng, M.Y. Exceptional fracture toughness in a high-strength Mg alloy with the synergetic effects of bimodal structure, LPSO, and nanoprecipitates. *Scr. Mater.* **2023**, *236*, 115675. [CrossRef]
23. Li, J.; Wang, F.; Zeng, J.; Zhao, C.; Jin, L.; Dong, J. Effect of the interspacing of intragranular lamellar LPSO phase on dynamic recrystallization behaviors of Mg-Gd-Y-Zn-Zr alloys. *Mater. Char.* **2022**, *193*, 112326. [CrossRef]
24. Su, N.; Deng, Q.; Wu, Y.; Peng, L.; Yang, K.; Chen, Q. Deformation-induced dissolution of long-period stacking ordered structures and its re-precipitation in a Mg-Gd-Zn-Mn alloy. *Mater. Char.* **2021**, *171*, 110756. [CrossRef]
25. Schmidt, J.; Beyerlein, I.J.; Knezevic, M.; Reimers, W. Adjustment of the Mechanical Properties of Mg2Nd and Mg2Yb by Optimizing Their Microstructures. *Metals* **2021**, *11*, 377. [CrossRef]
26. Frydrych, K.; Libura, T.; Kowalewski, Z.; Maj, M.; Kowalczyk-Gajewska, K. On the role of slip, twinning and detwinning in magnesium alloy AZ31B sheet. *Mater. Sci. Eng. A* **2021**, *813*, 141152. [CrossRef]
27. Huang, X.; Xin, Y.; Cao, Y.; Huang, G.; Li, W. A quantitative study on planar mechanical anisotropy of a Mg-2Zn-1Ca alloy. *J. Mater. Sci. Technol.* **2022**, *109*, 30. [CrossRef]
28. Xu, J.; Guan, B.; Xin, Y.; Wei, X.; Huang, G.; Liu, C. A weak texture dependence of Hall–Petch relation in a rare-earth containing magnesium alloy. *J. Mater. Sci. Technol.* **2021**, *99*, 251. [CrossRef]
29. Kleiner, S.; Uggowitzer, P.J. Mechanical anisotropy of extruded Mg-6% Al-1% Zn alloy. *Mat. Sci. Eng. A* **2004**, *379*, 258. [CrossRef]
30. Garces, G.; Medina, J.; Perez, P.; Stark, A.; Lim, H.K.; Kim, S.; Schell, N.; Adeva, P. Analysis of the Microstructure Role in the Yield Asymmetry of Extruded Mg-LPSO Alloys Using In Situ Diffraction Experiments. *JOM* **2022**, *74*, 2609–2621. [CrossRef]
31. Schindelin, J.; Arganda-Carreras, I.; Frise, E.; Kaynig, V.; Longair, M.; Pietzsch, T.; Preibisch, S.; Rueden, C.; Saalfeld, S.; Schmid, B.; et al. Fiji: An open-source platform for biological-image analysis. *Nat. Methods* **2012**, *9*, 676–682. [CrossRef] [PubMed]
32. Zhou, X.; Ha, C.; Yi, S.; Bohlen, J.; Schell, N.; Chi, Y.; Zheng, M.; Brokmeier, H.G. Texture and Lattice Strain Evolution during Tensile Loading of Mg–Zn Alloys Measured by Synchrotron Diffraction. *Metals* **2020**, *10*, 124. [CrossRef]

33. Lutterotti, L.; Bortolotti, M.; Ischia, G.; Lonardelli, I.; Wenk, H.R. Rietveld Texture Analysis from Diffraction Images. *Z. Krist. Suppl.* **2007**, *1*, 125–130. [CrossRef]
34. Schindelin, J.; Rueden, C.T.; Hiner, M.C.; Eliceiri, K.W. The ImageJ ecosystem: An open platform for biomedical image analysis. *Mol. Reprod. Dev.* **2015**, *82*, 518–529. [CrossRef] [PubMed]
35. Lutterotti, L.; Matthies, S.; Wenk, H.R.; Schultz, A.S.; Richardson, J.W. Combined texture and structure analysis of deformed limestone from time-of-flight neutron diffraction spectra. *J. Appl. Phys.* **1997**, *81*, 594–600. [CrossRef]
36. Egusa, D.; Abe, E. The structure of long period stacking/order Mg-Zn-RE phases with extended non-stoichiometry ranges. *Acta Mater.* **2012**, *60*, 166–178. [CrossRef]
37. Agnew, S.R.; Mulay, R.P.; Polesak, F.J., III; Calhoun, C.A.; Bhattacharyya, J.J.; Clausen, B. In situ neutron diffraction and polycrystal plasticity modeling of a Mg-Y-Nd-Zr alloy: Effects of precipitation on individual deformation mechanisms. *Acta Mater.* **2013**, *61*, 3769–3780. [CrossRef]
38. Zhu, Y.M.; Morton, A.J.; Nie, J.F. The 18R and 14H long-period stacking ordered structures in Mg-Y-Zn alloys. *Acta Mater.* **2010**, *58*, 2936–2947. [CrossRef]
39. Agnew, S.R.; Brown, D.W.; Tome, C.N. Validating a polycrystal model for the elastoplastic response of magnesium alloy AZ31 using in situ neutron diffraction. *Acta Mater.* **2006**, *54*, 4841–4852. [CrossRef]
40. Tane, M.; Nagai, Y.; Kimizuka, H.; Hagihara, K.; Kawamura, Y. Elastic properties of an Mg-Zn-Y alloy single crystal with a long-period stacking-ordered structure. *Acta Mater.* **2013**, *61*, 6338–6351. [CrossRef]
41. Tane, M.; Kimizuka, H.; Hagihara, K.; Suzuki, S.; Mayama, T.; Sekino, T.; Nagai, Y. Effects of stacking sequence and short-range ordering of solute atoms on elastic properties of Mg-Zn-Y alloys with long-period stacking ordered structures. *Acta Mater.* **2015**, *96*, 170–188. [CrossRef]

MDPI AG
Grosspeteranlage 5
4052 Basel
Switzerland
Tel.: +41 61 683 77 34

Metals Editorial Office
E-mail: metals@mdpi.com
www.mdpi.com/journal/metals

Academic Open
Access Publishing

mdpi.com

ISBN 978-3-7258-5634-3